Satellite

STUDY OF ENERGETIC PARTICLES ABOVE THE ~~EARTH'S~~ ATMOSPHERE

THESIS

Submitted by

GREGOR EUGEN MORFILL

For the Degree of

DOCTOR OF PHILOSOPHY

in the

UNIVERSITY OF LONDON

MAY 1971

ACKNOWLEDGEMENTS

I would like to thank Professor H. Elliot for providing me with the opportunity of working in the Space Physics Group at Imperial College.

I would also like to thank my supervisor, Dr. J.J. Quenby, for suggesting this work and for his constant encouragement.

I am indebted to Dr. A. Engel for making available to me the experimental results obtained so far with the UK5 prototype detector, Dr. R.J. Hynds and Dr. G. Haskell for many stimulating discussions, and Dr. A. Durney for successfully getting the S.28 detector into orbit.

Thanks are due to Dr. J. Engelmann of SACLAY for the S.72 data and Dr. G. Thomas of the Radio and Space Research Station, Slough, for cooperation with ESRO -1 data.

I would also like to thank Mrs. A. Evans for her invaluable help with the S.28 data processing.

Special thanks are due to my wife for typing and proof-reading this thesis.

Finally, I wish to thank the Science Research Council for providing the grant which permitted the execution of this work; and the Cosmic Ray and Space Physics Group as a whole with whom it has been a pleasure to work.

TABLE OF CONTENTS

PART I

DESIGN OF A SATELLITE DETECTOR TO MEASURE THE SPECTRA OF GALACTIC X-RAY SOURCES FROM 20 KEV TO 1 MEV, AND TO STUDY PULSED EMISSIONS FROM KNOWN PULSARS

		Page
1.	Abstract	1
2.	Introduction	2
3.	Review of x-ray Production Processes	7
	1. Processes Leading to a Continuous Spectrum	7
	2. Background formed by Unresolved Sources	10
	3. Line Structure	11
4.	Scientific Aim of the UK5 Project	13
5.	Design Considerations	14
	1. Active, Well-shaped Collimator	17
	2. Active Anticollimator	22
	3. Active Honeycomb Collimator	23
6.	Detailed Detector Design	24
	1. Monte Carlo Design Methods	24
	2. Comparison of Active and Passive Collimators	26
	3. The x-ray Telescope	30
	4. Spectrometer Properties	30
	5. Detector Operation	39

PART 2

HIGH ENERGY SOLAR PROTONS AND COSMIC RAYS. ANALYSIS OF DATA FROM EXPERIMENT S.28 ON THE ESRO II SPACECRAFT

		Page
1.	Abstract	51
2.	Description of the Detector	52
3.	Calculation of Geometric Factor	56
	1. Nominal Value	56
	2. Low Energy Contribution to Channel 5	57
	3. Energy Dependence of Geometric Factor	61
4.	Checking detector in Flight	67
	1. Cosmic Ray Time Variation	67
	2. Calculation of Effective Geometric Factor	68

Page

3. Longitude survey at Equator 73
4. Latitude Variation of Cosmic Ray Protons 74
5. Response to Electrons 75
6. Inner Belt Studies and Detector Saturation 78

5. The Entry of Solar Protons over the Polar Caps ... 94
1. Introduction 94
2. Magnetospheric Field Model 96
3. Structure Caused by Anisotropies 105
4. Structure Caused by Gradients 143
5. Delayed Entry into the Tail 146
6. Electrons 148
7. February 25th Flare 149
8. November 18th Flare 158

Appendix 1 178
Appendix 2 182

PART I

DESIGN OF A SATELLITE DETECTOR TO MEASURE THE SPECTRA OF GALACTIC X-RAY SOURCES FROM 20 KEV TO 1 MEV, AND TO STUDY PULSED EMISSIONS FROM KNOWN PULSARS

1. ABSTRACT

Electromagnetic radiation travels in straight lines (apart from small relativistic effects), and thus preserves a great deal of information about its point of emission and the galactic medium between the source and the observer. In the optical and radio wavelength range, the atmosphere is transparent, and measurements can be made from the ground. For x-ray and γ-ray measurements balloons, rockets and satellites have to be used.

Satellites are by far the most useful vehicle for x-ray experiments, since they combine long observation time with good attitude control, possibilities for pointing and scanning and the ability to study time variations over long periods of time with the same detector. The only drawback seems to be the cost of satellite programs, and, for the smaller satellites, weight and power restrictions.

The present work was carried out during the design stage of the Imperial College x-ray experiment, code named 'experiment F', which is to be launched on the UK5 satellite during 1973. Design concepts and calculations on the detector configuration, and details of the data analysis to be performed are given. Comparisons are made with measurements performed on the prototype model wherever these are available.

2. INTRODUCTION

Theories of x-ray production mechanisms applied to the diffuse component of cosmic x-rays, sources and pulsed emissions are given, and the role of experiment F in obtaining further information on these is examined.

A great deal of information has been obtained in recent years about the diffuse component of cosmic x-rays and about x-ray sources. Fig. 1 shows the diffuse x-ray spectrum as measured by several observers, and Fig. 2 gives a map of some of the stronger discrete sources which have been observed at energies of a few KeV (J. F. Dolan, 1970; F. D. Seward, 1970).

The 'diffuse' x-ray background has been observed to be isotropic to within the accuracy of most experiments ($\sim$ 10%). A line source, coinciding with the galactic plane, seems to exist at energies of a few KeV (Cooke, et. al., 1969) and at energies at around 100 MeV (Clark, et.al., 1968; Kniffen, et. al., 1970). Fig. 3 shows recent measurements and upper limits of this source. The origin of this line source is at present not well understood. The 100 MeV excess could be due to $\pi_o \rightarrow 2\gamma$ decays in nuclear interaction, or due to inverse Compton scattering from a galactic far infrared radiation. The strong correlation of γ-ray intensity with radio noise, rather than integral matter path length, (Cowsik and Pal, 1969) supports the Compton process, but direct measurement of this line at intermediate energies is necessary. The low energy anisotropy could be produced by unresolved x-ray sources, or by inverse Compton scattering.

The interstellar medium is transparent to x-rays of energies above a few KeV (Felten and Gould, 1966). This means that, in the absence of an isotropic distribution of galactic sources, the diffuse x-rays must be extragalactic in origin (Gould, 1965; Felten and Morrison, 1966). The two theories most discussed currently, which seek to explain the diffuse flux, involve inverse Compton scattering of high energy electrons by an ambient intergalactic $3^{\circ}K$ blackbody radiation, or the

superposition of many extragalactic x-ray sources. The diffuse x-ray flux then gives vital information about high energy processes in galaxies or in intergalactic space (Gould, 1967; Morrison, 1967); large scale structure of the universe can be deduced from angular variations in the diffuse flux; and since sources at distances of the Hubble radius ($R_H = \frac{C}{H} \simeq 10^{28}$ cm) must contribute significantly to the diffuse flux in both theories, the energy spectrum and intensity must contain information on evolutionary effects of the universe.

Observation of galactic x-ray sources will provide information on explosive events in stellar evolution, x-ray production mechanisms can be resolved provided that spectra are observed over a wide energy range, and time variations - either regular as in pulsars, or irregular as in Sco XR-1 and Cyg XR-1 (Rossi, 1967) will, in conjunction with measurements at optical and radio wavelengths, provide a good observational basis for models of the sources under study. Observation of extra-galactic sources could decide between the two rival theories on the diffuse background by providing an average x-ray intensity emitted from a typical galaxy. Studies involving clusters of galaxies would be most useful for this purpose.

Line emission, due to electron-positron annihilation near rest, the decay of r-process elements, i.e. heavy elements predicted to be formed during supernova explosions, and π_o decay would give a useful estimate of number densities of these particles, shed light on energetic processes in the universe, and increase understanding of the occurrence of matter with atomic number beyond iron. (Clayton, 1965)

Experiment F, the design of which will be described, is intended to study x-rays in the energy range 20 KeV - 1 MeV, and will provide new information on some of the outstanding problems just discussed.

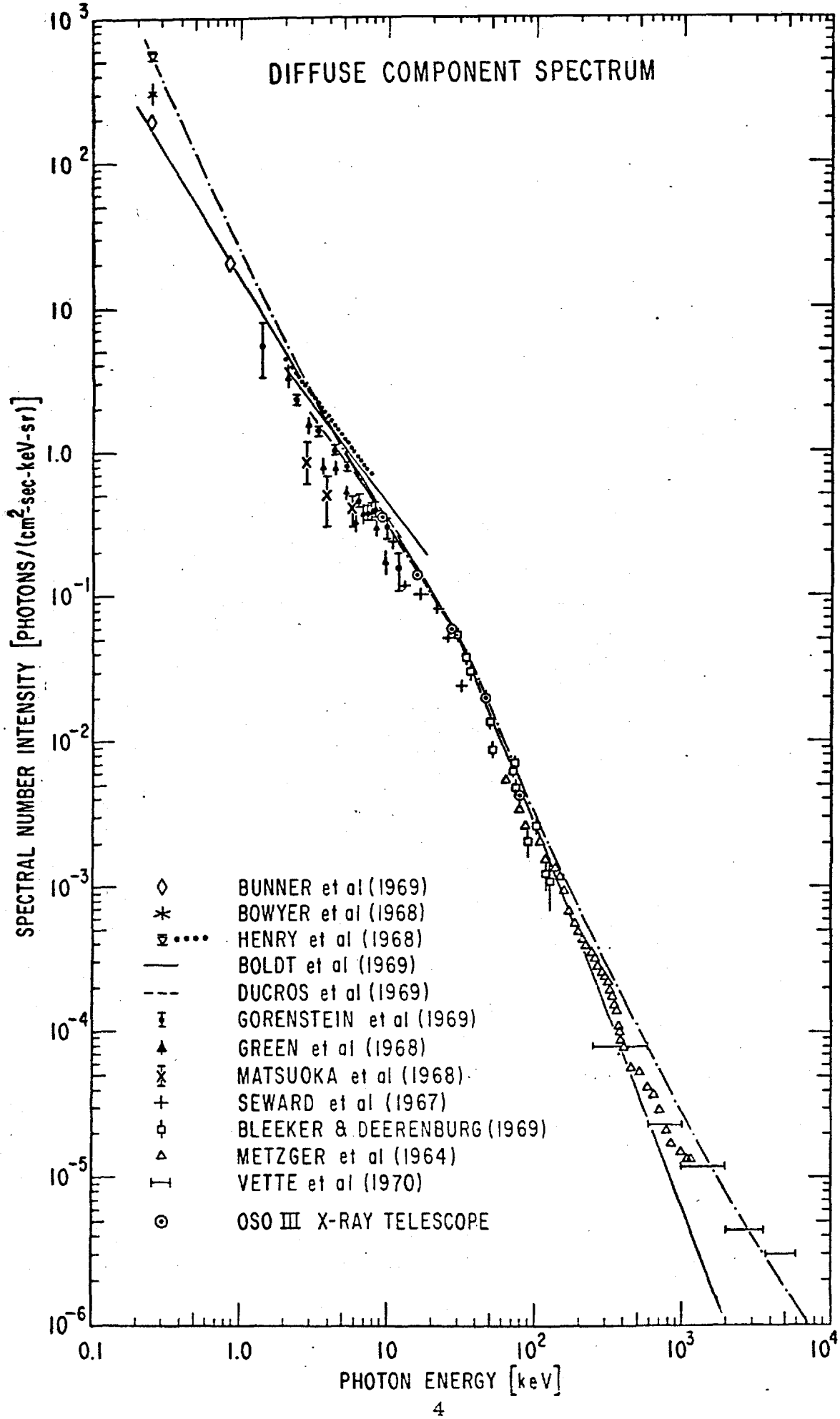
DIFFUSE COMPONENT SPECTRUM
SPECTRAL NUMBER INTENSITY [PHOTONS/(cm²-sec-keV-sr)]
PHOTON ENERGY [keV]
BUNNER et al (1969)
BOWYER et al (1968)
HENRY et al (1968)
BOLDT et al (1969)
DUCROS et al (1969)
GORENSTEIN et al (1969)
GREEN et al (1968)
MATSUOKA et al (1968)
SEWARD et al (1967)
BLEEKER & DEERENBURG (1969)
METZGER et al (1964)
VETTE et al (1970)
OSO III X-RAY TELESCOPE

FIGURE 1

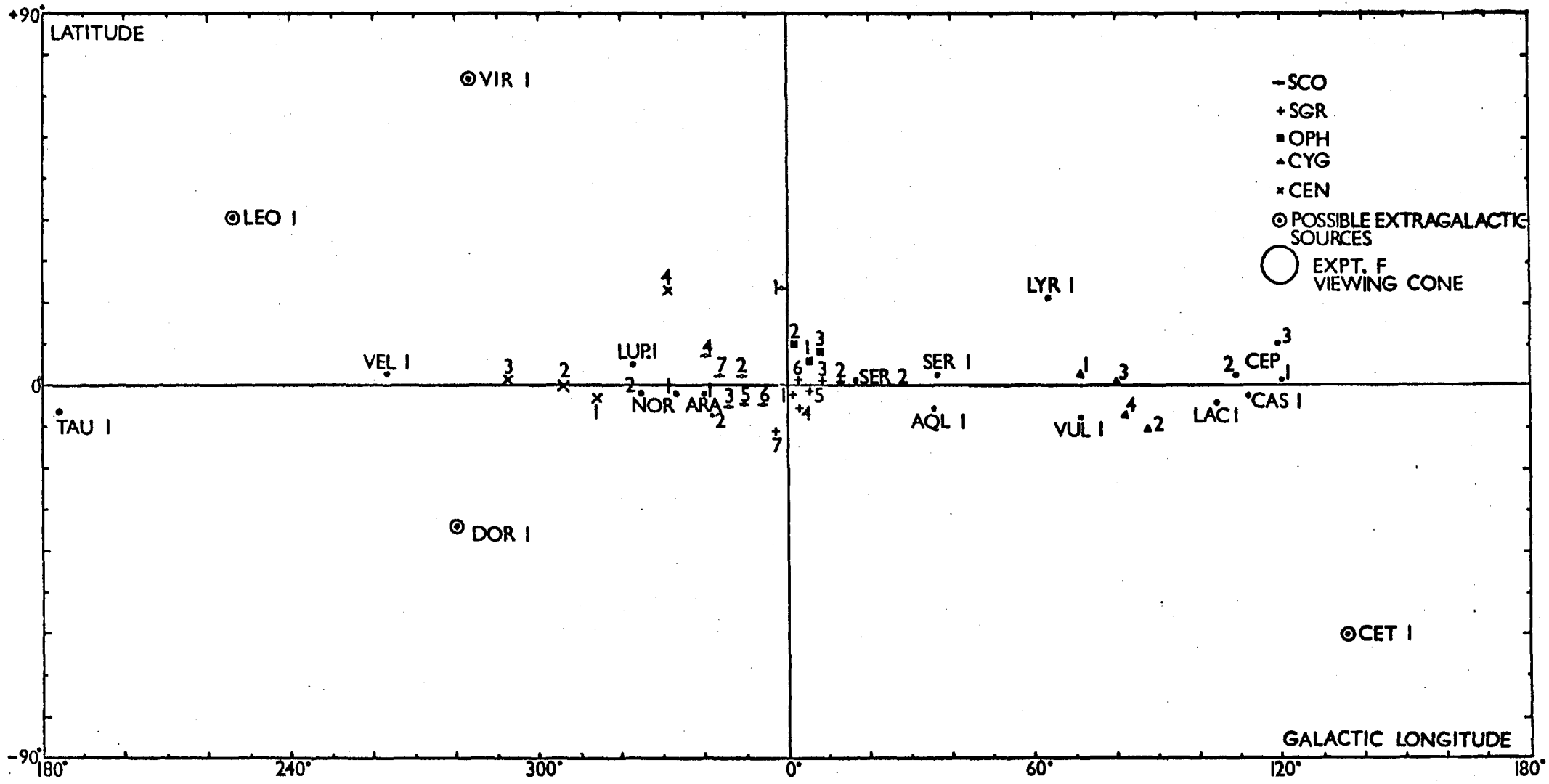

Fig. 2

Location of the stronger observed x-ray sources in galactic co-ordinates. Also shown is the experiment F viewing cone (full width at half maximum).

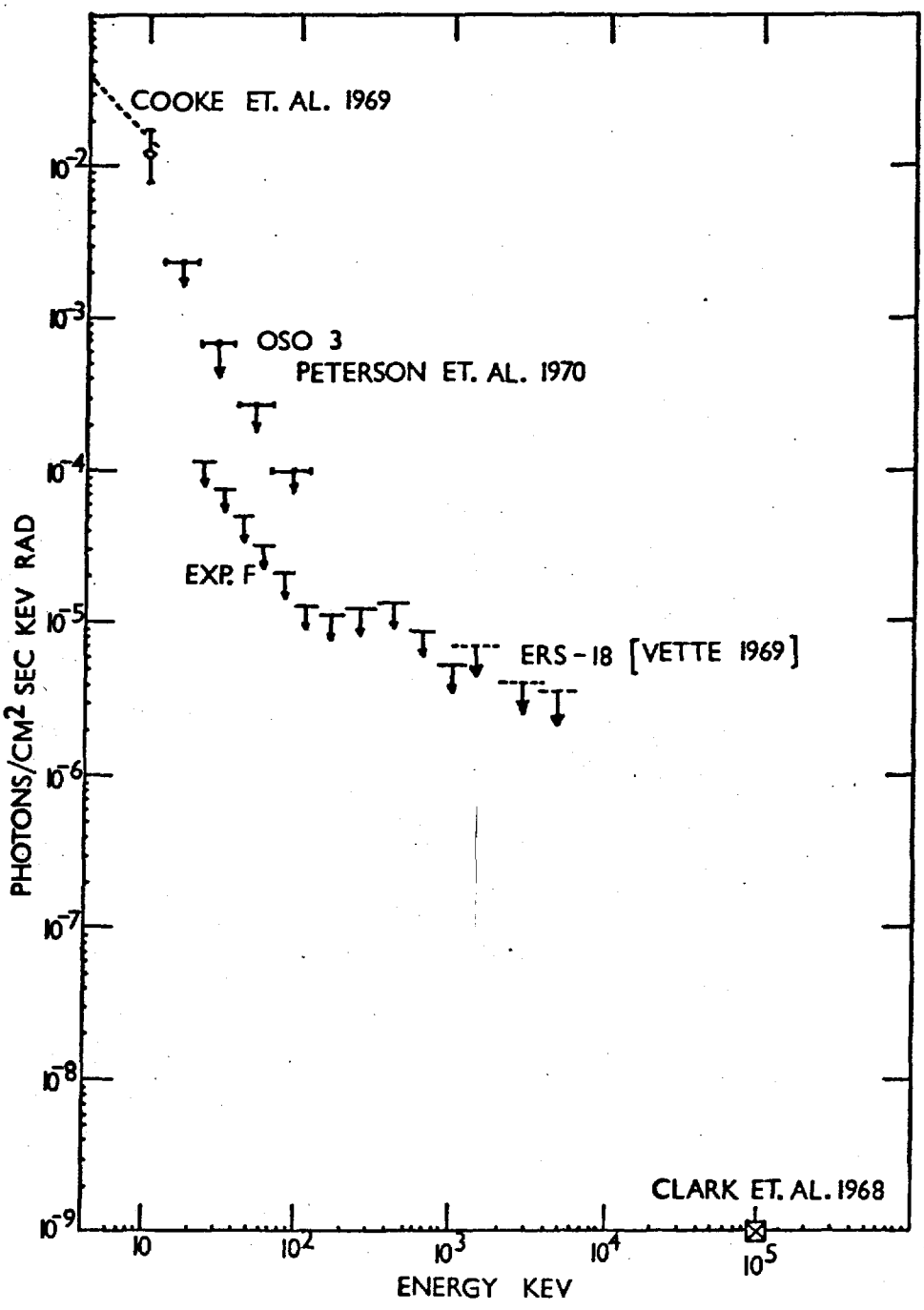

Fig. 3

Measurements and upper limits of the line x-ray flux along the galactic disc at different energies. Also shown are the UK5 upper limits calculated for a successful completion of the 40-day galactic disc scanning programme.

3. REVIEW OF X-RAY PRODUCTION PROCESSES

3.1 PROCESSES LEADING TO A CONTINUOUS SPECTRUM

Continuous photon spectra are produced by Bremsstrahlung emitted by relativistic electrons and positrons which are slowed down in the interstellar gas, or by inverse Compton interactions where relativistic electrons and positrons are scattered by thermal photons (e.g. the $3^{\circ}K$ black body radiation, or perhaps the $8^{\circ}K$ galactic far infrared radiation observed by Shivanandan et.al. (1968, 1969)), or by synchrotron radiation emitted by electrons and positrons moving in magnetic fields. Although continuous spectra are obtained for instance in the electron-positron annihilation in flight, processes which basically lead to line emission will be discussed in section 3.3.

The directional differential photon flux $F(E)$ is

$$F(E) = \frac{1}{4\pi E} \int_0^{\infty} f(E)\, d\underline{r} \qquad (3.1.1)$$

where $f(E)$ is the energy lost in the range E to E + dE by interactions in unit volume of space. This is assumed to be due to an isotropic particle distribution at the position $\underline{r}$, so that the factor $\frac{1}{4\pi}$ changes the expression into a directional flux. The factor $\frac{1}{E}$ converts the expression from an energy flux to a photon flux. The integration over $d\underline{r}$ takes place throughout the region of interest along the line of sight.

The electrons and positrons responsible for the spectra to be discussed here, have been observed to have a power law energy spectrum,

$$I(\gamma) = K\, \gamma^{-a}$$

where γ is the 'energy factor' expressed as a function of rest energy, i.e. $\gamma = E_e/m_e c^2$

Hence $$f(E) = \int_{\gamma = 1}^{\infty} I(\gamma)\, S_x(\gamma, E)\, d\gamma$$

$S_x(\gamma, E)$ is the energy loss rate of an electron with energy factor γ in the photon production process x. For a given interaction process, and particle energy factor γ, the photon production cross section has a maximum at a characteristic energy E_x. If the particle spectrum is continuous, the resulting photon energy spectrum will be continuous, and thus we can replace the curve of $S_x(\gamma, E)$ v. E with a delta-function without introducing great error, i.e.

$$S_x(\gamma, E) = S_x(\gamma) \cdot \delta(E - E_x) \qquad (3.1.2)$$

where $S_x(\gamma)$ is the total energy emitted by the electron,

$$S_x(\gamma) = \int_0^{\infty} S_x(\gamma, E)\, dE$$

Using the calculations of Gould and Burbidge (1965) and Felten and Morrison (1966) we get :

1) Bremsstrahlung in local hydrogen density n_H

$$S_B(\gamma) = 4 m_o c^3 r_o^3 \alpha_f\, n_H\, \gamma \log\left(\frac{1}{\alpha_f}\right) \qquad (3.1.3)$$

$$E_B = m_o c^2 \gamma$$

2) Synchrotron radiation in field $|\underline{H}|$

$$S_s(\gamma) = \frac{2}{3} c r_o^2 |\underline{H}|^2 \cdot \gamma^2 \qquad (3.1.4)$$

$$E_s = 2\pi\hbar\nu_L \gamma^2$$

3) Inverse Compton scattering with photon density ρ, temperature T

$$S_c(\gamma) = \frac{4}{3}\left(\frac{8\pi}{3} r_o^2\right) c\rho\gamma^2 \qquad (3.1.5)$$

$$E_c = 3.6\ kT\gamma^2$$

Here $r_o = \frac{e^2}{m_o c^2} = 2.8 \times 10^{-13}$ cm is the classical electron radius

$\alpha_f = 1/137$ is the fine structure constant

$\nu_L = \frac{e|\underline{H}|}{2\pi m_o c}$ is the Larmor frequency

The differential photon flux (photons/cm^2 ster sec KeV) is then :

$$1)\quad F_B(E) = \frac{c r_o^2 \alpha_f \log\left(\frac{1}{\alpha_f}\right)}{\pi m_o c^2} \int_o^\infty \left(\frac{m_o c^2}{E}\right)^a Kn_H\, dr \qquad (3.1.6)$$

provided $E > m_o c^2 \triangleq 0.511$ MeV

$$2)\quad F_s(E) = \frac{c r_o^2}{6\pi} \int_o^\infty \left(\frac{m_o c}{\hbar e}\right)^{\frac{1}{2}(3-a)} K|\underline{H}|^{\frac{1}{2}(1+a)} E^{-\frac{1}{2}(1+a)} dr \qquad (3.1.7)$$

$$3)\quad F_c(E) = \frac{4 c r_o^2}{9} \int_o^\infty K\rho\,(3.6\ kT)^{\frac{1}{2}(a-3)} E^{-\frac{1}{2}(1+a)} dr \qquad (3.1.8)$$

The constraints on the electron energy for the inverse Compton process are 10^3 eV $< \gamma m_o c^2 < 10^9$ eV. The lower energy limit is obtained from the characteristic cosmic expansion time $\tau_c = \frac{1}{3} H^{-1} \triangleq 10^{17}$ sec, (H = Hubble constant) using the steady state condition

$$-\left(\frac{\partial\gamma}{\partial t}\right)_c = \frac{4}{3}\left(\frac{8\pi}{3} r_o^2\right) c\rho\gamma^2 > \frac{\gamma}{\tau_c}$$

and the upper limit occurs when the approximation for Thomson scattering breaks down. The spectral index of the x-ray energy spectrum, b, due to the inverse Compton process, is related to the electron spectral index, a, by the equation $b = \frac{1}{2}(1+a)$. (See 3.1.8) From the magnetic Bremsstrahlung theory of galactic radio emission, the spectral index in the power law for radio emission intensity, d, is related to the same electron spectral index, a, by $a = 2d+1$. Felten and Morrison (1966) showed that when the electrons escaping from radiogalaxies are adjusted by their predominant energy loss mechanism (i.e. Compton scattering) the spectral index becomes $a' = a+1$, and hence we should use $b = \frac{1}{2}(1+a')$ for calculating the diffuse x-ray spectrum. Measurements show that $d = 0.7$. This gives $a = 2.4$; $a' = 3.4$ and $b = 2.2$, which is in very good agreement with observations of the diffuse x-ray spectrum power law exponent from 10 KeV to 100 MeV (see Fig. 1).

It may be added that if the measured diffuse x-ray background originates in the metagalaxy, the relativistic Doppler shift must be taken into account. The emission spectrum $F_e(E)$ is related to the observed spectrum $F_o(E)$ by

$$\int F_o(E)dE = f_m H^{-1} \int F_e(E)dE \qquad (3.1.9)$$

where f_m depends on the particular model of the galaxy used. If $F_e(E)$ is a power law spectrum, then $F_o(E)$ is also a power law spectrum with the same spectral index, but if there is a low energy cut-off, then $F_o(E)$ below this cut-off depends critically on the cosmological model.

3.2 BACKGROUND FORMED BY UNRESOLVED SOURCES

The mean x-ray emission spectrum per unit volume is

$$F_e(E) = \langle n_s \; F_s(E) \rangle$$

where n_s is the source number density and $F_s(E)$ is the emission spectrum of the source. If our galaxy is a typical source, then we can use n_s = number density of galaxies $\simeq 10^{-75}\text{cm}^{-3}$ (Sandage, 1965) and $F_e(E)$ from all the known sources in our galaxy. $F_e(E)$ must then be transformed to allow for relativistic effects, using equation 3.1.9. Such a calculation gives a photon flux which is one order of magnitude less than the observed diffuse flux, and shows that such an explanation for the x-ray flux is certainly plausible. However, measurements from other galaxies, such as M87, or better still galactic clusters are needed to evaluate the likely contribution to the diffuse x-ray flux from this model.

3.3 LINE STRUCTURE

3.3.1 π^o Production

π^o particles which decay via $\pi^o \rightarrow 2\gamma$ are created in cosmic ray collision with matter, e.g. $pp \rightarrow pp\pi^o$. The energy of this decay is $> \frac{1}{2}m_\pi c^2 \simeq 70$ MeV. We have for the production rate per unit volume of pions in the energy range $E_\pi \rightarrow E_\pi + dE_\pi$ at position $\underline{r}$:

$$N_\pi(E_\pi)dE_\pi = (4\pi n(\underline{r}) \sigma \int_{E_\pi}^{\infty} m(E, E_\pi)\, I(E)\, dE)\, dE_\pi \qquad (3.3.1)$$

where $n(\underline{r})$ is the density of atomic matter, σ is the proton-proton cross section (which is about $3 \times 10^{-26}\text{cm}^2$) $m(E, E_\pi)$ is the multiplicity of pions produced in the energy range $E_\pi \rightarrow E_\pi + dE_\pi$ in each collision of a particle with incident energy E, $(E > E_\pi)$ and $I(E) = 1.3E^{-2.6}$ p/cm^2 ster sec GeV is the cosmic ray intensity at energy E. We can write for the multiplicity :

$$m(E, E_\pi) = m(E) \cdot \delta\left(E_\pi - \frac{kE}{m(E)}\right) \qquad (3.3.2)$$

where the mean multiplicity $m(E) = \int m(E, E_\pi)\, dE_\pi \simeq 3E^{\frac{1}{4}}$. Substituting this in equation (3.3.1) and performing the integral over r along the line of sight, we get

$$N_\pi(E_\pi) = 0.12\sigma \int_0^L n(\underline{r}) E_\pi^{-2.8}\, d\underline{r} \quad (3.3.3)$$

π_o account for $\frac{1}{3}$ of this flux, if equipartition is assumed.

The γ-ray spectrum obtained from $\pi^o \rightarrow 2\gamma$ decay is, from the kinematics involved

$$N_\gamma(E_\gamma) = 0.036\sigma \int_0^L n(\underline{r}) E_\gamma^{-2.8}\, d\underline{r} \quad (\gamma/cm^2 \text{ sec ster Gev})$$

Photoproduction of neutral pions, where $p\gamma \rightarrow p\pi^o\gamma$ is negligible and only relevant at extremely high energies.

3.3.2 Positron Annihilation

The cross section for $e^+e^- \rightarrow 2\gamma$ interaction at energies $E \gg m_o c^2$ is

$$\sigma(E_\gamma, E) \simeq \pi r_o^2 \frac{m}{E} \left(\log \frac{2E}{m} - 1\right) \cdot \delta(E_\gamma - E)$$

where the two photon annihilation probability is much greater than that for larger numbers (by the factor $\alpha_f = 1/137$ for each additional photon), and one of the photons has energy $E_\gamma \simeq E$. The photon spectrum resulting from this interaction is

$$N_\gamma(E) = \pi r_o^2 \int_{r=o}^{L} n(\underline{r}) \frac{m}{E} \left(\log \frac{2E}{m} - 1\right) \frac{1}{2} I(E)\, d\underline{r} \quad (3.3.4)$$

where I(E) is the electron energy spectrum.

For slow galactic electron-positron annihilation, we have for the rate of annihilation per unit volume :

$$= n(\underline{r}) \pi r_o^2 c\, n_{e^+}(\underline{r}) \quad (3.3.5)$$

where $n_{e^+}(\underline{r})$ is the slow positron density, and $n(\underline{r})$ is the electron density, which at charge neutrality should be the same as the gas atom density.

When integrating this expression along the galactic disc and the galactic halo, there should be an anisotropy, since in the galactic disc the positron lifetime is much shorter. Determination of this 0.51 MeV line source as a function of position (or direction of viewing) is very important cosmologically, since it provides information on the diffusion rate from the galaxy or on the galactic evolution.

3.3.3 Nuclear γ-Rays

These can be either due to cosmic ray nuclei which undergo transitions to their ground state, or nuclei at rest which then emit discrete spectra.

One particular problem of nucleogenesis is the understanding of the origin of elements with atomic number greater than Iron. The energetic processes taking place in a supernova explosion should be capable of producing these elements, and a search for their transition lines, mostly around 0.8 MeV, is important. Intensities of 4×10^{-5} photons/cm^2 sec, as estimated theoretically, must be observable for this.

4. SCIENTIFIC AIM OF THE UK5 PROJECT

The UK5 mission is specifically designed to make a wide range of x-ray measurements on celestial sources. It contains scanning experiments with high angular resolution which search for sources in the energy range 1.5 to 20 KeV, and pointing experiments which make detailed measurements on the particular objects to which they are pointed.

The energy range covered by the pointing experiments is 0.3 KeV to 1 MeV, nearly four decades, and in addition polarisation measurements and pulsar detection provides further scope for the study of individual objects.

Experiment F is a pointing experiment designed to extend spectral information of cosmic x-ray sources from 20 KeV upwards to 1 MeV, i.e. nearly two decades in energy. There will also be a mode of operation to search for pulsar fluctuations in this energy range.

In the case of source observations, knowledge of the spectrum and its time variations should help to distinguish between a synchrotron or a plasma-bremsstrahlung origin of the radiation. There is also an interest in searching for a line emission around 0.8 MeV from Supernova remnants and for the 0.511 MeV positron annihilation line which might result from secondary cosmic rays.

5. DESIGN CONSIDERATIONS

The best way to emphasize the important features of the detector which influence the design, is to calculate the detector sensitivity, but first we must describe the basic processes leading to photon detection.

The interaction of photons with matter is well understood. The processes which lead to absorption are photoelectric, Compton and pair production interactions. Photoelectric absorption of a photon and the resulting emission of a photoelectron from the atom of the absorber results in a total energy loss, which can be measured, apart from possible detection inefficiencies due to edge effects. Compton interactions occur when a photon collides with a free electron (or one which is only lightly bound to its atom) and thus transfers some of its energy onto the electron. This results in a partial energy loss only. Pair production occurs when the photon is transformed into an electron-positron pair. Such an event only takes place in the vicinity of an atom, as can be readily shown from the conservation laws of energy and momentum. The energy loss observed in the detector due to pair production depends on the energy of the electron and positron, and the position inside the detector where the positron is annihilated. Positron annihilation in the interaction $e^+e^- \rightarrow 2\gamma$ takes place at rest,

with the emission of two 0.511 MeV γ-rays, only if the annihilation cross section of the positron is much less than the ionisation cross section - otherwise an electron photon cascade is produced inside the detector.

All detectors of photons use these three basic interaction modes. Low energy photons (energy less than 30 KeV) interact mainly by photoelectric effects, and the detectors used most frequently in this energy range are scintillators or proportional counters. Very high energy photons (energy greater than 20 MeV) interact predominantly in the pair production mode, hence the detectors used in this region usually employ a lead converter (of one radiation length thickness), which produces an electron-positron pair. These secondary particles are then observed in a lead-glass Cherenkov detector or another suitable material of high stopping power. Improved angular resolution is often obtained by the addition of a spark chamber to pinpoint the incident charged secondary particle direction, which at high initial photon energies is the same as the direction of the photon itself. In the intermediate energy range, where a large fraction of the total interaction cross section is due to Compton processes, the main requirement for efficient particle detection is that enough detector mass is present to allow multiple Compton interactions of the incident photon to take place inside the detector.

In these multiple collisions the energy of the photon is successively reduced until eventually photoelectric absorption ensures that the photon has lost all its energy in the detector. For this energy region, scintillators provide the most efficient detectors. Materials with high Z (atomic charge) have a photoelectric absorption region which extends to high photon energies (about 200 KeV) so that scintillators with high Z values are most useful for making measurements at energies greater than 20 KeV.

For experiment F, operating in the energy range 20 KeV to 1 MeV, a CsI scintillator was chosen as the detector. CsI has high atomic charge, and, when activated with Thallium or Sodium, it also has a high light output for a given energy deposited in the crystal.

When the detector is pointing at a source, the number, N, of photons counted in a given time is $N_s + N_B$ where the subscripts refer to source and background respectively. When the detector is pointing away from the source, the number of photons counted in the same time interval is $N_s' + N_B$. The criterion for detecting the source to better than 3 standard deviations is then :

$$\frac{N_s - N_s'}{\sqrt{N_s' + N_B}} \geqslant 3 \qquad (5.1)$$

If $F_s(E)$ is the differential energy spectrum of x-rays from a source (photons/cm^2 sec MeV) then N_s is given by

$$N_s = \int_{E_1}^{E_2} F_s(E).\ A.\ t.\ \rho(E)\ dE$$

where A is the detector area, t is the time of observation and $\rho(E)$ is the absorption efficiency of the detector at energy E. The energy interval over which measurements are made is E_1 to E_2. Similarly, background counts are given by :

$$N_B = \int_{E_1}^{E_2} F_B(E).\ t.\ (Ad\Omega + (4\pi - d\Omega)A'\eta(E))\ \rho(E)\ dE$$

where F_B is the differential energy spectrum of the diffuse background (photons/cm^2 sec. ster. MeV), $d\Omega$ is the solid angle in the detector viewing cone, $\eta(E)$ is the transmission efficiency of the collimator and A' is the average area presented by the detecting crystal to the omnidirectional background flux. Also, N_s' is given as :

$$N_s' = \int_{E_1}^{E_2} F_s(E).\ A'.\ t.\ \rho(E).\ \eta(E)\ dE$$

From these equations it follows that, for a given observation time, the detection efficiency is greatest, if the detector area A is large, the absorption efficiency of the detector $\rho(E)$ is high, the transmission efficiency of the collimator $\eta(E)$ is low, and the solid angle of the viewing cone, $d\Omega$, is small. Clearly, some of these conditions will conflict, and, if in addition measurements are to be made over a wide energy range, the detector can only be optimised for a given energy region. A crude optimisation method was used initially to establish the basic detector design. The detailed design was then made using more sophisticated techniques. The mass of the detector was fixed at approximately 5 kg due to constraints on the spacecraft payload, and design optimisation was chosen at around 0.5 MeV, the electron-positron annihilation line. Three possible detector configurations were studied, active well-shaped collimator, active anticollimator and active honeycomb collimator. The reasons for rejecting passive collimator systems are given in the detailed design study, but it may be mentioned here, that since weight was the limiting factor rather than cost, the preliminary design study is not affected very much by the choice of materials, all of which must have high atomic charge.

5.1 ACTIVE, WELL-SHAPED COLLIMATOR

An idealised detector was chosen for the active, well-shaped collimator, and is shown in Fig. 4.

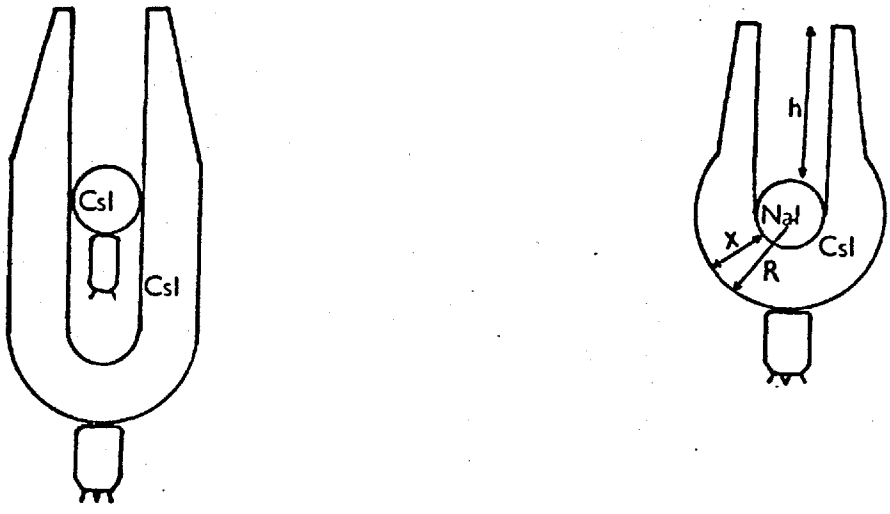

(a) (b)

Fig. 4

In (a) the central detector and collimator are made of the same material, and in (b) detector and collimator are viewed by the same photomultiplier.

μ = absorption coefficient at energy E, hence $\eta(E)$, the collimator transmission efficiency, is given as $\eta(E) = e^{-\mu(E)X}$

$A = \pi (R - X)^2$ = area of central crystal

$\Omega = A / (X + h)^2$ = solid angle of telescope aperture

If the detecting crystal and the collimator are made of different materials (e.g. NaI and CsI) a phoswich technique can be used for rejecting charged particles. In this case, both detector and collimator are viewed with the same photomultiplier, and pulse shape discrimination is used to identify pulses produced in the different materials. In the case of NaI and CsI, such a discrimination needs to resolve decay times of $\sim 0.3\,\mu$sec and $\sim 1\,\mu$sec respectively. Past experience with phoswich circuits showed that attainment of reliable discrimination was a new development area, and it was decided that it was too risky to base the detector design on the assumption that this problem could be overcome in time for delivery of the first unit. For this reason, allowance must be made for increased detector weight because the central crystal is viewed by a separate photomultiplier. Using the same symbols as equation 5.1, we get :

$$N_S = F_S\, A t\, (1 - e^{-\mu 2(R-X)})$$

$$N_S' = F_S\, A t\, (1 - e^{-\mu 2(R-X)})\, e^{-\mu X}$$

$$N_B = F_B\, A t\, (1 - e^{-\mu 2(R-X)}) \cdot (\Omega + (4\pi - \Omega) e^{-\mu X})$$

At low x-ray energies, where absorption is good, (i.e. μ is large) equation 5.1 becomes (in the limit of $\mu \to \infty$) :

$$\frac{F_s \sqrt{A.t}}{\sqrt{F_B \, \Omega}} \geq 3 \qquad (5.2)$$

The background is due entirely to x-rays entering the aperture, and greater sensitivity is achieved through decreasing the telescope opening angle at constant A.

At high x-ray energies, where absorption is poor, the fraction of the background counts due to x-rays entering through the detector aperture is small, provided Ω is small, and equation 5.1 becomes :

$$\frac{F_s \sqrt{At \, (1 - e^{-\mu 2(R-X)})} \; (1 - e^{-\mu X})}{\sqrt{F_B \; 4\pi \; e^{-\mu X}}} \geq 3 \qquad (5.3)$$

We can re-write equation (5.3) as :

$$\frac{F_s}{kS} \geq 3$$

where

$$S = \frac{\sqrt{e^{-\mu X}}}{\sqrt{1 - e^{-\mu 2(R-X)}}} \; (R - x)^{-1} \; (1 - e^{-\mu X})^{-1} \qquad (5.4)$$

In equation 5.4 the substitution $A = \pi \, (R - X)^2$ has been made. When S is plotted as a function of collimator thickness X, at constant R (i.e. constant detector mass) and constant μ, we see from equation 5.4 that S approaches infinity as $X \rightarrow 0$ (no collimator) and as $X \rightarrow R$ (no central detector). There is a minimum somewhere in between, at the point of greatest detector sensitivity. Fig. 5 shows the result of such calculations. The collimator thickness (cm) for the optimised

design is plotted as a function of absorption coefficient μ (cm^{-1}) for different values of R. The reason why the collimator thickness increases with absorption efficiency for the optimised design, is because it is more advantageous to reduce the background than to increase the viewing area. When μ increases further, the collimator thickness, X, will eventually become smaller again, since then $e^{-\mu X}$ will vary less rapidly than R - X. The directional accuracy required by experiment F is 8^{o} at full width half maximum in order to resolve the closely spaced x-ray sources along the galactic disc. Using this fact, it is possible to calculate R corresponding to the allowed detector mass, and to interpolate for the optimisation of the detector at a particular value for μ in Fig. 5.

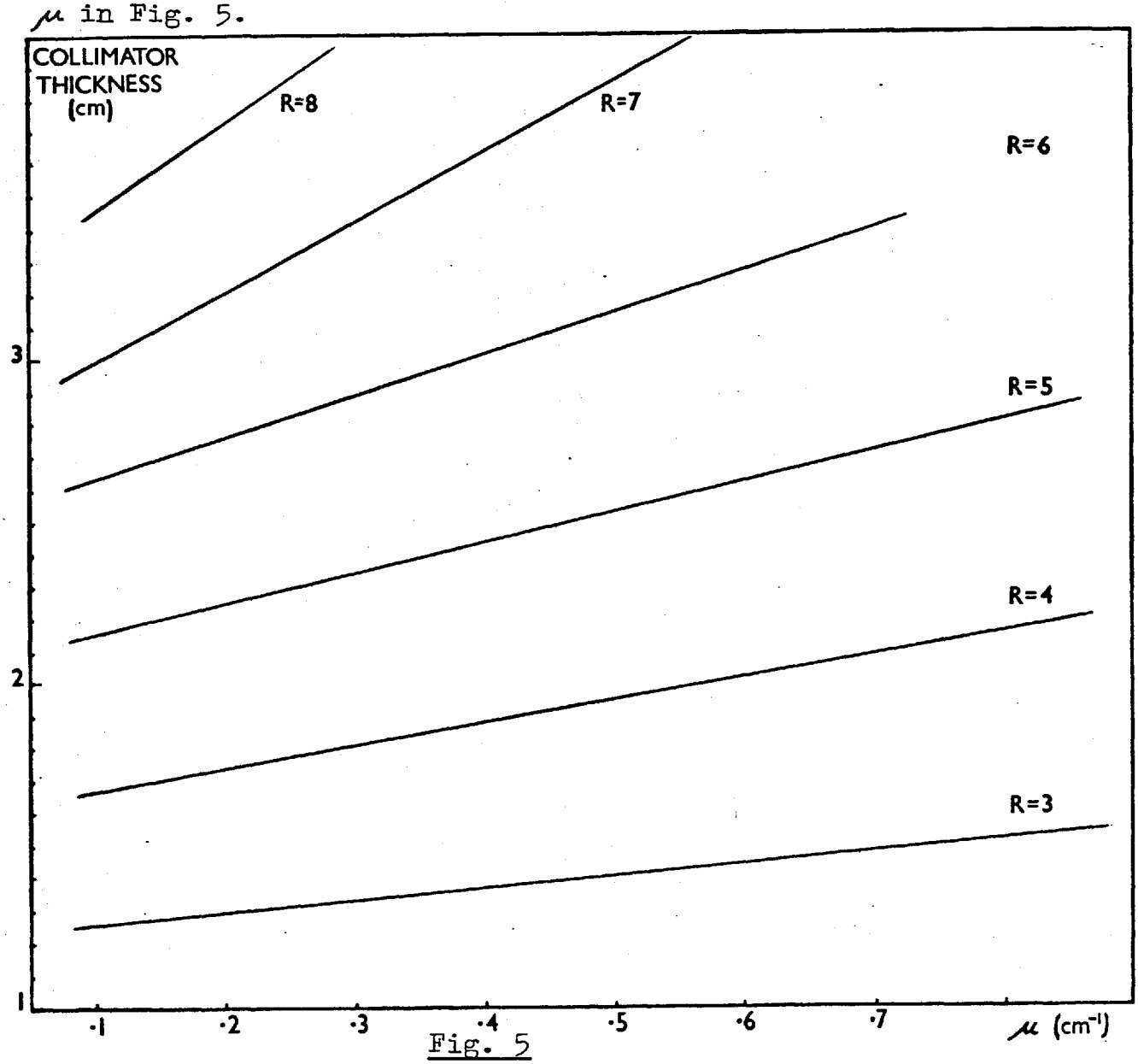

Fig. 5

For experiment F, (detector mass 5 kg) R was calculated to be approximately 5 cm, and from Fig. 5 we obtain X = 2.5 cm as the optimum value at μ = 0.45 cm^{-1}. (μ = 0.45 cm^{-1} corresponds to ~0.5 MeV)

Fig. 6 gives the sensitivity factor S as a function of R at different values for μ. The conversion from S to source strength will be given later.

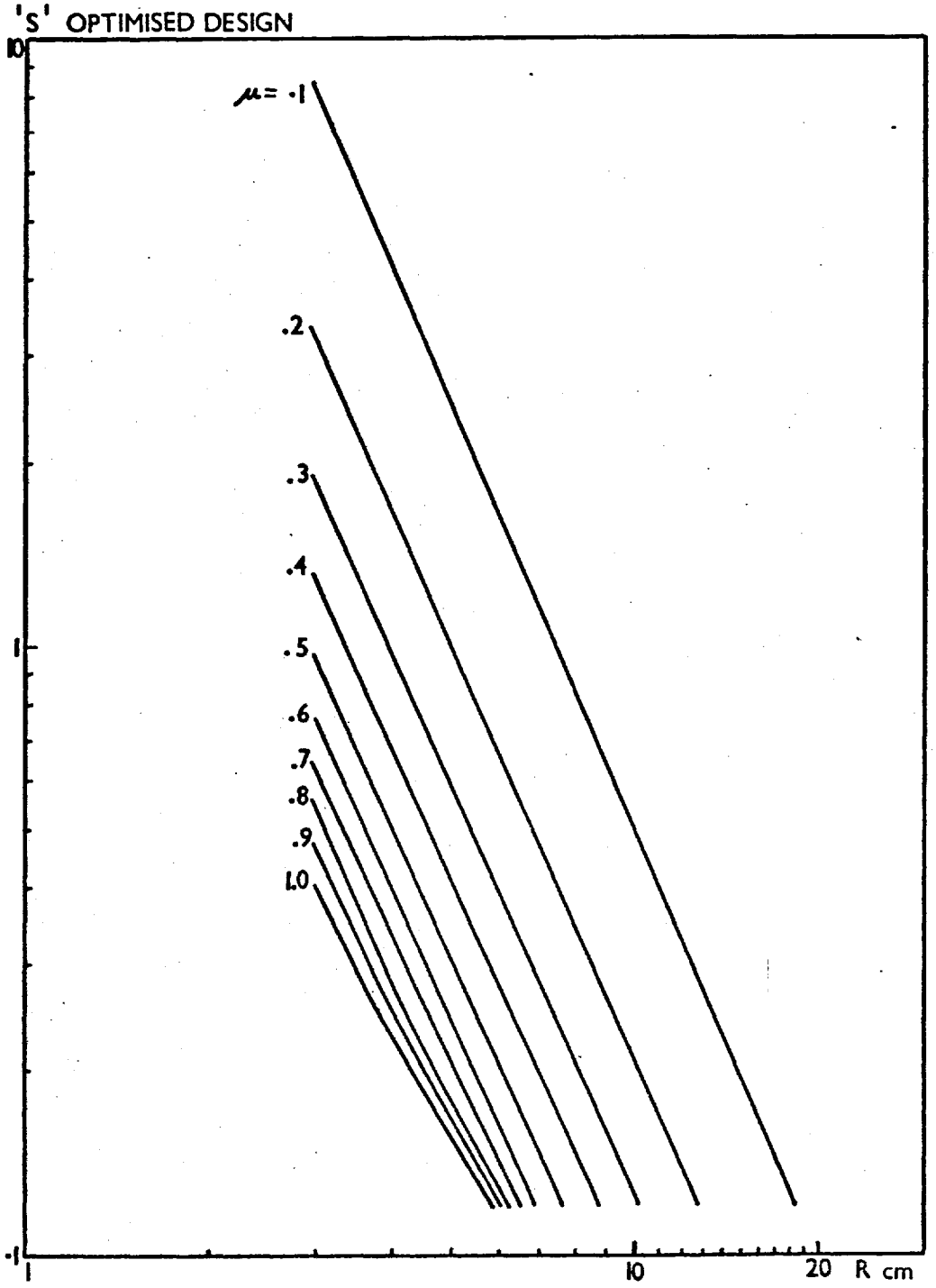

Fig. 6

5.2 ACTIVE ANTICOLLIMATOR

When the collimator transmission factor is high, it may be advantageous to dispense with it altogether, and instead to cut out the source for the required modulation. Using the same criterion as for equation 5.1, but this time applied to the decrease in counting rate when the source is obscured, we obtain for S, the sensitivity factor :

$$S = X\,(1 - e^{-\mu 2X})^{-3/2} \qquad (5.5)$$

where we have chosen two identical spheres, radius X, to form the detector and absorber.

Fig. 7 gives the ratios in sensitivity obtained for the active collimator and the active anticollimator configurations discussed as a function of detector mass available. This shows that at low absorption efficiencies (μ small) and small available detector mass, great improvements (nearly a factor of 10) in sensitivity can be obtained by employing an anticollimator rather than a collimator.

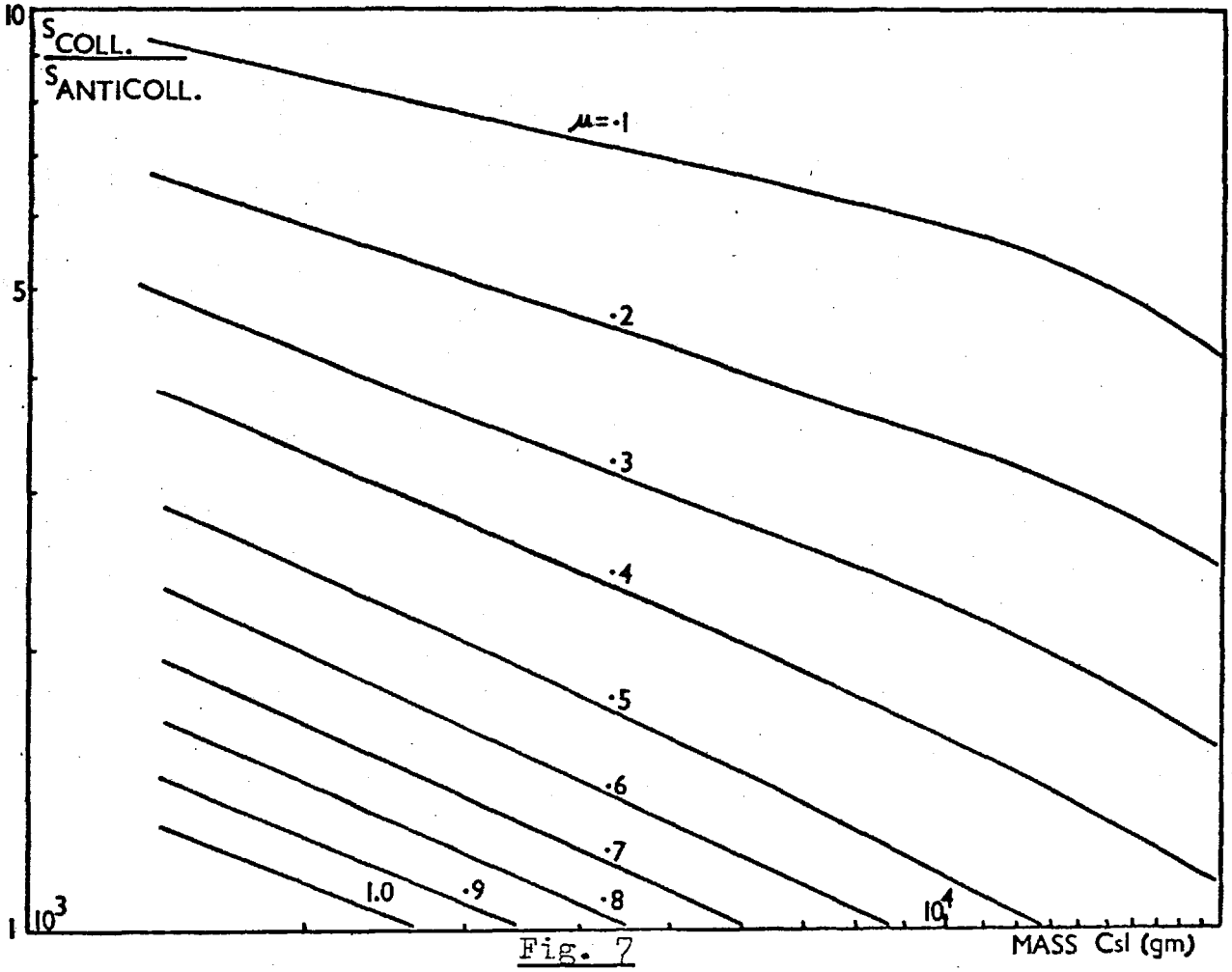

Fig. 7

For experiment F an active collimator arrangement is more sensitive than the equivalent active anticollimator at absorption coefficients $\mu > 0.75$, i.e. at energies below ~ 320 KeV.

5.3 ACTIVE HONEYCOMB COLLIMATOR

If the opening angle of the detector is intended to be small, and the detector area A is large, a well-shaped configuration can become too long, and impracticable. In this case, a honeycomb collimator is used, and the detector configuration is as shown in Fig. 8.

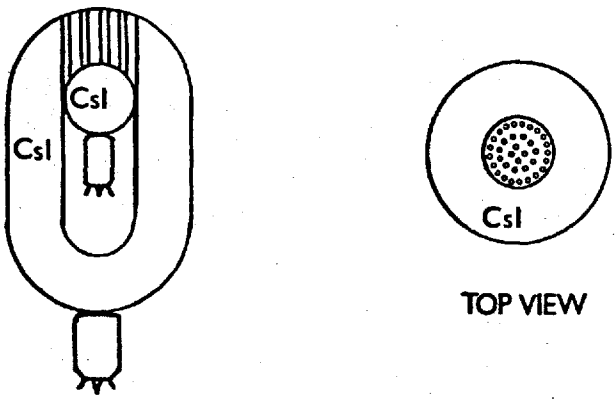

Fig. 8

In such a configuration, the effective viewing area is approximately halved, and thus the value for 'S' (equation 5.4) corresponding to this arrangement is twice the value for the equivalent well-shaped collimator. There is, however, a small weight saving, which in the case of experiment F is about 10% of the detector mass.

The parameter 'S' can be used to express the sensitivity of the detector in terms of a standard reference x-ray source, such as TAU XR - 1.

Using the following expressions for the diffuse background flux and the Crab source,

$$F_B = 0.026\ E^{-2} \text{ photons/cm}^2 \text{ ster. MeV sec}$$

$$F_{Crab} = 0.009\ E^{-2} \text{ photons/cm}^2 \text{ MeV sec}$$

we obtain for another source of strength F_S

$$\frac{F_S}{F_{Crab}} = S.\ \ 107.5\ \left(\frac{1}{E_1} - \frac{1}{E_2}\right)^{-\frac{1}{2}}\ \ t^{-\frac{1}{2}} \qquad (5.6)$$

where the comparison is made in the energy range E_1 to E_2 (MeV) and the observation time is t. Thus, using Fig. 6 and equation (5.6) the best available sensitivity can be found for a detector optimised in the desired energy range.

6. DETAILED DETECTOR DESIGN

6.1 MONTE CARLO DESIGN METHODS

Since only photoelectric interactions result in total photon energy loss, and experiment F is designed to operate in the energy region when Compton interactions predominate, the detector response is best determined using a Monte Carlo method of calculation. A computer program was developed, which used random numbers from the CDC 6600 random number generating routine (RANF(X)) to follow a photon through the detector. RANF(X) gives a random number distribution with equal probability of the number being between 0 and 1 and zero everywhere else. The position of the interaction point was calculated using the total absorption coefficient, and the type of interaction from the ratio of the different interaction cross sections.

For a photoelectric interaction the energy lost is the total photon energy. In the program the range of photoelectrons in CsI is taken to be negligibly small, and no allowance is made for K-xray escape.

For a Compton interaction, the differential cross section for scattering into solid angle $d\Omega$ at angle θ is obtained from the Klein-Nishina equation. This is used in conjunction with random numbers to determine θ. Any phase angle ϕ has equal probability and is measured anticlockwise from the plane formed by the detector axis and the incident photon direction. The new photon energy is $E' = E/(1 + \frac{E}{m_o c^2} (1 - \cos\theta))$. At the energies considered here, the electron range in CsI is negligible.

For a pair production interaction near the low energy limit of $2m_o c^2$, the kinetic energy of the electron and positron is small. As a result, this energy is lost at or near the interaction point, and the annihilation of the positron, with the emission of two 0.511 MeV photons, also takes place at roughly the original interaction point. The two photons move in opposite, but random directions, if annihilation takes place after the positron has become thermalised by ionisation. The two photons are then traced in the same way as the original one.

The model used for the detector is a cylinder, radius R, height H, with the middle section, radius r, height h, forming the central detecting crystal, and the remainder is the collimator. Input variables are : photon energy, incidence direction cosines, and incidence position. Output values are the energy deposited in the central detector, or whether an anticoincidence is registered, i.e. whether more than a critical energy E_c is deposited in the collimator. Provisions are made for broad, parallel beams of photons or for photons travelling along a line. By making the value of E_c greater than the incident photon energy, the detector effectively has a passive collimator of the same proportions as the active collimator which results when E_c is made small. This allows performance comparisons to be made.

6.2 COMPARISON OF ACTIVE AND PASSIVE COLLIMATORS

In the energy region where Compton interactions predominate, the photopeak, which corresponds to total energy loss of the incident photon, is due to a small photoelectric interaction probability or to multiple Compton interactions terminating with a photoelectric energy loss. All other interactions, where the energy loss is only partial, form the Compton plateau. This plateau extends from the lowest energy to the Compton edge, which marks the largest photon energy loss in a single interaction. Expressed in terms of the incident photon energy, this loss is $E - E\,(1 + 2\frac{E}{m_o c^2})^{-1}$. Above this energy and below the photopeak, counts must be due to multiple Compton interactions with escape of some of the photon energy from the detector. The fraction of the detected photon flux which is observed in the photopeak, depends on the size of the detecting crystal. In the case of experiment F, the weight restriction determines the maximum size of the central crystal and at 0.5 MeV it is estimated that only half the interactions will actually be registered as total energy losses. In order to resolve line structure at these energies, it is desirable to restrict the detection of partial energy losses as much as possible. This can be done using an active collimator, since a photon which interacts in the central crystal with partial energy loss, and then escapes from this crystal, can be detected in the collimator which forms an anticoincidence with the central detector. The energy threshold of the collimator must be low, and E_o = 50 KeV has been selected for experiment F. Active collimators, therefore, produce a much cleaner spectrum than passive ones.

A passive collimator relies on total energy losses of photons, whereas an active collimator only requires partial energy loss, either before or after the incident photon has been counted in the central detector. Using the Compton equation to calculate the photon scattering angle, $\theta_o(E)$, which results in energy loss E_o, and the Klein-Nishina equation for the

differential cross section for photons scattered into $d\Omega$ at angle θ, $\frac{d\sigma}{d\Omega}(\theta,E)$, it is possible to calculate the effective 'active absorption cross section', $\sigma_E(E)$ at energy E, since a photon is effectively 'absorbed' provided it interacts with an energy loss $> E_o$.

$$\sigma_E(E) = \int_{\theta_o(E)}^{\pi} \frac{d\sigma}{d\Omega}(\theta,E)\, d\theta \qquad (6.1)$$

In Fig. 9 the result of such a calculation has been plotted. The percentage of photons which interact in the Compton mode, and in their first interaction are effectively absorbed, is plotted as a function of energy for different discriminator levels E_o.

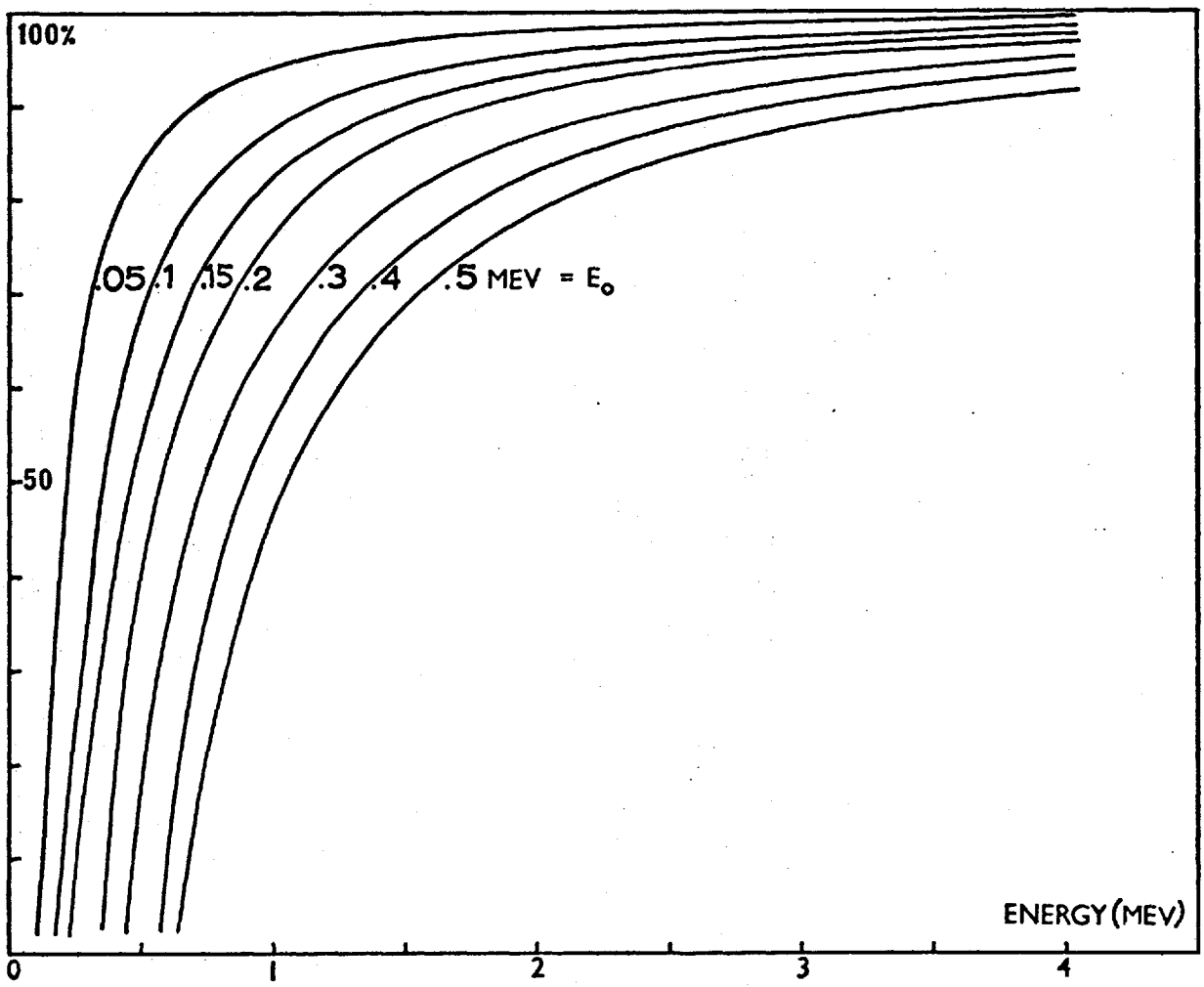

Fig. 9

The percentage shown (at given E_o) gives the minimum contribution to the total absorption coefficient by the Compton cross section. Multiple Compton interactions, or energy losses in the collimator after the photon has been observed in the central detector all contribute to increase the percentage, so that the effective absorption length can be greater than the total absorption length in the case of partial energy loss detection.

Particle fluxes are usually large, and an effective method of discrimination must be employed. This can be done with an active collimator, or with a combination of active and passive screening. Electrons passing through the heavy collimator emit Bremsstrahlung photons which can be detected in the central crystal. In order to eliminate this source of background, and retain a passive collimator, the whole assembly must be surrounded on the outside by a scintillator, such as NE102A, to detect the initial electron.

Finally, Cosmic rays and inner belt particles produce radioactive isotopes in the spacecraft as a whole, in the collimator and in the central detector. These isotopes decay and some of the decays are accompanied by the emission of x-rays (Schwartz, 1969; Peterson, 1965, Dyer and Morfill, 1971). The number of isotopes produced is proportional to the mass of matter present, so that the collimator acts as an x-ray source, especially if the satellite passes through the inner belt. An active collimator will always detect radioactive decays accompanied by particle emission, whereas a passive detector cannot do this. Hence the background produced by these decays is much more serious in the case of passive absorbers than for active collimators.

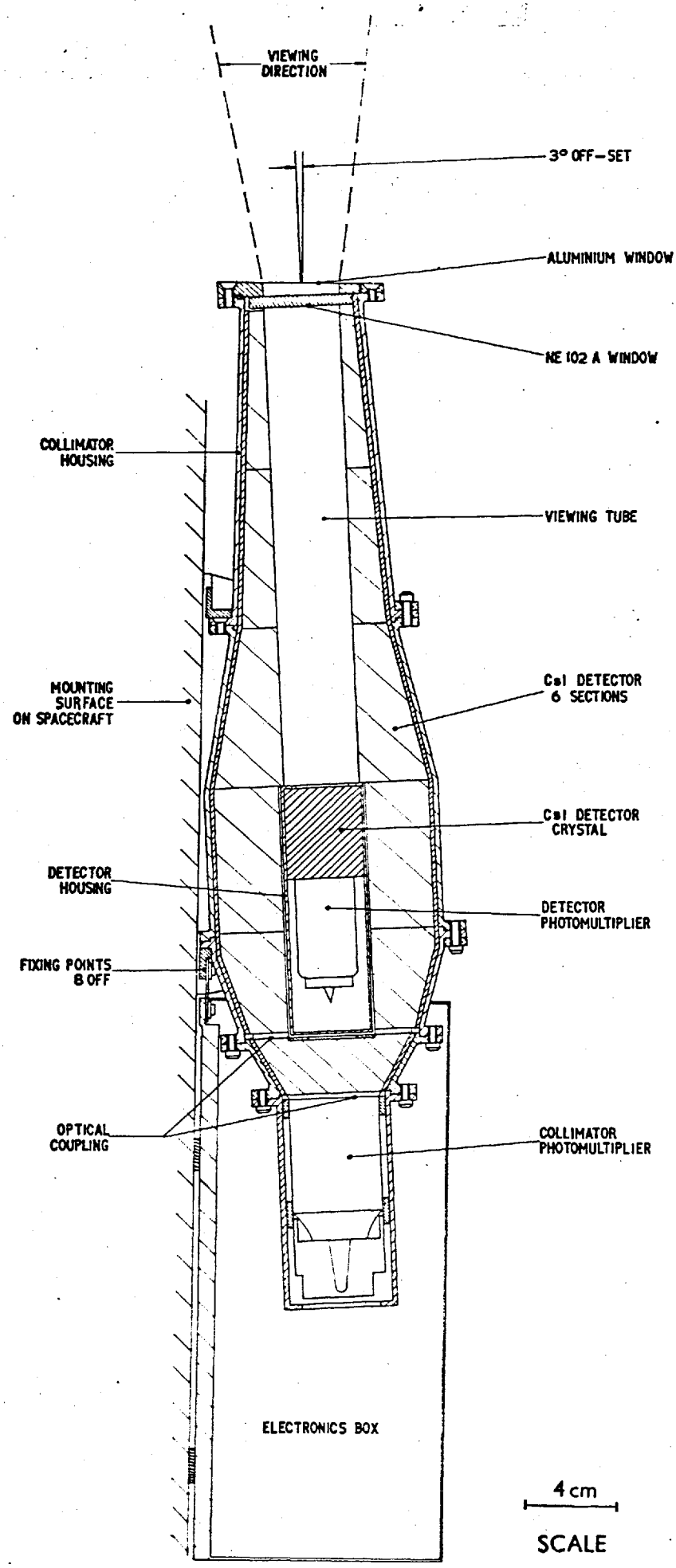
VIEWING DIRECTION
3° OFF-SET
ALUMINIUM WINDOW
NE 102 A WINDOW
COLLIMATOR HOUSING
VIEWING TUBE
MOUNTING SURFACE ON SPACECRAFT
CsI DETECTOR 6 SECTIONS
CsI DETECTOR CRYSTAL
DETECTOR HOUSING
DETECTOR PHOTOMULTIPLIER
FIXING POINTS 8 OFF
OPTICAL COUPLING
COLLIMATOR PHOTOMULTIPLIER
ELECTRONICS BOX
4 cm
SCALE

FIG.10

6.3 THE X-RAY TELESCOPE

Fig. 10 is a diagram of the adopted design. The central detector is a CsI (Na) cylinder , height 4 cm and sensitive area 9 cm^2. The collimator is made of six optically coupled sections, which are shaped to provide approximately the same absorption for all viewing directions. Central detector and collimator are viewed by separate photomultipliers.

The solid angle of the telescope aperture is 0.0144 steradian, which corresponds to a detector angular resolution of about 8^o at full width half maximum. Charged particles entering through the aperture are rejected using a NE102A plastic scintillator of thickness $\frac{1}{2}$cm which is optically coupled to the CsI (Na) collimator. Tests, carried out with a photodiode, showed that the light collected from this scintillator was a maximum when its position was as shown in Fig. 10.

6.4 SPECTROMETER PROPERTIES

If a photon of energy E interacts inside a scintillator, its energy loss E' is converted into light output with the characteristic crystal emission spectrum. The efficiency of conversion is usually low (about 7% in CsI (Na)), and the crystal emission spectrum does not always overlap the photomultiplier spectral response completely, so that the energy available for producing photoelectrons from the photocathode is small. However, photomultiplication in the dynode chain results in a measurable charge pulse at the anode, and it is found (Birks, 1964) that this charge is very nearly proportional to the energy lost in the scintillator. Statistical fluctuations and variations in light collection efficiency produce a distribution in the final charge pulse even at constant energy loss E' in the crystal. The probability of observing an energy loss E' due to a photon of energy E is given by :

$$P(E')=P_1(E')\,\delta(E-E')+P_2(E'+E_k)\,\delta((E-E_k)-E')+P_3(E',E)+P_4(E',E) \quad (6.2)$$

where: $P_1(E')$ is the probability of photoelectric absorption at energy E' for those interactions which are not accompanied by escape of a K-shell x-ray

$P_2(E'+E_k)$ is the probability of photoelectric absorption at energy $E'+E_k$ with escape of a K-shell x-ray of energy E_k (about 34 KeV for CsI).

$P_3(E',E)$ is the probability that a Compton interaction at energy E eventually results in energy loss E' in the central detector without generating an anticoincidence

$P_3(E',E)$ is the probability that a pair production interaction at energy E eventually results in energy loss E' in the central detector without generating an anticoincidence pulse.

The fraction of incident photons which are accompanied by escape of a K-shell x-ray from the illuminated or rear crystal face respectively is :

$$f_1(E) = \tfrac{1}{2} w_k \, d_k \frac{\mu_p(E)}{\mu(E)} \left(1 - \frac{\mu_k}{\mu(E)} \log\left(1 + \frac{\mu(E)}{\mu_k}\right)\right) \qquad (6.3)$$

$$f_2(E) = \tfrac{1}{2} w_k \, d_k \, e^{-\mu(E)t} \frac{\mu_p(E)}{\mu(E)} \left(\frac{\mu_k}{\mu(E)} \log\left(\frac{\mu_k}{\mu_k - \mu(E)}\right) - 1\right) \qquad (6.4)$$

These equations (Liden and Starfelt, 1954) apply to crystals of dimensions much greater than the absorption length of a K-shell x-ray, which in the case of CsI (Na) is approximately $1/\mu_k = 0.04$ cm. The K-fluorescence yield, w_k, is 0.84 and the fraction of the photoelectric processes involving K-shell electrons, d_k, is 0.80 according to the above authors. $\frac{1}{\mu(E)}$ is the total interaction length, and $\frac{1}{\mu_p(E)}$ is the photoelectric absorption length. Results of the above equations agree with independent calculations of Stein and Lewin (1966) and will be used here to determine the spectral response and

detection efficiency of experiment F. The K-shell energies for Cs and I are 32 KeV and 34 KeV respectively, and on the assumption that both escapes are equally probable an average loss of 33 KeV has been used here.

It has already been mentioned that a pulse distribution is obtained even for monoenergetic losses in the detecting scintillator. The observed spread in the photopeak for different monoenergetic x-ray sources is shown in Fig. 11 for experiment F.

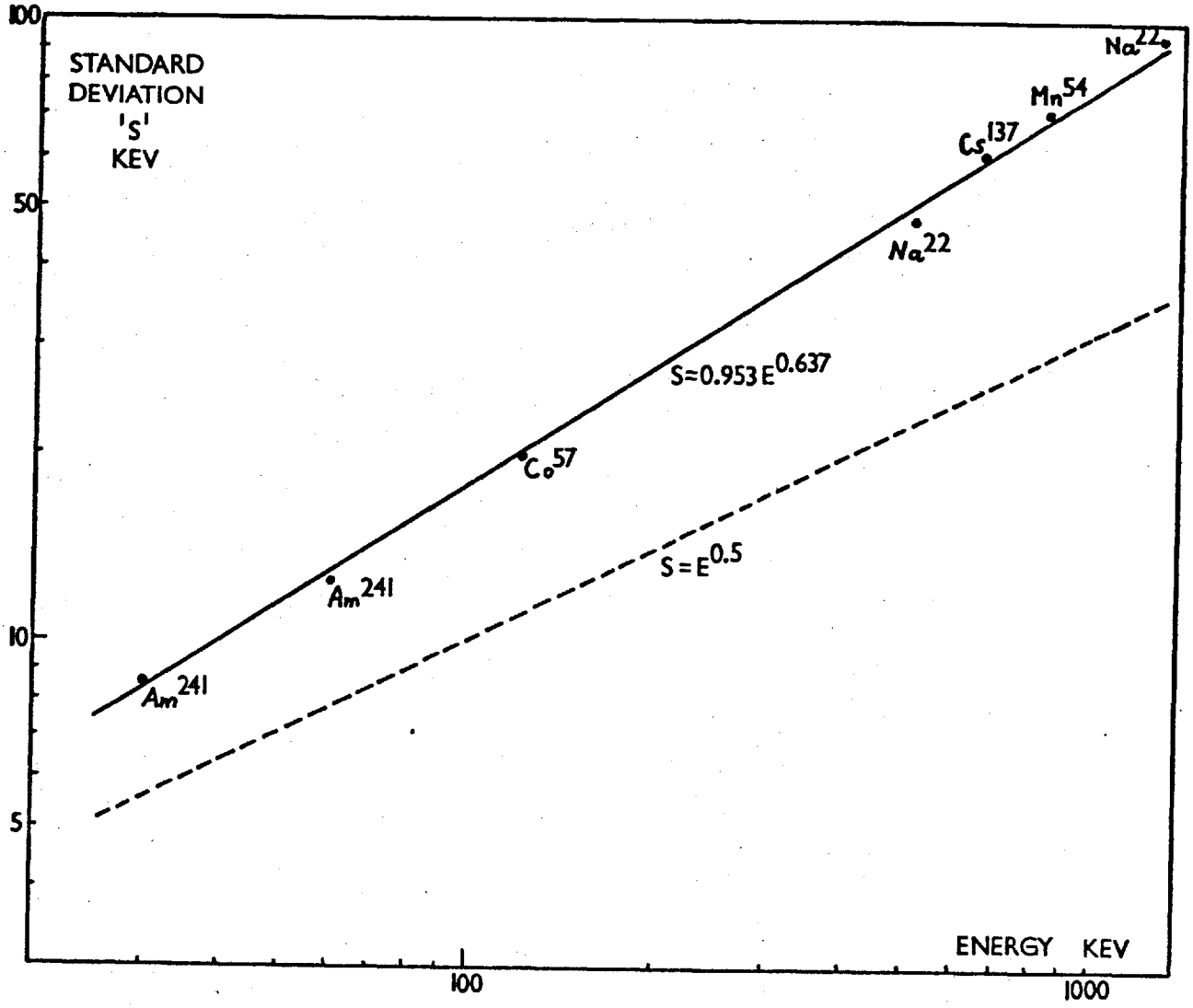

Fig. 11

In this figure the standard deviation, S, has been plotted for the photopeaks of various x-ray sources as a function of the energy, E of the x-rays emitted. If the charge pulse at the anode results from a large number of photoelectrons, N, a Gaussian distribution is expected, so that the standard deviation, S, is related to the energy loss in the detector, E, by the following relation :

$$S^2 \propto N \propto E$$

However, variations in light collection efficiency increase S somewhat, and for the photomultipliers used here the relation, $S = 0.953E^{0.637}$ was obtained. The normal distribution, where $S = E^{0.5}$, is also shown in Fig. 11.

Using this expression, and the fact that a Gaussian distribution provided a good fit to the photopeak data for the whole energy range considered, Fig. 12 was produced. In this figure the interaction probability ($1 - e^{-\mu(E)t}$) was plotted as a function of incident photon energy E, and so was the detection efficiency. The detection efficiency is the probability that an interaction in the detecting crystal is recorded, and depends on the energy range in which the detector operates, as well as the type of interaction and the collimator. The Monte-Carlo program (broad parallel beam) described earlier was used at energies greater than 100 KeV. It is of particular interest to notice the small percentage of measured partial energy losses predicted, equivalent to observing approximately 2% of the photopeak flux (in photons/MeV sec cm^2) at all lower energies. An energy channel of width ΔE_1 has a probability P_c of measuring $\frac{1}{50} \frac{\Delta E_1}{\Delta E_2}$ times the flux of a higher energy channel of width ΔE_2, i.e. $P_c \simeq \frac{1}{50} (\frac{E_1}{E_2})^{0.637}$. Below this energy, the probability of detection was calculated using a normal distribution with standard deviation S(E) obtained

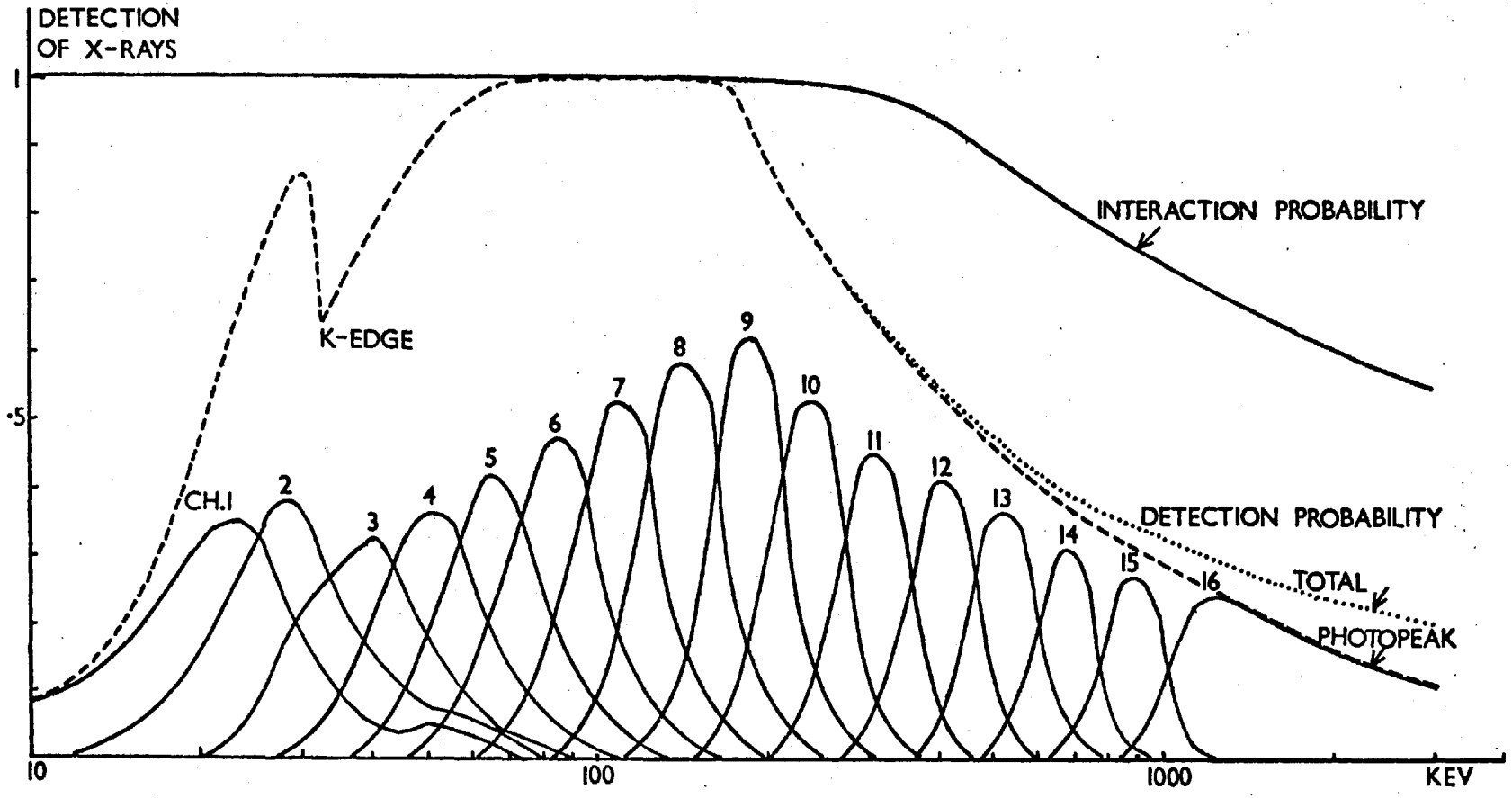

Fig.12

Interaction probability, detection probability and individual energy channel response curves of the detector shown in Fig. 10 as function of photon energy.

from Fig. 11, and the K-shell x-ray escape correction of equation (6.3). The contribution of the rear crystal face is negligible. Fig. 12 also shows the probability of actually recording a photon of energy E in a given energy channel. K escape effects and reduced efficiency at high energies are clearly shown. Using these curves it is possible to calculate the contribution to each energy channel from photons of energy outside the nominal limits, and thus to produce the true measured photon spectrum. Trombka (1970) has outlined a mathematical procedure for doing this, but basically it is just a question of solving sixteen simultaneous equations and assuming that the trend of the observed spectrum continues without dramatic changes down to about 10 KeV.

In order to understand the behaviour of the detector and the collimation efficiency better, figures 13a and 13b have been produced using the Monte Carlo program.

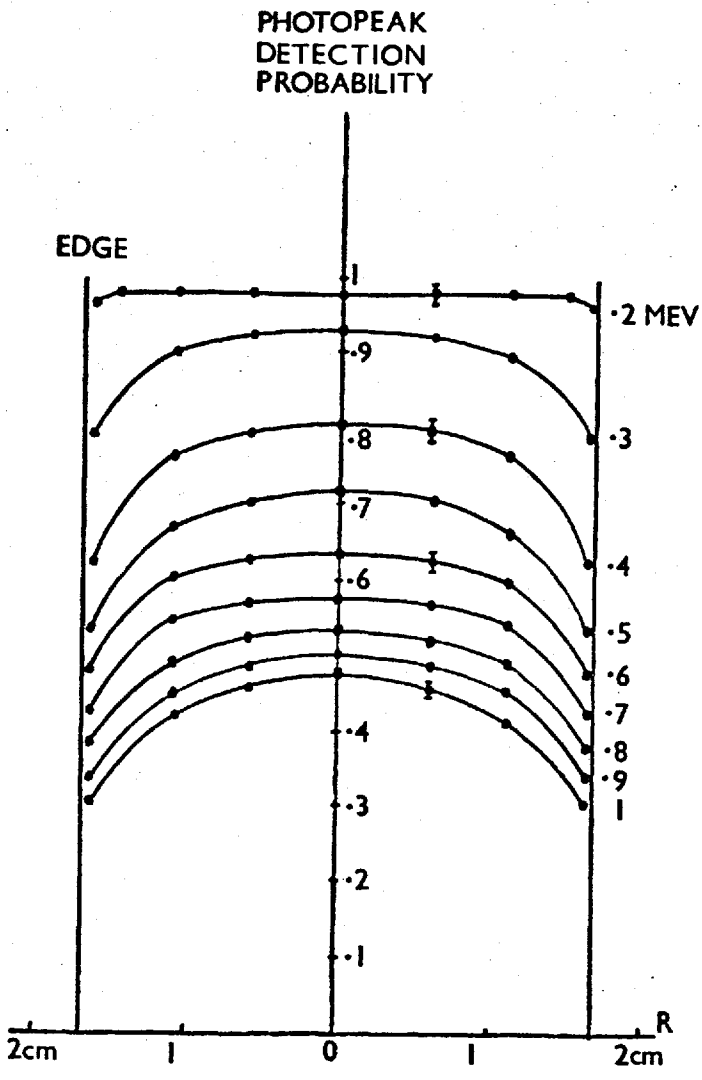

Fig. 13a

The photopeak detection efficiency has been plotted at different points along the crystal radius, for a thin beam of photons travelling parallel to the detector axis and at different energies. The curves show the reduction in detector efficiency as the beam approaches the edge of the scintillator.

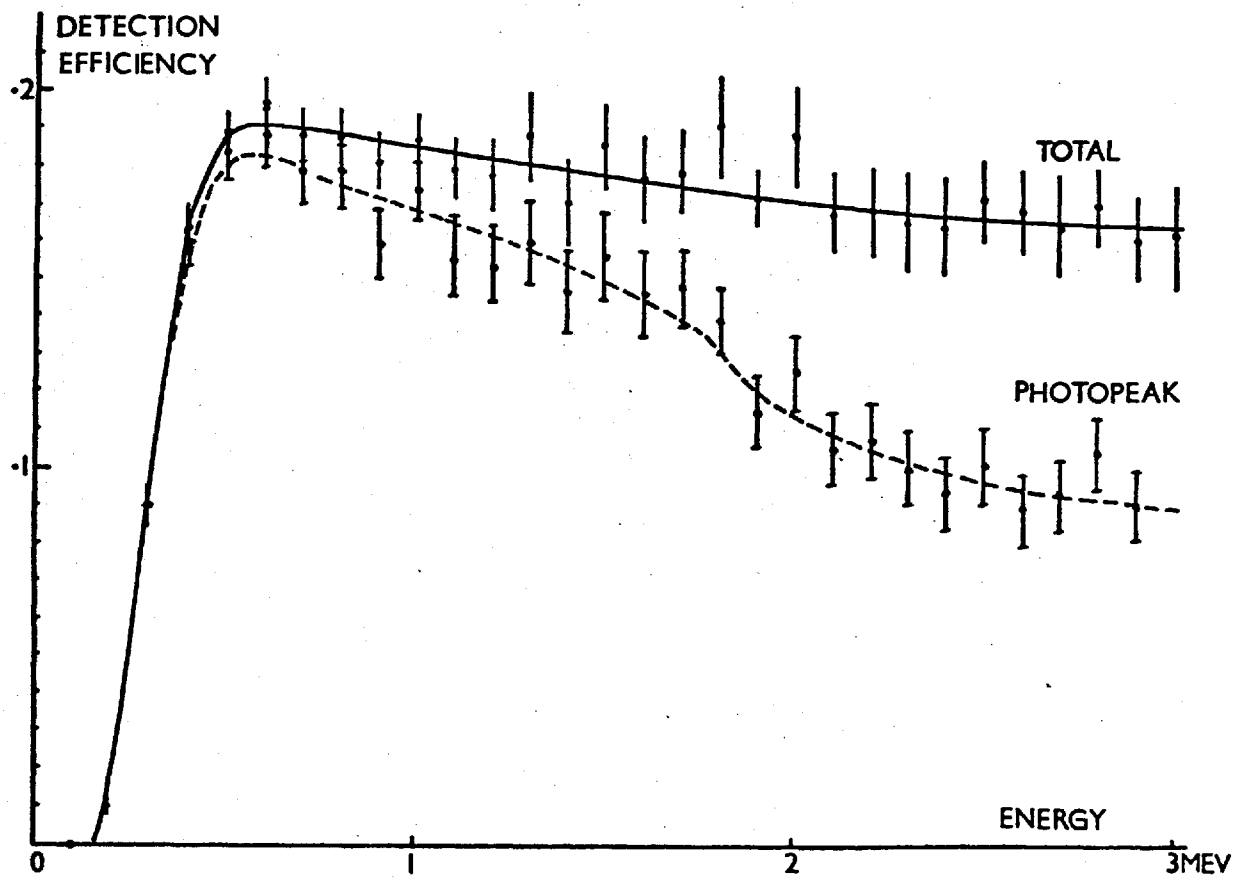

Fig. 13b

In Fig. 13b, the detection efficiency has been plotted as a function of energy for a thin photon beam entering through the side of the collimator, at right angles to the detector axis and incident half way down the side of the central scintillator. The overall detection efficiency is shown, as

well as the photopeak efficiency, defined here as : energy loss $\geq 5/6$ incident photon energy. These calculations refer to the smallest collimator thickness and highest detection probability in the central crystal, so that the detection efficiency of Fig. 13b is the upper limit, and the average background rejection will be higher.

Comparison with experimental measurements are shown in Fig. 14. A Cs ^{137} x-ray source, which has a line emission at 660 KeV, was used, and the output from the photomultiplier viewing the central crystal was measured with a 128 channel pulse height analyser. Results were obtained for side entry through the collimator and for photon entry through the detector aperture. In the first case the source was placed 12 cm away from the detector axis and the photons were collimated with a lead absorber to produce a radial beam incident mainly near the centre of the detecting crystal. In the second case the source was placed along the detector axis, 30 cm from the centre of the detecting crystal, and the lead absorber was used to provide a near-parallel beam of x-rays travelling along the detector axis. Results for active and passive detector operation were obtained. The Monte Carlo calculation for side entry, which applies to the detector configuration of experiment F, predicts a reduction in the photopeak intensity to 35% of the intensity when no collimator is present, compared with an experimental value of 33%.

Fig. 14 shows clearly the improvement in energy resolution obtainable with an active collimator over a similar, but passive system.

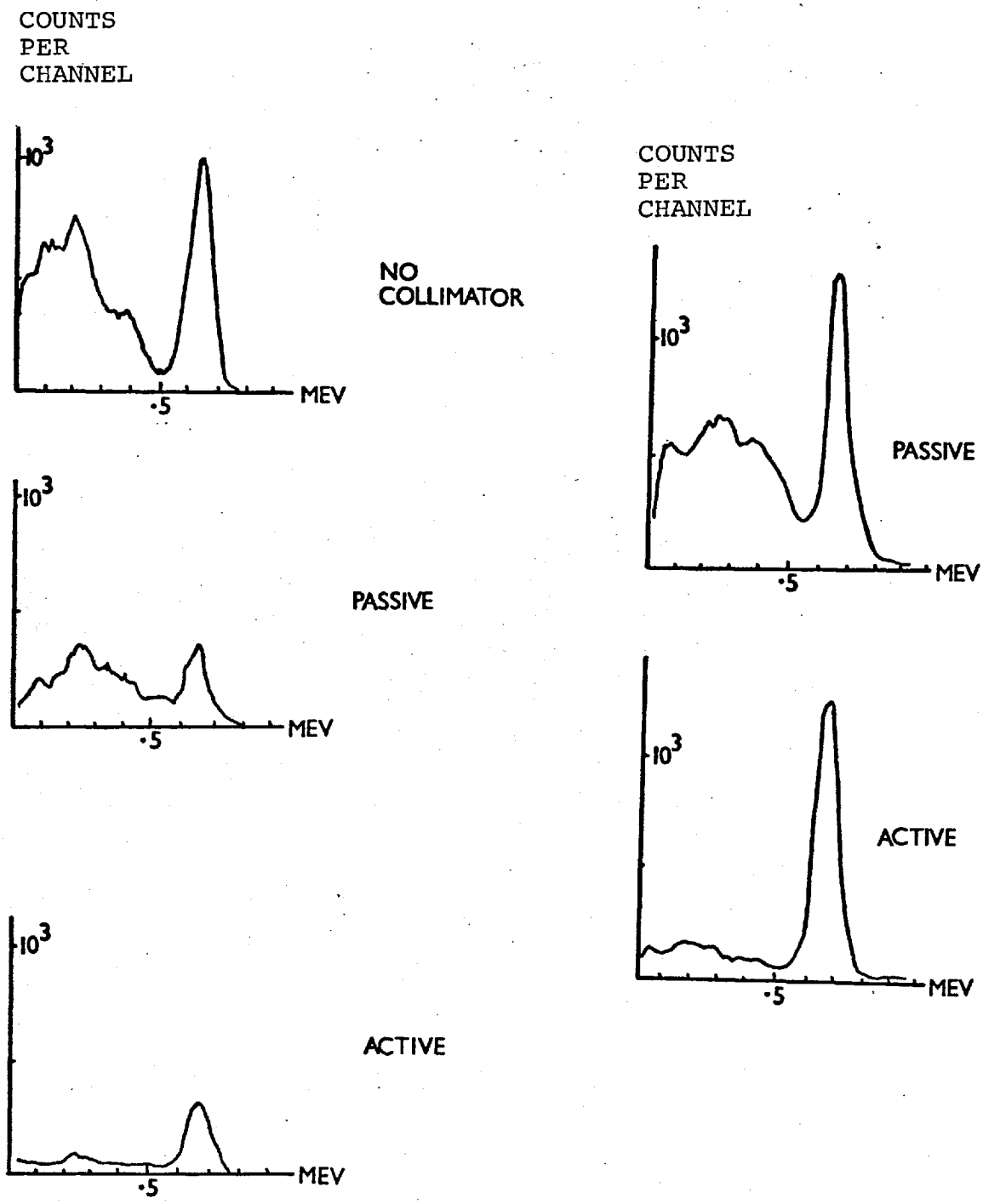

Entry Through Collimator

Entry Through Aperture

Fig. 14

6.5 DETECTOR OPERATION

6.5.1 Spectral Mode

In the spectral mode of operation, experiment F is pointed at the object under study. The pointing accuracy of the spacecraft is nominally $\frac{1}{2}$ degree maximum drift per day, and the direction of viewing can be determined to a few minutes of arc. Observation times are one day or longer, and therefore it is important to single out time variations in the source and background fluxes (e.g. x-rays produced by sudden auroral electron precipitation, solar x-ray bursts, decays of induced radioactive isotopes, latitude changes in atmospheric x-ray background). The method employed to do this is a modulation technique. As shown in Fig. 10, the axis of experiment F is inclined by an angle of 3° to the spacecraft spin axis. If the satellite spin axis is pointed 3° away from the x-ray source to be studied, the detector observes the source over a range of inclinations 0° to 6° during any one spin cycle. Data is accumulated in four spin sectors and stored approximately every 5 minutes (one sixteenth orbit period), so that source variations which are slower than 5 minutes can be resolved within the detector sensitivity. The detector tilt of 3° was chosen because it was the best compromise between large modulation and high sensitivity when the spacecraft spin axis points directly at the source.

At low energies (less than 200 KeV) the angular response of experiment F is determined by the geometry only, since the collimator is nearly 100% efficient, and this is plotted in Fig. 15. The detector geometry consists of two parallel circular areas both of radius 1.75 cm, separated by a distance of 25 cm.

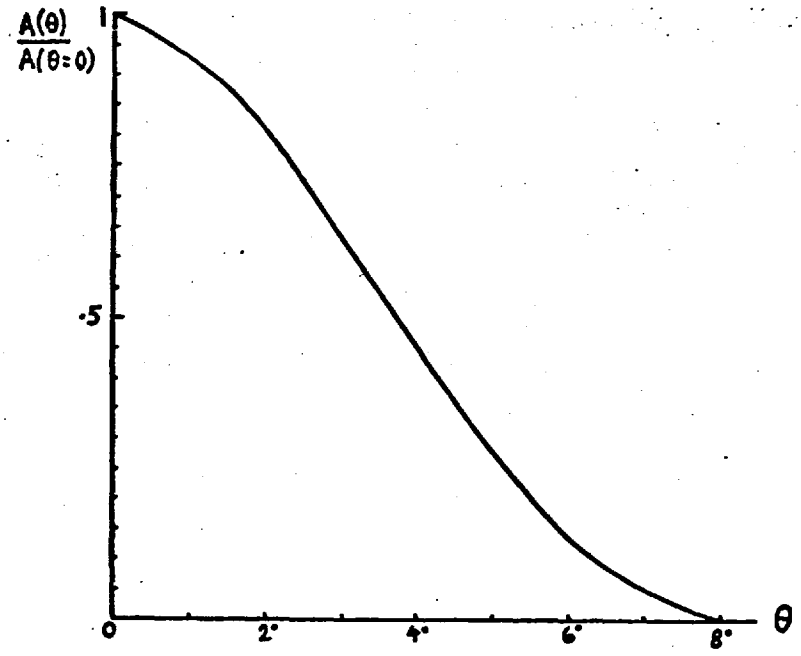

Fig. 15

Using the angular response of Fig. 15, the modulation of a source signal during one satellite revolution can be calculated. If the telescope tilt angle is α and the angle between the satellite spin axis and the x-ray source is β , it is a simple matter to calculate the angle between the telescope axis and the source, θ, for different spin phase ϕ (the angle between the two planes containing the spin axis and source direction, and the spin axis and detector axis respectively)

$$\cos\theta = \cos\alpha \cos\beta + \sin\alpha \sin\beta \cos\phi$$

The modulation has been calculated for telescope tilt angle $\alpha = 2^{\circ}$, 3° and 4°, and for a variety of source inclinations, β . This is shown in Fig. 16a, b, c.

Due to the limited data storage availability only four spin sectors are employed. A sine wave is fitted to the output from these four sectors, and from this analysis it is possible to obtain the amplitude and phase of the first harmonic. (Bartley et.al. 1966)

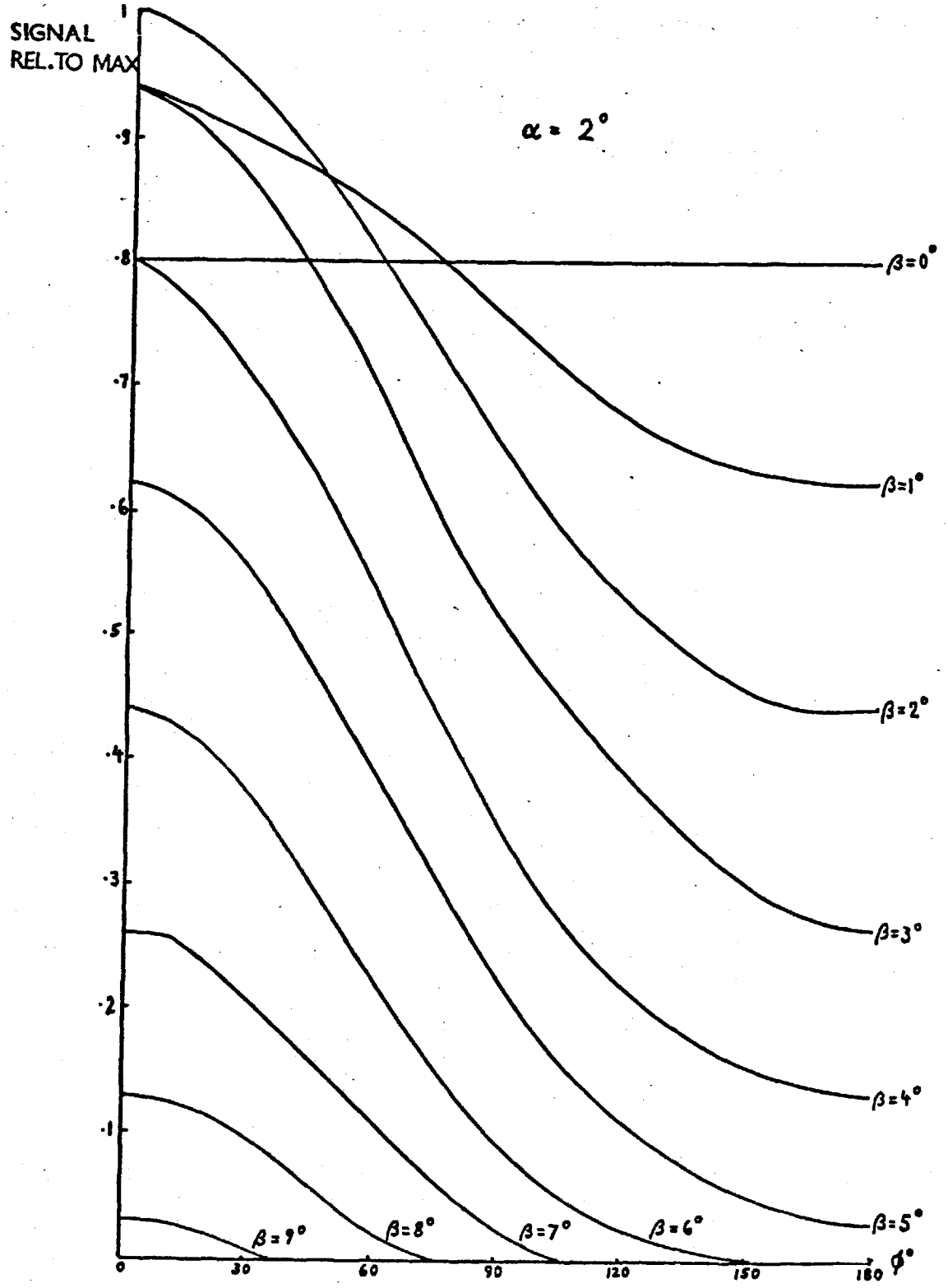

Fig. 16a

Modulation of the detector of Fig. 10 at low energies (< 200 KeV) at constant telescope tilt angle of 2° for different satellite inclinations to the source.

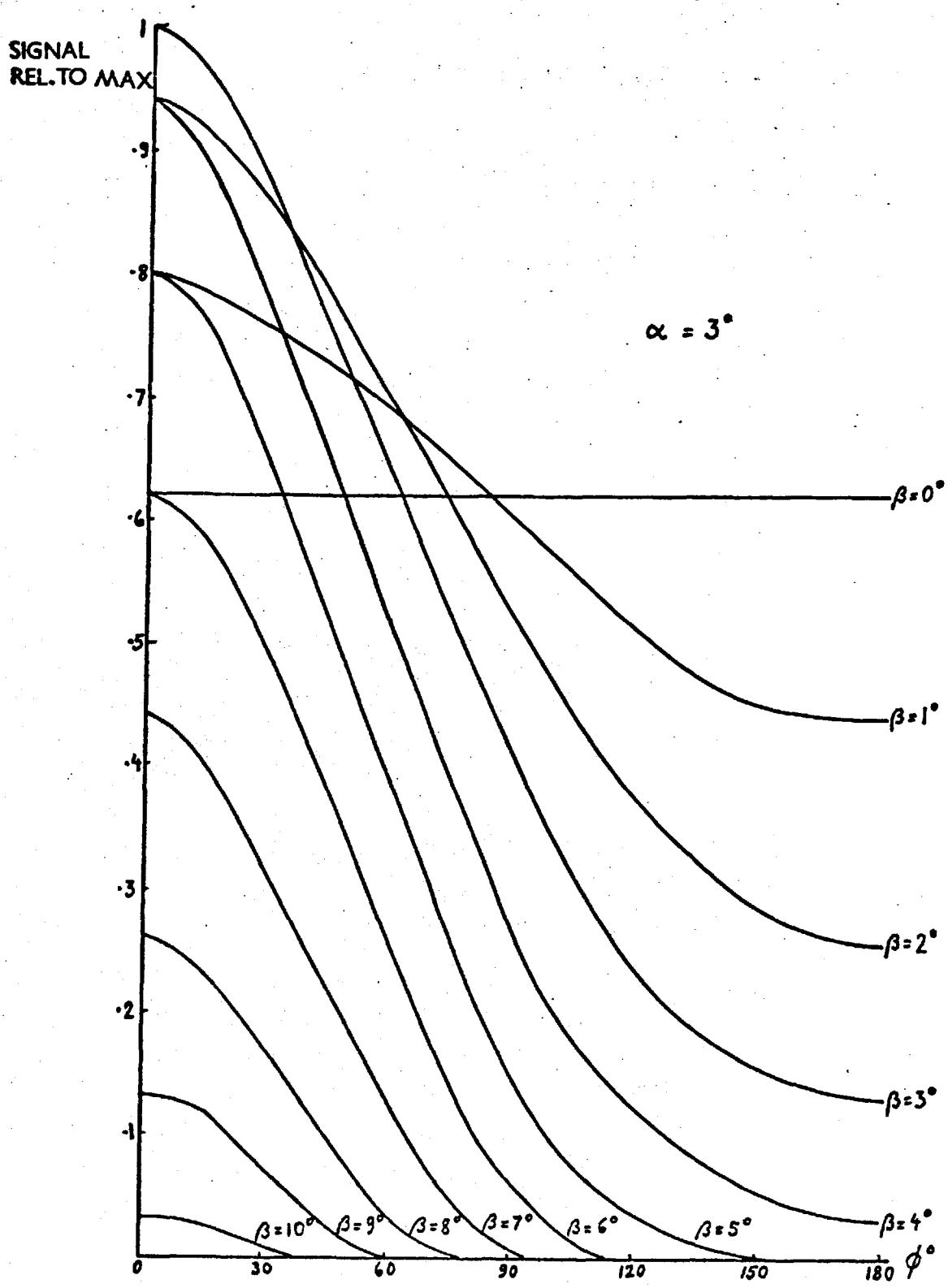

Fig. 16b

Modulation of the detector of Fig. 10 at low energies (< 200 KeV) at constant telescope tilt angle of 3° for different satellite inclinations to the source.

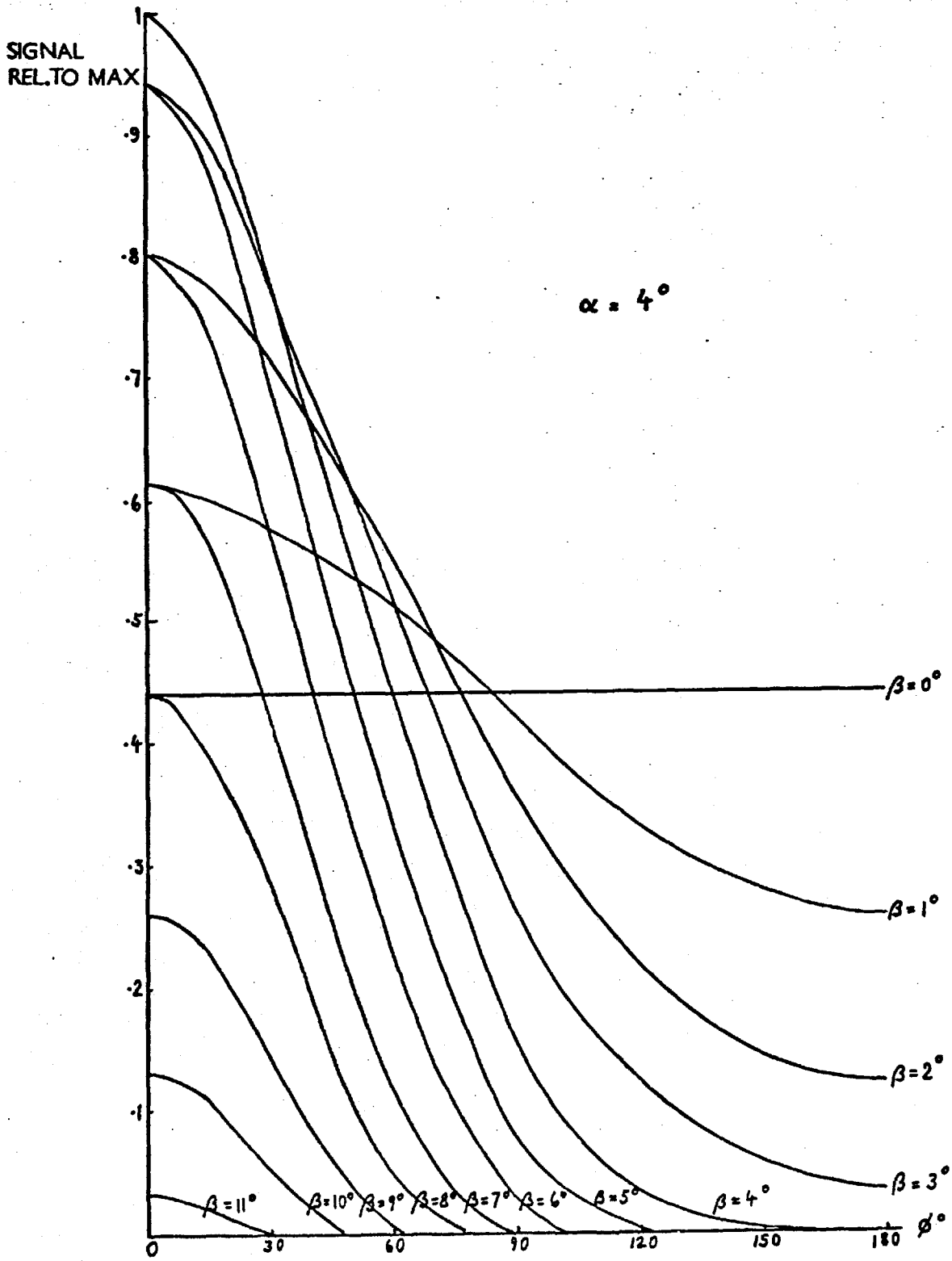

Fig. 16c

Modulation of the detector of Fig.10 at low energies (< 200 KeV) at constant telescope tilt angle of 4° for different satellite inclinations to the source.

$$X = \overline{X} + X_A \cos (\phi - \phi_A)$$

$$X_A = 0.555\sqrt{(X_4 - X_2)^2 + (X_3 - X_1)^2}$$

$$\phi_A = \text{Atan}\,((X_4 - X_2) / (X_3 - X_1))$$

where X_i = counting rate in channel i

$\overline{X}$ = mean counting rate

ϕ_A = phase angle measured from channel 1

X_A = ½ peak to peak amplitude of signal

If there is more than one source in the field of view, simple first harmonic analysis becomes inaccurate, and to avoid this the detector opening angle has been chosen to be small.

The modulation curves of Fig. 16 are not sine curves, so that harmonic analysis does not represent the true variation. This is shown in Fig. 17, where the peak to peak amplitude of the first harmonic has been plotted for a 3° detector tilt as a function of star tilt β. Also shown is the amplitude variation of the real modulation. As can be seen, the difference between the two curves is not great. Also plotted in Fig. 17 is the phase of the x-ray source as calculated from the four sector analysis, and this is compared with the actual phase used. As can be seen, the agreement is within $\frac{1}{2}^\circ$ as long as the star tilt angle is less than 6°. This angle thus marks the predictable operating limit for experiment F. Requirements of other pointing experiments are similar, so that no spacecraft operation is envisaged where the x-ray source under study is more than 6° off the satellite spin axis.

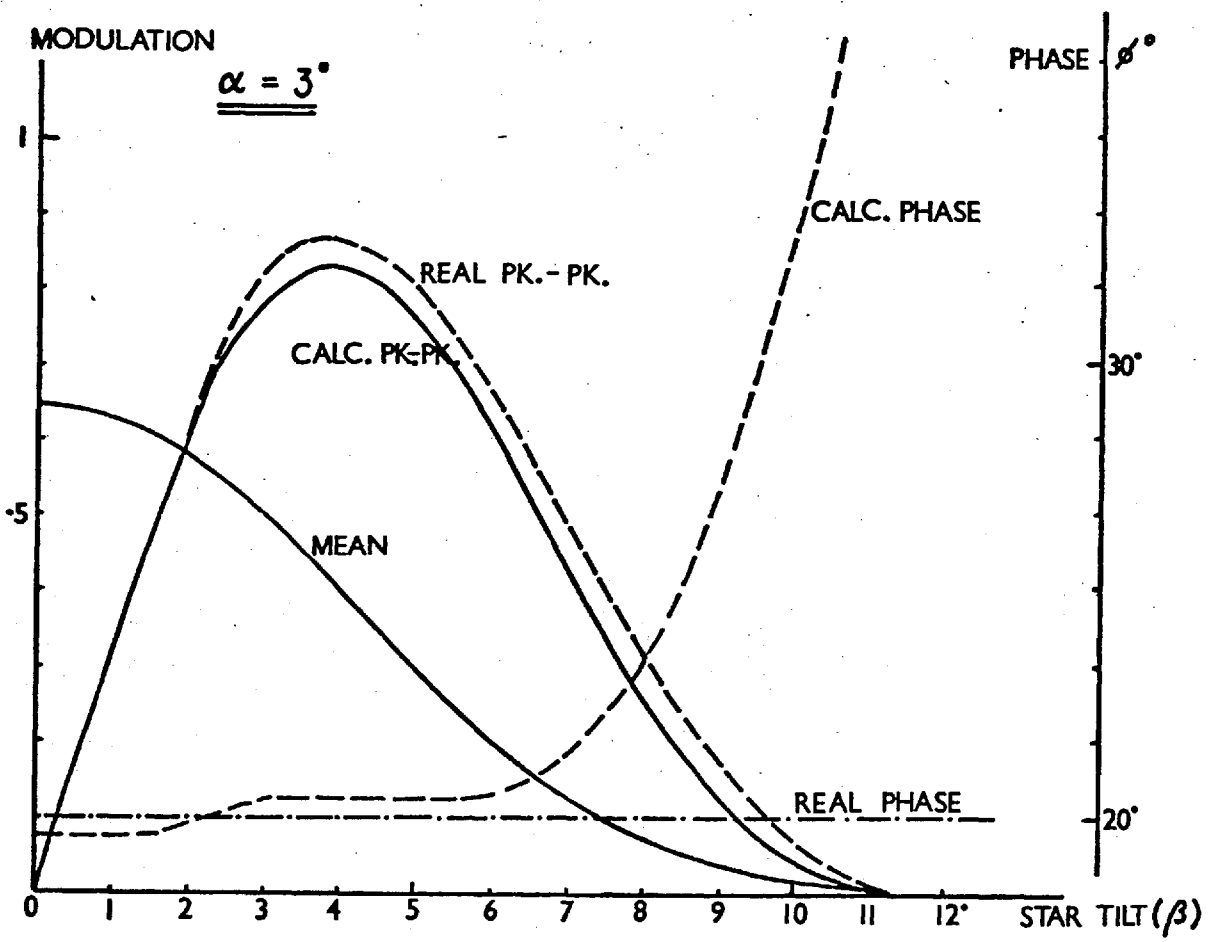

Fig. 17

Also shown in Fig. 17 is the mean of the first harmonic, which gives a measure of the detector sensitivity (compared with the highest sensitivity attainable) at different source inclinations β . Greatest sensitivity is thus obtained provided the spacecraft spin axis points directly at the object under study, and this is the operating procedure for the pulsar mode.

The sensitivity of experiment F is plotted, for a 12 hour viewing time, in Fig. 18. The three standard deviation confidence level is shown.

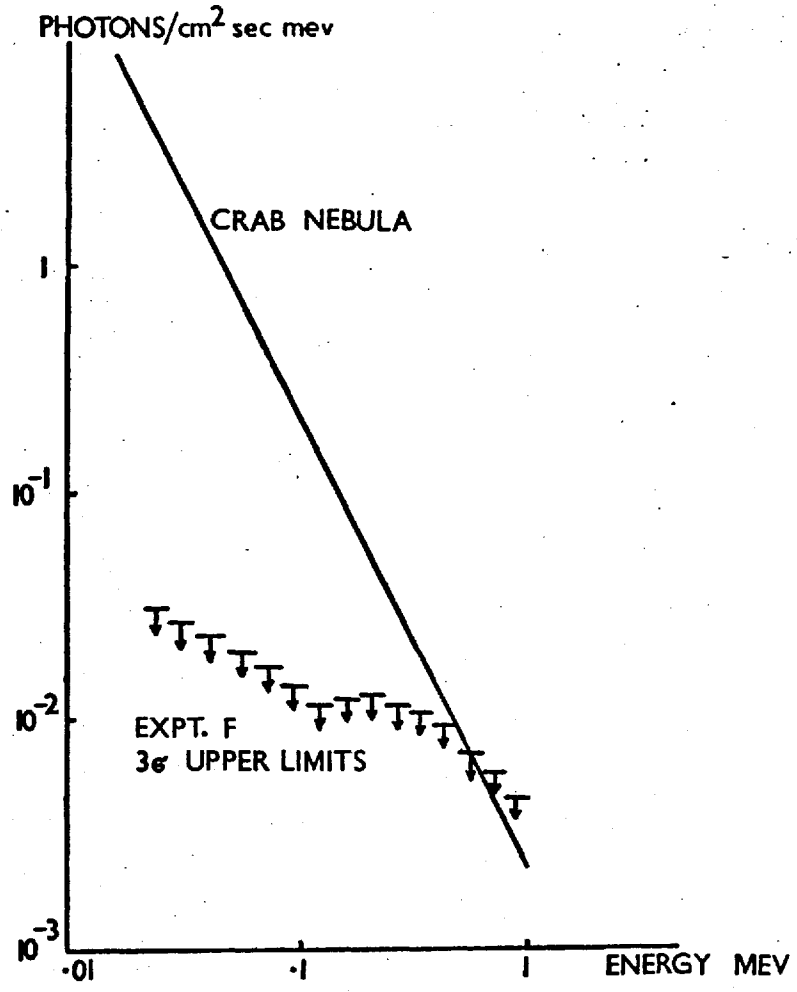

Fig. 18

6.5.2 Pulsar Mode

Pulsars are objects which emit electromagnetic radiation in discrete bursts at a frequency which can be measured very accurately (typically 1 in 10^8). Although this frequency changes as the structure of the pulsar evolves with time, such changes are slow, and for experimental purposes the frequency may be regarded as constant. A large number of radio pulsars have been discovered in recent years, but so far only two x-ray pulsars have been observed, one in the Crab nebula (NP 0532), and the second one in the Cygnus region.

It is of great importance to extend the spectral information of these known pulsars into the energy range covered by experiment F, in order to determine any correlation between pulsar period and emission spectrum which could provide new information on the origin of these objects.

Various methods of analysis have been studied for the pulsar mode, including the recording of x-ray arrival times (to the nearest millisecond) and a full on-board autocorrelation analysis. Both these methods were found to be unsuitable because they required either a great deal of data storage or else too much additional electronics. In addition, since the envisaged programme only intends to study known pulsars with known periods, this information should be an input into the analysis rather than an output in order to reduce data transmission rates.

The method to be used for the pulsar analysis, which has subsequently been adopted by two more experiments on board the UK5 satellite, is based on counting the main satellite crystal oscillator up to a preselected period of time to control the repetitive feeding of a store. Limitations imposed by quantisation of clock frequency, drift of clock frequency due to temperature changes, propagation delays in counters and Doppler effects due to satellite motion and the orbital velocity of the earth, are considered.

If m counters are cycled with period T, the pulsar period, the time that each counter spends looking at the pulsar during one cycle is t, where $t = \frac{T}{m}$. All the pulsar x-rays should be accumulated in the same counter, provided the drifts mentioned above are less than the 'channel width', t. The time 't' is determined by counting the spacecraft clock, which is a crystal oscillator with a 2.2 Mhz frequency, and 't' can be defined to within $\frac{1}{2}$ quantum of the clock period in the worst case. If data is accumulated in the same set of m counters for a period of time P, we have :

Drift allowed in time P is one channel width t, where $t = \frac{T}{m}$

Drift allowed in time t is : $\frac{T}{m} \cdot \frac{t}{p} = (\frac{T}{m})^2 \cdot \frac{1}{p}$

if the drift is always in the same direction, which it is in the case of quantisation errors. The maximum quantisation error is $\frac{1}{2f}$ where f is the crystal oscillator frequency so that

$$\text{drift in time } t < \left(\frac{T}{m}\right)^2 \cdot \frac{1}{p} \leqslant \frac{1}{2f} \qquad (6.5)$$

This is the condition that time correlated counts are kept in one channel during the whole observation time, P, with m channels cycled at the pulsar frequency f.

Pulsars to be studied have periods ranging from 30 msec (NP 0532) to 1 sec or higher.

Using 16 channels, and $f = 2.2 \times 10^6$ Hz, we can calculate the minimum observation time, P_{min}, (corresponding to maximum quantisation inaccuracy $\frac{1}{2f}$) for pulsars of different periods, e.g. 30 msec :

$$P_{min} = 15.5 \text{ sec}$$

e.g. 1 sec :

$$P_{min} = 1.72 \cdot 10^4 \text{ sec.}$$

Hence, if the restriction of one channel drift is relaxed, to perhaps 4 channels for the 30 msec pulsar, P_{min} is greater than 1 minute. Since it is estimated that 50% of each 90 minute orbit is useful observation time, several sets of m channels are required to overcome quantisation drifts at the higher frequencie to be observed. An autocorrelation analysis on the ground is then required to extract time correlated counts. Store allocation for the pulsar mode is 1024 16-bit words, allowing 64 sets of 16 channels with no pulse height information or alternatively $\frac{64}{K}$ sets of 16 channels with K pulse heights to be recorded. The quantisation drift is expected to cause the dominant restriction in viewing time with the same set of m counters.

The Doppler effect is calculated from

$$T = T_e \left(1 - \frac{\underline{v} \cdot \hat{\underline{r}}}{c}\right) \Big/ \sqrt{1 - \frac{v^2}{c^2}} \qquad (6.6)$$

where $\underline{v}$ is the velocity of the observer, $\hat{\underline{r}}$ is the unit direction vector of the source seen from the observer and T_e is the emission period of the pulsar.

Hence, for a source approaching the observer, $\underline{v} \cdot \hat{\underline{r}} = v$, for a receding source $\underline{v} \cdot \hat{\underline{r}} = -v$, and for a source moving at right angles to the line of sight $\underline{v} \cdot \hat{\underline{r}} = 0$.

The effect of the orbital motion of the earth can be calculated, and allowed for when programming the pulsar mode. The satellite motion introduces changes in the observed pulsar period of magnitude $10^{-5} \cdot T$.

The observed drift in the clock period due to temperature variations is $0.3 \times 10^{-6} T$ per ^{o}C temperature change, and the temperature variation expected for the clock during an orbit is $2^{o}C$ peak to peak. The stability of the oscillator has been measured over a period of 17 months at constant temperature and is found to be substantially better than 1 part per million.

Effects of propagation delays in the counter logic can be measured before launch since the pulsar periods to be investigated are known.

The conclusion from these calculations is that Doppler effects due to the satellite orbital motion introduce the largest drift, apart from the quantisation effects, so that the analysis to be used for examining known pulsars is feasible and provides the greatest sensitivity available with small storage capability.

Sensitivity of Pulsar Mode

The minimum flux observable at the 3 standard deviation confidence level is obtained from

$$\frac{\int_{E_1}^{E_2} F_p(E)\, A\, t\, \rho(E)\, dE}{\sqrt{\int_{E_1}^{E_2} F_B(E)\, A\, t\, d\Omega\, \rho(E)\, .\, \frac{\Delta}{T}\, dE}} \geq 3 \qquad (6.7)$$

where the background counts are only those which arrive through the aperture, i.e. the pulsar mode is restricted to energies below 200 KeV. Δ is the pulse duration or the channel width, whichever is longer, and T is the pulsar period. Since the detection efficiency $\rho(E) \doteq 1$, and $d\Omega = \frac{A}{h^2}$, we can rewrite 6.7 as

$$\int_{E_1}^{E_2} F_p(E)dE \geq \frac{3}{h}\sqrt{\frac{\Delta}{t.T}\int_{E_1}^{E_2} F_B(E)dE} \qquad (6.8)$$

Using $F_B(E) = 0.026\ E^{-2}$ photons/cm^2 sec ster MeV for the background flux, and putting $\frac{\Delta}{T} = \frac{1}{m} = \frac{1}{16}$ if all the pulsar counts occur in one channel, and for h = 25 cm, we find the pulsar sensitivity for an observation time of one day, assuming 50% data recovery (equivalent to $t = 4.3 \times 10^4$ sec). This is plotted in Fig. 19.

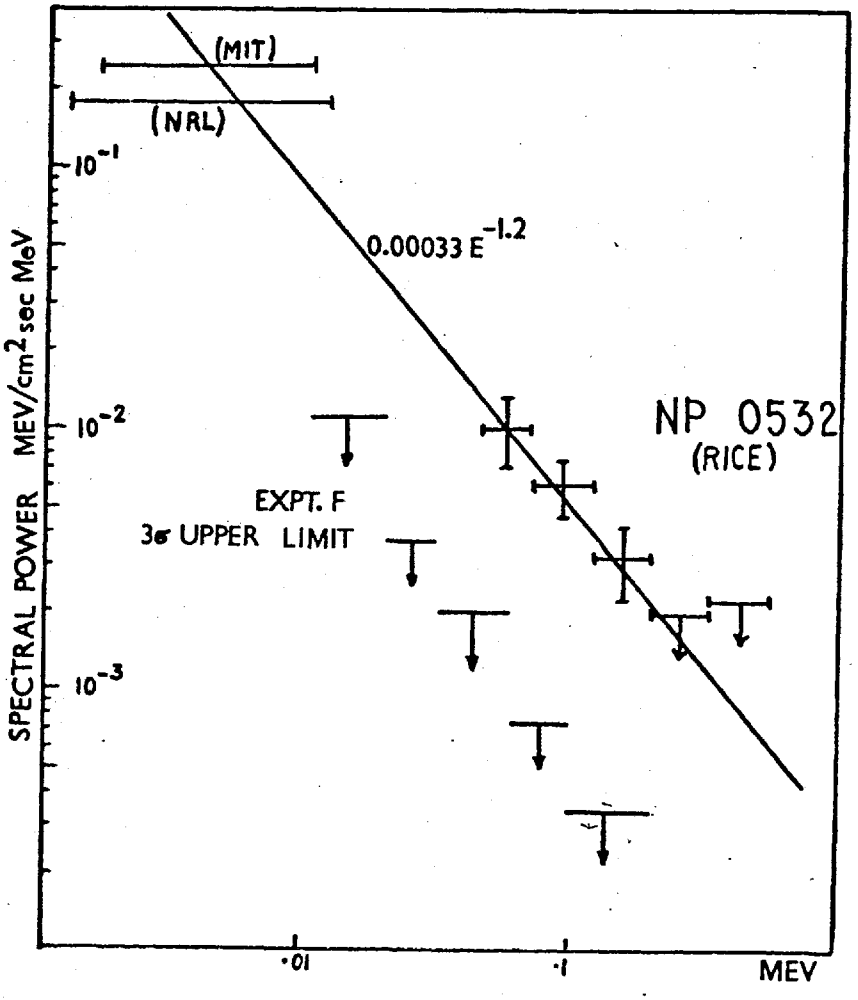

Fig. 19

PART II

HIGH ENERGY SOLAR PROTONS AND COSMIC RAYS
ANALYSIS OF DATA FROM EXPERIMENT S.28 ON THE ESRO II SPACECRAFT

1. ABSTRACT

In this section data from the experiment S.28 on board the ESRO II satellite is analysed. The factors influencing the detector design are described, and the telescope optics is calculated and compared with experimental values. The detector performance in orbit is examined, including the response to electrons and to high particle fluxes. The effects of atmospheric losses have been predicted accurately using an effective atmospheric height and a loss cone centred around the magnetic field line.

The entry of solar protons to low altitudes over the polar caps is studied with the aid of trajectory integrations in a high simulation of the geomagnetic field. Local particle gradients and anisotropies are found to cause most of the observed structure, and in addition new information about the distant magnetotail and the magnetopause is obtained from solar protons of energy > 27 MeV. The magnetic field model used here for the trajectory work is valid far enough in the tail (20-25 R_E) to allow adiabatic extrapolation of particle trajectories to further distances. Other presently available trajectory programs become unrealistic at distances greater than 10 R_E. The field model used here applies to dipole tilts of less than 15^o with good accuracy.

Observations of proton entry into the magnetosphere by various authors are examined using the knowledge gained from the trajectory integrations performed here, and all the observations are found to be consistent with the same magnetosphere/magnetotail model.

2. DESCRIPTION OF THE DETECTOR

Figure 1 is a diagram of the essential pieces of the detector which is basically a four-element telescope drawn to scale. The top element consists of an EMI. 9526 one inch photo-multiplier looking sideways at a piece of NE-102-A scintillator, 25 mm square and 2 mm thick. A wedge-shaped reflector made of 0.03 cm thick aluminium and painted white on the inside is used to direct the light onto the phototube face. There is no direct optical coupling between the tube and the scintillator. The response of this system was investigated using protons from the Harwell synchrocyclotron, and found to be satisfactory, with the width of the response curve due mainly to Landau fluctuations. This element of the telescope was used to reject 0.2 to 0.43 Gv protons from the 0.43 - 0.88 Gv alpha-particles by the requirement that the pulse height should be at least 15 times minimum ionizing before the logic would accept it as a slow alpha-particle. The detector was calibrated by using sea-level μ-mesons to find the pulse height for a minimum ionizing particle.

The viewing cone of the telescope is set by a combination of this top element and the second element which consists of two small proportional counters, 20th Century Electronics type 2.5 MA. Proportional counters were chosen here for their reliability and simplicity; no pulse height analysis is made of their outputs. The proportional counters have an outside diameter of 1.25 cm and a sensitive length of approximately 2.5 cm. The counters were specially produced for this experiment. They have a copper wall with a thickness of 0.38 mm (equivalent to 0.34 gm/cm^2) and a tungsten wire of 0.03 mm diameter as the anode. They are filled with a mixture of 10 per cent methane and 90 per cent argon at a pressure of about 65 cm Hg. The counters were checked using the Harwell synchrocyclotron protons and their relative gains measured. They were fitted into the S.28 units in matched gain pairs.

Analysis of the materials in the sensitive angle of the telescope shows that a particle must pass through 0.78 gm/cm^2 before it meets the gas of the proportional counter. No particle will be detected by the logic if it fails to reach these counters. This restricts the lower energy limit for the detector to 96 Mev (0.43 Gv) for an alpha-particle.

Underneath the proportional counters lies a block of lead 10 mm thick, representing 11.3 gm/cm^2, and below this is a scintillator which forms the third element of the telescope. The amount of material a particle must pass through to reach this scintillator is a total of 12.4 gm/cm^2. Particles which pass through the top two elements, and are recognised as alpha-particles by the top element, are rejected from the slow alpha-particle channel if they are detected by this third element. This fixes the upper energy limit for this channel at 346 Mev, i.e. a rigidity $\sim$ 0.88 Gv.

The third element consists of a 5mm thick sheet of NE-102-A with edges raised to the level of the top of the lead. These raised edges reduce the effect of showers produced in the lead by particles not in the viewing angle of the telescope. The scintillator is connected by a perspex light guide to a one inch diameter photomultiplier. The use of this light guide improves the distribution of pulse heights from the scintillator.

Slow protons must produce a coincidence between the top three elements in order to be detected. Hence, the lower energy limit for the slow proton channel is 90 Mev (0.42 Gv). Also, they must not behave like alpha-particles in the top element, or be detected by the fourth element, which is a perspex cerenkov detector mounted immediately below the large scintillator. The threshold for cerenkov light from a proton in perspex is 350 Mev, corresponding to a rigidity of 0.88 Gv, and this is the upper limit for the slow proton channel.

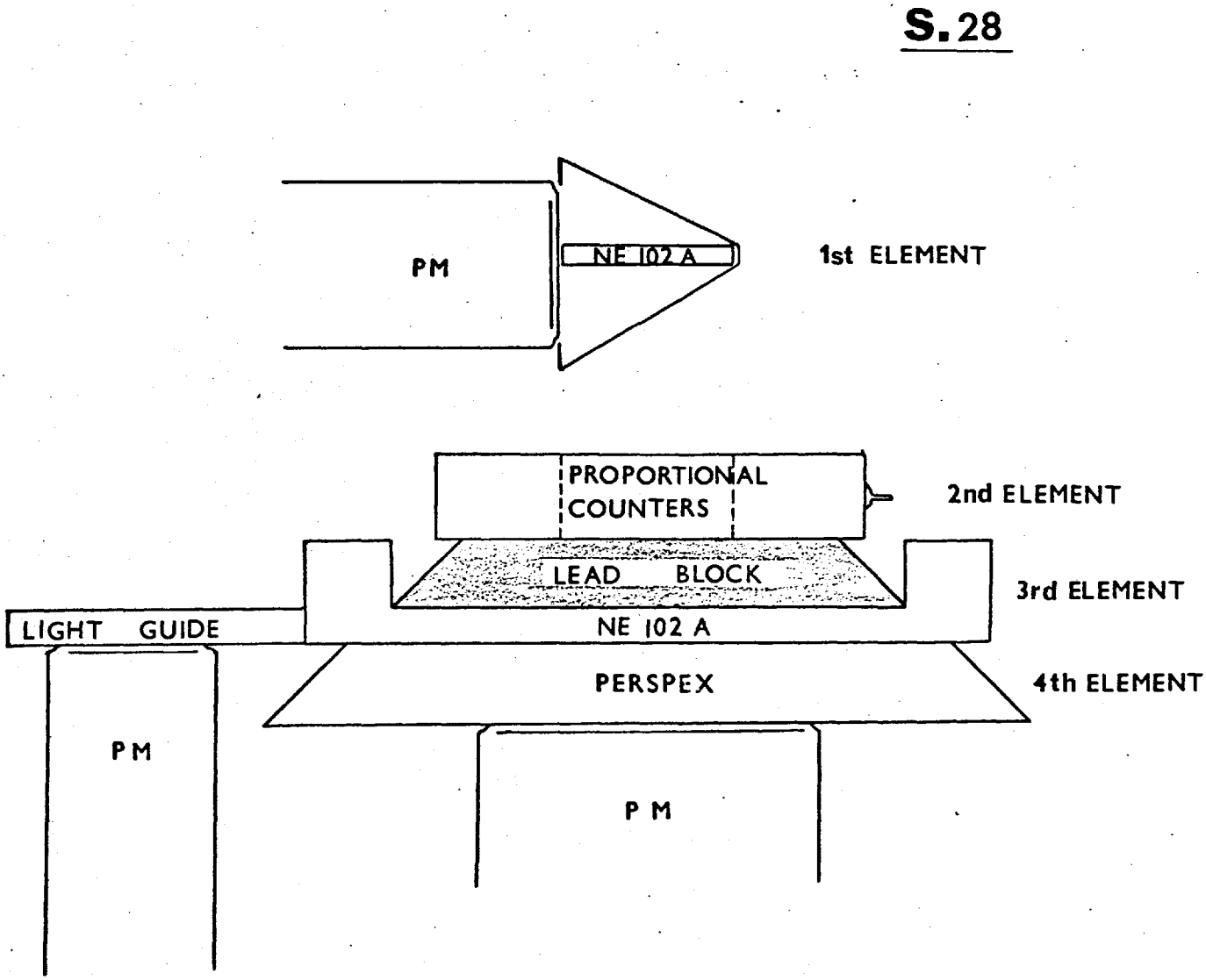

Fig. 1

Diagram of the S.28 detector on board the ESRO II satellite, drawn to scale. Positions of photomultipliers and the elements making up the particle telescope are shown.

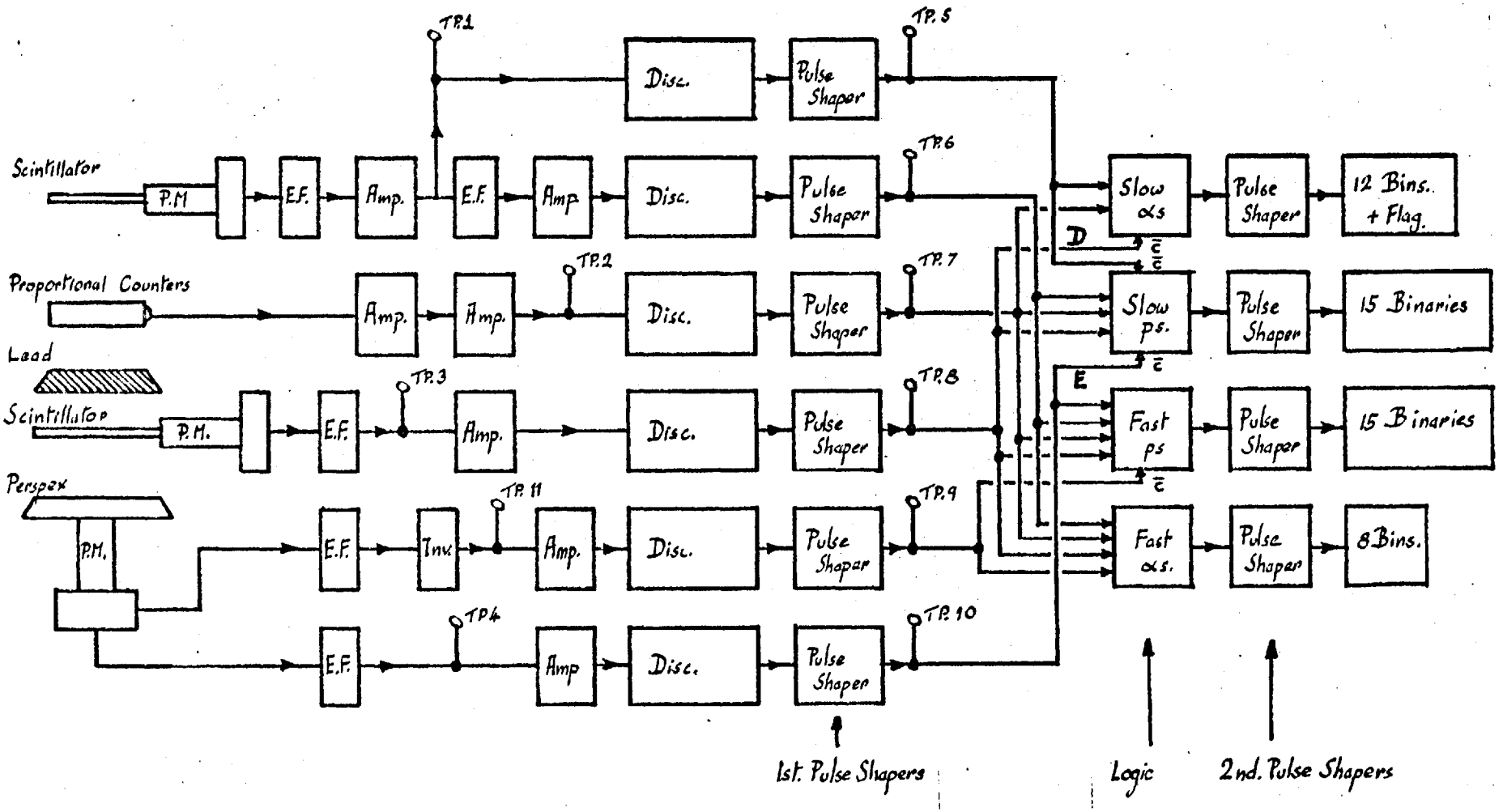

Fig. 2

Block diagram of the electrical circuit of S.28. $\overline{C}$ denotes anticoincidence. PM = Photomultiplier, EF = Emitter follower, Inv = Inverter, Amp = Feedback pair voltage amplifier, Disc = Discriminator, TP = Test Point

A two inch diameter photomultiplier (EMI. 9644A) was used in conjunction with the perspex detector as it gave a better pulse height distribution than the smaller and lighter one inch diameter phototube. The perspex is 1.25 cm thick and acts as its own guide for the light from particles that pass near to its edges.

In addition to the measurement of the slow alpha-particles and protons, coincidences between all four elements give a measure of the relativistic particle flux. This is split into protons and multiply charged particles by separating the pulse heights in the cerenkov element. This separation is necessarily simple because of the low resolution of the perspex; in practice, the lower channel was set to observe all relativistic particles passing through the perspex with an anticoincidence from the upper channel, which had its discrimination level raised until none of the singly charged relativistic particles were registered. A block diagram of the electrical circuit is shown in Fig. 2.

3. CALCULATION OF GEOMETRIC FACTOR

3.1 NOMINAL VALUE

The elements which define the sensitive solid angle are two square area detectors, each of side 'a', separated by a distance 'd'. The effective area presented by such a detector to a parallel beam of particles, incident at an angle θ to the telescope axis and a phase angle ϕ (measured from one of the sides of the square) is :

$$A(\theta\phi) = (a - d \tan\theta \sin\phi).\ (a - d \tan\theta \cos\phi)$$

Since the expression is symmetrical about $\phi = \frac{\pi}{4}$, $A(\theta,\phi)$ is integrated from ϕ_{min} to $\frac{\pi}{4}$ in order to calculate the average area presented to the θ component of an isotropic flux of particles, where

$$\phi_{min} = 0 \text{ if } \tan\theta \leqslant \frac{a}{d}$$

$$\text{or} \quad \phi_{min} = \cos^{-1} \frac{a}{d\tan\theta} \text{ if } \tan\theta > \frac{a}{d}$$

Hence the average area is :

$$\overline{A(\theta)} = \frac{4}{\pi}\int_{\phi_{min}}^{\frac{\pi}{4}} (a - d\tan\theta\sin\phi)(a - d\tan\theta\cos\phi)\, d\phi \quad (3.1.1)$$

$$= \frac{4}{\pi}\left\{a^2(\frac{\pi}{4} - \phi_{min}) + adtan\theta(sin\phi_{min} - cos\phi_{min}) + \frac{d^2tan^2\theta}{2}(sin^2\frac{\pi}{4} - sin^2\phi_{min})\right\}$$

Thus for $\tan\theta > \frac{a}{d}$

$$\overline{A(\theta)} = a^2(1 - \frac{2}{\pi}) - \frac{4a^2}{\pi}\cos^{-1}(\frac{a}{dtan\theta}) + \frac{4a}{\pi}\sqrt{d^2tan^2\theta - a^2} - \frac{d^2tan^2\theta}{\pi} \quad (3.1.2)$$

and for $\tan\theta \ll \frac{a}{d}$

$$\overline{A(\theta)} = a^2 - \frac{4adtan\theta}{\pi} + \frac{d^2tan^2\theta}{\pi} \quad (3.1.3)$$

The component of area perpendicular to the incident beam at angle θ is :

$$A(\theta) = \overline{A(\theta)}\cos\theta$$

which gives the geometric factor

$$G.F. = 2\pi\int_0^{\frac{\pi}{2}} \overline{A(\theta)}\cos\theta\sin\theta\, d\theta$$

For S.28 this value was 2.48 cm^2 ster.

This result was checked using sea-level μ-mesons. Allowing for the μ-meson intensity variation with zenith angle, the experimental value for the geometric factor was $2.4 \pm 0.2 cm^2$ ster. The detector efficiency has been measured over the whole operational temperature range. It was found that the efficiency is greater than 96%.

3.2 LOW ENERGY CONTRIBUTION TO CHANNEL 3

The Cherenkov detector is set to a very sensitive level, in order to keep the channel 3 low energy threshold as near as possible to the estimated value of ~360 MeV for protons. As

a result of this, it was found that scintillation in the glass photomultiplier face, caused by protons of energy less than the Cherenkov limit, produces enough light to register these particles in channel 3 also. Fig. 3 shows the channel 3 response to 145 MeV protons as measured with particles produced by the Harwell synchrocyclotron. The calculated response for scintillation in the photomultiplier face is also indicated. This experiment also shows that the sensitive proportional counter volume is approximately the same as the geometric volume, since otherwise Fig. 3 would show a decrease in the measured response curve at $\theta = 0^{\circ}$ for the proton beam incident in the X-Xplane.

We approximate the telescope optics in this case by two parallel circular areas, radii r_1 and r_2 (with $r_1 > r_2$) separated by a distance d. The telescope is cylindrically symmetric. Although in reality the top element is square, calculations have shown that the circular approximation employed here is only 2% in error.

The effective area presented by such a detector to a parallel beam, incident at angle θ, is :

$$A_{\perp}(\theta) = \pi r_2^{\,2} \cos\theta$$

if $\tan\theta \leqslant \dfrac{r_1 - r_2}{d}$

For larger θ

$$A_{\perp}(\theta) = \left[r_1^{\,2}\left(\beta - \frac{\sin 2\beta}{2}\right) + r_2^{\,2}\left(\alpha - \frac{\sin 2\alpha}{2}\right)\right] \cos\theta \quad (3.2.1)$$

α and β are obtained from

$$\sin\beta \cdot r_1 = \sin\alpha \cdot r_2$$

$$r_2\cos\alpha + r_1 \cos\beta = d \tan\theta$$

The geometric factor is :

$$G.F. = 2\pi \int_0^{\frac{\pi}{2}} A_{\perp}(\theta) \sin\theta \, d\theta$$

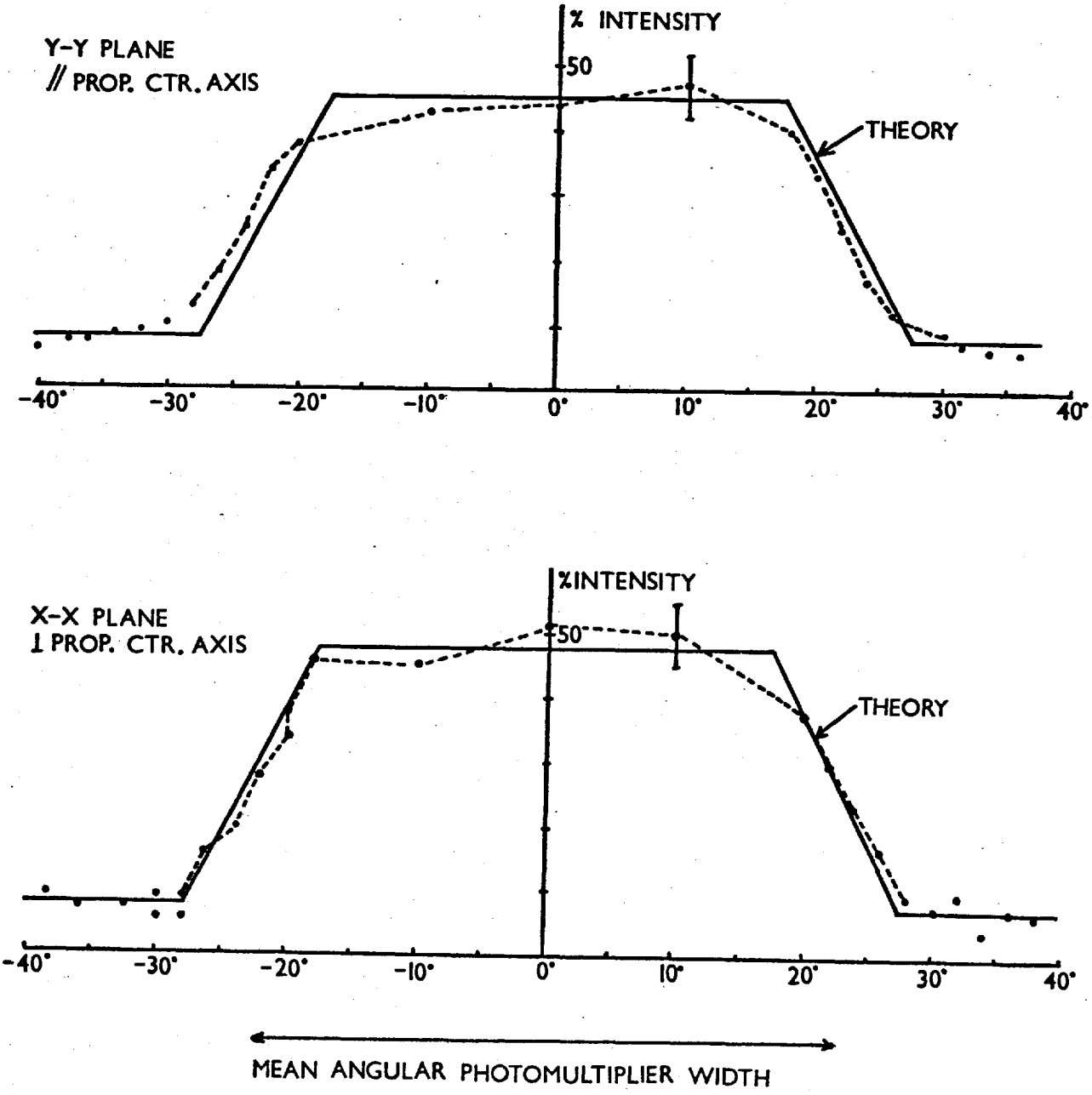

Fig. 3

Angular response of the high energy channel (ch. 3) to 145 MeV protons. The solid curve gives the expected variation in angular response if the observations are due to scintillation in the photomultiplier face.

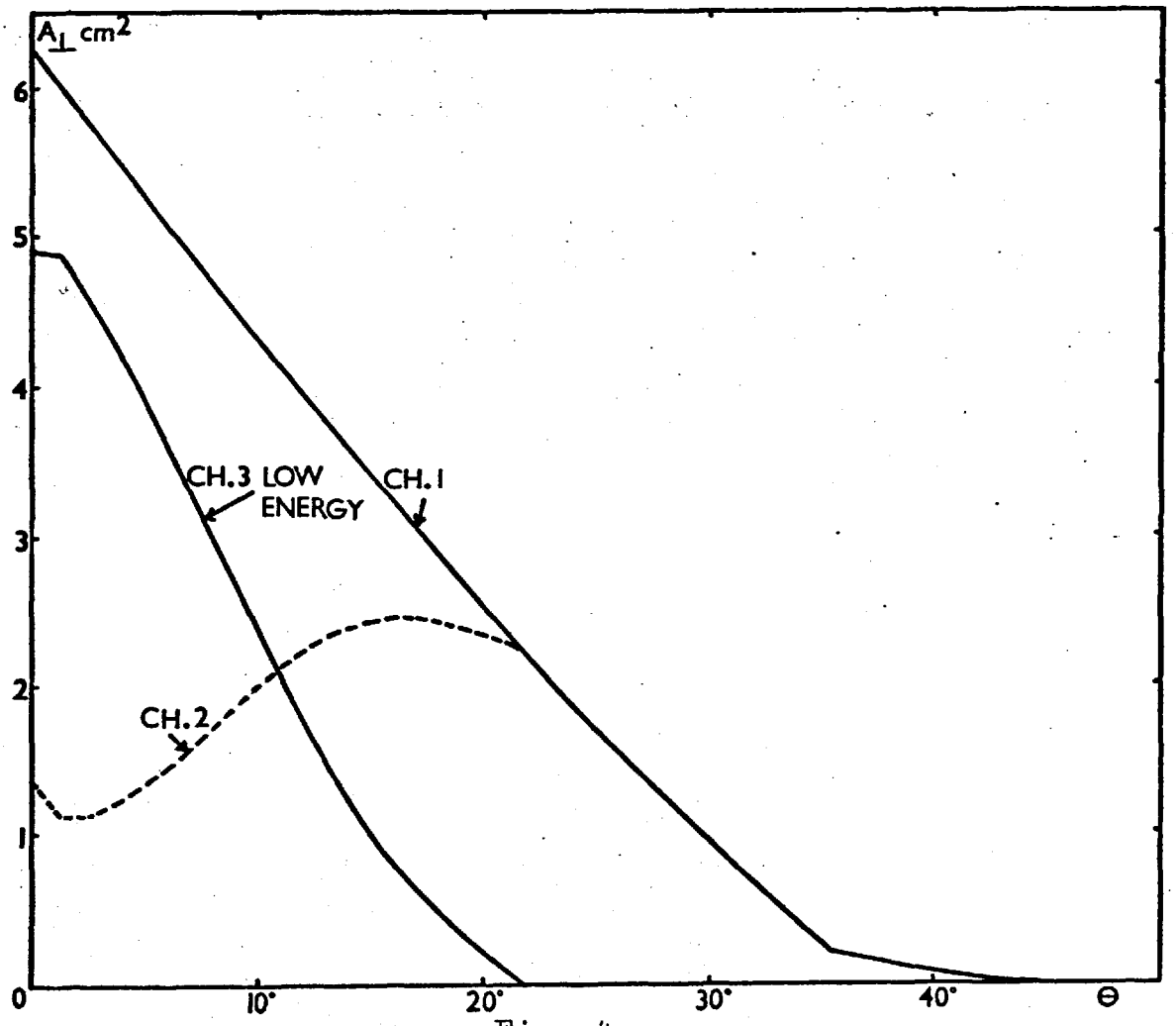

Fig. 4a

Area presented to a proton beam as a function of angle of incidence. Angular variations of Channels 1 and 2 and the low energy contribution to channel 3 are presented.

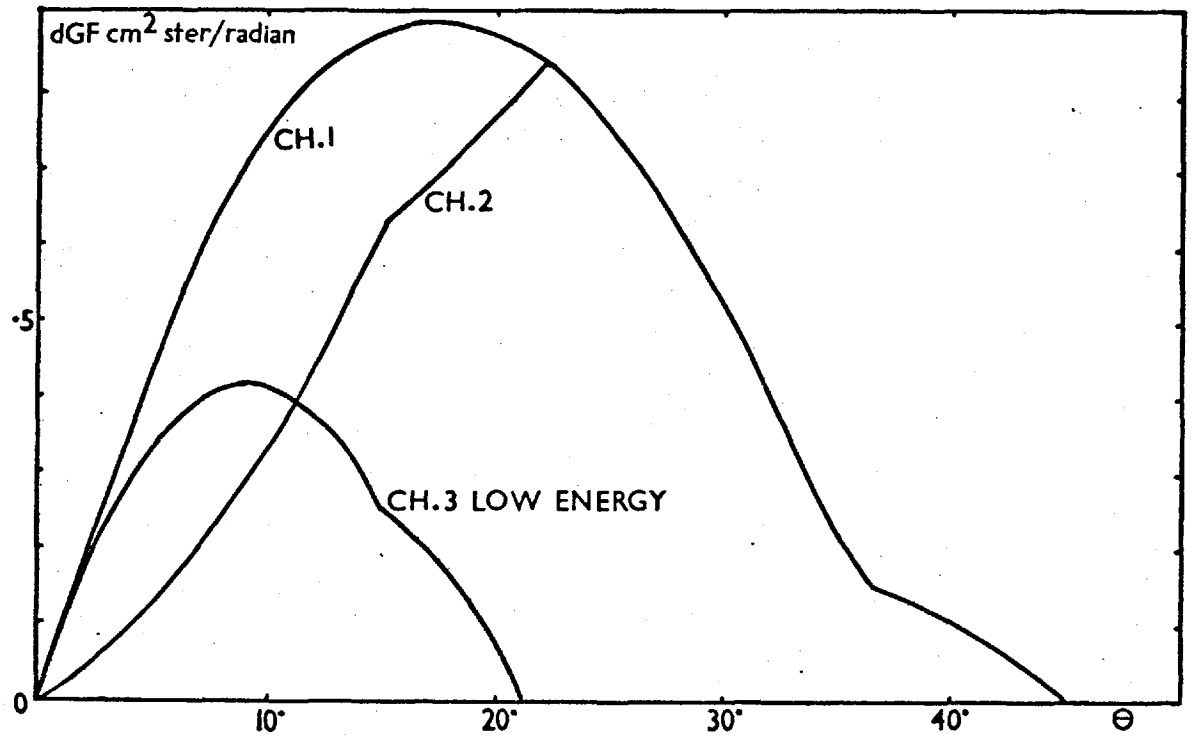

Fig. 4b

Differential geometric factor as function of angle from the telescope axis for the three geometries involved.

For S.28 this value was 0.64 cm^2 ster, but some allowance must still be made for the detection efficiency. If this efficiency is $\overline{\rho_3}$ for channel 3, and $\overline{\rho_4}$ for the α channel 4, we obtain the following geometric factors :

Channel 1	α-particles ($0.43 \leqslant R < 0.88$ GV)	2.48 cm^2 ster.
Channel 2	protons ($0.42 \leqslant R < 0.88$ GV)	2.48 $-\overline{\rho_3}$ 0.64 cm^2 ster.
Channel 3	protons ($0.44 \leqslant R < 0.88$ GV)	$\overline{\rho_3}$ 0.64 cm^2 ster.
	protons ($0.88 \leqslant R < \infty$ GV)	2.48 cm^2 ster.
Channel 4	α-particles ($0.95 \leqslant R < 1.78$ GV)	$\overline{\rho_4}$ 0.64 cm^2 ster.
	α-particles ($1.78 \leqslant R < \infty$ GV)	2.48 cm^2 ster.

Fig. 4a is a plot of $A_\perp(\theta)$ for the three cases of Channel 1, Channel 2 (using $\overline{\rho_3} = 1$), and channel 3 low energy proton response (using $\overline{\rho_3} = 1$), and Fig. 4b shows the differential geometric factor $A_\perp(\theta) \sin\theta$ as a function of θ for the three cases.

3.3 ENERGY DEPENDENCE OF GEOMETRIC FACTOR

Refinements to these calculations are possible and must be introduced when analysing, for instance, inner belt data.

(a) Variation of Low Energy Limit With Angle of Incidence

Since the experiment employs a range technique for defining the low energy thresholds of Channels 1 and 2 and the upper limit of Channel 1, these thresholds must depend on the angle of incidence of observed particles.

The range at angle θ is $R_o/\cos\theta$ where R_o is the vertical range. From range-energy curves we get for the region of interest

$$\text{Range} \propto E^n$$

Hence

$$\frac{E_\theta^{\,n}}{E_o^{\,n}} = \frac{R_o}{R_o \cos\theta}$$

$$E_\theta = E_o (\cos\theta)^{-\frac{1}{n}}$$

n is measured to be ~ 1.66 for both protons and α-particles. Thus for a steeply falling spectrum, contribution to the counting rate from large angles are less significant. For a given spectrum this is best expressed as a weighting factor. If the integral energy spectrum is of the form E^{-a}, and the energy channel has a range E_θ to E_2 where $E_2 = k_2 E_o$ then the weighting factor for the differential geometric factor of channel 2 is :

$$\eta_2(a) = \left(\frac{\cos\theta^{\frac{a}{n}} - k_2^{-a}}{1 - k_2^{-a}}\right) \qquad (3.3.1)$$

For channel 1, where both limits are determined by range methods, the weighting factor at angle θ is :

$$\eta_1(a) = (\cos\theta)^{\frac{a}{n}} \qquad (3.3.2)$$

(b) Efficiency of Channels 3 and 4 Low Energy Response

The mean efficiency over the energy range is given by :

$$\overline{\rho_3(a)} = \frac{\int_{E_o}^{E_2} j(E)\rho_3(E)dE}{\int_{E_o}^{E_2} j(E)\,E} \qquad (3.3.3)$$

where j(E) is the differential particle energy spectrum. $\rho_3(E)$ has been determined experimentally to be 50% for 145 MeV protons incident from the forward direction, and 30% for 145 MeV protons incident from the rear. From $\frac{dE}{dx}$ curves in glass, it is possible to find the approximate shape of the $\rho_3(E)$ v. E curve and to use this to calculate $\overline{\rho_3(a)}$. For low energy cosmic rays (0.43 GV - 0.88 GV) for instance, the efficiency for front entry has been calculated as 30%. Since ionisation loss $\frac{dE}{dx} \propto z^2$, α-particles produce four times as much light as protons and are detected more efficiently. It has been assumed here that the low energy α-contribution to channel 4 is ~ 100% efficient.

(c) Particles Passing Through the Spacecraft

Since the satellite is not a homogeneous body, the incident cut-off energy is a complicated function of direction. The average low energy cut-off which takes into account the average shielding effect of the spacecraft material is 0.52 GV. For cosmic rays this method of averaging is sufficient to analyse data, because the contribution to the total counting rate in channel 2 due to ~ 0.52 GV particles is small. For a steeply falling spectrum, however, the low energy cut-off is important and greater care must be taken.

(d) Range Straggling

The effect of straggling has been investigated using protons from the Harwell synchrocyclotron. Results, shown in Fig. 5, indicate that the effect is small.

A computer program which takes all these refinements into account has been written and is used to analyse S.28 data.

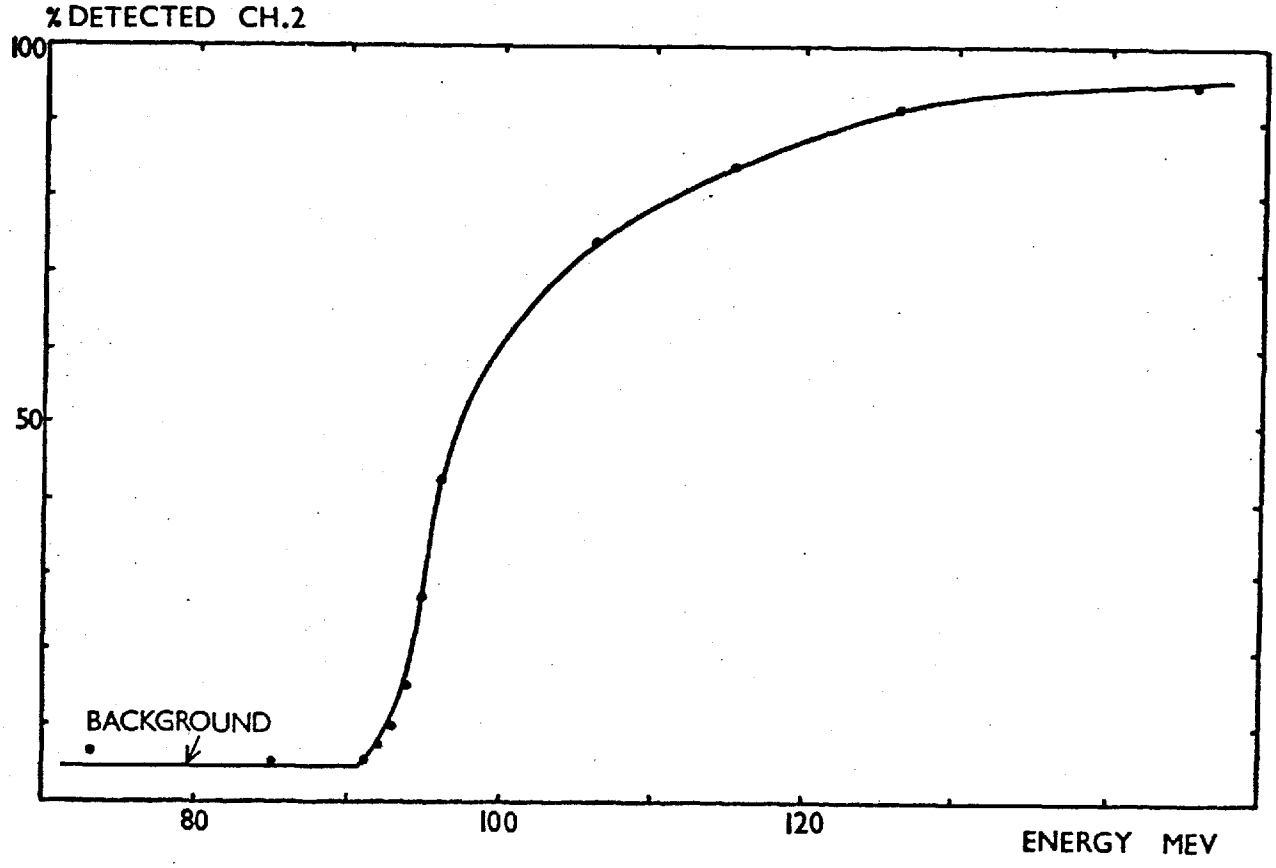

Fig. 5

(e) Cherenkov Detector Response

The amount of light produced by a Cherenkov detector depends on the charge of the particle detected and its velocity. The basic Cherenkov relation for a coherent wavefront is :

$$\cos\theta \doteq {}^{1}/_{\beta n} \qquad (3.3.4)$$

where θ = angle of light emission w.r.t. particle direction $\underline{V}$

$$\beta = {}^{|\underline{V}|}/_{C} > \frac{1}{n}$$

n = refractive index (1.495 for perspex)

The number of photons produced by a particle moving along a track of length l in the wavelength range λ_1, to λ_2 is :

$$N = 2\pi\alpha_f z^2 \, l \left(\frac{1}{\lambda_2} - \frac{1}{\lambda_1}\right) \cdot \left(1 - \frac{1}{\beta^2 n^2}\right)$$

α_f is the fine structure constant $e^2/\hbar c \doteq {}^{1}/_{137}$

λ_2 and λ_1, are the wavelength limits of the photocathode.

β is related to rigidity, R, by the following equation :

$$\frac{1}{\beta^2} = \frac{(mc^2/Ze)^2 + R^2}{R^2}$$

Hence we can calculate the number of photons as a function of particle rigidity :

$$N = 2\pi\alpha_f Z^2 l \left(\frac{1}{\lambda_2} - \frac{1}{\lambda_1}\right).\left(1 - \frac{(mc^2/Ze)^2 + R^2}{R^2 n^2}\right) \qquad (3.3.5)$$

when $\beta = 1$, and Z = 1, $N = N_{max}$ and we can rewrite (3.3.5)

$$N = N_{max} Z^2 \left(1 - \frac{1}{n^2}\right)^{-1} \cdot \left(1 - \frac{(mc^2/Ze)^2 + R^2}{R^2 n^2}\right)$$

$$N = N_{max} Z^2 \left(1 - \frac{(mc^2/Ze)^2}{R^2(n^2 - 1)}\right) \qquad (3.3.6)$$

The relationship of N with R (equation 3.3.6) is useful for determining the response of channels 3 and 4 to relativistic particles. It shows, for instance, that secondary pions and

muons produced by nuclear interactions of primary protons with the spacecraft will be detected in channel 3. Using atmospheric production rates of secondary pions and muons at a depth of 30 gms/cm^2 (approximately the same depth as the spacecraft) it is found that an extra 4 counts per frame (16 seconds) would be added to channel 3, when the detector is pointing at the earth, due to this source. This is indeed the spacecraft produced background observed over the southern polar cap in the first month of detector operation. Equation 3.3.6 also shows that α-particle rigidity spectra at greater than 4 GV and proton spectra at greater than 1.5 GV need not be corrected for low photon production and resulting detection inefficiencies.

Evaluating the numerical constants, we get for different particles :

α-particles : $N = N_{max} \cdot .4(1 - 2.84/R^2)$

protons : $N = N_{max} (1 - 0.71/R^2)$

pions : $N = N_{max} (1 - 0.0157/R^2)$

muons : $N = N_{max} (1 - 0.0090/R^2)$

electrons : $N = N_{max} (1 - 2.1 \cdot 10^{-7}/R^2)$

The variation of N/N_{max} with R is shown in Fig. 5a. In this figure, $\frac{1}{4} N/N_{max}$ is plotted for the α-particles; and for electrons, the rigidity value has been multiplied by 100.

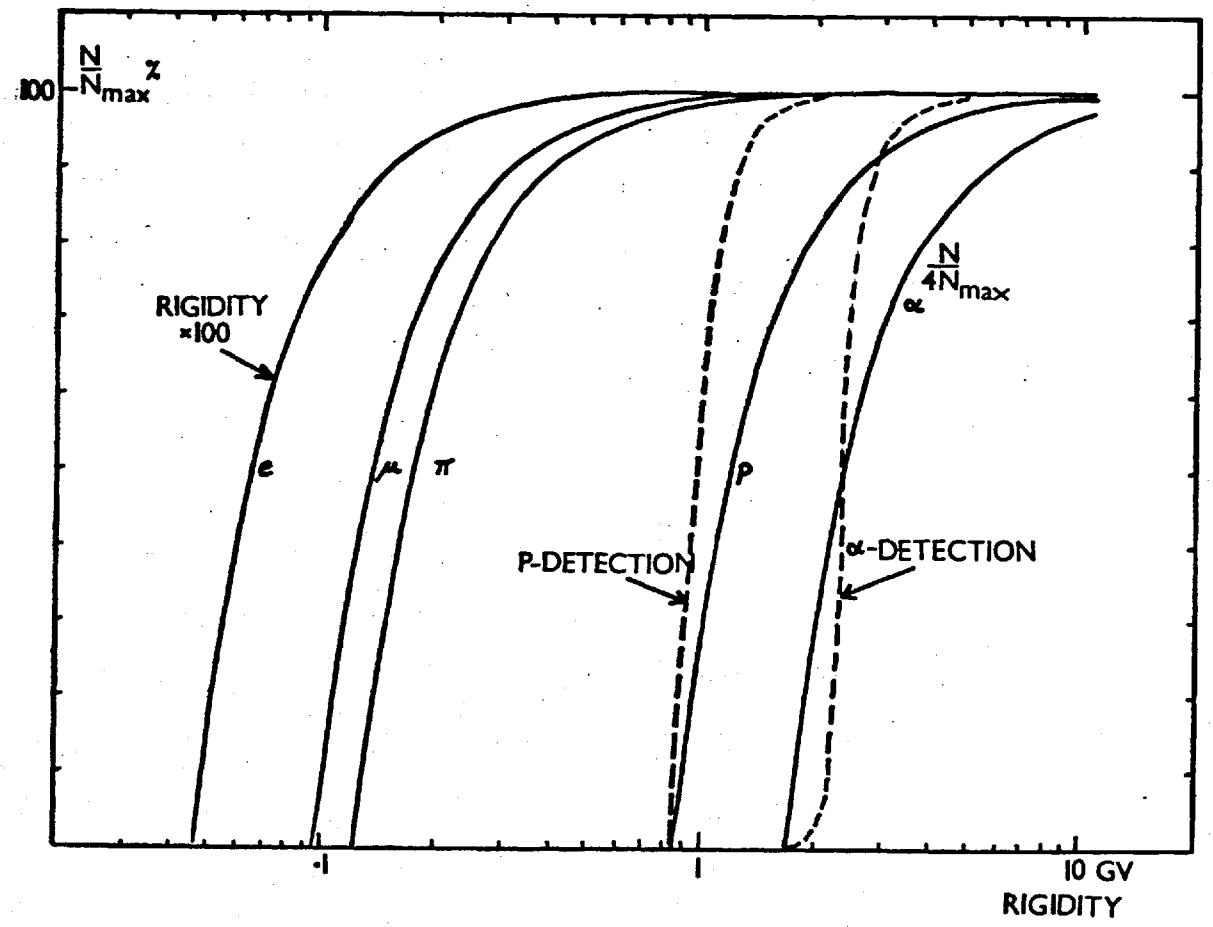

Fig. 5a

Sea level muons are highly relativistic and thus produce the maximum number of photons. Using a detector threshold set at approximately one-fifth of the muon peak, and a 40% spread about the mean of the muon pulse (at half maximum), the detector response curve to protons was produced. The α threshold was set so that no muons were detected in this channel, at about twice the muon pulse height. This yields the approximate α-particle detector threshold and response given in Fig. 5a. These results are complicated somewhat due to the scintillation in the photomultiplier face, which contributes to the spread of the sea level muon pulse. However, the response curves shown in Fig. 5a represent the best available estimate.

4. CHECKING DETECTOR IN FLIGHT

4.1 COSMIC RAY TIME VARIATIONS

Counting rates over the polar caps, where the cut off rigidity is less than 0.4 GV, are analysed. In general, the measured counting rate is made up of the true cosmic ray component, some splash albedo and spacecraft produced background, i.e. any individual measurement, i, is of the following form :

$$j_i(K) = CR(K)\cdot g_i(K) + AL(K)\cdot f_i(K) + B(K)\cdot h_i(K)$$

where $j(K)$ is the measured flux in channel K

$CR(K)$ is the cosmic ray component

$AL(K)$ is the albedo contribution

$B(K)$ is the background produced in the spacecraft mainly by the cosmic rays

$g(K)$, $f(K)$ and $h(K)$ are the geometric factors effective for each contribution. The cosmic ray contribution is isotropic everywhere, except in the atmospheric loss cone, where it is zero. The albedo contribution has been assumed here to be isotropic inside the atmospheric loss cone, and zero everywhere else, since only splash albedo is present. The background due to cosmic ray interactions with the spacecraft is proportional to the backward geometric factor (i.e. looking through the satellite) which lies outside the atmospheric loss cone.

The differential energy spectrum for albedo protons has been measured, at Palestine - Texas: (cut off 4.9 GV)

$$\left(\frac{dJ}{dE}\right)_{splash} = 6 \pm 4\left(\frac{E}{10}\right)^{-1.4 \pm 0.2} \quad \text{Protons/m}^2\text{/ster/sec/MeV}$$

in the energy range $37\ \text{MeV} < E < 334\ \text{MeV}$.
Webber (1967) finds that the integral flux above ~ 20 MeV for splash albedo is almost independent of latitude, so that we may take the above measurement as being representative over the polar caps also.

Since the albedo spectrum decreases sharply with energy, it is not expected that these protons contribute very much to the spacecraft production of background. Spacecraft produced

background is due to inelastic collisions which generate new particles or antiparticles. When averaging, the following expression is obtained :

$$\frac{1}{n}\sum_{i=1}^{n} j_i(K) = \frac{CR(K)}{n}\sum_{i=1}^{n} g_i(K) + \frac{AL(K)}{n}\sum_{i=1}^{n} f_i(K) + \frac{B(K)}{n}\sum_{i=1}^{n} h_i(K)$$

The polar cap is divided into several regions and the above calculation is performed. This allows evaluation of CR(K), AL(K) and B(K) since several simultaneous equations can be solved. Usually there are more equations than variables so that redundant solutions are obtained. If in all these solutions CR(K), AL(K) and B(K) are constant within the errors, then one can safely assume that the problem has been understood sufficiently well to separate out all the contributions to the counting rate. Only then meaningful comments can be made about proton/alpha ratios and their time variation. Preliminary results indicate that the treatment outlined here is accurate.

4.2 CALCULATION OF EFFECTIVE GEOMETRIC FACTOR

For a dipole field, the size of the atmospheric loss cone, α, at altitude h and magnetic latitude λ, is found using conservation of the first adiabatic invariant. The expression for α is :

$$\sin^2\alpha = \left(\frac{R + h_a}{R + h}\right)^3 \sqrt{\frac{4 - 3\cos^2\lambda}{4 - 3\left(\frac{R + h_a}{R + h}\right)\cos^2\lambda}} \qquad (4.2.1)$$

where R is the radius of the earth, and h_a is the effective height of the atmosphere. Although in reality the atmosphere does not produce a sharp loss cone, the use of h_a provides a very accurate means of loss cone correction for particle data. This is demonstrated in Fig. 6, where the counting rate variation has been predicted for two polar passes during the November 18th solar flare. The loss cone corrected polar cap profile should have been flat as there were no anisotropies at the time. The following method was used.

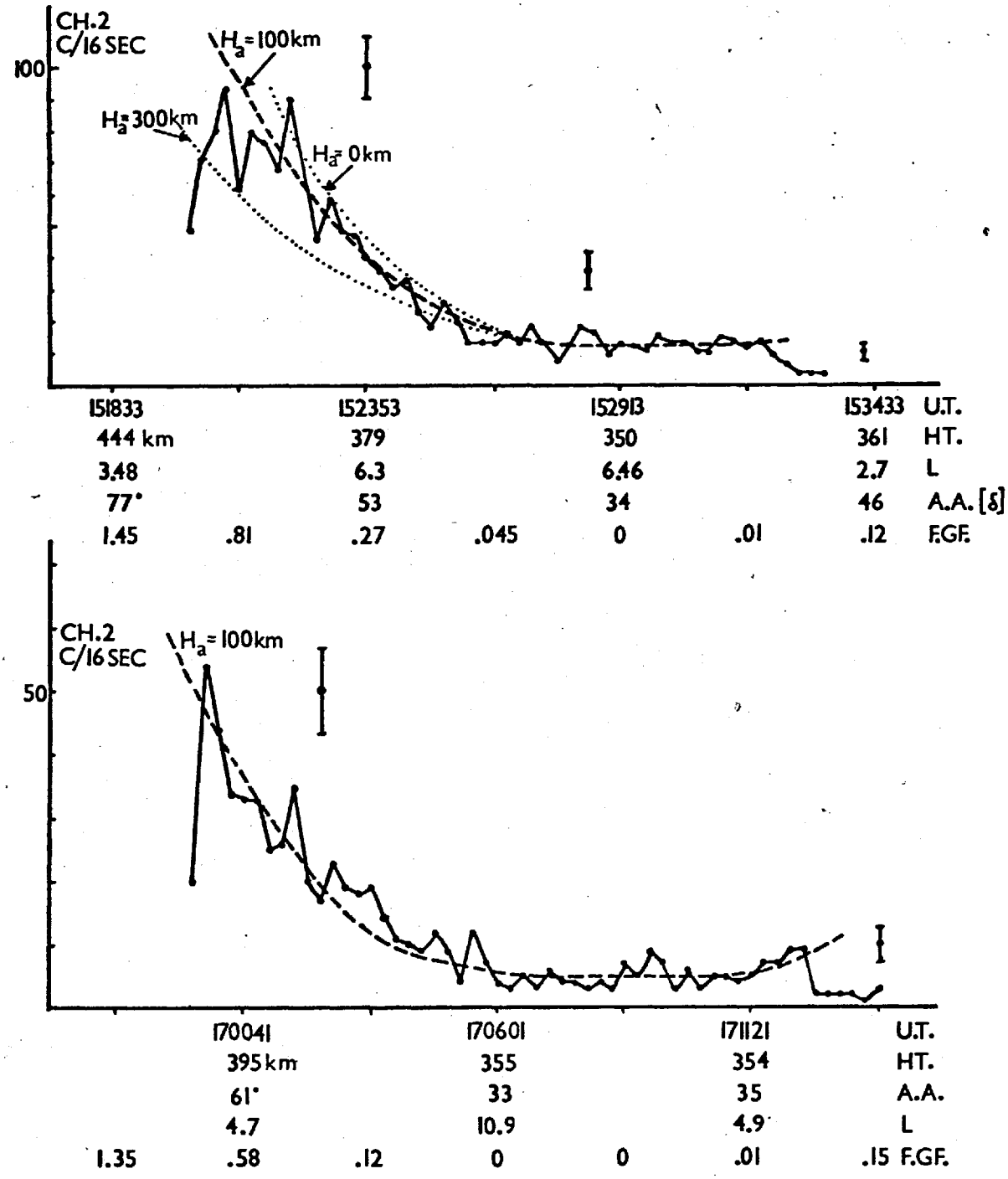

Fig. 6

Polar cap structure caused by detector orientation. The dashed lines are the calculated variations due to the atmospheric loss cone, if the polar cap distribution is flat.

The axis of S.28 is parallel to the satellite spin axis. Knowing the satellite position λ, and altitude h, we can calculate the loss cone from the above formula. A value of 100 km for h_a was found to provide a good fit to the data. The aspect angle (i.e. the angle between the magnetic field vector and the satellite spin axis) is also known, so that the fraction of the geometric factor which lies inside the atmospheric loss cone can be found by integrating the detector angular response (i.e. the differential geometric factor) in the overlap region. This is shown in Fig. 7.

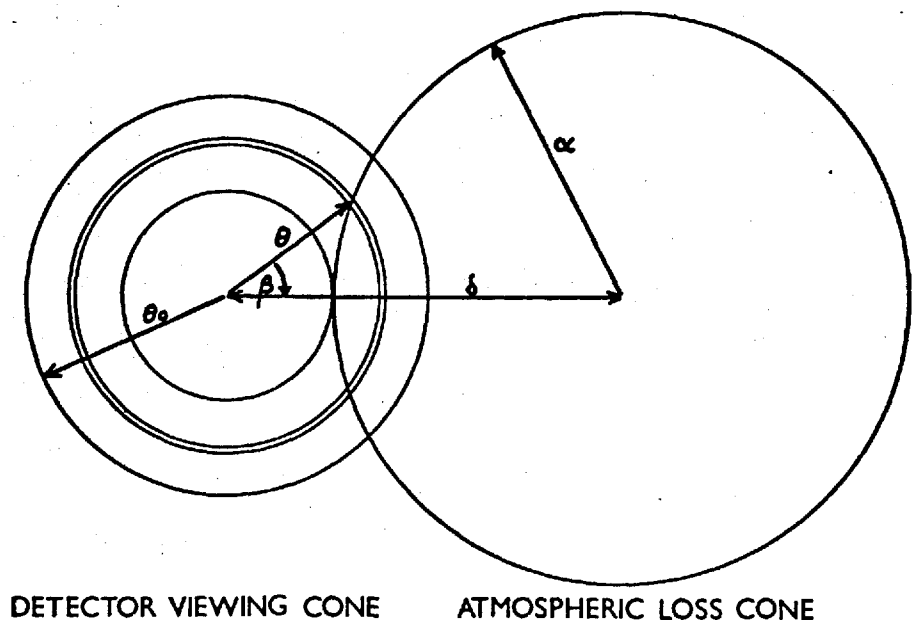

Fig. 7

α = loss cone angle
θ_o = maximum detector opening angle
δ = aspect angle

The fraction of the circle which lies inside the atmospheric loss cone at angle θ ($\theta < \theta_o$) from the detector axis is $\frac{\beta(\theta)}{\pi}$. β is calculated from the half angle formula

$$\sin \frac{\beta}{2} = \sqrt{\frac{\sin (s - \delta) \sin(s - \theta)}{\sin \delta \sin \theta}} \qquad (4.2.2.)$$

where $s = \frac{1}{2} (\delta + \theta + \alpha)$

The geometric factor is :

$$G.F. = \int_{\theta=o}^{\theta_o} dGF(\theta)$$

If some part is obstructed (in this case by the loss cone) this becomes :

$$F.G.F. = \int_{\theta=o}^{\theta_o} dGF(\theta).(1 - \frac{\beta(\theta)}{\pi}) \qquad (4.2.3)$$

The limits of the integration are set by the geometry. If $\delta > \alpha$, all detector viewing angles from θ = o to $\theta = \delta - \alpha$ are free, and all angles from $\theta = \delta - \alpha$ to $\theta = \theta_o$ are partially obscured. If $\delta < \alpha$, all detector viewing angles from θ = o to $\theta = \alpha - \delta$ are totally obscured, and all angles from $\theta = \alpha - \delta$ to θ_o are partially obscured. Also, if $\delta > \alpha + \theta_o$, the detector viewing cone lies outside the loss cone, and if $\alpha > \theta_o + \delta$, it lies totally inside the loss cone.

The modified geometric factor is calculated for each satellite position both for forward and rear entry, and these values are used in evaluating cosmic ray data over the polar caps. Since the experiment has also a low energy component in the high energy channels, this is allowed for and separated out.

Fig. 8 shows the time variation in channel 3 cosmic rays measured over the northern polar cap. Also shown is the Explorer 33 > 60 MeV particle flux and the Deep River neutron monitor variation. During May and June, the spacecraft was at apogee over the northern polar cap, and during November - December at perigee. The data is not loss cone corrected,

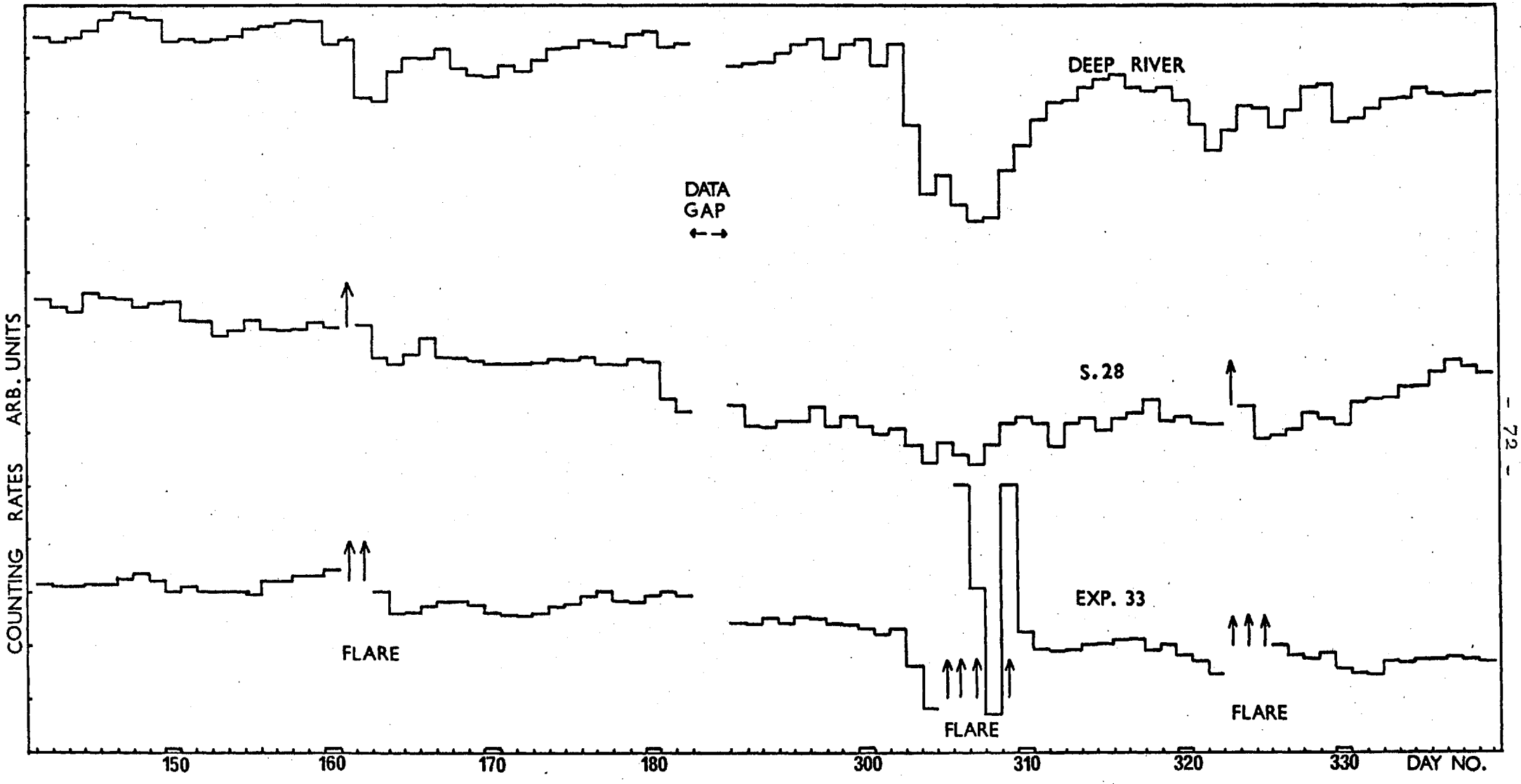

Fig. 8

Time variation of cosmic rays, showing S.28 channel 3, Explorer 33 (energy > 60 MeV) and Deep River Neutron monitor counting rates.

which explains the greater counting rate in the early part of the time history. The graph shows that the detector is operating correctly,because the time variations are similar.

4.3 LONGITUDE SURVEY AT EQUATOR

Previous experiments on Ariel have shown that radioactive decays of spallation products, generated by inelastic proton collisions with the spacecraft in the inner belt, enhance the equatorial counting rate after passages through the South Atlantic Anomaly (Elliot, 1965). Fig. 9 shows the longitude variation in the telescope counting rate for the high energy proton channel (Ch.3), together with the predicted variation calculated from the vertical cut-off rigidity and the measured integral rigidity spectrum $j(P) \propto P^{-1.5}$, at high rigidities, given by Webber (1967). The data was collected over magnetic latitudes between -30° and $+30^{\circ}$ and for altitudes less than 450 km. Measurements are restricted to those times when the apogee of the satellite orbit was in the southern hemisphere, so that the spacecraft must have passed through the South Atlantic Anomaly. Orbits are nearly parallel to the meridian lines, and enhanced counting rates due to inner belt effects are expected for longitudes 300° to 360°. Fig. 9 shows that no inner belt effects are observed within the resolution of the experiment.

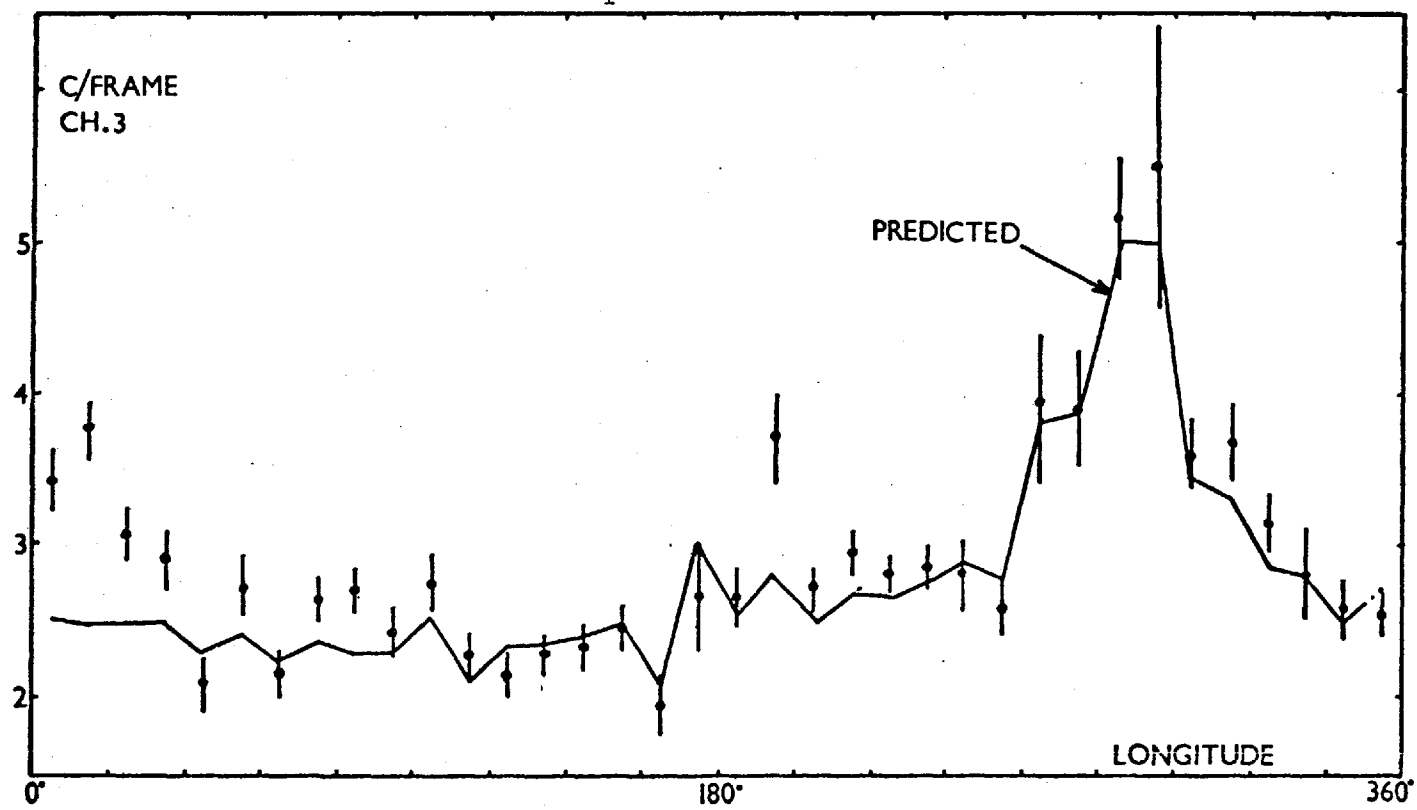

Fig. 9

4.4 LATITUDE VARIATION OF COSMIC RAY PROTONS

The rigidity spectrum of cosmic rays has been measured extensively at different times during the sunspot cycle. 1968/9 was near sunspot maximum, and figure 10 shows the measured rigidity spectrum for protons, together with Webber's (1967) curve for near sunspot maximum. As can be seen, agreement between the two curves is extremely good once the data has been corrected for the effects of the earth shadow. Data selection was obtained by the criterion that the Anton 302 geiger counter on board the ESRO II spacecraft did not register inner belt particles. Also, only the northern hemisphere was used to reduce the effects of spacecraft production of particles. In the northern hemisphere most of the effective geometric factor is due to forward incidence of particles.

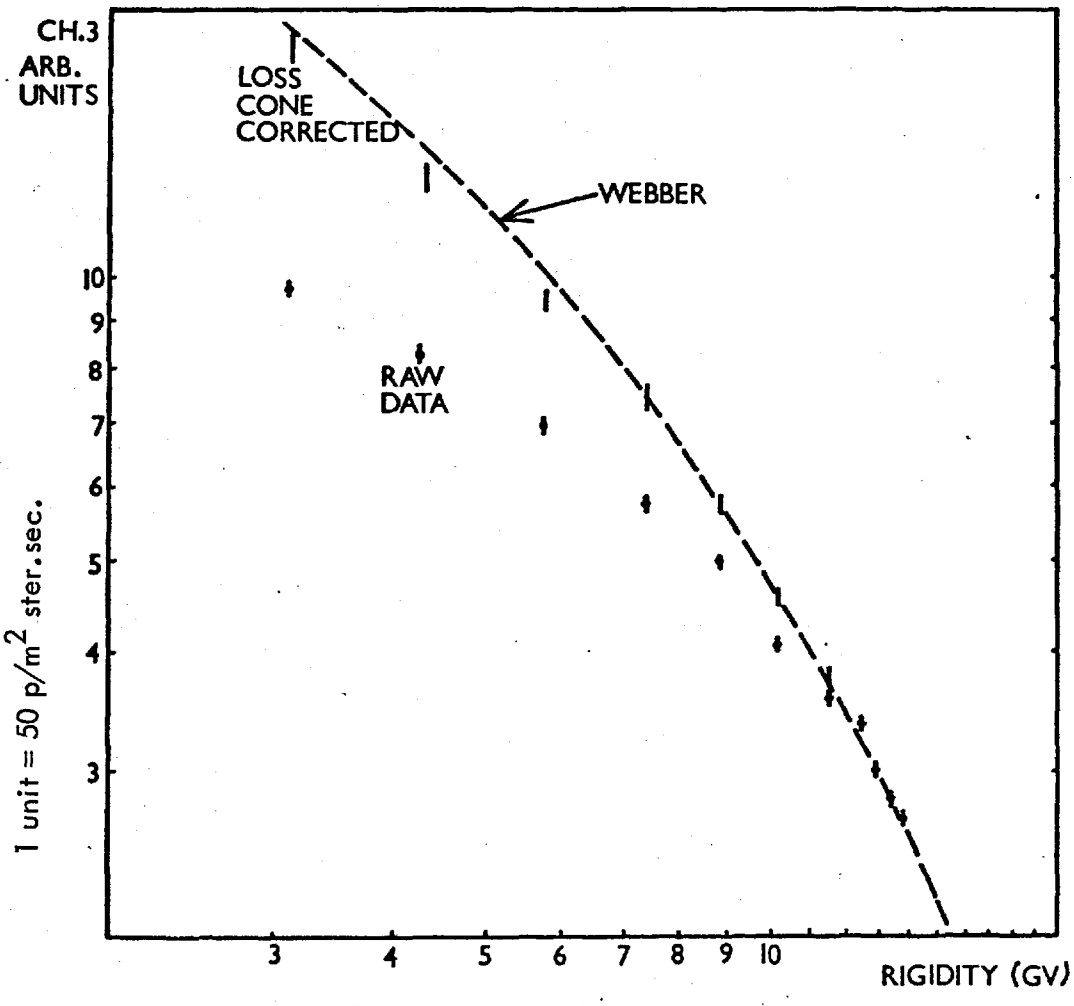

Fig. 10

4.5 RESPONSE TO ELECTRONS

When the detector passes through the outer belt, it is exposed to high fluxes of electrons. The response of the detector under these conditions must be investigated. For this purpose, the S.28 counting rate in the four channels was plotted as a function of Anton 302 geiger tube counting rate. If the detector is insensitive to electrons, such a plot will show a constant S.28 counting rate. The α-particle channels are found to be insensitive, but poor statistics due to low counting rates reduce the confidence limits of this result.

Channel 2 responds to electrons as shown in Fig. 11.. The scatter in the points is greater than the Poisson error, but this is largely due to the variations in spacecraft attitude when sampling over long periods of time.

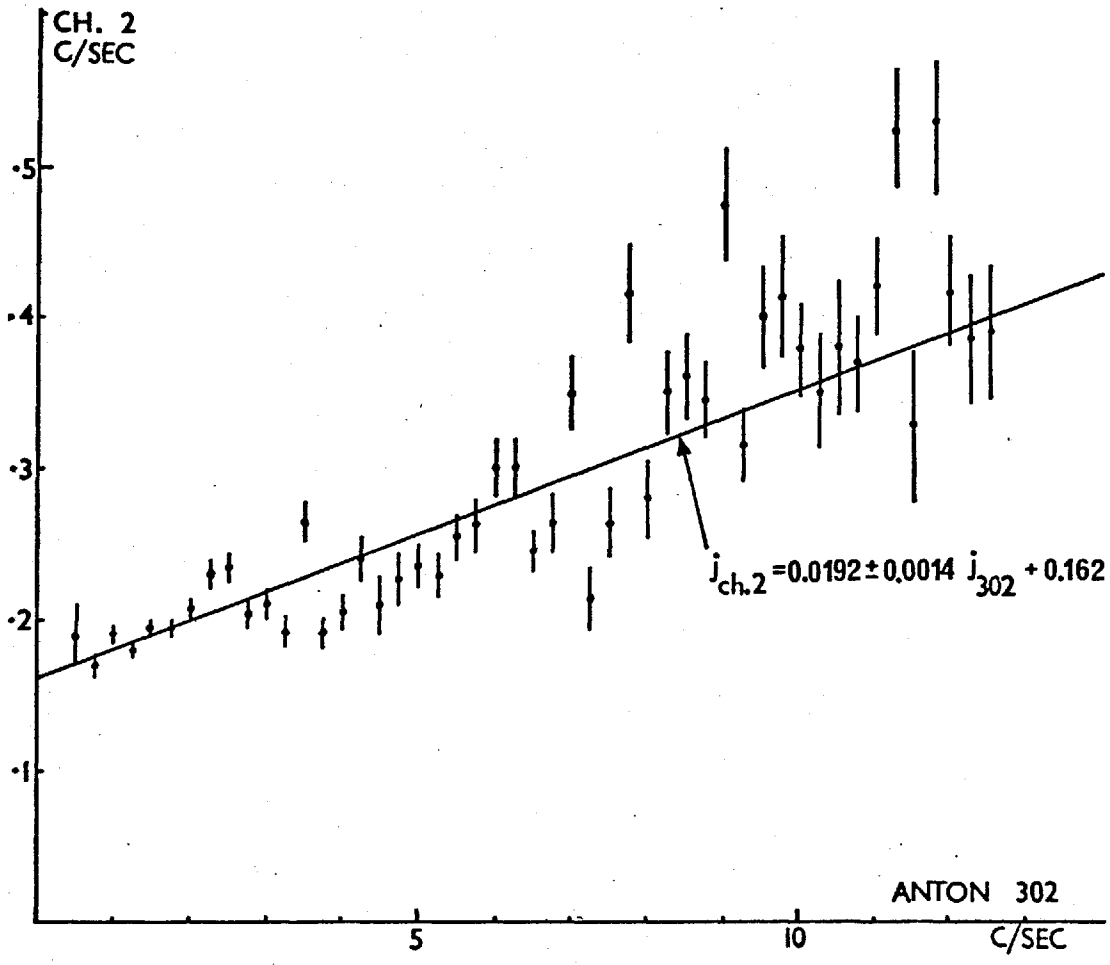

Fig. 11

A best straight line fit has been drawn, of the form

$$j_{ch.2} = 0.0192\ j_{302} + 0.16 \qquad (4.5.1)$$

where $j_{ch.2}$ and j_{302} are in counts/sec. Electron response in channel 2 can be due to :

(a) increased chance coincidences

(b) electrons of energy $>$ 70 Mev passing through 1 cm of lead

(c) electrons of energy $>$ 2.5 MeV which bypass the lead block and register in the first three elements

If either (a) or (b) are the cause of the electron response in channel 2, then channel 3 (high energy protons) counting rates should also increase with Anton 302 rate. Fig. 12 shows the channel 3 response to outer belt electrons. As can be seen, the counting rate in S.28 ch.3 decreases with increasing Anton 302 counts. The spread in the distribution is due to the different satellite altitudes and the resulting variation in the effective geometric factor of the detector for cosmic rays at the four 'horns' of the outer belt sampled during each orbit. The decreasing trend in the S.28 counting rate is caused by the large detector dead time. The time during which the detector is inactive, after a particle is registered in one of its elements, has been measured to be 3 μsec. From the results of Fig. 12 it is concluded that the electron response in channel 2 is caused by particles which bypass the lead block. The Anton 302 low energy electron threshold is $\sim$ 2.3 Mev, with a geometric factor $\sim$ 2.2 cm^2 ster. This energy threshold is very similar to the channel 2 electron cut-off, which explains the good straight line approximation to figure 11. It is possible to determine the geometric factor for particles bypassing the lead block, using Fig. 11 and assuming that both detectors measure particle fluxes above the same energy threshold. This gives GF (ch.2) $\triangleq$ 0.04 cm^2 ster. A small geometric factor such as this is equivalent to the

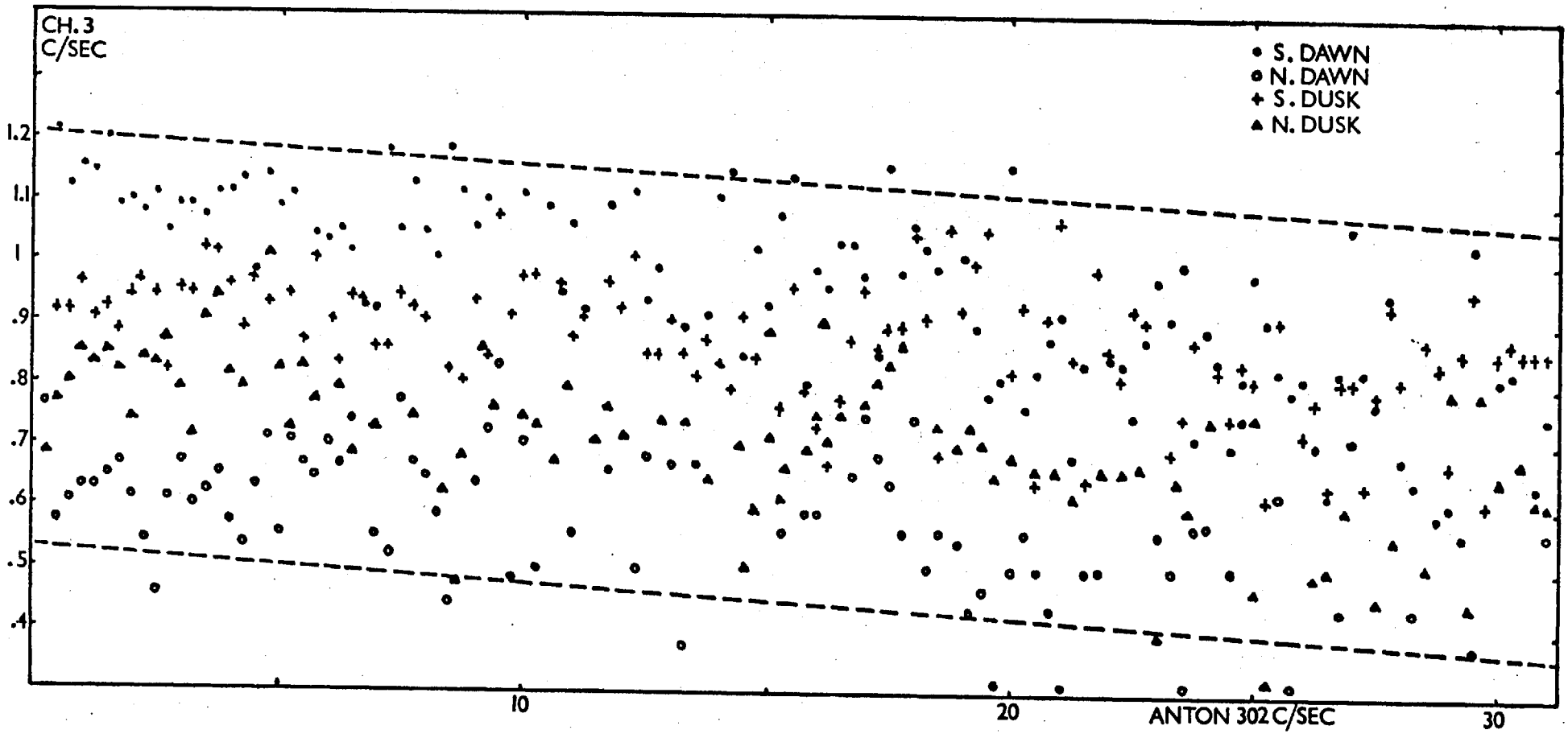

Fig. 12

Channel 3 counting rate in the outer electron belt as a function of Anton 302 (electrons of energy > 2.3 MeV) counting rate.

sensitive volume of the proportional counters extending by 1 mm beyond their theoretical boundary. Since this boundary is never sharp, and earlier experiments indicated that the full geometrical volume of the counters was sensitive (section 3.2) this explanation of the electron response is very plausible.

4.6 INNER BELT STUDIES AND DETECTOR SATURATION

4.6.1 Results

Fig. 13 shows a typical pass through the inner belt for S.28 channels 2 and 3, and also for the Anton 302 Geiger counter. L (in earth radii), B (gauss) and aspect angle are shown. While the 302 counting rate varies smoothly, the S.28 rate shows a completely different profile, which cannot be explained by a pitch angle effect alone. Ordering of the data is achieved using Mc.Ilwain's B, L co-ordinate system. Fig. 14 is a plot of 302 counts/sec at constant L as a function of B. This should be compared with figures 15, 16 and 17 where the S.28 channel 2 and 3 counting rate is plotted for the same L values as a function of B, and at constant pitch angle. The 302 geiger counter is omnidirectional, and no correction needs to be made for the position of the satellite spin axis with respect to the magnetic field vector.

As can be seen, the data is well ordered in both cases, but the shape of the S.28 curves differs markedly from that of the >32 MeV geiger counter curve. The plot of counting rate v. magnetic field strength at constant L (calculated from the high order expansion of Jensen and Cain) essentially gives a measure of the equatorial pitch angle distribution. Ordering the data to constant L is equivalent to measuring the particle intensity at different altitudes along the same field line. Only particles mirroring at or below the satellite can be detected. An omnidirectional detector thus measures :

$$j_T(\alpha_o) = 2\pi \int_0^{\alpha_o} \sin\alpha \; j(\alpha)\, d\alpha \qquad (4.6.1)$$

where $j(\alpha)$ is the equatorial pitch angle distribution of particles in the energy range of the detector, and α_o is

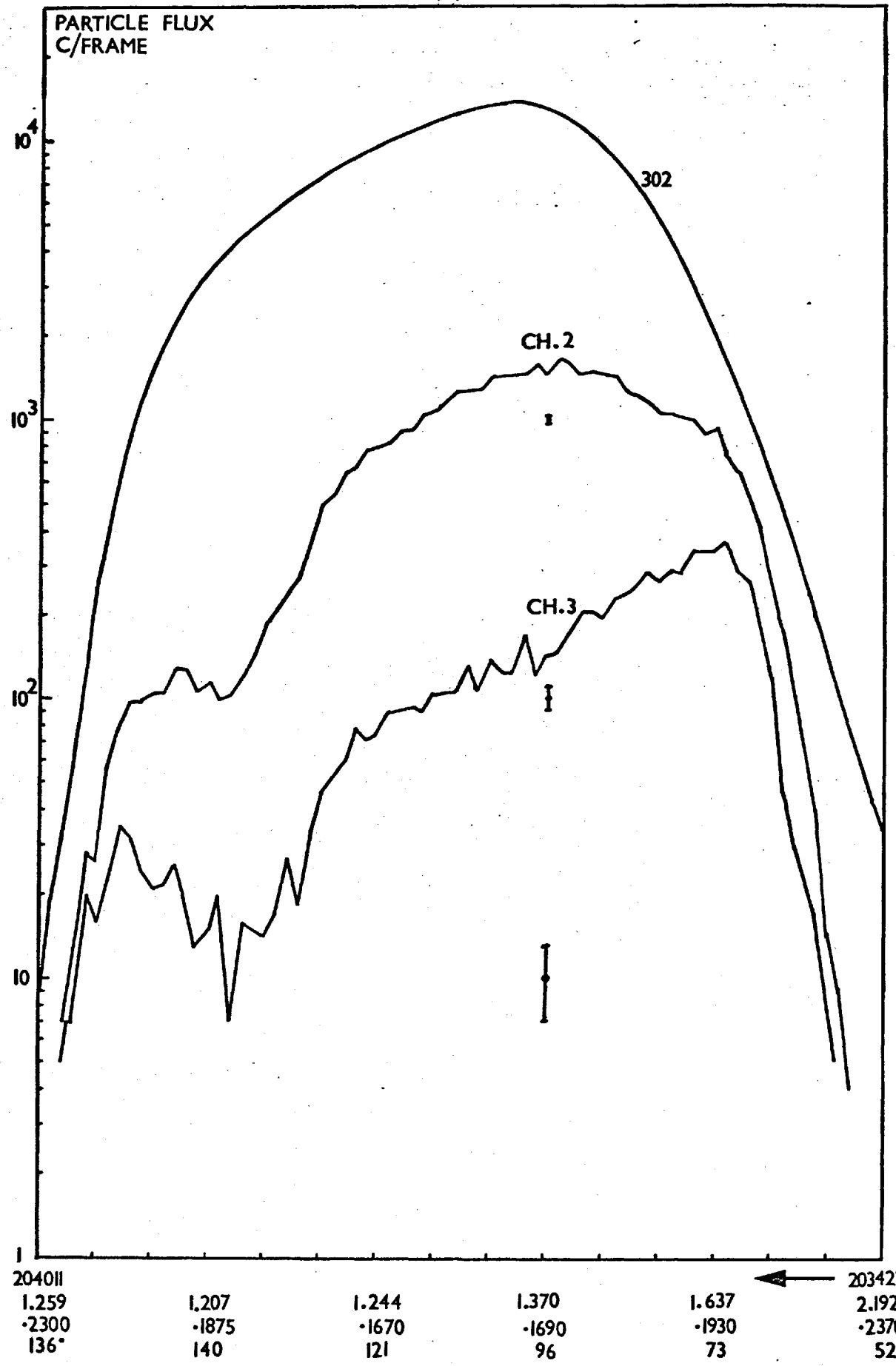

Fig. 13

Typical inner belt pass showing S.28 channels 2 and 3 and Anton 302 variations.

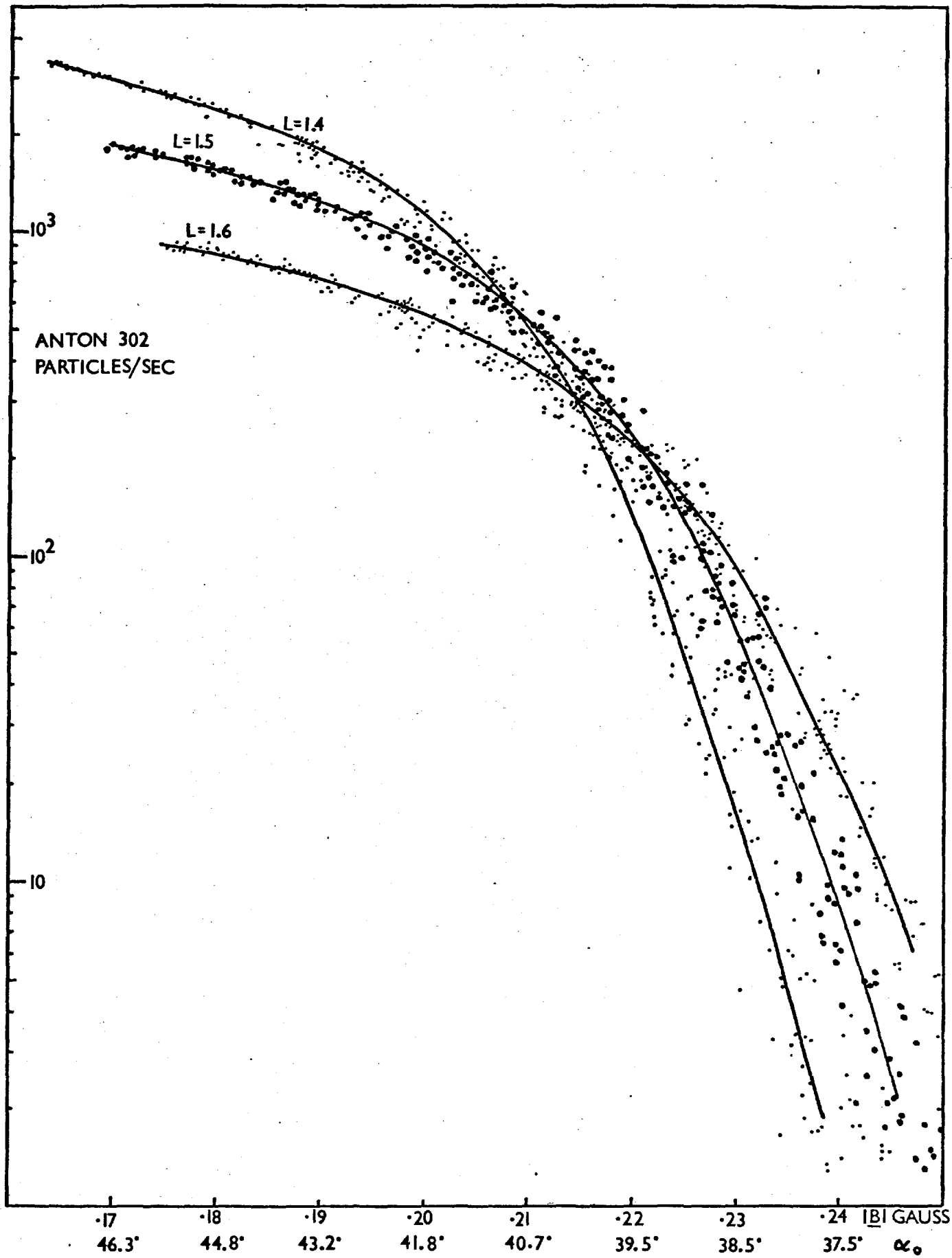

Fig. 14

Counting rate variation with magnetic field B at constant L for the Anton 302 (protons of energy > 30 MeV)

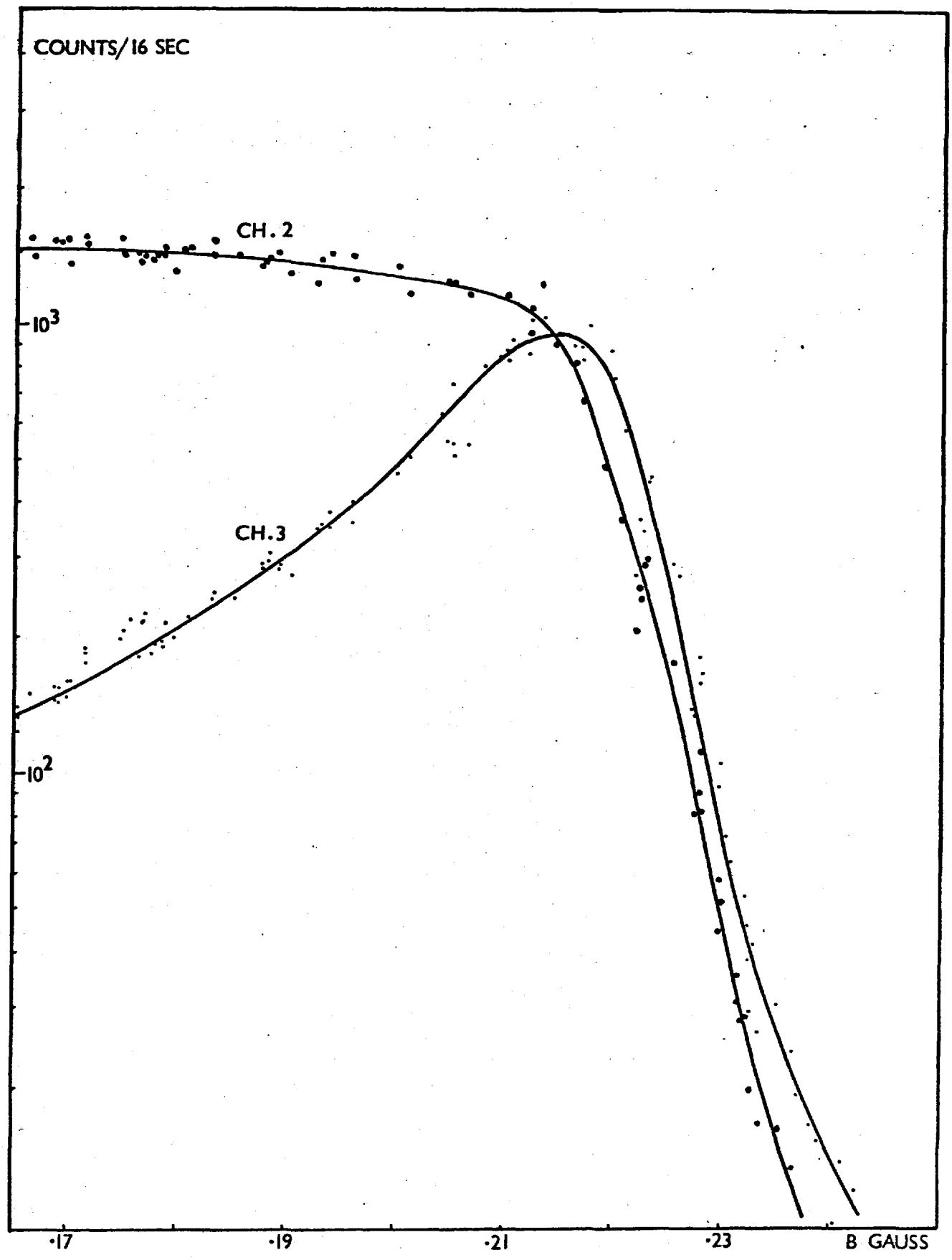

Fig. 15

S.28 channels 2 and 3 counting rate variation with magnetic field B at L = 1.4 and pitch angle 90°.

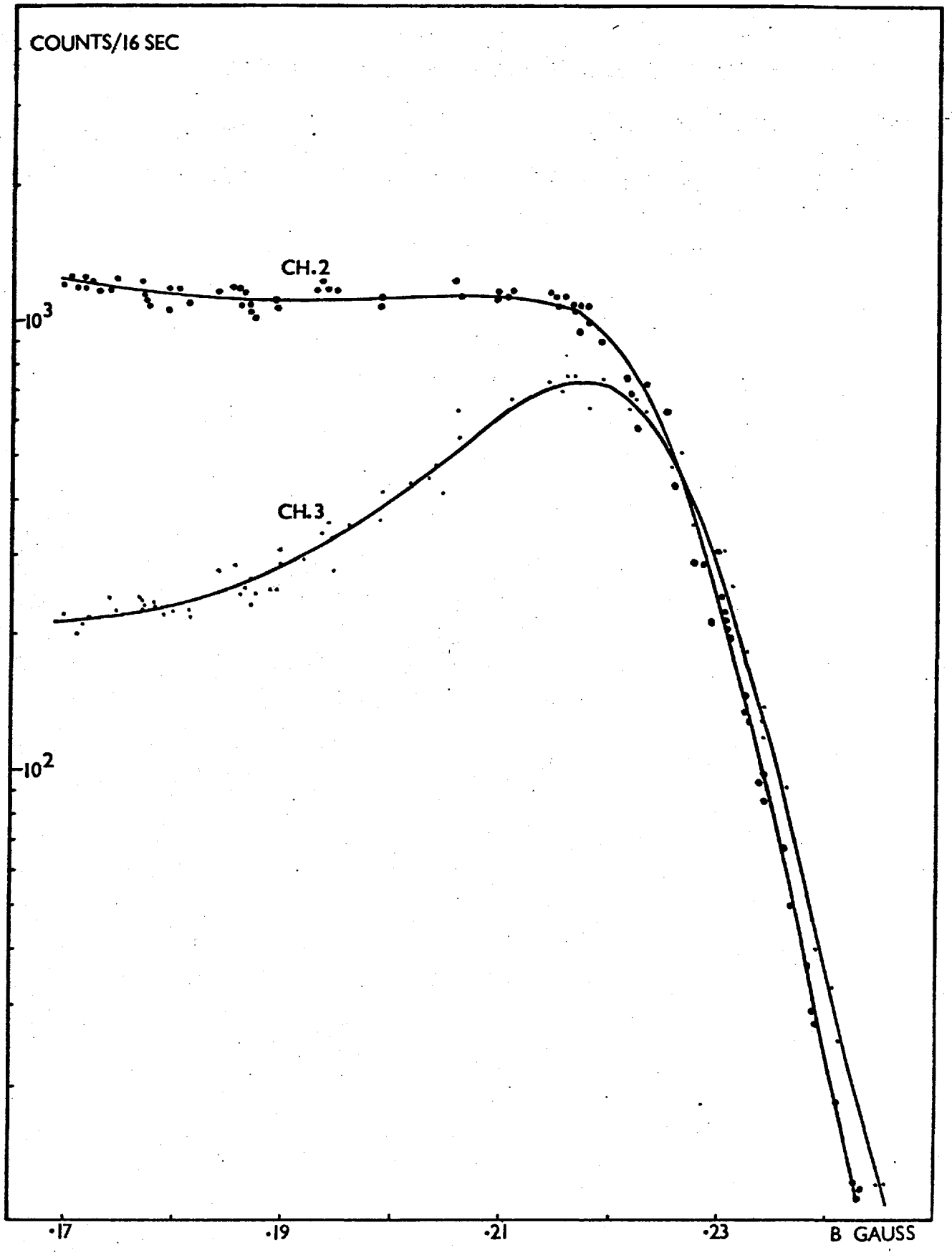

Fig. 16

S.28 channels 2 and 3 counting rate variation with magnetic field B at L = 1.5 and pitch angle 80°.

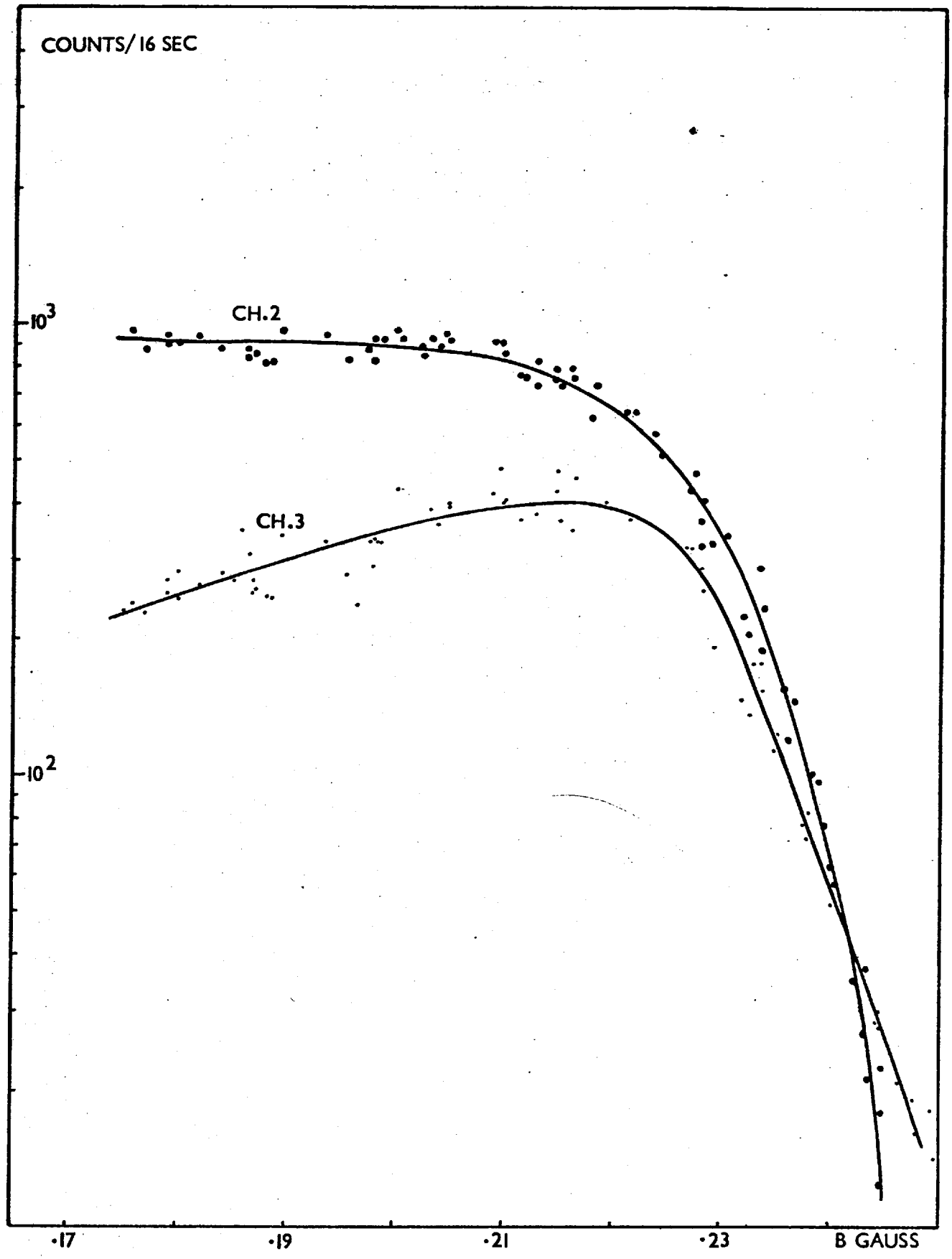

Fig. 17

S.28 channels 2 and 3 counting rate variation with magnetic field B at L = 1.6 and pitch angle 73°.

the equatorial pitch angle corresponding to mirroring at the satellite position. If B_o is the field strength at the equator for the field line passing through the detector, and B is the magnetic field strength at the satellite position, then :

$$\sin^2 \alpha_o = \frac{B_o}{B}$$

For a dipole this becomes :

$$\sin^2 \alpha_o = \left(\frac{H}{L}\right)^3 \sqrt{\frac{4 - 3/L}{4 - 3H/L^2}} \qquad (4.6.2)$$

where H is the satellite altitude in earth radii measured from the geocentre. $j(\alpha)$ can be obtained from equation (4.6.1) by differentiating with respect to α_o, i.e.

$$\frac{\partial}{\partial \alpha_o} \left(j_T(\alpha_o)\right) \cdot \frac{1}{2\pi \sin \alpha_o} = j(\alpha_o) \qquad (4.6.3)$$

since at the lower limit of the integration, $j_T(\alpha = 0) = 0$. A unidirectional detector on the other hand, measuring particles at pitch angle α_H at altitude H, samples the equatorial pitch angle distribution $j(\alpha)$ at angle $\alpha = \alpha_o$, where α_o is obtained from the first adiabatic invariant:

$$\sin^2 \alpha_o = \frac{B_o}{B} \sin^2 \alpha_H$$

For a dipole this is :

$$\sin^2 \alpha_o = \sin^2 \alpha_H \left(\frac{H}{L}\right)^3 \sqrt{\frac{4 - 3/L}{4 - 3H/L^2}} \qquad (4.6.4)$$

This is approximately the situation for S.28.

4.6.2 Interpretation of Inner Belt Results

There are two possibilities which could produce the observed S.28 counting rate v. B curves. Either the pitch angle distribution has a maximum at the edge of the atmospheric loss cone, or the data is affected greatly by detector

saturation due to the large particle fluxes encountered in the inner belt. Using proton and electron maps produced by Vette (1966), we get the following results.

Table 1 Electrons of Energy > 0.5 MeV

L	Particles/cm^2 sec (extrapolated to 1968)		
	B=0.17 gauss	B=0.2 gauss	B=0.22 gauss
1.4	1.8×10^6	3.6×10^5	7.8×10^4
1.5	1.4×10^6	3.8×10^5	9.5×10^3
1.6	0.3×10^6	1.0×10^5	3.4×10^4

The 1968 fluxes were estimated using the decay constants of 600 days for L = 1.5 and 500 days for L = 1.4 and 1.6. The variation of this decay constant with B was not considered.

Table 2 Protons

L	Particles/cm^2 sec (energy > 4 MeV)	
	B=0.17 gauss	B=0.2 gauss
1.4	5×10^4	1.5×10^4
1.5	5×10^4	1.5×10^4
1.6	5×10^4	1.5×10^4

If the insensitive time per event in any of the elements is τ, and particle incidence is random, we get :

Observed counting rate : n counts/sec

insensitive time per second : $n\tau$

If the true particle rate is N counts/sec, the number of counts per second missed due to dead time is $Nn\tau$.

$$\text{i.e.} \quad n = N - Nn\tau \qquad (4.6.5)$$

$$N = \frac{n}{1 - n\tau}$$

For S.28, counts in the first element of the detector can be due to electrons of energy $\geqslant \frac{1}{2}$ MeV or protons of energy $\geqslant$ 10 MeV. Also, protons of energy greater than $\sim$ 100 MeV are counted as events provided they pass through all the elements when the detector is sensitive. If N_1 is the true proton flux above $\sim$100 MeV, and N_2 all the other true particle fluxes contributing to singles rates, equation (4.6.5) becomes :

$$n_s = (N_1 + N_2) - (N_1 + N_2)\, n_s \tau$$

where n_s is the counting rate of the first element. The fraction of time for which the detector is insensitive is then $n_s\tau$, and thus the number of particles of energy $\geqslant$ 100 MeV which are not counted is :

$$= n_s \tau N_1$$

$$= N_1 \frac{(N_1 + N_2)\,\tau}{1 + (N_1 + N_2)\,\tau}$$

The particle flux of energy $\geqslant$ 100 MeV actually observed is, therefore,

$$n_{obs} = N_1 - N_1 \frac{(N_1 + N_2)\,\tau}{1 + (N_1 + N_2)\,\tau} \qquad (4.6.6)$$

Thus the amount by which the true counting rate is depressed is :

$$\eta = 1 - \frac{(N_1 + N_2)\,\tau}{1 + (N_1 + N_2)\,\tau}$$

Since usually $N_1 \ll N_2$ we obtain for this depression factor :

$$\eta = 1 - \frac{N_2 \tau}{1 + N_2 \tau}$$

τ was measured to be 3 μsec, hence for different values of η we get :

Table 3 Detector Insensitive Time

$\eta = 1$	$N_2 = 0$	dead time = 0%
$\eta = 0.5$	$N_2 = 3.3 \times 10^5$	dead time = 50%
$\eta = 0.1$	$N_2 = 3 \times 10^6$	dead time = 90%
$\eta = 0.01$	$N_2 = 3.3 \times 10^7$	dead time = 99%

The calculations performed so far do not allow for chance coincidences. There will be some such additional counts, but due to the geometry of the detector, this should be less than ~10% of the measured flux.

At the low altitudes considered here, the particle distribution is only a few degrees wide, since the atmospheric loss cone is large. It is possible, therefore, to treat the distribution as a line source. If the omnidirectional flux above energy E_o is $j(B,L,E_o)$ counts/cm^2 sec, then the equivalent line flux is $\frac{1}{2\pi} j(B,L,E_o)$ counts/cm^2 sec radian.

A plane detecting area A, the normal $\underline{n}$ of which makes an angle α_d with the magnetic field $\underline{B}$, presents an area 'A $\sin\alpha_d \cos \phi$' to a beam of particles incident from a direction making a 90° angle with $\underline{B}$, and a phase angle ϕ measured from the plane containing $\underline{B}$ and $\underline{n}$. If particles incident from one hemisphere only are detected, then the average detecting area is :

$$\frac{2}{\pi} \int_{\phi=0}^{\frac{\pi}{2}} A \sin\alpha_d \cos\phi \, d\phi$$

$$= \frac{2}{\pi} A \sin\alpha_d$$

The particle flux incident on the detector, if the line source approximation holds, is then :

$$j_d = \frac{1}{2\pi} j(B,L,E_o) . \pi . \frac{2}{\pi} A \sin \alpha_d \quad \text{counts/sec}$$

$$j_d = \frac{1}{\pi} j(B,L,E_o) A \sin \alpha_d \quad \text{counts/sec}$$

In the case of S.28, $A = 6.25\ cm^2$, hence :

$$j_d \triangleq 2\, j(B,L,E_o) \sin \alpha_d$$

The back of the detector is shielded by the spacecraft. Tables 1 and 2 show that detector dead time is almost exclusively caused by the large electron fluxes in the inner belt, and that the dead time (see table 3) is large enough to explain the observed results. Channel 2, in addition, is able to detect the more energetic electrons, which explains why the counting rate here is not so depressed as that of channel 3.

The counting rate variation with aspect angle has been investigated for a particle pitch angle distribution of the form

$$j(\alpha) = 0 \quad \alpha < \alpha_o$$
$$j(\alpha) = 1 \quad 90^\circ > \alpha \geqslant \alpha_o$$

This is shown in figures 18 and 19 for channels 2 and 3 respectively. In addition, Fig. 20 gives the ratio of 'channel3/channel2' low energy proton counts. This graph shows that the channel 3 counting rate is expected to be greater than that of channel 2, provided $\alpha_o > 72^\circ$ and aspect angle $> 79^\circ$. Channel 3 low energy proton efficiency has been assumed in these diagrams to be 100%, although for typical inner belt proton spectra, it is calculated to lie between 60% and 70%. No dead time effects have been considered.

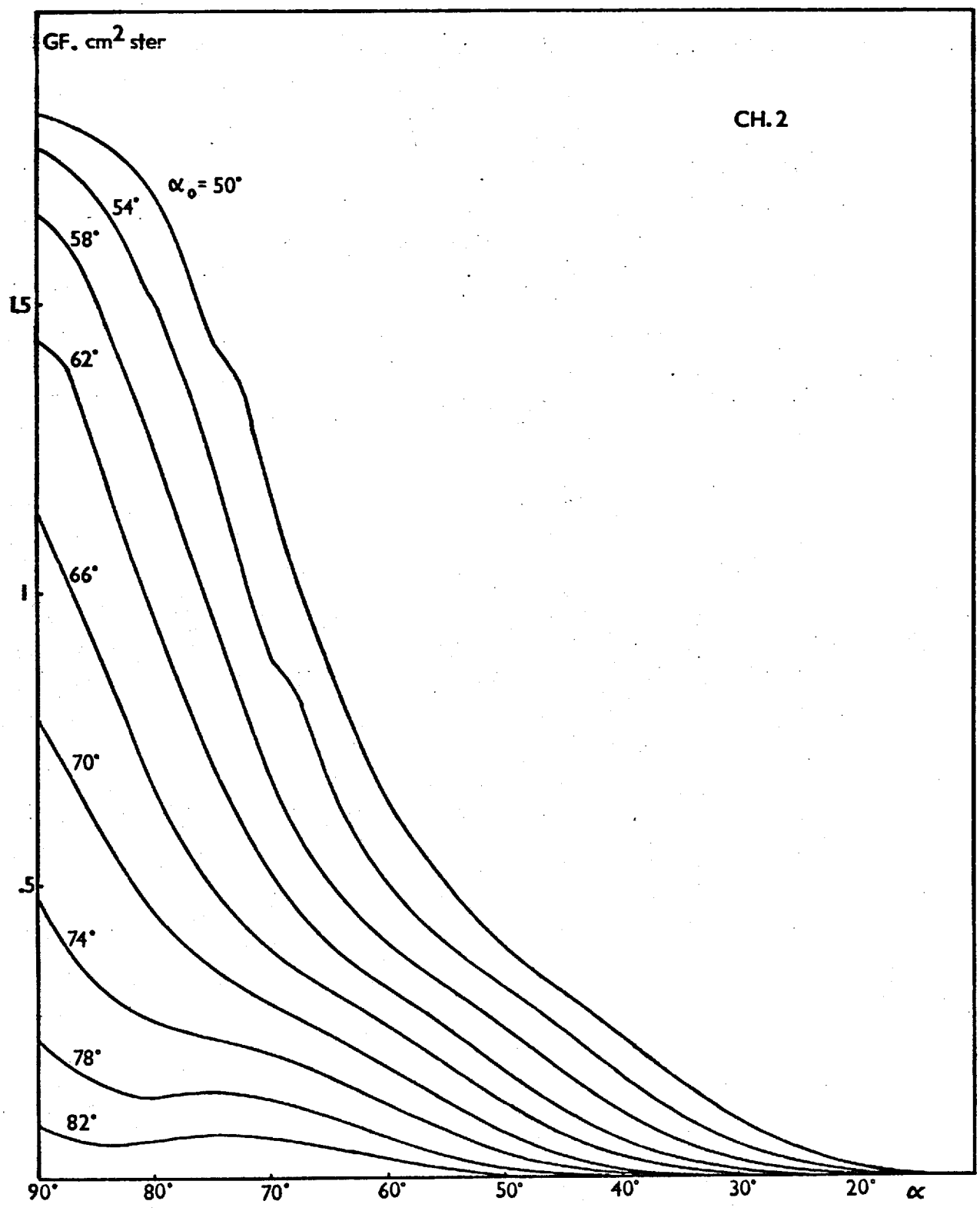

Fig. 18

S.28 channel 2 angular response to a rectangular particle pitch angle distribution, where the loss cone extends to the angle α_o.

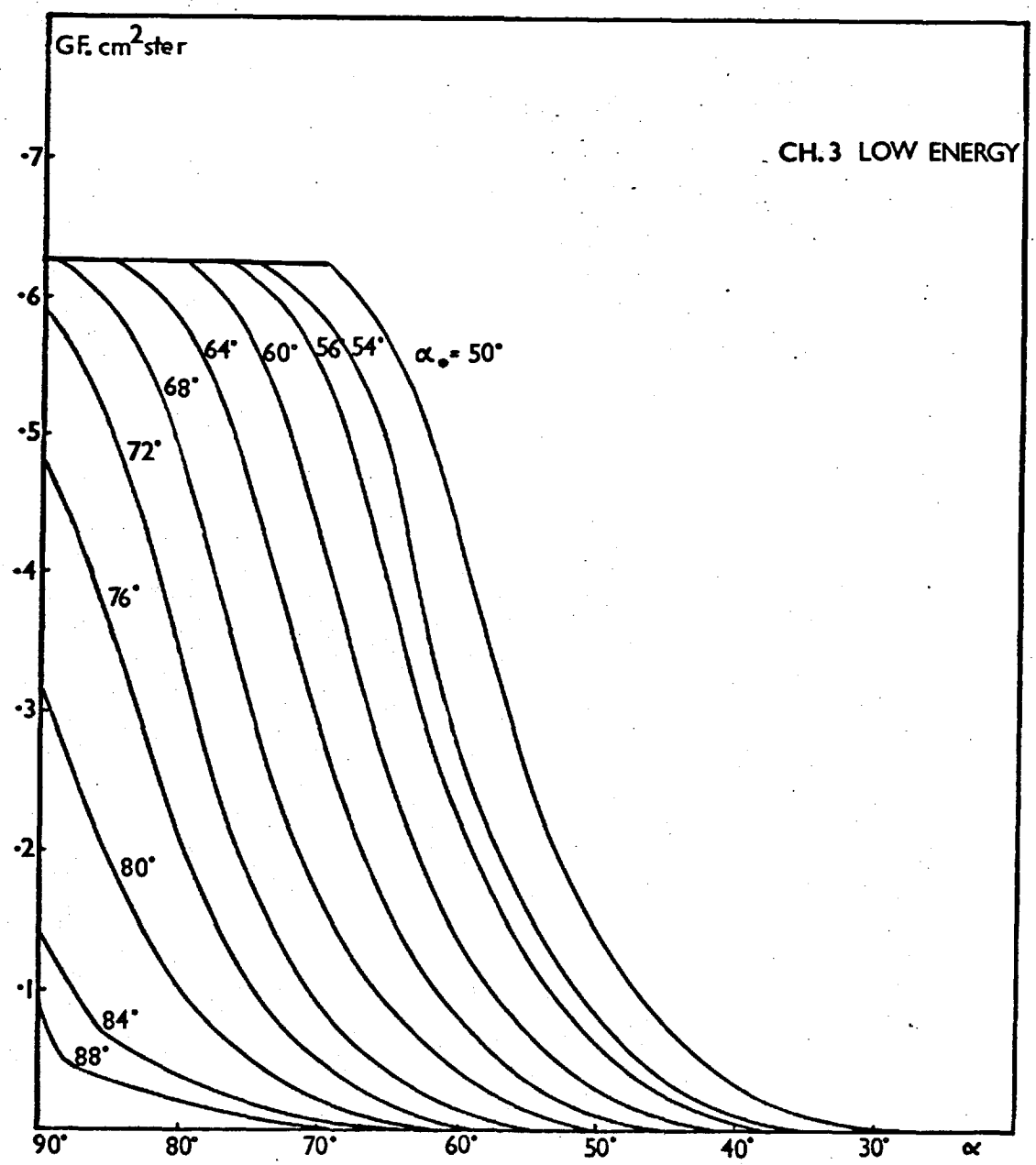

Fig. 19

S.28 channel 3 angular response to a rectangular particle pitch angle distribution, where the loss cone extends to the angle α_0.

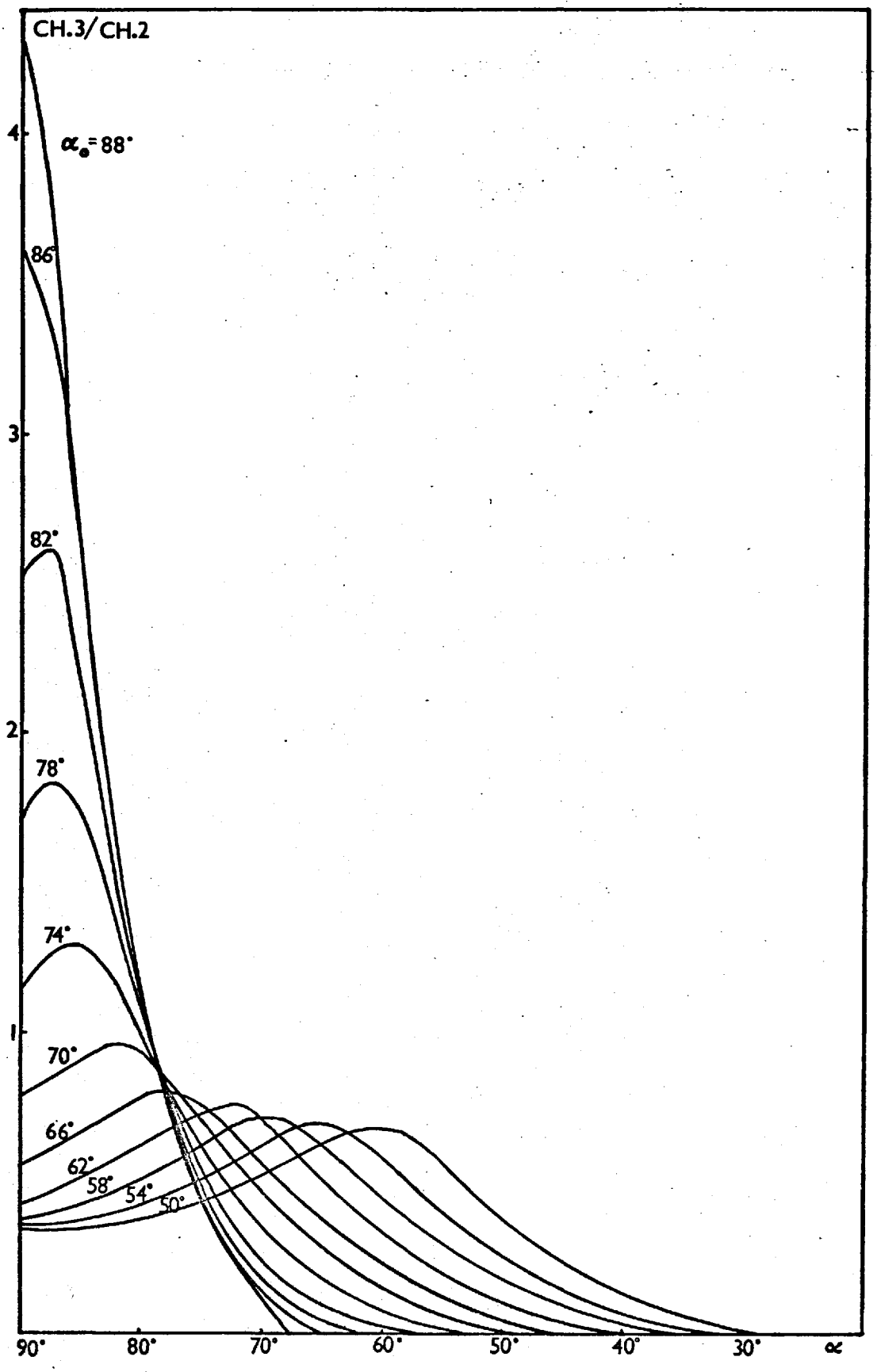

Fig. 20

Ratio of channel 3/channel 2 response as a function of pitch angle for a rectangular particle pitch angle distribution with a loss cone extending to α_o.

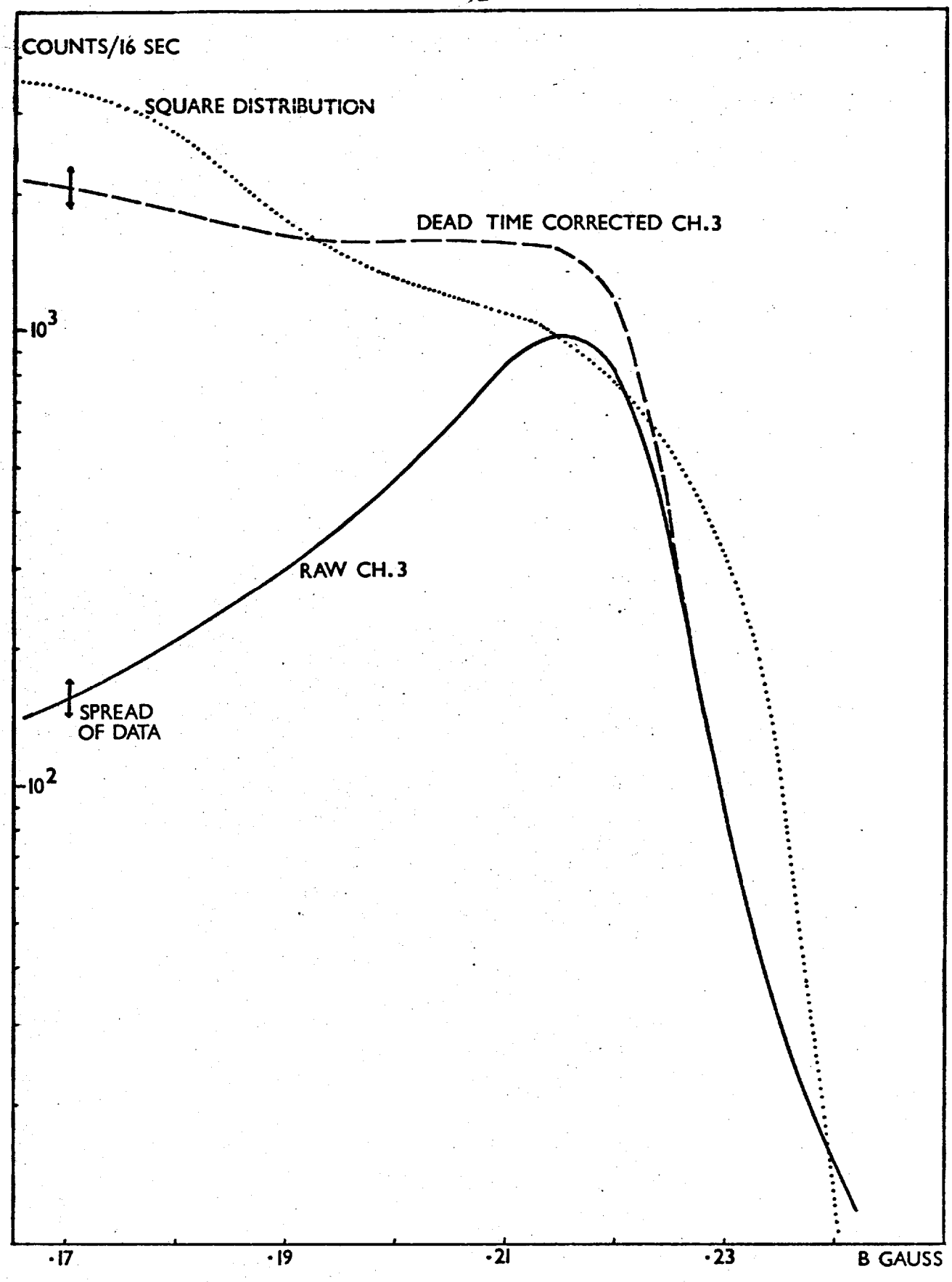

Fig. 21

Comparison of dead time corrected flux v. B curve at L = 1.4 and 90° pitch angle with the same curve calculated from the assumption that the pitch angle distribution is rectangular.

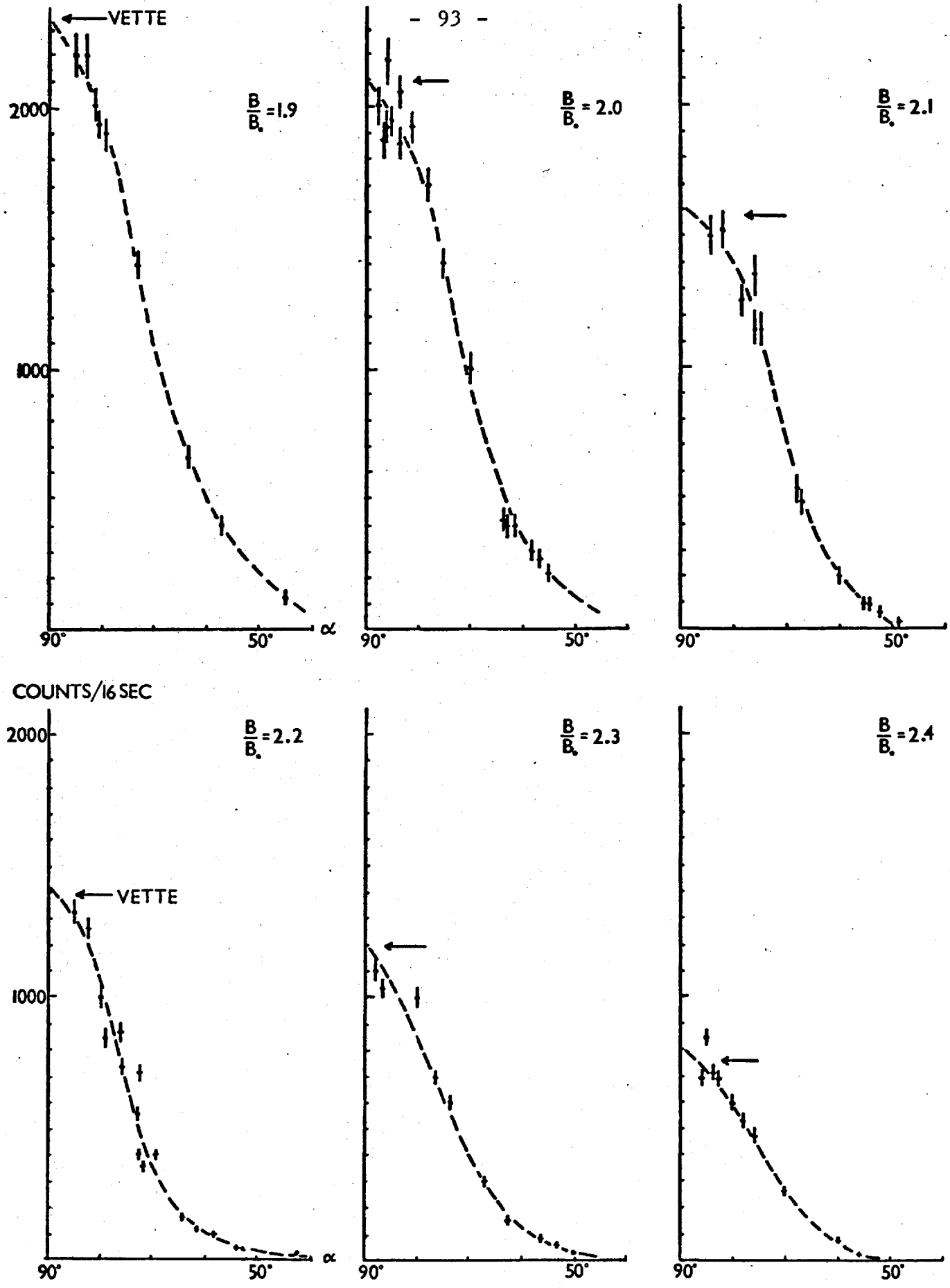

Fig. 22

Pitch angle distribution observed at > 95 MeV at different B values for L = 1.5. These results are corrected for dead time. Intensities at 90° pitch angles extrapolated from the curves given by Vette (1966) are also indicated.

Using these curves, Fig. 21 has been produced, which shows the expected channel 3 counting rate variation with magnetic field B at L = 1.4 and for 90° aspect angle. As can be seen by comparison with the dead time corrected experimental curve, agreement between observations and calculations for the square pitch angle distribution model is fairly good. The larger channel 3 counting rate, compared with channel 2, at $|\underline{B}| > 0.215$ gauss, where the electron contribution to channel 2 is still small, is also in agreement with the model prediction.

Fig. 22 shows some sample pitch angle distributions at L = 1.5 for $0.43 \text{ GV} < E < 0.88 \text{ GV}$ data corrected for the above effects. Intensities shown are found to be in agreement with $E > 100$ MeV fluxes extrapolated from the curves of Vette, and pitch angle distributions are also as expected from results at lower energies.

5. THE ENTRY OF SOLAR PROTONS OVER THE POLAR CAPS

5.1 INTRODUCTION

Previous to the advent of spacecraft experiments, solar and cosmic ray proton measurements were used to probe the configuration of the distant geomagnetic field.

Although work by Quenby and Webber (1959) showed that above a rigidity of about 1 GV only the effects of non-dipole terms of internal origin were readily observable, it became apparent in the early 1960's that external current systems needed to be taken into account to explain polar cap intensity distributions at lower rigidities (e.g. Review by Quenby and Webber, 1962).

The gross configuration of the magnetopause, magnetic tail and consequent magnetospheric tail distortions is now understood at low latitudes out to about 80 R_E, due especially to the work of Ness (e.g.Ness, 1965). Outstanding problems include the reconnection of polar and tail field lines to the interplanetary field (Dungey, 1961) and the length and degree of inhomogeneity of the magnetotail (Dessler, 1964, 1970). It is the purpose of this chapter to investigate what

information solar proton measurements over the polar cap may give concerning these particular problems.

Solar protons with energies extending in the range from 10^6 - 10^9 eV provide a suitable probe of the field, since they can only arrive at auroral or higher latitudes and, at the lower energies at least, follow field lines fairly closely. If the proton intensity were uniform in space and time, with no anisotropies, Liouvilles theorem would guarantee a uniform intensity at all allowed pitch angles over the polar cap, equal to the interplanetary directional intensity and extending down to the threshold latitude which for 1 MeV particles is approximately that of the last closed drift shell, and which at midnight coincides with the last closed field line. A pseudo-trapping region exists between the last closed field line and the last closed drift shell at other local times, since particles entering on the night side can drift around to the day side, preserving the longitude invariant which is roughly proportional to the length of the field line between the mirror points. Since the length of the last closed field line at midnight is less than the last closed field line at noon, particles which drift around in longitude do so everywhere within the pseudotrapping region.

In practice, anisotropies aligned along interplanetary field lines, local and large-scale intensity gradients and time variations of the overall flux all exist in interplanetary space. Thus structure in the polar cap intensity is expected and has indeed been observed by, for example, Pieper et al. (1962), Williams and Bostrom (1969), Hudson and Anderson (1969). To predict the polar cap directional intensity it is necessary to follow a typical particle trajectory back to the boundary of the magnetopause, which is at least 10 R_E distant, and in the case of trajectories going down the tail may be up to $\sim$1000 R_E away. Provided scattering is small, the distribution function $f(\underline{p},\underline{r})$ is conserved along the trajectory and since any electric fields integrated over a trajectory are unlikely to amount to more than a few tens of kVolt, $f(\underline{p},\underline{r})$ is the same at both end of the trajectory. This procedure is merely an extension to low energies of the impact zone work originally done by Firor (1954).

Increased understanding of particle trajectories in a field model composed of both dipole terms and non dipole terms of internal origin and due to external current systems has come from the work of McCracken et.al. (1962), Shea and Smart (1969), Gall et.al. (1968, 1969).

In the sections 3 and 4 we will discuss separately the expected effects of anisotropies and gradients on the polar cap distribution in terms of possible magneto-tail field models, in order to determine whether experimental data is able to distinguish various possibilities. Anomalous entry to the closed magnetospheric field lines due to scattering (Lanzerotti, 1968) or more likely quasi-static electric fields associated with magnetospheric convection (Quenby, 1969) will not be considered here.

As a preliminary, we will define the field model used in the trajectory work and show that scattering in the outer magnetosphere or magneto-tail is likely to be an unimportant process.

5.2 MAGNETOSPHERIC FIELD MODEL

At present there is no adequate co-ordinate system for use with low altitude polar data. Invariant latitude and eccentric dipole magnetic local time have been used by most workers, but these co-ordinates contain insufficient information on the distant field. Integration of particle trajectories in a high simulation of the magnetic field probably provides the best method for studying solar proton events (Morfill, 1971). The requirements for such a study are :

1. The field model used must correspond fairly well to the magnetic conditions at the time the observations were made, i.e. solar wind data and tail field strengths must be known, or inferred from related observations such as the high energy electron trapping boundary and the 40 keV electron boundary.

2. Trajectories must be started at the satellite position. Although ideally trajectories should be computed over all opening angles of the detector, collimation due to magnetic field decrease with distance away from the earth makes such a refinement unnecessary.

3. The field model should represent the magnetosheath field and interplanetary field as well as the magnetospheric field so that the particle trajectory can be integrated until no more magnetopause crossings occur. Only then comparison with the interplanetary particle pitch angle distribution is meaningful.

4. Trajectories must not be integrated further than one or two mean free paths. Scattering theory (applied to actual conditions at the time of measurements) provides an estimate of the uncertainty in the calculated viewing directions.

5. Trajectories should be computed for all energies to which the detector responds, and the calculated viewing direction should be weighted for the detector energy response and the energy spectrum of the incident particles. In practice the weighted mean energy of the detector can be used for trajectory work provided that the energy channel is not too wide.

The configuration of the geomagnetic field and the magnetosheath field is known from satellite magnetometer measurements out to about 80 earth radii in the antisolar direction (D. H. Fairfield, 1970, K. W. Behannon and D. H. Fairfield 1969, K. W. Behannon, 1970). An extended magnetic tail has been observed at distances near 500 R_E and 1000 R_E (Woolfe et.al, 1967; Fairfield, 1968; Mariani and Ness, 1969). In general it can be stated that the geomagnetic tail is well defined out to lunar distances, and that the magnetosheath field behaves on average as predicted theoretically (Spreiter et.al, 1968, 1969) at these relatively near earth distances. It is also known that the tail field decreases after a substorm and that the magnetospheric field becomes more dipolar. The two halves of the tail are separated by a plasma sheet. There is evidence that the plasma sheet is thicker when the interplanetary magnetic field is northerly directed than when there is a southerly component (Coleman, 1970). Noise variations in the tail field tend to be random, and the power spectrum is approximately $1/f^2$ with no preference parallel or perpendicular to the magnetic field.

The magnetic field model employed in the trajectory calculations is derived from :

$$\underline{B} = \underline{B}_i + \underline{B}_s + \underline{B}_{cs}$$

where

$\underline{B}_i$ = the internal field

$\underline{B}_s$ = the external field due to currents in the magnetopause

$\underline{B}_{cs}$ = the external field due to the current in the neutral sheet of the magnetospheric tail.

5.2.1 Internal Source

The internal field is obtained from the equation

$$\underline{B}_i = \nabla V$$

where V is the magnetic potential. V is given by a spherical harmonic expansion

$$V(r,\theta,\phi) = a\sum_{n=0}^{6}\sum_{m=0}^{6}(g_n^m \cos m\phi + h_n^m \sin m\phi)\, P_n^m(\cos\theta)(a/r)^{n+1} \qquad (5.2.1)$$

where :

a = average radius of earth

g_n^m and h_n^m are the Finch and Leaton coefficients

r = distance from geocentre

θ = colatitude

ϕ = longitude

The internal field components B_r, B_θ, B_ϕ are obtained in the geographic co-ordinate system.

The external field is obtained in solar magnetospheric co-ordinates, transformed into the geographic frame and then added to the internal field. Full details of the transformations are given in appendix 2.

Trajectories of particles are computed by a modified McCracken (1962) program, using numerical integration of the differential equation of motion,

$$\ddot{\underline{r}} = \frac{q}{m} \dot{\underline{r}} \times \underline{B} \qquad (5.2.2)$$

where q is the charge and m is the mass of the particle which moves in the model field $\underline{B}$.

5.2.2 Formulation of External Sources

(a) Currents in the Magnetopause

The magnetic field produced by magnetopause currents is calculated from

$$\underline{B}_s = \nabla V_s$$

where V_s is the magnetic potential. V_s is given by a spherical harmonic expansion

$$V_s(r,\theta,\phi) = a \sum_{n=1}^{6} \sum_{m=0}^{n} A_n^m \cos m\phi \, P_n^m (\cos\theta)(\frac{r}{a})^n \qquad (5.2.3)$$

The coefficients A_n^m are of the form

$$A_n^m = c_n^m / r_s^{n+2}$$

where $r_s(\theta_o, \phi_o)$ is the position of the magnetopause at $\phi_o = 0^o$ and $\theta_o = 90^o$ in solar magnetic co-ordinates (Olson, 1970): For the zero tilt dipole case, this is the stand off distance used by Mead (1964).

If $V_s(r, \theta, \phi)$ is fitted in solar magnetospheric co-ordinates, V_s is symmetric in longitude, ϕ, and hence only terms of $\cos(m\phi)$ are non-zero. $\phi = 0$ corresponds to the noon direction. For the zero tilt case, there is also a North-South symmetry, so that all coefficients, A_n^m, where n+m is even, are zero.

In this work, $\underline{B}_s$ is calculated using the 6-term expansion fitted by Mead (1964) although dipole tilt varied from 5^o to 15^o. This model is inaccurate near the neutral points, where the magnetopause deviates most from the zero tilt case (Olson, 1969). For larger dipole tilts the model becomes increasingly inaccurate as the even n+m terms become more significant. None of the trajectories here passed close enough to the neutral points to affect the results significantly. Trajectories calculated in a field model including all the terms confirm this.

Various workers (Gall et.al., 1968; Shea and Smart, 1969) have used a two term expansion for magnetic field due to surface currents. The magnetic field resulting from such a model is unrealistic at distances greater than 10 R_E. This is shown in Appendix 1.

(b) Current Sheet Forming the Tail

The plane infinite current sheet of Williams and Mead (1965) was used :

$$B_x = 2j\ (\theta_2 - \theta_1)$$
$$B_y = 0$$
$$B_z = -2j \log (r_2/r_1) \qquad (5.2.4)$$

where the field has been expressed in solar magnetospheric cartesian co-ordinates. θ_1, θ_2 and r_1, r_2 are defined in Williams' and Mead's paper (1965).

The current sheet is parallel to the solar magnetospheric x-y plane and displaced from this plane by an amount depending on the tilt of the magnetic axis of the earth. The front end of the neutral sheet is 'hinged' at the magnetic equator at a distance of 10 R_E (Speiser and Ness, 1967; Bame et.al., 1967). This is equivalent to shifting the tail co-ordinate system from (0,0,0) to $(-R_1(1-\cos\lambda), 0, R_1 \sin\lambda)$.

R_1 is the distance of the front edge of the current sheet from the geocentre, and λ is the angle between the solar ecliptic z-axis and the projection of the inclination of the magnetic axis onto the solar ecliptic x-z plane.

The adjustable Williams and Mead parameters used were :

r_s = 10 earth radii (R_E)

B_{cs} (tail field associated with the current sheet)
= 40 γ for pass 1 during November 1968 flare
= 15 γ for passes 2, 3 and 4 during November 1968 flare
= 40 γ for pass 1 during February 1969 flare

R_1 (inward termination point of the current sheet)
= 10 R_E for all passes.

R_2 (outward termination point of the current sheet)
= 40 R_E when B_{cs} = 40 γ
= 200 R_E when B_{cs} = 15 γ

These values were shown by Roederer (1969) to agree best with ATS data.

Field distortions due to ring currents were not considered in this work.

A disadvantage of the plane current sheet used by Mead and Williams is the sharp termination of the front edge. It is known that in reality the front edge is more diffuse. This abrupt termination causes trajectories calculated for invariant latitudes near cut off to fluctuate more widely for a small change in invariant latitude, than would be expected for a more realistic field description.

Position and velocity vectors are computed in geographic, solar ecliptic and solar magnetospheric co-ordinates at selected points along the particle trajectory. The appendix gives more details of the co-ordinate transformations used. Pitch angle, α , and the first adiabatic invariant $\sin^2\alpha/|\underline{B}|$ are also calculated at these points, and can be used to

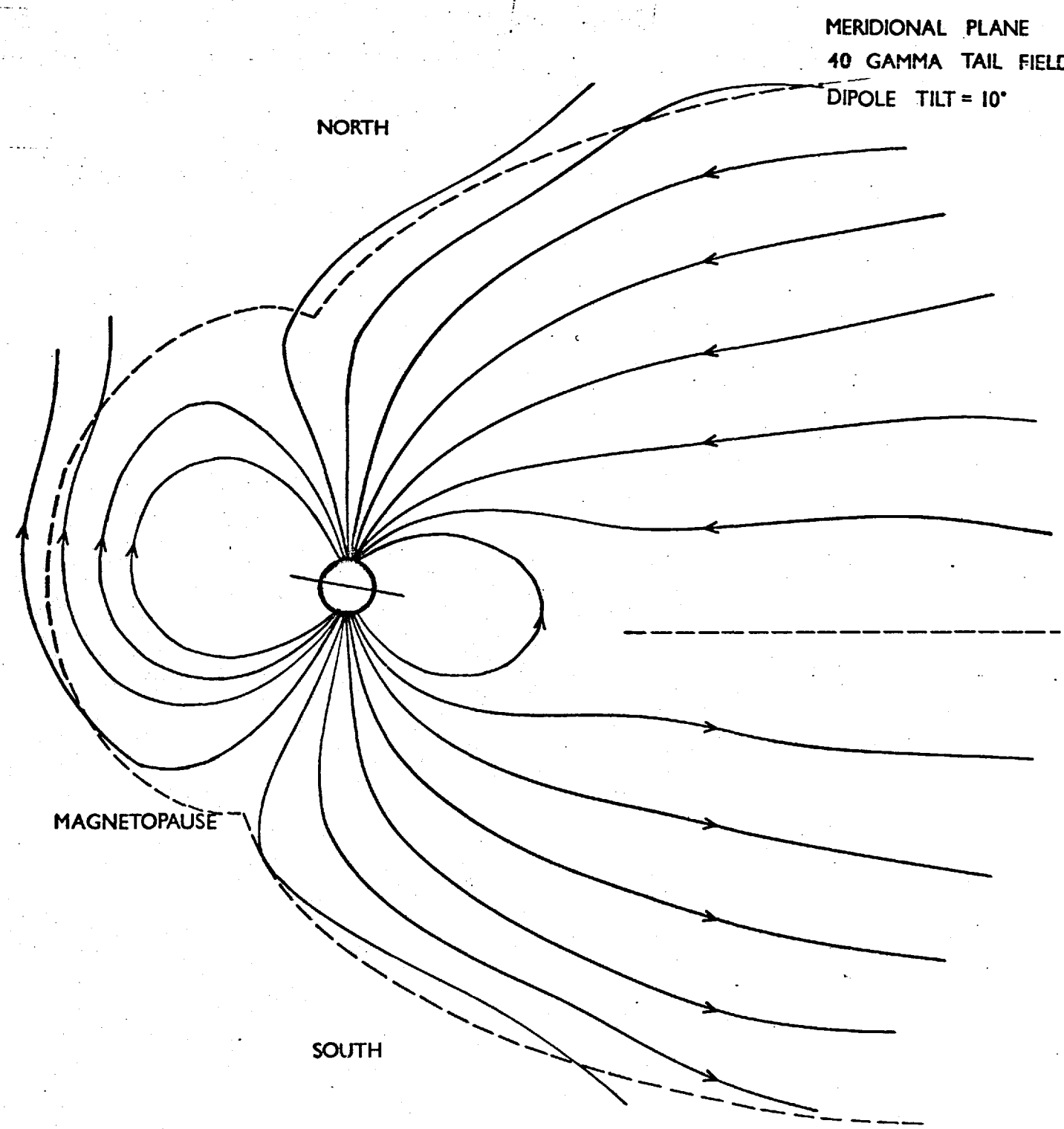

Fig. 23

Noon-midnight meridional cross section of the geomagnetic field using the Mead 0° tilt coefficients for the magnetic field due to magnetopause currents and the plane semi-infinite current sheet of Williams and Mead hinged at the equator, 10 R_E from the earth, together with an internal dipole tilted by 10° in the noon-midnight meridional plane.

decide if adiabatic extrapolation of particle motion down the tail is justified. It is found that the description of the magnetospheric field is reasonable out to about 25 R_E on the night side. For example, Fig. 23 shows a plot of the field for 10^o dipole tilt in the noon-midnight meridional plane.

5.2.3 Calculation of Mean Free Path

Use of trajectory calculations in the adopted model field out to several tens of earth radii presupposes that perturbations to the field are small. Williams and Bostrom (1969) have assumed that significant radial diffusion may take place across the tail in order to explain the spatial and temporal variations of polar cap proton measurements. Michel (1965) originally mentioned the diffusion process.

It is possible to estimate the scattering mean free path using the fluctuation power spectra of the tail field obtained by Pioneers 7 and 8, (Mariani et.al., 1969) and hence verify the validity of the static field trajectories.

Particle scattering will be assumed to be due to the gyroresonance interaction with small amplitude waves, which brings about multiple changes in pitch angle. In this approximation the basic particle motion is that of a helix in a uniform field. It is assumed that the waves propagate isotropically with the Alfven speed and thus a satellite magnetometer observing the time dependence of the field is essentially measuring the distribution of wavelengths. Solar protons, of course, move much faster than the Alfven speed, and hence see a stationery field of irregularities. The plasma density in the tail is estimated to be no greater than $10^{-2}/cm^3$ (Frank and Owens, 1969). Although at large distances of 1000 R_E, the plasma density is greater (Wolfe et.al., 1967), it is still much less than the plasma density in the magnetosheath. Using a tail field strength of 16 gammas yields an Alfven speed

$$V_A = B / \sqrt{4\pi n m_p} \qquad (5.2.5)$$

$$V_A = 3500 \text{ km/sec}$$

Gyro-resonance for the average particle of rigidity R in a magnetic field of strength B occurs for an observed field frequency f, at the satellite, given by

$$R = \frac{\sqrt{3}\, V_A\, B}{2\pi f} \qquad (5.2.6)$$

This leads to $f = 3 \times 10^{-3}$ Hz at 0.5 GV
and $f = 4 \times 10^{-2}$ Hz at 0.043 GV (1 MeV)

for protons.

The scattering mean free path for motion along the field lines due to the multiple pitch angle scattering is then

$$\lambda = \frac{R^2}{P_\perp V_A} \qquad (5.2.7)$$

where $P_\perp$ is the power in the transverse fluctuations spectrum at frequency f. (Jokipii, 1966). From the work of Mariani et.al. (1969) a value for $P_\perp$ inside the magnetopause on the night side of $200\gamma^2$/Hz at 3×10^{-3} Hz is obtained, and by extrapolating their curves to higher frequencies, a further value of $5\gamma^2$/Hz at 4×10^{-2} Hz is found.

The Kp index of magnetic activity was 3+3. during the period of observations.

The resulting values of the mean free paths are :

$$\lambda = 700\ R_E \text{ at } 0.5 \text{ GV}$$

$$\lambda = 200\ R_E \text{ at } 0.043 \text{ GV}$$

For an isotropic wave field, scattering of the particle guiding centre across the field lines by a distance of one Larmor radius occurs only once every mean free path.

traversed in the parallel direction. Thus we conclude that diffusion transverse to the field direction and pitch angle scattering during the motion along the field are both unimportant in the magnetotail at solar proton energies, at least to 40 R_E, the limit of the Pioneer observations. If the possibility of the tail breaking into filaments at very large distance is neglected, corresponding λ values at 1000 R_E are 700 R_E and 150 R_E respectively. In the magnetosheath within 40 R_E of the earth we estimate λ = 1000 R_E and 50 R_E respectively.

Measurements using lunar occultation techniques show that perpendicular diffusion is insignificant for electrons. (Van Allen, 1969). It was found that the drift velocity of 50 keV electrons (velocity 10^8 m/sec) in a direction transverse to the tail field, must be less than 10^5 m/sec due to all causes. Assuming that perpendicular diffusion is the dominant process, this would be equivalent to a maximum transverse drift of 1 R_E for every 10^3 R_E travelled along the field.

Because scattering in the tail has been shown above to be unimportant it is possible to use the asymptotic trajectories of solar protons arriving at the polar caps to obtain information about the extended tail.

5.3 STRUCTURE CAUSED BY ANISOTROPIES

Collimation of solar proton fluxes by the interplanetary spiral field was first suggested by McCracken (1962) on the basis of neutron monitor measurements and subsequently confirmed for 10 MeV particles using spacecraft measurements by McCracken and Ness (1966), although Quenby et.al.(1969) show that large angular discrepancies between the flow direction and field direction can exist on occasions. On a simple isotropic diffusion model, the anisotropy decays as $f(r,t) = 3r/2vt$ (Fisk and Axford, 1968) for $\lambda \neq f(r)$ and it is observationally true that for low energy particles the anisotropy persists for a day or more. After two or three days, the anisotropy reduces to about 10% and moves to the radial direction. This is explained by outward convection of particles with the solar wind velocity.

Finally, there is a reverse flow along the field lines towards the sun which together with the convective component ends in a net flux roughly at right angles to the Archimedes spiral direction (McCracken et.al. 1971).

For a detector viewing in a particular direction, the maximum amplitude of polar cap structure possible is given by the percentage amplitude of the anisotropy in interplanetary space. Practical detectors are often omni-directional, and their intensities need to be corrected for the atmospheric loss cone. Trajectories calculated for initial pitch angles which lie outside the loss cone finish up in a well collimated beam at large distances from the earth, provided that the initial position is not too near the particle cut off rigidity. The intensity seen at low altitude over the polar cap is then the same as the directional intensity in interplanetary space in the asymptotic viewing cone of the low altitude detector. The final asymptotic direction of a trajectory may only be obtained after several magnetopause crossings as mentioned earlier. Since most experimental results relate to structure greater than 10% in amplitude, it is probably only necessary to consider the initial outward and diffusion dominated phase of a solar proton event when polar cap structure due to interplanetary anisotropies is considered.

5.3.1 Structure for Energies > 30 MeV

Two examples of flare events, when anisotropies at high energies (> 30 Mev) seemed to have caused polar cap structure, are those of November 18, 1968 and February 25th, 1969. In figures 24a and 25a data from particular passes for the 90 MeV - 360 MeV detector on the ESRO II satellite is plotted on a diagram of particle position (latitude and longitude in solar ecliptic co-ordinates). The trajectory integration was terminated either because the particle crossed the magnetopause, or because a plane situated at a distance of 25 R_E down the tail perpendicular to the earth-sun line was reached. The longitude of 180° corresponds here to the antisolar direction, and the position of the average magnetopause at a distance of 25 R_E down the tail is indicated and so is the neutral sheet. The particle velocity vector at 25 R_E is not shown, but in

general is close to the position vector of the particle. The energy of 125 MeV (0.5 GV) was chosen for these trajectories, as it was the approximate weighted mean of the detector energy response. Fig. 25c shows the full energy window for the February 25th event, and Figs. 24b and 25b give the Intensity v. invariant latitude plots for the two events. The direction of the peak interplanetary particle flux, and the interplanetary magnetic field vector are also indicated. Asymptotic directions were computed corresponding to the satellite positions according to the methods of section 2. In each case the asymptotic directions of the maximum intensity correspond to the interplanetary field direction from the sun, and the minimum intensity to the anti-sun field direction. Peak intensities are also seen down the tail, and this is shown more clearly in Fig. 26, where the intensity is plotted against pitch angle for 11.15 on November 18, 1968. It appears that particles can arrive from down the tail with the full intensity, that is, without scattering, corresponding to the most favoured flow direction from the sun. For measurements of the polar structure of two energies at 10.55 U.T. on February 25th, an anisotropy of between 15% and 31% at $>$ 360 MeV (defined as $\frac{I_{max}-I_{min}}{I_{max}+I_{min}} \times 100$) in interplanetary space is expected while the HEOS $>$ 360 MeV directional detector showed an anisotropy of 18% at the time of observation (Engel et.al., 1969). A flux directed only outward along the magnetic field from the sun is expected at 11.15 U.T. from the November 18 pass on ESRO II and indeed using neutron monitor and Explorer 33 data (Van Allen et. al., 1969), which showed a particle flux directed entirely away from the sun at 100's of MeV and at a few MeV respectively, we estimate an anisotropy of $\sim$ 100% at 90 MeV - 360 MeV for pass 1 on November 18. Both the size and direction of the interplanetary anisotropy seem of the correct value to explain the polar cap results, apart- at present - for the problem of entry directly down the tail. In later chapters we will demonstrate in greater details the correctness of the idea, for particles of energy greater than $\sim$ 30 MeV.

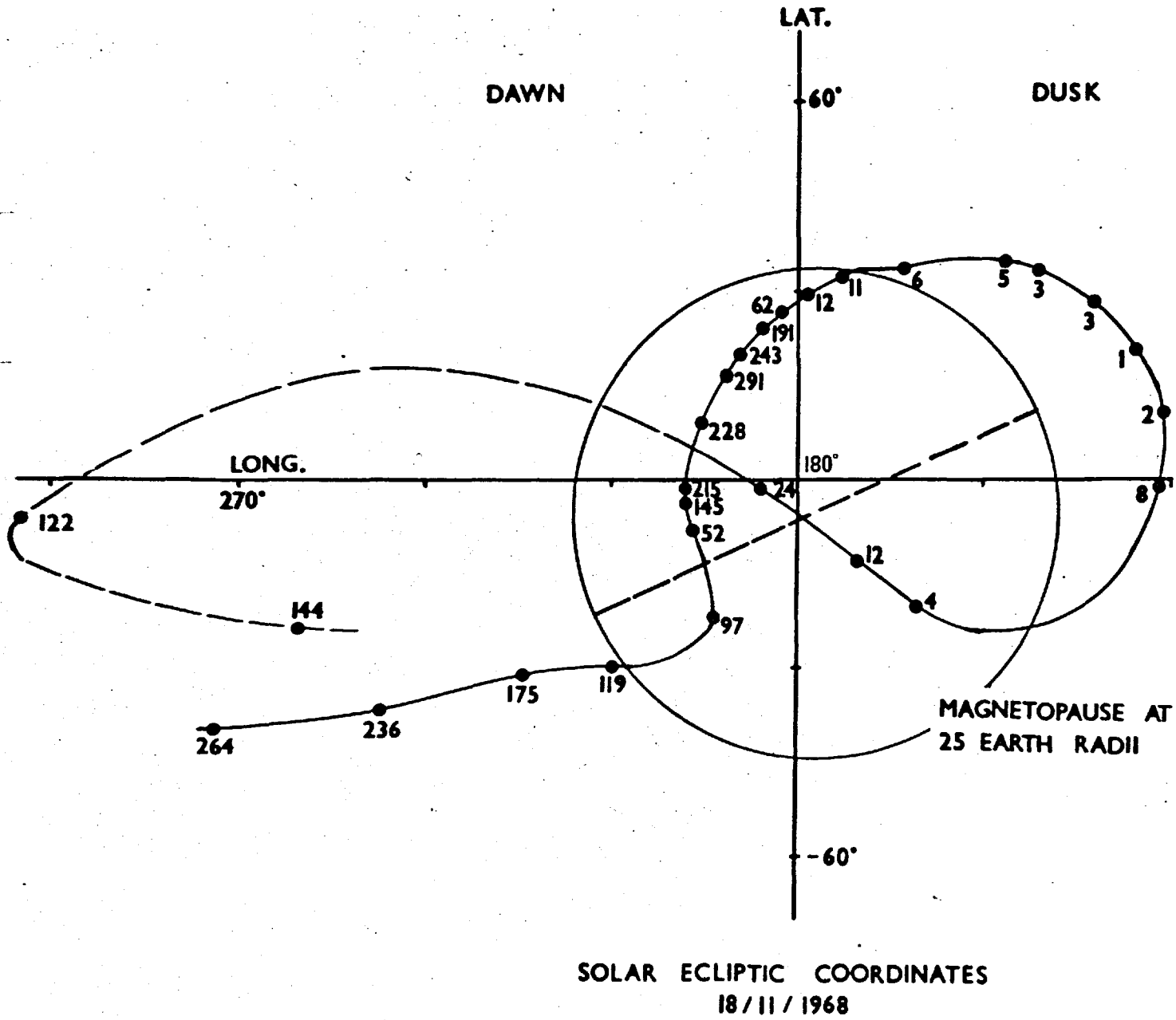

Fig. 24a

Magnetopause entry diagram for November 18th polar pass. Position of 125 MeV protons at the termination of particle trajectory integrations are shown on a latitude-longitude diagram.

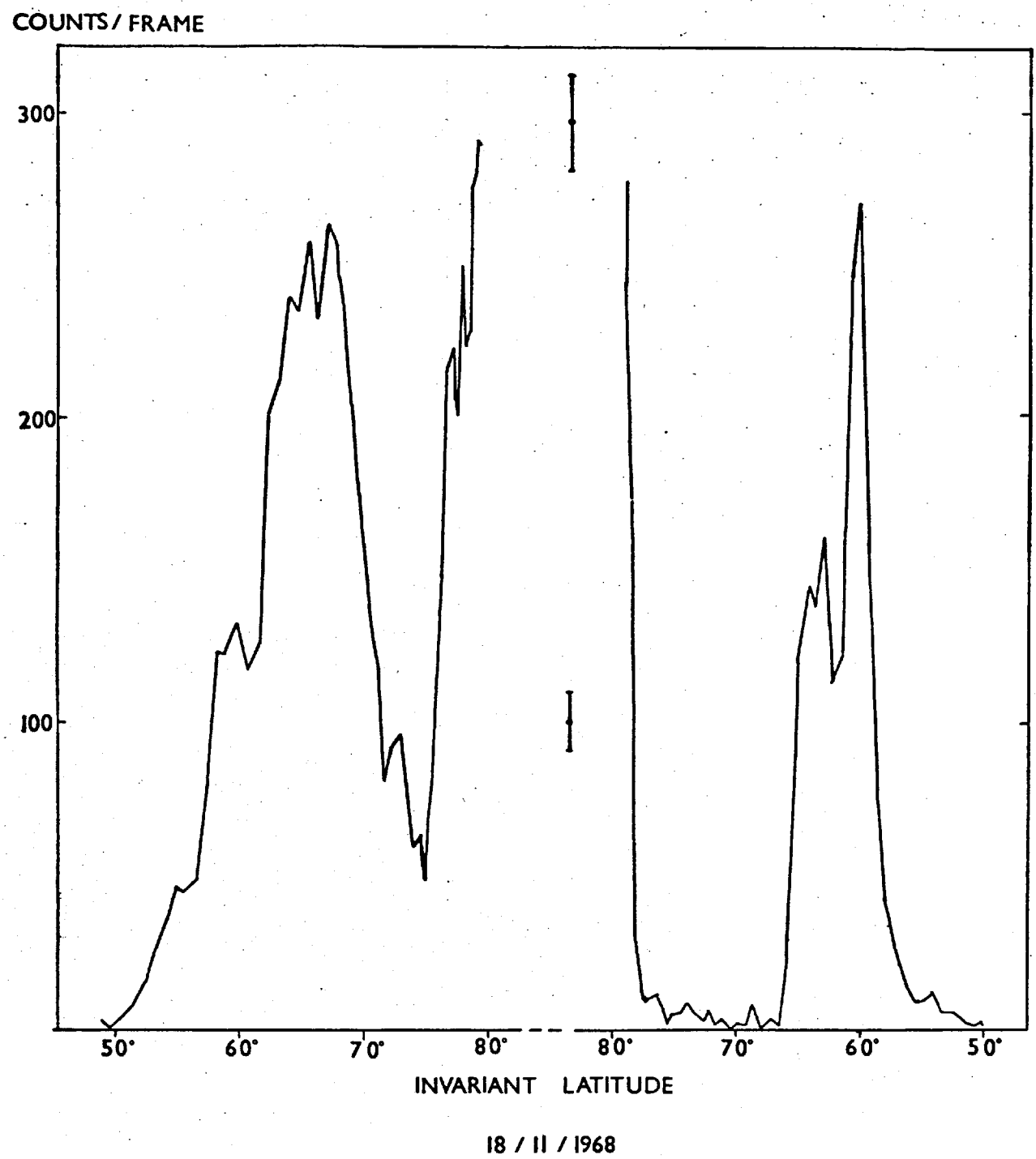

Fig. 24b

Counting rate for 90-360 MeV solar protons at ~ 11.15 U.T. on November 18th 1968 as a function of invariant latitude over the northern polar cap. The data is not corrected for atmospheric loss cone.

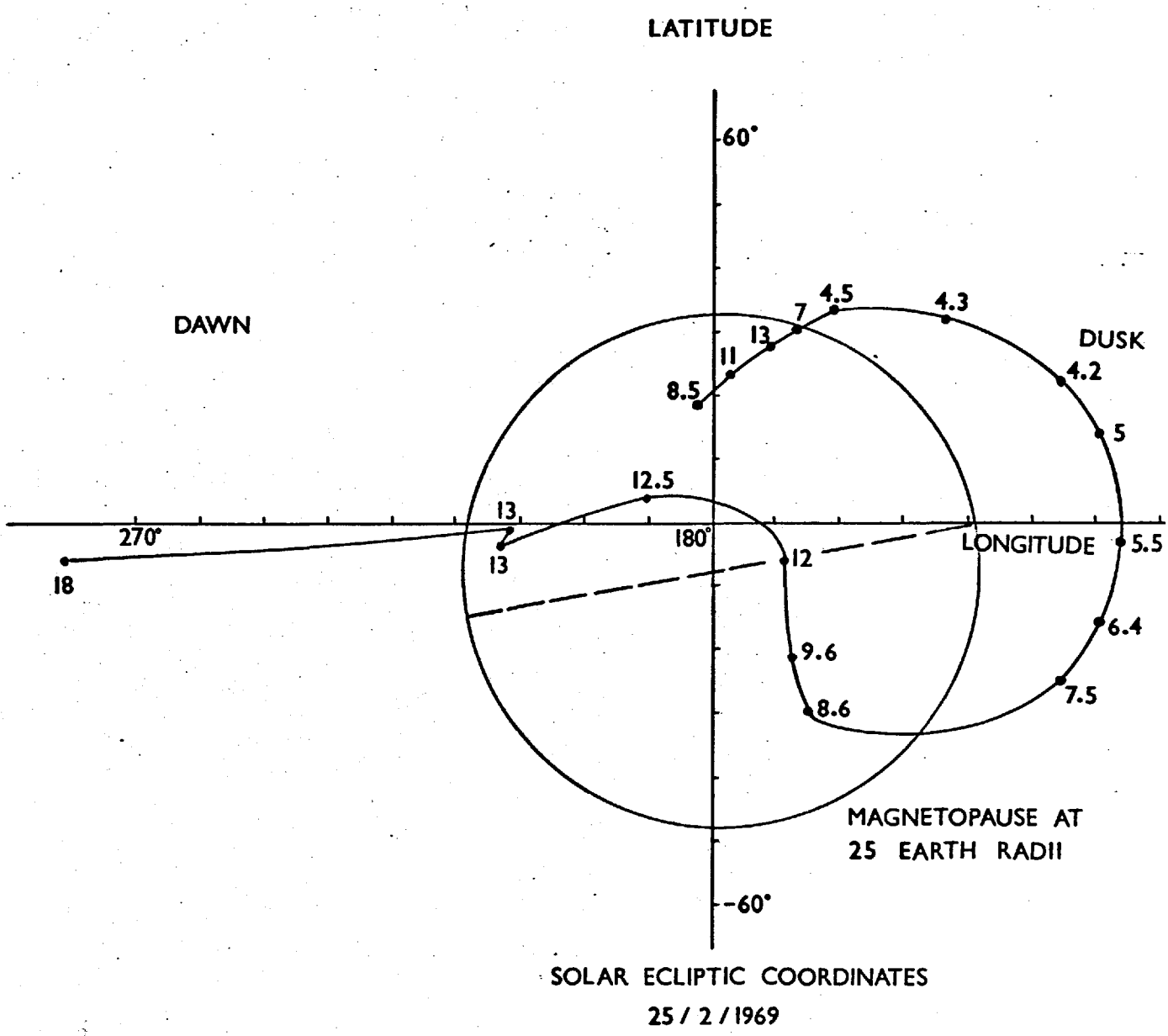

Fig. 25a

Magnetopause entry diagram for February 25th polar pass. Positions are for 125 MeV protons.

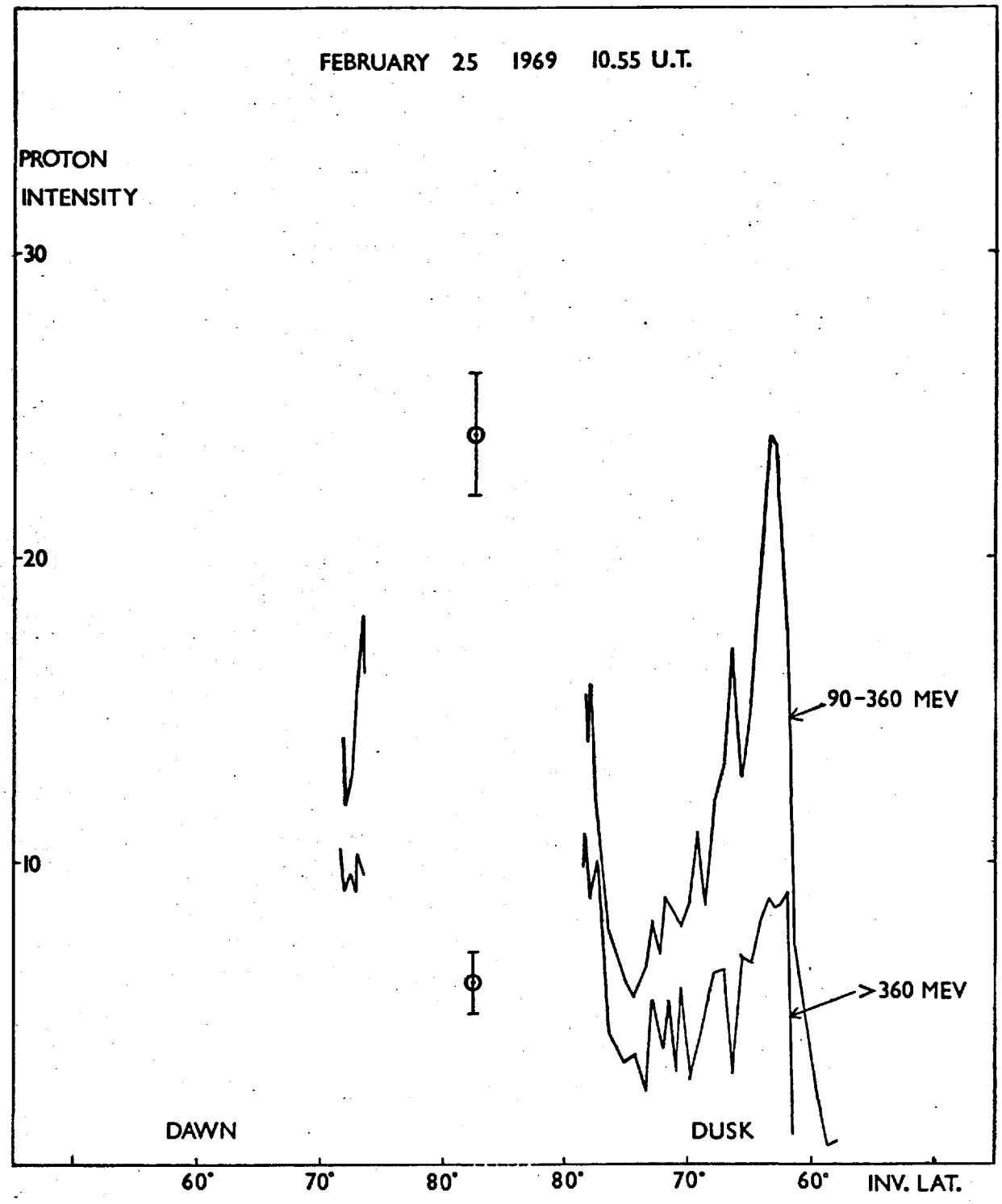

Fig. 25b

Counting rate for 90-360 MeV solar protons at ~10.55 U.T. on February 25th 1969 as a function of invariant latitude over the northern polar cap. The data is loss cone corrected.

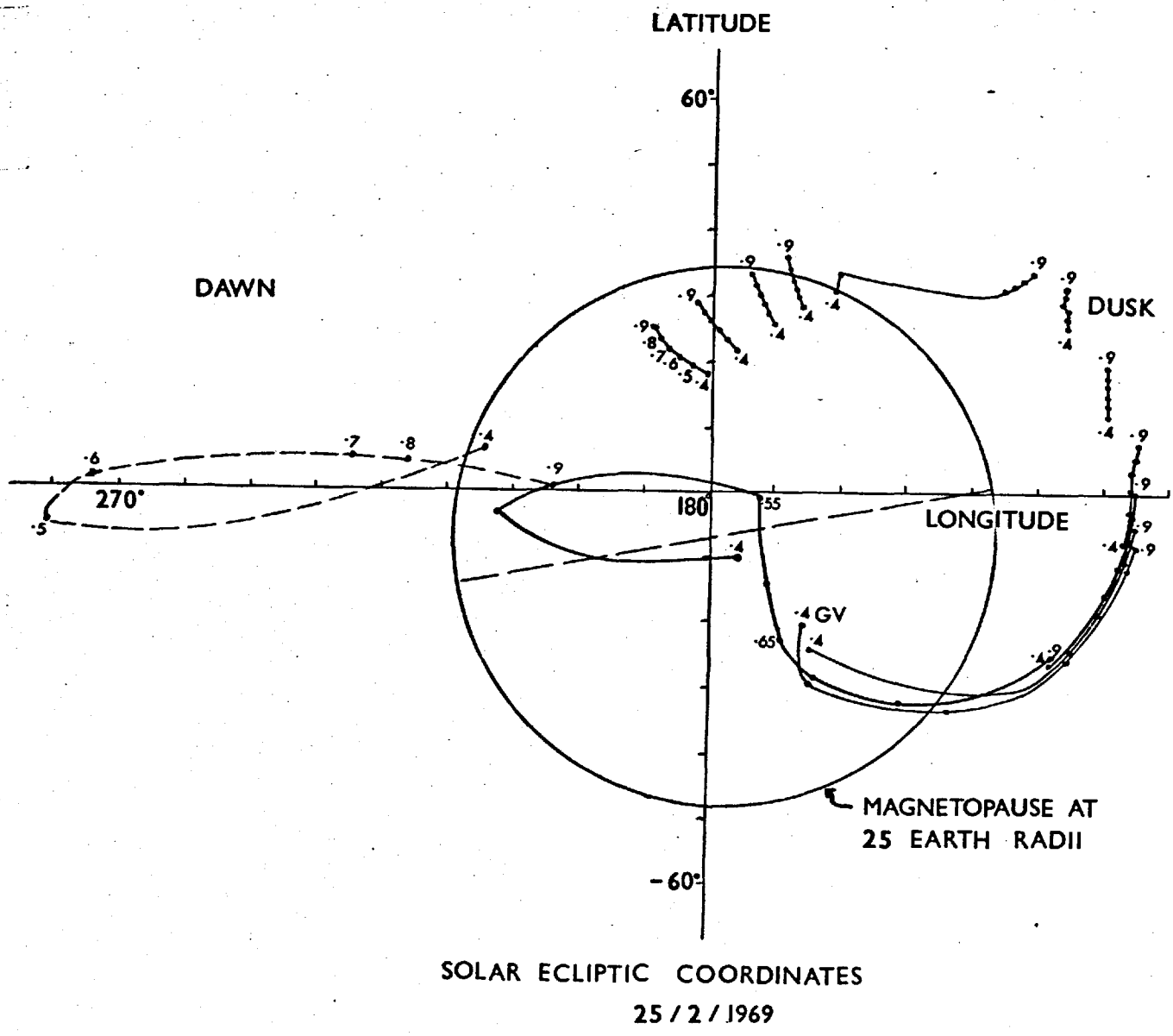

Fig. 25c

Magnetopause entry diagram for February 25th polar pass. Positions of protons at the termination of particle trajectory integrations are shown on a latitude-longitude diagram for the full rigidity range of the S.28 proton detector, i.e. 0.4 - 0.9 GV. This shows clearly how the viewing cone widens for near cut-off positions.

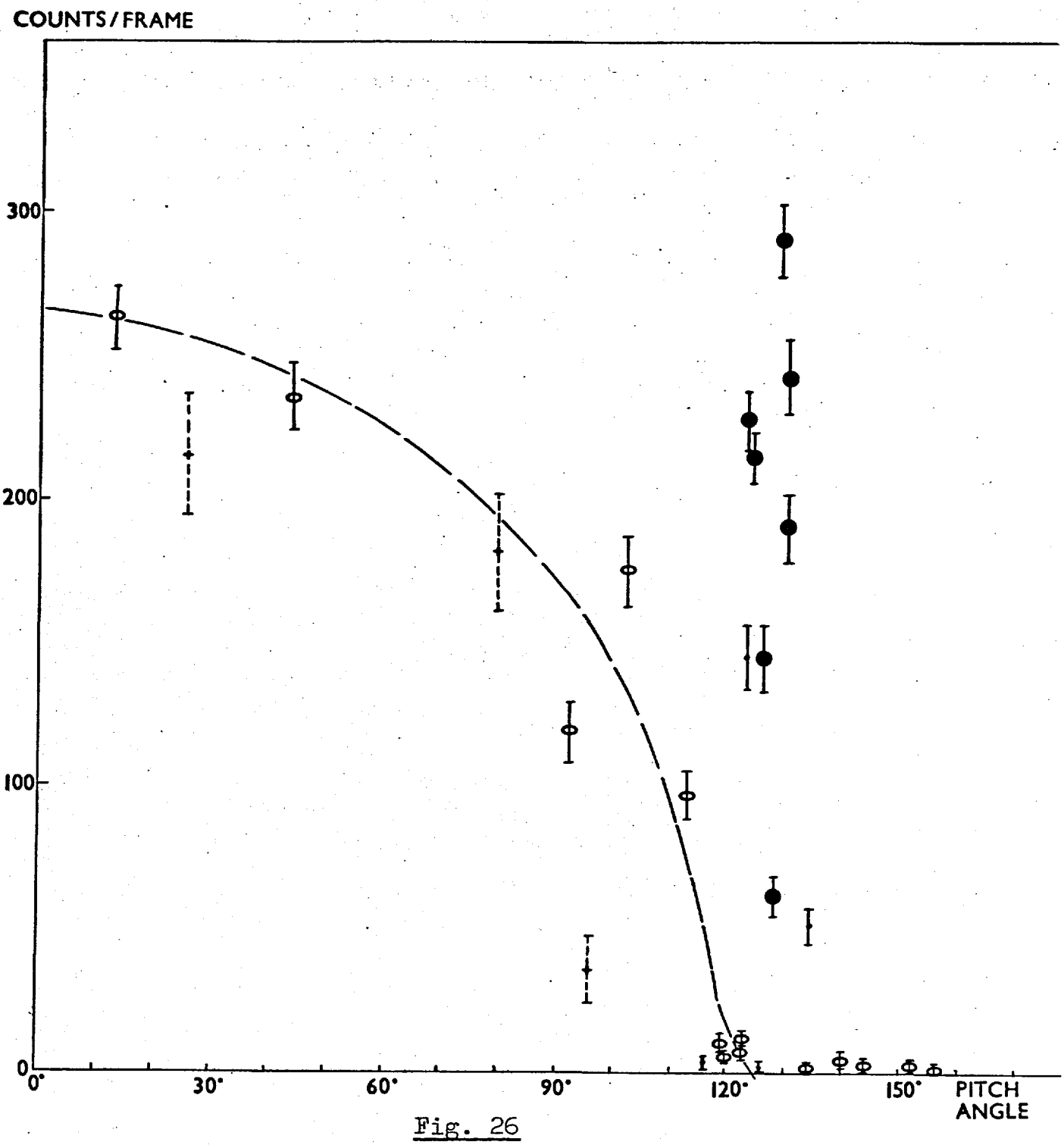

Fig. 26

Pitch angle distribution in interplanetary space for November 18th derived from the trajectory integrations and the known interplanetary magnetic field directions. Pitch angles were calculated from $\cos\alpha = \underline{B}.\underline{v}$ where $\underline{B}$ = interplanetary magnetic field, and $\underline{v}$ = particle velocity vector at the termination of the trajectory integration. Symbols are : ⧱ Proton entry into magnetotail at $> 100\ R_E$, I Entry into magnetotail, $< 100\ R_E$, ⋮ Entry through magnetopause near earth, large loss cone correction, ⧱ Entry through magnetopause near earth, small loss cone correction.

There remains the problem of entry into the tail. Since the Larmor radius of 130 MeV protons is ~ 24 R_E, in a 10 γ field, particles with small pitch angles can remain inside the tail for many R_E, and the question is how does the flux streaming out from the sun get turned around into the tail ? Efficient scattering of protons at the boundary and in the tail would probably fill up all pitch angles with a near-isotropic distribution and the intensity observed over the polar cap by a low altitude satellite would most likely be the same as the omni-directional averaged interplanetary flux otherwise there would be a problem in conserving particle flow across the dawn and dusk tail boundaries. However figure 26 shows that we may see the peak, anisotropic interplanetary flux. Our estimated mean free paths (section 5.2) are too long for scatter across the tail to be important. Even if we took the Dessler and Michel (1970) filamentary model, and allowed a much shorter mean free path at distances of 1000 R_E, there is still the problem of losing the structure of the interplanetary particle distribution.

The estimated length to drift 1 R_E in a tail electric field of 1.2 kV/R_E (the upper limit set by lunar occultation techniques) perpendicular to the field lines is ~ 1400 R_E for 1 MeV protons and ~ 14000 R_E for 100 MeV protons (when the pitch angles are less than 10^o) and hence is too long. Similarly a 1γ/R_E magnetic field gradient requires a ~ 100 R_E path length for 1 R_E drift across the field at 100 MeV, and ten times that value at 1 MeV, for pitch angles of 10^o. This path length increases as $\cos\alpha/\sin^2\alpha$ with decreasing pitch angle, α . It is also difficult to imagine how the big field gradients required could exist over a large enough volume, if the overall field strength in the tail is only typically 10 γ .

Field line draping in the magneto sheath inside an extended shock region a few hundred R_E down the tail could be proposed as a means of guiding solar protons around and into the tail. Spreiter (1967) has calculated flow patterns in the magnetosheath near the earth, predicting the field line draping around the magnetopause from gasdynamic theory. These predictions are roughly in accord with magnetic field measurements of Behannon and Fairfield (1969).

Although field line draping exists - and is of importance near the earth - it appears most unlikely from the results of Behannon and Fairfield, that field line draping in the magnetosheath beyond $\sim$40 R_E down the tail is marked enough to guide the incident solar protons in such a way as to explain the observed results. Their results indicate that at these distances down the tail, where the shock is weak, the magnetosheath field is approximately interplanetary, even close to the magnetopause.

Instead, we suppose that one of two extreme versions of the reconnection field model is possible. Connection of the interplanetary field to the tail field - the machanism for transmitting solar wind energy via tension in the tail to the magnetosphere - during the November and February events would be as shown in Fig. 27 for the Dungey (1961) model, or as shown in Fig. 28 where according to Axford, we approximate the magnetopause to a sharp discontinuity.

In both models some divergence of the tail field is required to bring about reconnection and hence particles following tail field lines from deep in the polar cap are all eventually brought to the surface. Transfer of interplanetary protons to the tail field lines is done by the obvious process of following round the slow bend on the first model (Fig. 27). The radius of this bend, $R = \frac{\nabla B}{|B|}$, can be estimated knowing that the injection process works at $\sim$ 250 MeV (Engelman et.al., 1971) from $\rho/R \leqslant 0.1$ in a 5γ magnetosheath field. Hence $R \geqslant 400\ R_E$. This picture fits the February 25th event, but must be rejected for the November 18th event, because there, according to the field connection, most of the intensity should have been seen over the southern polar cap. No such difference was observed. On the contrary, trajectory projections of the polar cap fluxes show that the northern tail lobe possibly had a higher intensity injected.

Transfer from interplanetary to tail field lines on the discontinuity model (Fig. 28) is demonstrated by considering an idealised rotational discontinuity for the interface. This

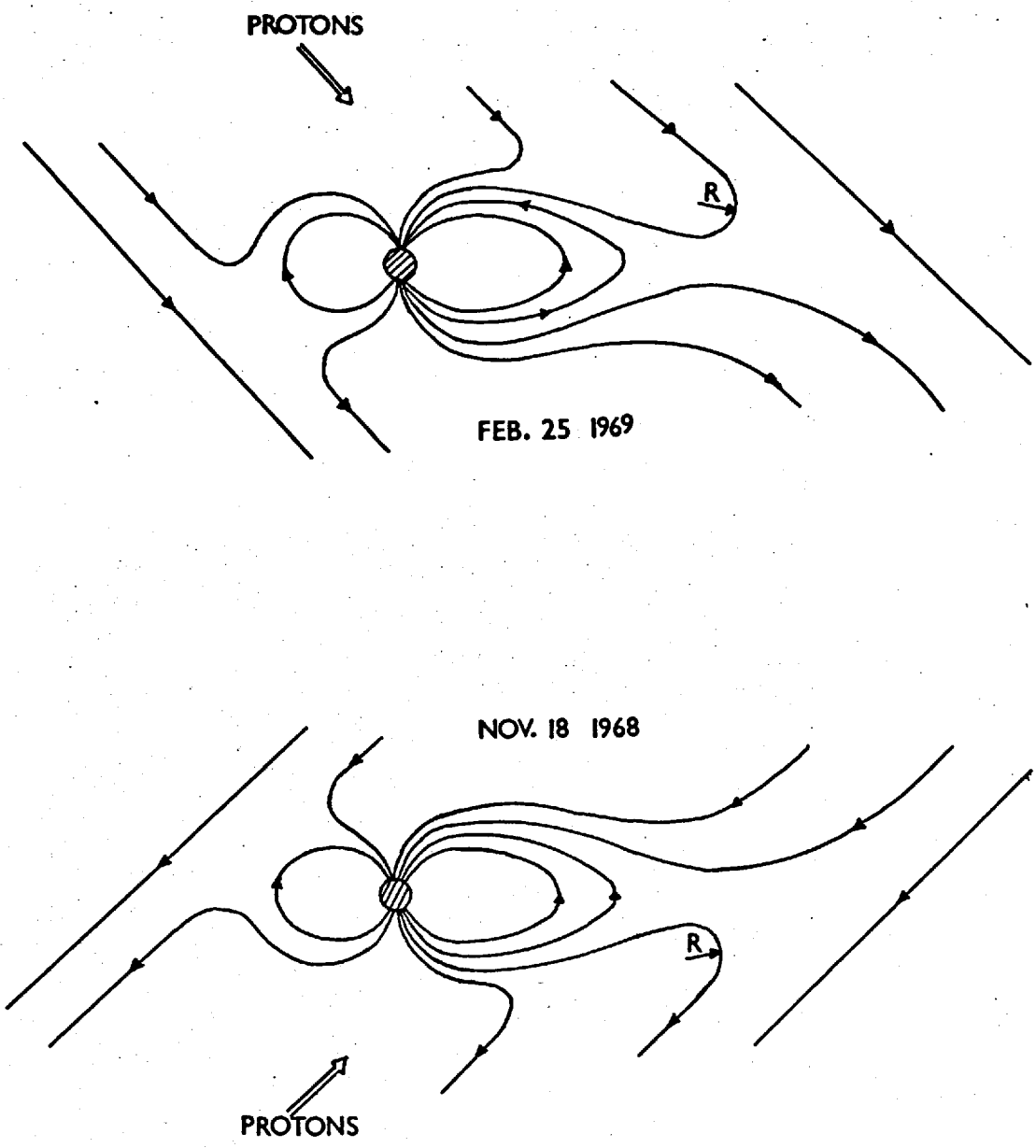

Fig. 27

Noon-midnight meridional cross-section of magnetic field conditions during November 18th and February 25th using the Dungey (1961) model of the magnetosphere. R is the typical radius of curvature of the magnetic field connected to the polar caps.

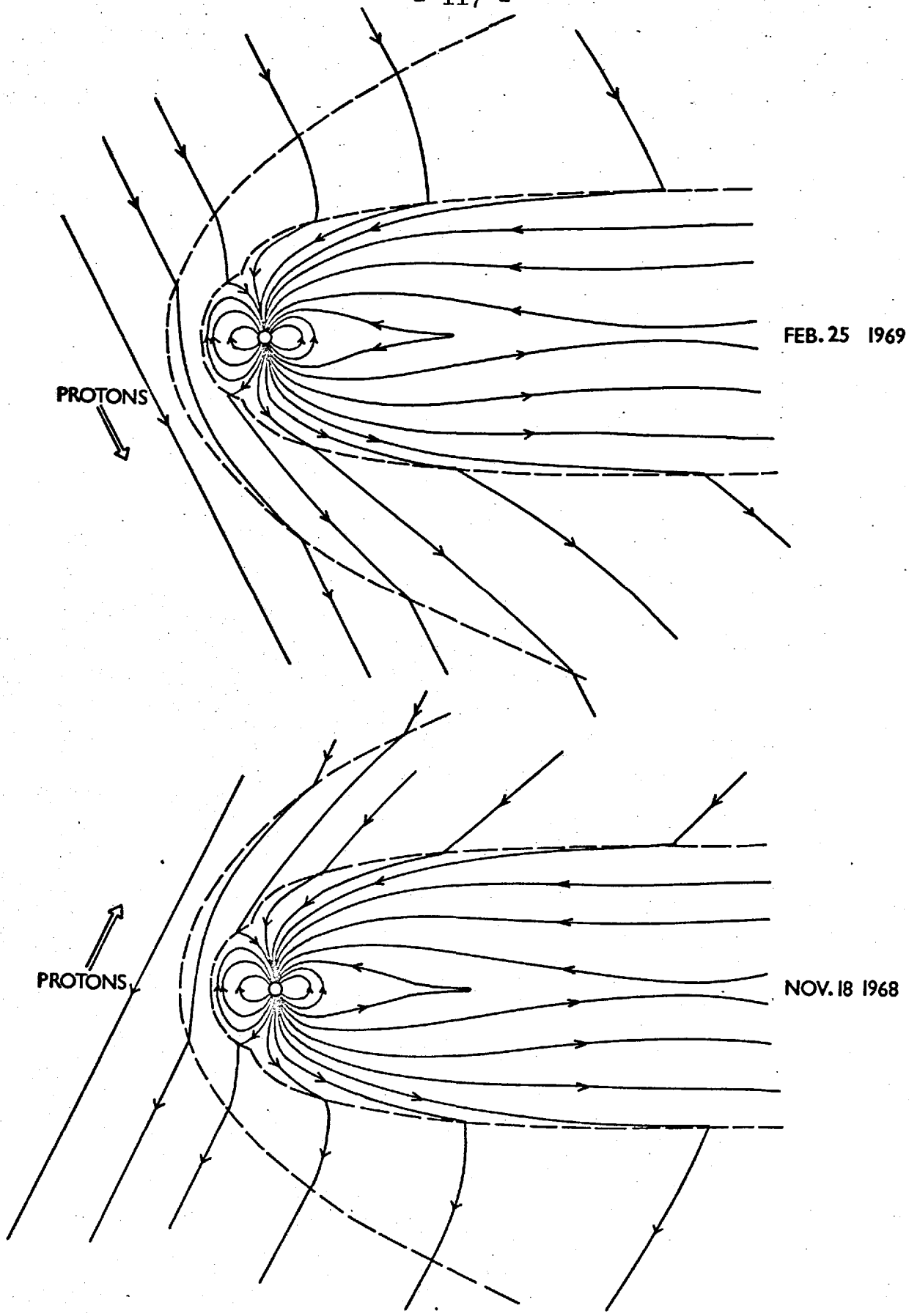

Fig. 28

Noon-midnight meridional cross-section of magnetic field conditions during November 18th and February 25th using the model of Axford and Dungey with a sharp transition of field lines across the magnetopause.

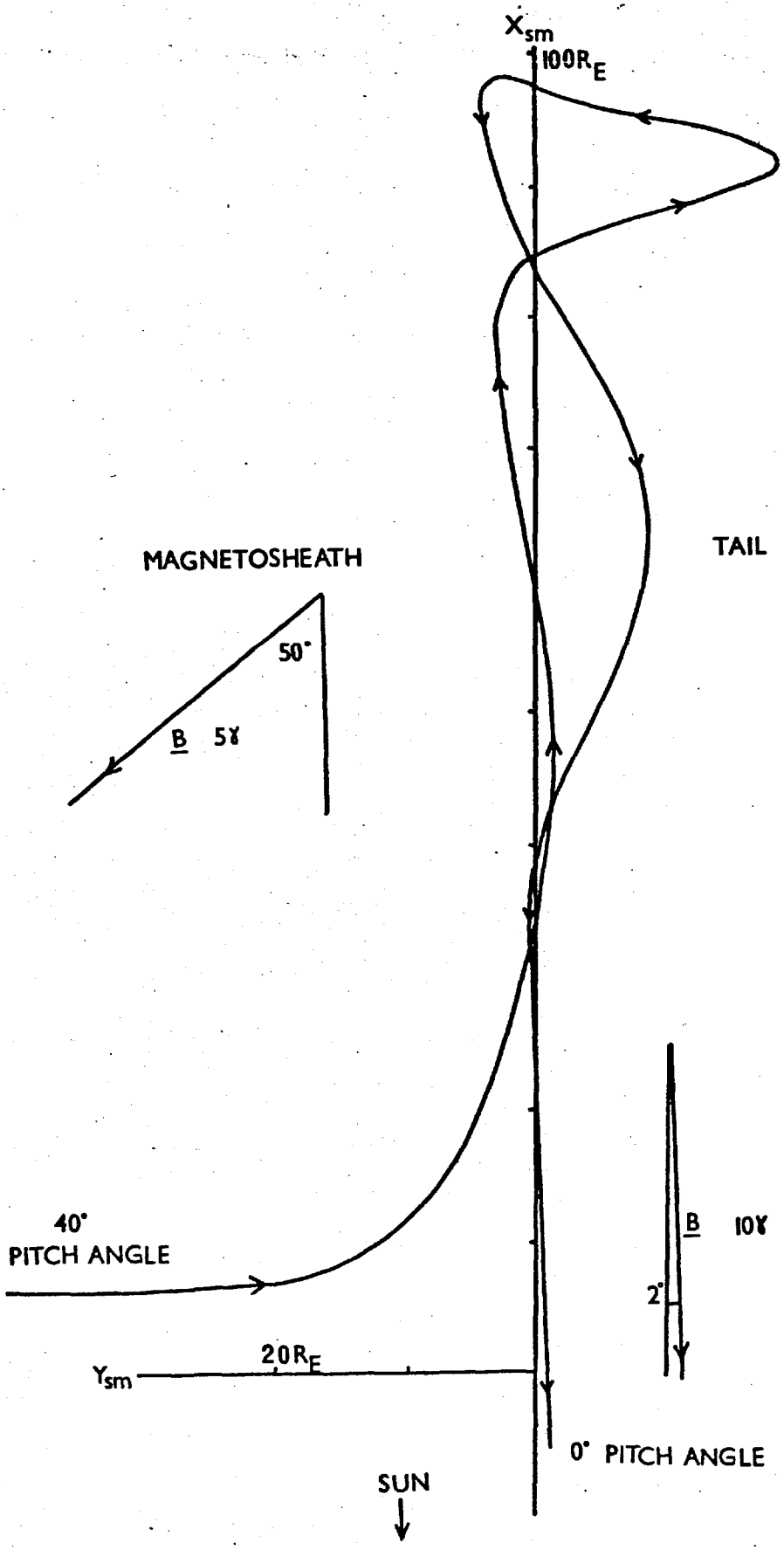

Fig. 29

Proton motion across a discontinuity for magnetic conditions similar to those of November 18th. Multiple discontinuity traversals produce large angle changes in particle velocity vector. Final pitch angle in the tail is 0° in this example.

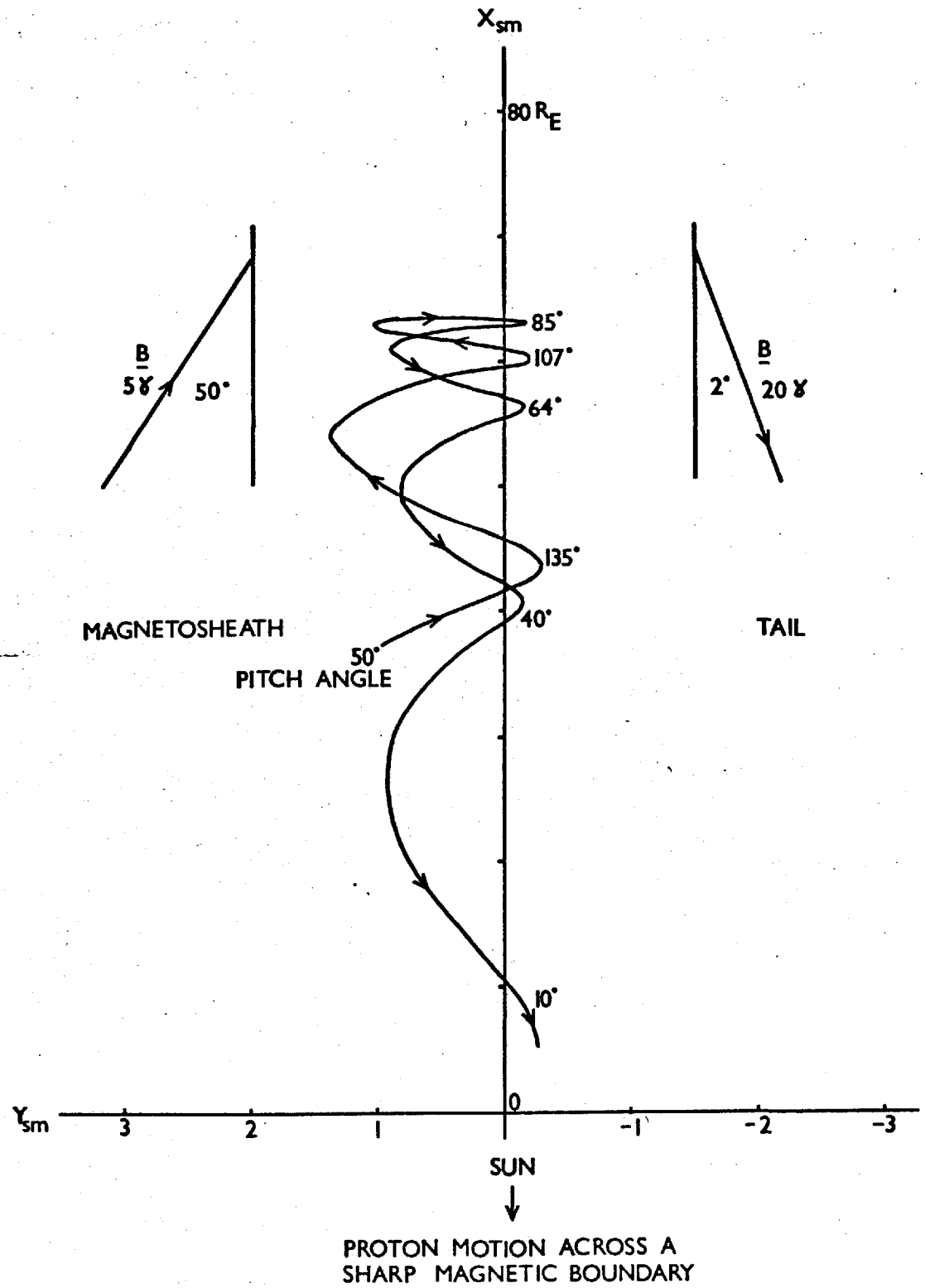

Fig. 30

Proton motion across a discontinuity for magnetic conditions similar to those of February 25th. Multiple magnetopause crossings almost reverse particle motion. Final pitch angle in the tail is 10^{o} in this example.

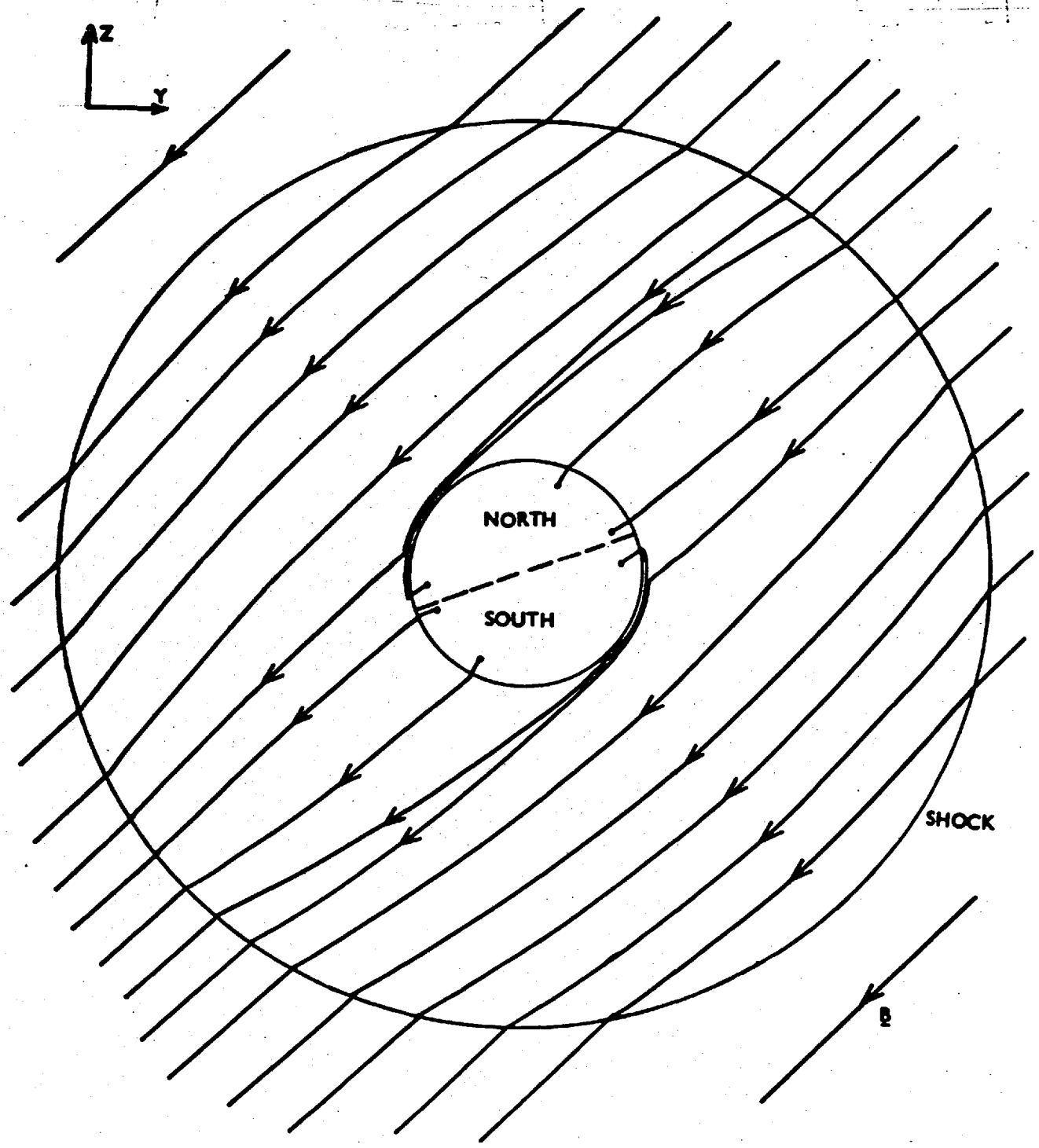

Fig. 31

Z_{sm} -Y_{sm} Cross section of magnetic field conditions in the magnetosheath for November 18th, showing the discontinuity at the magnetopause, field line reconnection and the negligible effect of a weak shock region at large distances away from the earth, as well as illustrating access for a discontinuity transfer process to both tail lobes.

is illustrated in Fig. 29, where a 2^{o} angle of the tail field (strength 10 γ) to the interface is taken together with magnetosheath values of 50^{o} and 5 γ. Note the discontinuity is of the more general type of Hudson (1970) implying a different pressure anisotropy on either side. Negative particle trajectories, leaving the earth have been integrated to demonstrate a $> 90^{o}$ angle change on transfer for cases where the fields are both nearly parallel and nearly antiparallel (Fig. 29 and 30). These results show that on November 18th particles from the sun could be turned around at the interface by more than 90^{o}. A sectional view (Fig. 31) indicates that both North and South tail lobes now become accessible, since field lines from the sun and coming up from a southerly direction touch both north and south tail lobes. This transfer process takes $\sim$100 to 200 R_E to complete for 100 MeV protons, and in general, the distance over which transfer is complete is proportional to the gyro-radius of the particle concerned. Note that this applies to particles with pitch angles less than $\sim 10^{o}$, i.e. particles which can go to low altitudes over the polar cap. Larger pitch angles can also become populated by intensities corresponding to near-maximum interplanetary values, but they cannot penetrate the magnetosphere to low altitudes.

Discussion of the transfer process has assumed that the turbulent layer in the magnetosheath, expected near the magnetopause where the supersonic flow is possibly slowed in a boundary layer, remains small compared to the solar particle Larmor radius. Assuming the usual analogy with hydrodynamics, an estimate of the layer thickness, L, is obtained by putting the magnetic Reynolds number R_m of the order unity

$$R_m \simeq 1 \simeq \frac{4\pi \sigma u L}{c^2} \qquad (5.3.1)$$

If the electric field is given by

$$E = - \underline{u} \times \underline{B} / c + \underline{j} \times \underline{B} / nec, \qquad (5.3.2)$$

the conductivity at low frequencies neglecting heavy ions is

$$w_p^2 / 4\pi(\Omega_e - w) \qquad (5.3.3)$$

and at high frequencies, neglecting electrons and allowing Hall current to dominate is

$$c^2 / 4\pi V_A^2 \left(1/w + 1/\Omega_p\right) \qquad (5.3.4)$$

at Alfven speed V_A, plasma frequency w_p and gyrofrequency Ω_e or Ω_p. In our situation, $V_A \doteq 50$ km/sec and $w_p^2 \doteq 100\Omega_e^2$ which makes the low frequency approximation the appropriate one to use. The conductivity, σ , is calculated as a weighted mean using the measured power spectra $P_\perp(w)$ of Mariani et.al. (1969) from

$$\bar{\sigma} = \frac{\int_{w_1}^{w_2} \sigma(w)\, P_\perp(w)\, dw}{\int_{w_1}^{w_2} P_\perp(w)\, dw} \qquad (5.3.5)$$

with $w_2 = \frac{1}{2}\Omega_e$ and $w_1 = (2\pi/\lambda)V_A$ at $\lambda \doteq 40\ R_E$ (the magneto-tail dimension). This yields $\bar{\sigma} \doteq w_p^2/4\pi\Omega_e$ if $P_\perp \propto 1/w^2$ and

$L \doteq 10$ km with $u \doteq 350$ km/sec.

This rough order of magnitude calculation shows that the effect of turbulence at the magnetopause can be neglected.

If the magnetopause boundary thickness, L_M, is proportional to the gyroradius of an ion in a 10 γ field, then for

$$T = 6 \times 10^3\ ^\circ K\ (\equiv\ 4\ eV) \quad L_M = 30\ km$$

$$T = 6 \times 10^4\ ^\circ K\ (\equiv\ 40\ eV) \quad L_M = 100\ km$$

so again this is not thought to be an important consideration for high energy solar protons.

The boundary layer of the magnetopause seems to get thinner down the tail (Mihalov et.al., 1970). Estimates at positions near the stagnation point of the magnetopause are of the order of 10^3 km, whereas at lunar distances the thickness is a factor of 10 thinner.

Some general comments can be made about the proton intensity distribution and energy dependence over the polar cap for this tail model :

1. The process works in a limited energy range, the lower limit being formed by the relationship between magnetopause irregularities and particle gyroradii, resulting in a low energy cut-off of about 1 MeV. Below this energy no information of the anisotropy is transmitted across the magnetopause. The upper limit is decided by the size of the tail in comparison with particle gyroradii and should occur at about 300 MeV.

2. There should be a particle intensity gradient across the tail, in the direction of the anisotropy at all energies below the upper cut-off.

5.3.2 Trajectories Which Cross the Neutral Sheet

For particle trajectories crossing the neutral sheet, the tail field was modified to take into account observations in that region.

Magnetic merging across the neutral sheet is allowed and the flux loss across the magnetopause is assumed not to contribute to the divergence of the tail field at distances less than 100 R_E where the present model is used.

A region of constant thickness, 8 R_E, either side of the neutral sheet was taken to represent the extent of the plasma sheet. In this region, we have depressed magnetic field strengths due to the diamagnetic effects of the plasma. The decrease of $|\underline{B}|$ with x (in solar magnetospheric co-ordinates) in this plasmasheet region is due to field merging across the neutral sheet.

Outside this region, divergence of the tail, which results in an elliptic cross section, with the major axis along the solar magnetospheric z direction, again causes $|\underline{B}|$ to decrease with distance down the tail. We have assumed that B_x is a separable function of x and z, of the form

$$B_x = B_o x^{-n} . f(z) \qquad (5.3.6)$$

and for simplicity,

$$B_y = 0$$

Conservation of magnetic flux gives B_z at z=0, i.e. the neutral sheet.

$$B_z\ (z=0)\ .\ l\ dx = l\ z_c \eta\ B_o x^{-n}(-\tfrac{n}{x})\ dx \qquad (5.3.7)$$

where l = tail diameter along the neutral sheet

z_c = extent of plasma sheet in the z direction

$$\eta = \overline{f(z)} = \frac{1}{z_c} \int_o^{z_c} f(z)\ dz$$

a rectangular approximation to the plasma sheet cross section has been employed.

This gives $B_z\ (z=0) = - z_c \eta\ B_o x^{-n} \frac{n}{x}$

At other values of z, we assume that B_z is given by

$$B_z(z) = B_z\ (z=0)\ .\ g(z)$$

where $g(z) = 1$ at $z = 0$

Using div $\underline{B} = 0$, gives the relation

$$f(z) = z_c \eta\ g^1(z) \qquad (5.3.8)$$

A general solution for f(z) is of the form :

$$f(z) = - \sum_{k=1}^{\infty} \sin \left(\frac{k\pi}{2} \frac{z}{z_c}\right) \qquad (5.3.9)$$

In this work the simplest solution was used,

$$f(z) = - \sin \left(\frac{\pi}{2} \frac{z}{z_c}\right)$$

Hence

$$B_x = - B_o x^{-n} \sin \left(\frac{\pi}{2} \frac{z}{z_c}\right)$$

$$B_y = 0$$

$$B_z = \frac{2z_c}{\pi} B_o x^{-n} \frac{n}{x} \cos \left(\frac{\pi}{2} \frac{z}{z_c}\right)$$

At values for $z > z_c$ we use

$$B_x = - B_o x^{-n}$$

Then div $\underline{B} = 0$ requires that

$$B_z \ (z > z_c) = - n B_o \frac{x^{-n}}{x} (z - z_c) \qquad (5.3.10)$$

Hence the tail field diverges.

We can find the equation of the magnetopause at $y = 0$ (i.e. the semi major axis) from

$$\frac{\partial z}{\partial x} = \frac{B_z}{B_x} = n(z - z_c)/x$$

This gives

$$\left(\frac{x}{x_o}\right)^n = \frac{z - z_c}{z_o - z_c} \qquad (5.3.11)$$

Values for x_o, z_o and z_c are 20 R_E, 20 R_E and 8 R_E respectively. n, the exponent in $B_x = B_o x^{-n}$ has been determined experimentally to be 0.3. Using these values we can calculate z, the semi major axis of the tail cross section, at lunar distances of ~ 60 R_E. This gives $z \simeq 28.7$ R_E, which is in agreement with observations (Behannon, 1970).

The results from these integrations across the neutral sheet may be summarised as follows :

1. Proton trajectories, integrated backwards from the earth and crossing the neutral sheet, finish up on the dawn side of the magnetopause.

2. The length of the trajectory in the tail is usually less than 100 earth radii for small initial pitch angles, i.e. the protons must have entered the tail where it is still well defined.

3. During successive neutral sheet crossings, the proton pitch angle increases by approximately

$$\Delta\alpha \simeq 2 \tan^{-1} (B_{z_o} + B_{z_o}(\text{dipole}))/B_x(z > z_c)$$

$$2 \tan^{-1} \left(\frac{2 z_c n}{\pi x} + \frac{0.31}{B_o x^{3-n}} \times 10^5 \right) \quad (5.3.12)$$

where B_z and B_x are the magnetic field components defined earlier. Pitch angles are indicated in Fig. 32, which shows such a trajectory.

4. If neutral sheet crossings occur often enough, for example particle trajectories starting near the dusk side of the tail, particles are turned round as their pitch angles increase, and are seen to enter the magneto-tail from a direction close to the Parker spiral field direction, which in most instances also corresponds to the maximum of an interplanetary pitch angle distribution (see Fig. 32). This process is effective for energies up to ~90 MeV.

5. If there is only one neutral sheet crossing, or two, - corresponding to trajectories starting near the dawn side of the tail - the particle trajectory has not 'bent' sufficiently to correspond to particle access from the direction of the interplanetary intensity maximum, and hence some intensity intermediate to the maximum and minimum in interplanetary space will be observed.

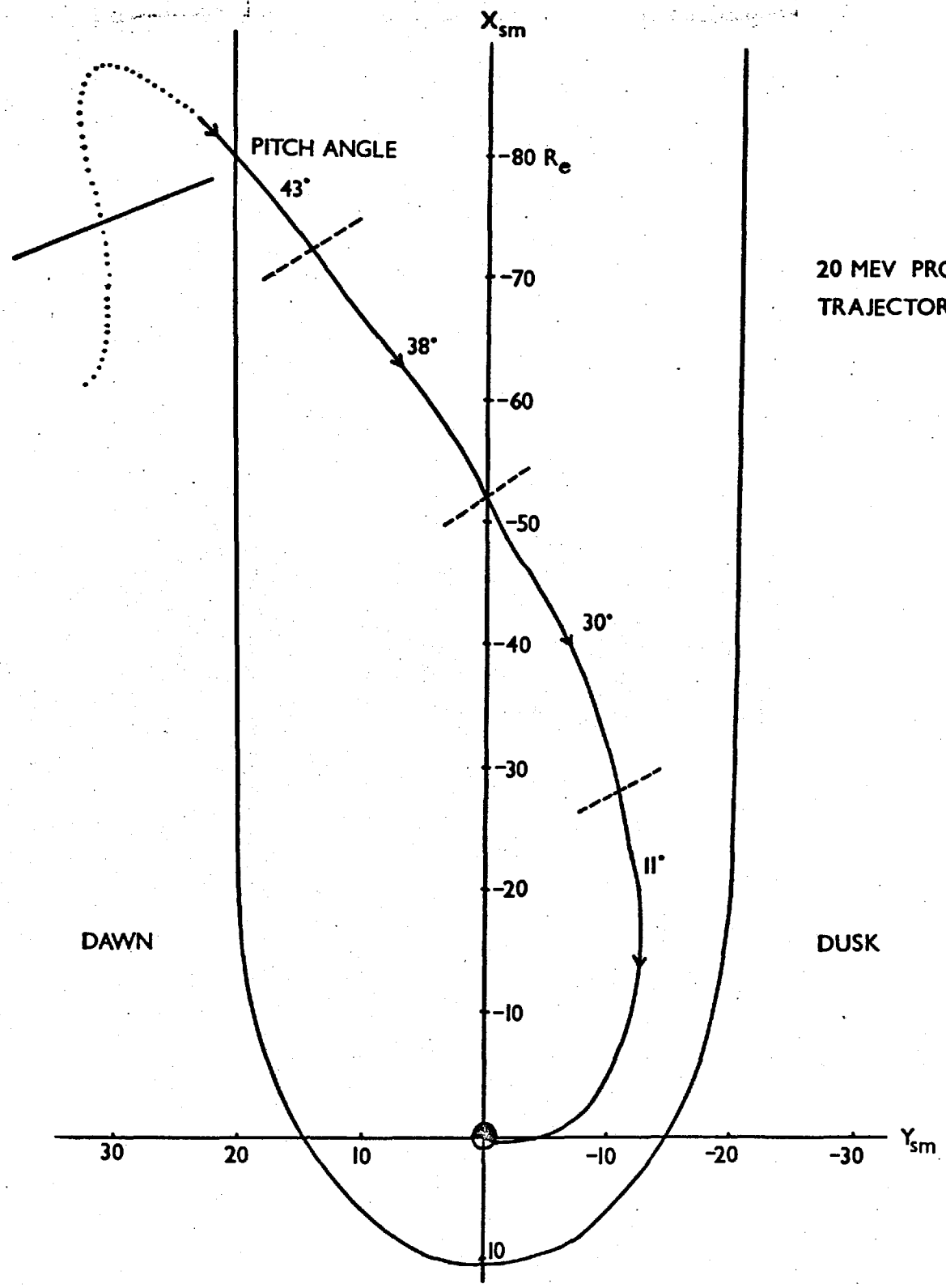

Fig. 32

20 MeV proton trajectory with multiple neutral sheet crossings, showing the change in particle pitch angle after each crossing, and the bending of the particle trajectory which produces access to the dusk auroral zone from the Parker spiral direction.

6. There is significant dispersion in the trajectories for low energy protons starting from the same point in the tail with different pitch angles. Trajectories with large inital pitch angles reach the magnetopause nearer the earth than those with small initial pitch angles (Fig. 33).

Applied to observations made by satellite detectors, these results give the following conclusions :

(a) During the February 25th flare (section 5.7) auroral zone intensity enhancement on the dusk side at high energies (> 90 MeV) are easily explained by impact zones which connect to the Parker spiral direction. Trajectory calculations for lower energies have shown fine structure, with some going down the tail close to the neutral sheet, and others crossing the magnetopause at dawn, similar to the higher energy trajectories from the dusk side. However, no correlated fine structure is seen in the auroral zone peaks. It is suggested that a more realistic tail field model than the Williams and Mead plane infinite current sheet smoothes out any rapid irregular variation of asymptotic longitude. This conclusion has been shown here, by the trajectory calculations starting near the dusk magnetopause in a realistic tail field, to be correct.

(b) During the November 18th flare, it was found that the structure over the polar cap is typically three-peaked at high energies, for a dawn-dusk orbiting polar satellite (section 5.8). Similar structure is indicated for the February 25th event, although complete polar passes are not available here. (Figs. 24b and 25b)

The low proton intensity observed over the polar cap at latitudes intermediate to the dawn auroral zone peak and the high latitude peak can be explained by the trajectory integrations calculated here, when only one, or at mosttwo, neutral sheet crossings take place, and the trajectory has not curved sufficiently to correspond to proton entry from the Parker spiral direction.

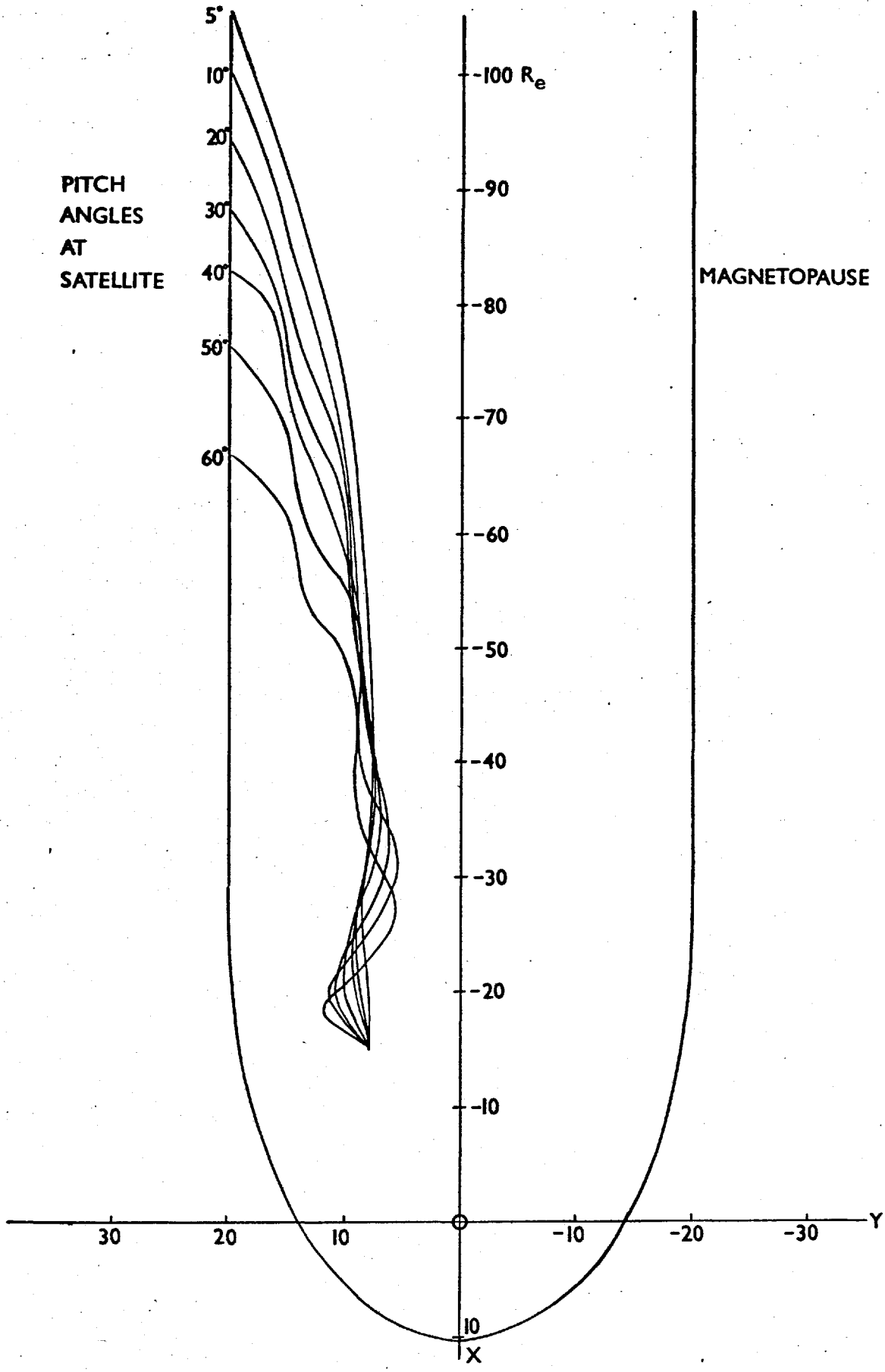

Fig. 33

Dispersion of low energy proton trajectories, in a realistic tail field model, for the Vela 4A position at 14.30 U.T. during the September 18th 1967 flare. Dispersion is due to pitch angle variation and the multiple neutral sheet crossings involved.

(c) Time delays of different duration for proton entry into the tail can be explained if the satellite positions in the tail are close to the neutral sheet, but at different distances from it. Some smoothing of an interplanetary particle intensity change is also predicted due to the dispersion of proton trajectories of different initial pitch angles. This will be treated more fully in section 5.4.2.

5.3.3. Structure for Energies Close to 1Mev

At low energies (few MeV) magnetopause irregularities, whether they are due to Kelvin Helmholtz instabilities (Southwood, 1968; Mihalov et.al., 1970) or convection in the magnetosheath of magnetic fluctuations, excited at the bow shock near the sun-earth line (McKenzie and Westphal, 1968), will tend to smooth out any anisotropies that may exist in interplanetary space and in the magnetosheath some distance away from the magnetopause. Montgomery and Singer (1969) observed a drastic reduction in the size of the anisotropy at distances $< 1\ R_E$ from the magnetopause for 1 MeV protons while the detector was still in the magnetosheath. We can use the power spectra calculated by Mariani et.al. (1969) in the magnetosheath to estimate the mean free path of particles. They find an exponentially decreasing power density in the magnetosheath as the distance from the magnetopause increases. They fit a curve

$$P_\perp = P_{\perp_o}\, e^{-(y-y_o)/\rho} \qquad (5.3.13)$$

to their data, where the chief contribution to $P_\perp$ is the component of power spectral density in the solar ecliptic z direction, y is the solar ecliptic distance along the y-axis, the subscripts o refer to the point at the magnetopause, and ρ is the scale length of the exponential decrease in power. Their value for ρ was 24 R_E for the frequency corresponding to 130 MeV protons, and 35 R_E for 1 MeV protons. These results give scattering mean free paths in the magnetosheath of $\sim 50\ R_E$ and $\sim 1000\ R_E$ for 1 MeV and 130 MeV protons respectively, much too long to explain the results of Montgomery and Singer. It seems more likely then, that the magnetopause effects observed are caused by the sudden change of magnetosheath to

magneto-tail field regimes, and the effect of this discontinuity on the particle distribution, bearing in mind that the magnetopause surface is always distorted with waves of amplitudes similar to the Larmor radii of a few MeV protons (Mihalov, 1969). For low energy protons, therefore, the magnetopause can distort the incoming particle distribution in a random, incoherent manner - leading to a near isotropic distribution at the magnetopause, whereas for high energy protons, the overall field configuration will produce coherent refraction and reflection of an incoming proton beam. For very high proton energies, the Larmor radius is greater than the tail diameter, and in this case the presence of the tail will not disturb the particle pitch angle distribution very much. The tail then acts as a small angle scattering centre.

In spite of any observed isotropisation of low energy protons at the magnetopause, an anisotropy can lead to tail structure. By following reconnected field lines or by a scattering or discontinuity transfer process, particles will preferentially populate the side of the tail onto which the maximum of the interplanetary pitch angle distribution impinges. Since the Larmor radius for 1 MeV protons is small, a gradient across the tail should result. During the November 18th flare, anisotropies of 100% amplitude, lasting for long periods (Van Allen et.al., 1969), occur at 1 MeV and are capable of explaining similar amplitude structure over the polar caps provided these can be shown to be due to a gradient across the tail.

5.3.4 Losses during Longitude Drift in the Pseudotrapping Region

Access to the neutral sheet has already been described. As a result of the easy access to the polar cap via the neutral sheet from the near earth magnetopause, regions near the last closed field line and in the pseudotrapping regime (which connect via their particle trajectories to near the neutral sheet), are expected to have similar particle intensities. Especially when local particle intensity gradients have convected past the earth, large intensity differences

are expected between high latitudes and the pseudotrapping regions. The intensity in the pseudotrapping region can be reduced by scattering into the atmospheric loss cone during the eastward drift of the particles. The amount of scattering depends on the length of the trajectory of the particles, and on the scattering strength at the particle positions. In general, if a particle undergoes many bounces, its trajectory is longer and loss is more likely. This effect should, therefore, be energy dependent, with high energy protons becoming affected at lower invariant latitudes than low energy protons.

Simultaneous observation of particle intensities at different magnetic local times on the same drift shell in the pseudo-trapping or stable trapping regions provides information on the strength of the scattering processes acting on the particle distribution which is drifting eastward around the earth. The stable trapping region is defined for these purposes as all latitudes below the outer belt 1 MeV electron boundary.

When scattering is weak, the atmospheric loss cone remains empty after a few bounces, and low altitude detectors will then see a greatly reduced particle flux. When scattering is strong, the atmospheric loss cone is filled up in between each bounce, hence this corresponds to the fastest particle loss rate. Also, the equatorial pitch angle distribution is isotropic. If particle motion is adiabatic, and the magnetic field is dipolar, the size of the atmospheric loss cone at the equator is roughly $\frac{\pi}{L^3}$ steradian. L is the distance between the field line concerned and the geocentre in the equatorial plane. The longitudinal drift per bounce is

$$\Delta \phi = 0.1285 \sqrt{E} \quad L^2 \text{ degrees}$$

where E is the particle energy in MeV.

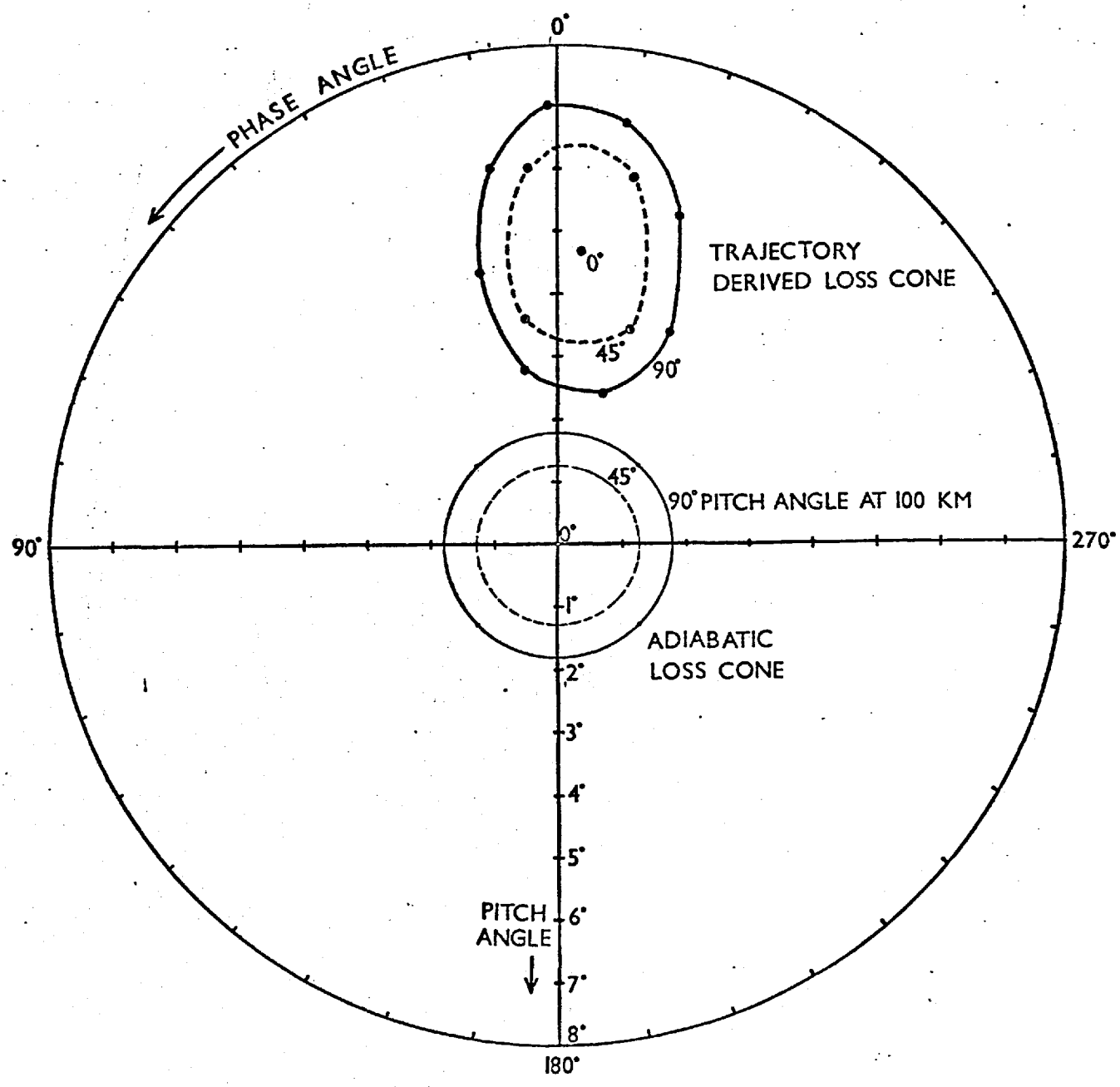

Fig. 34

Polar diagram of pitch angle v. phase angle (obtained from trajectory integrations) in the equatorial plane, for particles entering the atmosphere. Comparison with adiabatic loss cone shows that a static field model can produce results equivalent to strong pitch angle scattering, when particle motion is nonadiabatic.

The total loss of particle flux during a drift ϕ is :

$$\frac{\phi}{\Delta\phi} \cdot \frac{\pi}{L^3} \cdot \frac{1}{4\pi} \simeq \frac{\phi}{0.51\sqrt{E}} \cdot \frac{1}{L^5}$$

e.g. for 180° drift and 1 MeV protons at L=10, the fraction of the particle flux lost to the atmosphere is approximately 3.5×10^{-3} of the total omnidirectional flux at the equator. Hence low altitude satellites will observe an almost constant intensity at all local times along the same drift shell.

However, there is an effect which produces the same result as strong pitch angle scattering, even if there is very little scattering. In a magnetosphere distorted by the flow of the solar wind, particle motion is nonadiabatic, especially in the pseudotrapping region near the last closed field line. This means that the atmospheric loss cone, when projected into the equatorial plane via trajectory integrations, does not coincide with the equatorial loss cone calculated from adiabatic particle motion. If, for any trajectory integrated backwards from the earth to the equator

$$\left|\alpha_{\text{nonadiabatic}} - \alpha_{\text{adiabatic}}\right| > \frac{1}{\sqrt{L^3}} \simeq \sqrt{\frac{B_{\text{equator}}}{B \text{ at } 1\ R_E}}$$

the nonadiabatic loss cone fluctuates so much that the net result is the same as strong pitch angle scattering.

Fig. 34 shows a diagram in polar co-ordinates of the adiabatic and nonadiabatic equatorial loss cones. The radial co-ordinate is pitch angle at the equator, the azimuthal co-ordinate is phase angle. This effect must be borne in mind when drawing conclusions from low altitude solar proton data.

5.3.5 Guide to Future Work

As an aid to future work, figures 35a and 36a show on a latitude-longitude plot the position of a particle trajectory at the magnetopause or in the tail at a radial distance of 25 R_E. The initial invariant latitude and magnetic local time (0° = midnight) are indicated, and the particle is incident vertically at the earth. Fig. 35a is for 125 MeV

protons, figure 36a for 44 MeV protons. As the proton energy increases, the constant invariant latitude lines tend to be more horizontal, with uniform magnetic local time variation along the line. Also shown are the corresponding regions over the polar cap connected via trajectories to the tail and the solar and antisolar spiral field direction (figures 35b and 36b). The structure in the pseudotrapping region is only coarsely indicated. The width in longitude of different regions is proportional to the longitudinal drift per bounce.

Assuming an anisotropy in the Archimedes spiral direction, regions I, II and III should correspond to peaks and regions IV, V and VI to troughs.

Fig. 37a is a plot of field lines integrated from the polar cap to 15 R_E in the tail. Electrons or very low energy protons should follow trajectories similar to the field lines. Fig. 37b is a latitude-longitude plot of the position of 3.4 MeV proton trajectories either at the magneto-pause or at 15 R_E in the tail. The asymmetry is due to the azimuthal drift of these protons and indicates the breakdown of the method of tracing trajectories just using field lines. On the dusk side, the drift takes the proton trajectories deeper into the tail, on the dawn side the proton trajectories move closer to the last closed field line, i.e. closer to the neutral sheet or the dawn magnetopause. Fig. 37c shows the different polar cap regions arising from these trajectory calculations.

Calculations for Figs. 35 to 37 were performed for the perpendicular dipole Williams and Mead field model to illustrate basic effects of anisotropies. The dipole tilt (especially in the plane perpendicular to the earth-sun line) can change the position of these boundaries just as if the interplanetary anisotropy had changed in direction by the amount of the tilt angle. A more accurate field model as described earlier (section 2), with the earth tilted, gives a better correlation. Care must be taken, however, that the model is only used for small tilt angles ($<15^{\circ}$) and that the trajectories concerned do not get too close to the neutral points. The region where the model is expected to be most accurate is the night side

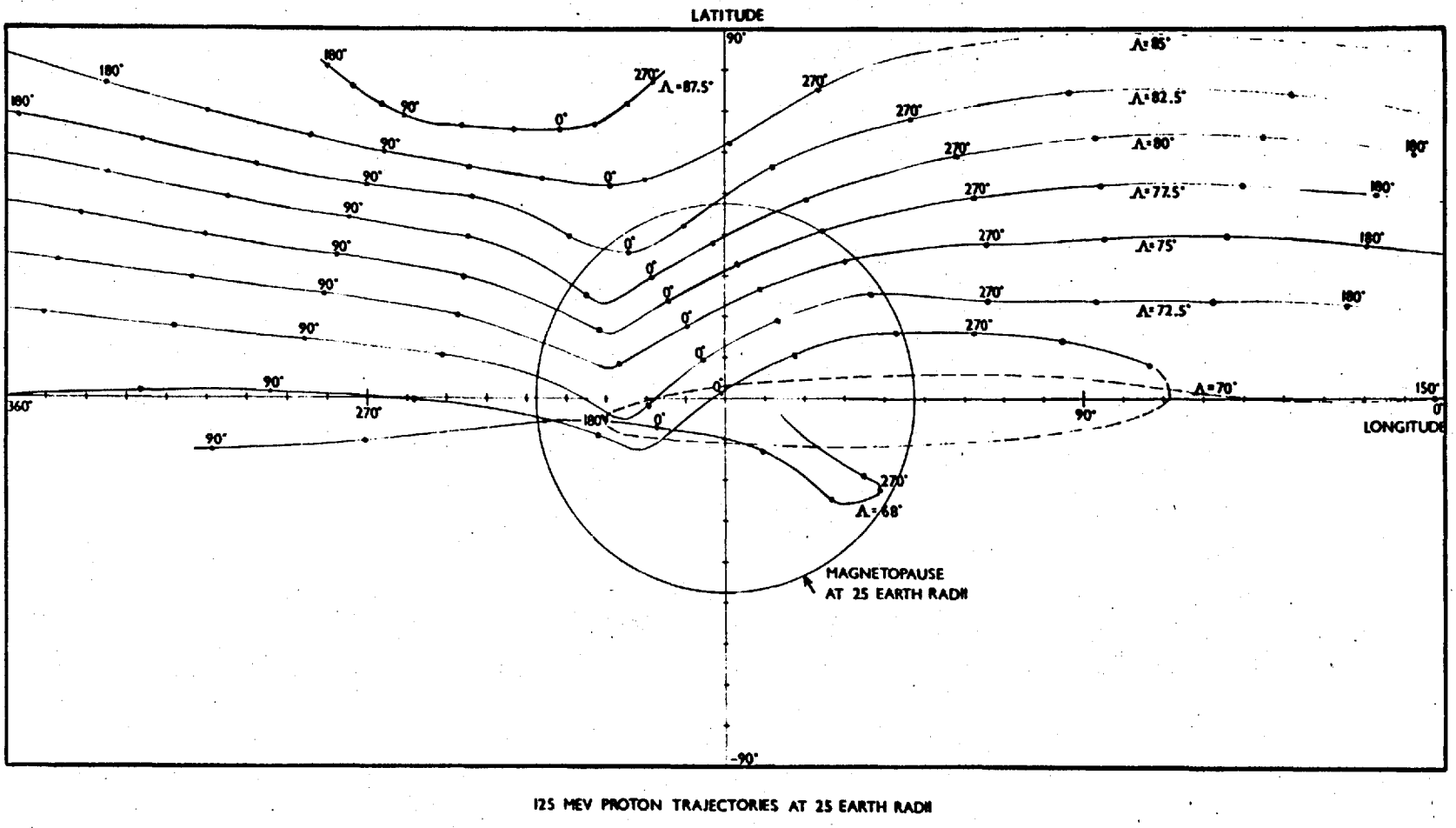

Fig. 35a

Magnetopause entry diagram for the northern polar cap for 125 MeV protons, derived from trajectory calculations. Particle position (latitude, longitude in solar magnetospheric co-ordinates) is shown for trajectories integrated backwards from the earth at 100 km altitude, with 0^{o} pitch angle at the starting point. The starting point is given in terms of invariant latitude, and magnetic local time longitude (0^{o} = midnight). These curves are useful for altitudes up to $\sim 4\ R_E$ where the adiabatic approximation to the particle motion breaks down. Particle position is given either when the magnetopause is crossed, or when the trajectory exceeds 25 R_E in the tail.

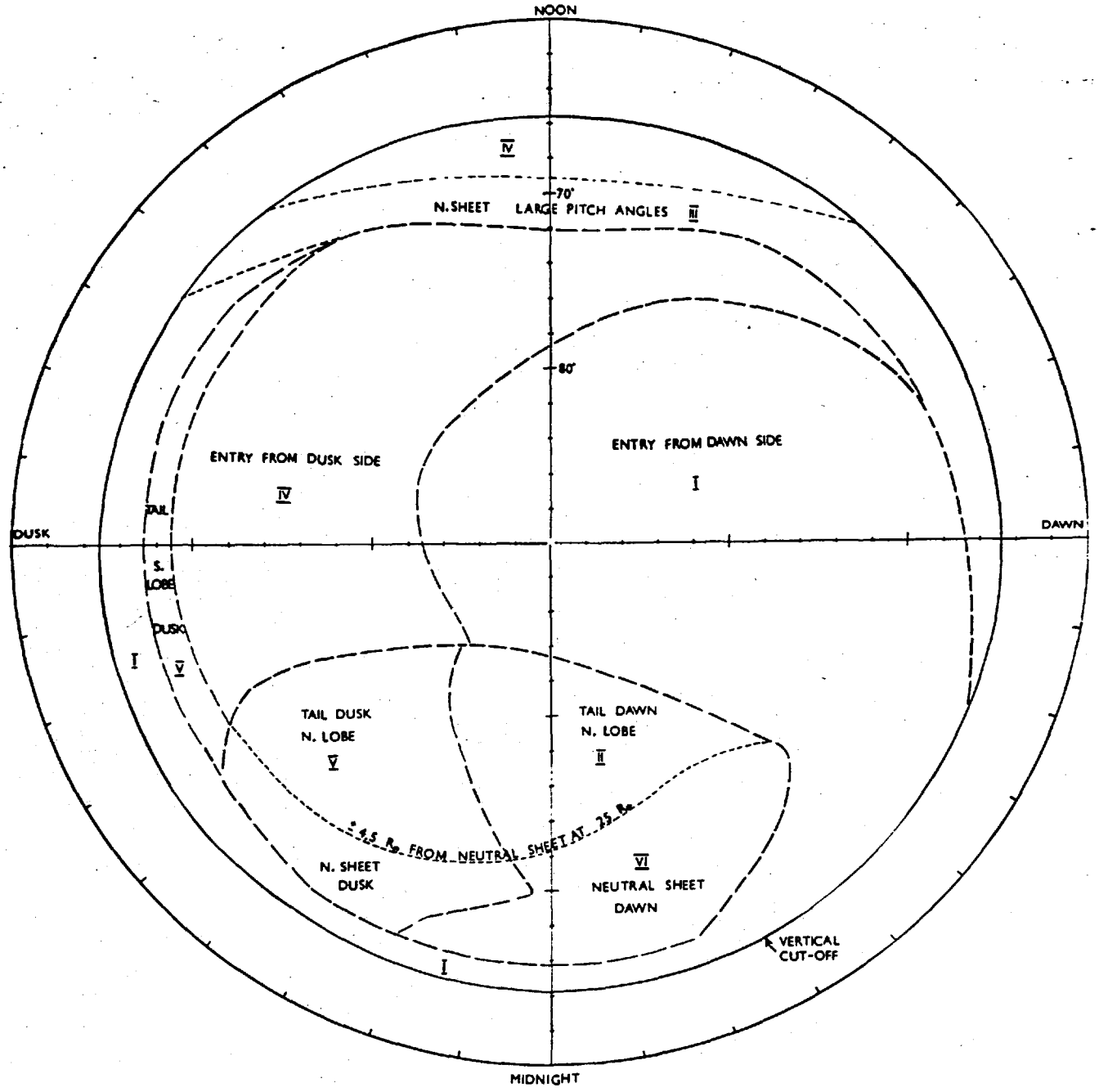

EXPECTED STRUCTURE OVER THE NORTHERN POLAR CAP FOR 125 MEV PROTONS

INV. LATITUDE V. MAG. LOC. TIME

Fig. 35b

Polar cap intensity structure expected for an interplanetary anisotropy along the Parker spiral direction for 125 MeV protons. Maxima in structure are expected to be produced by direct impact zone effects and by discontinuity transfer at large distances down the tail.

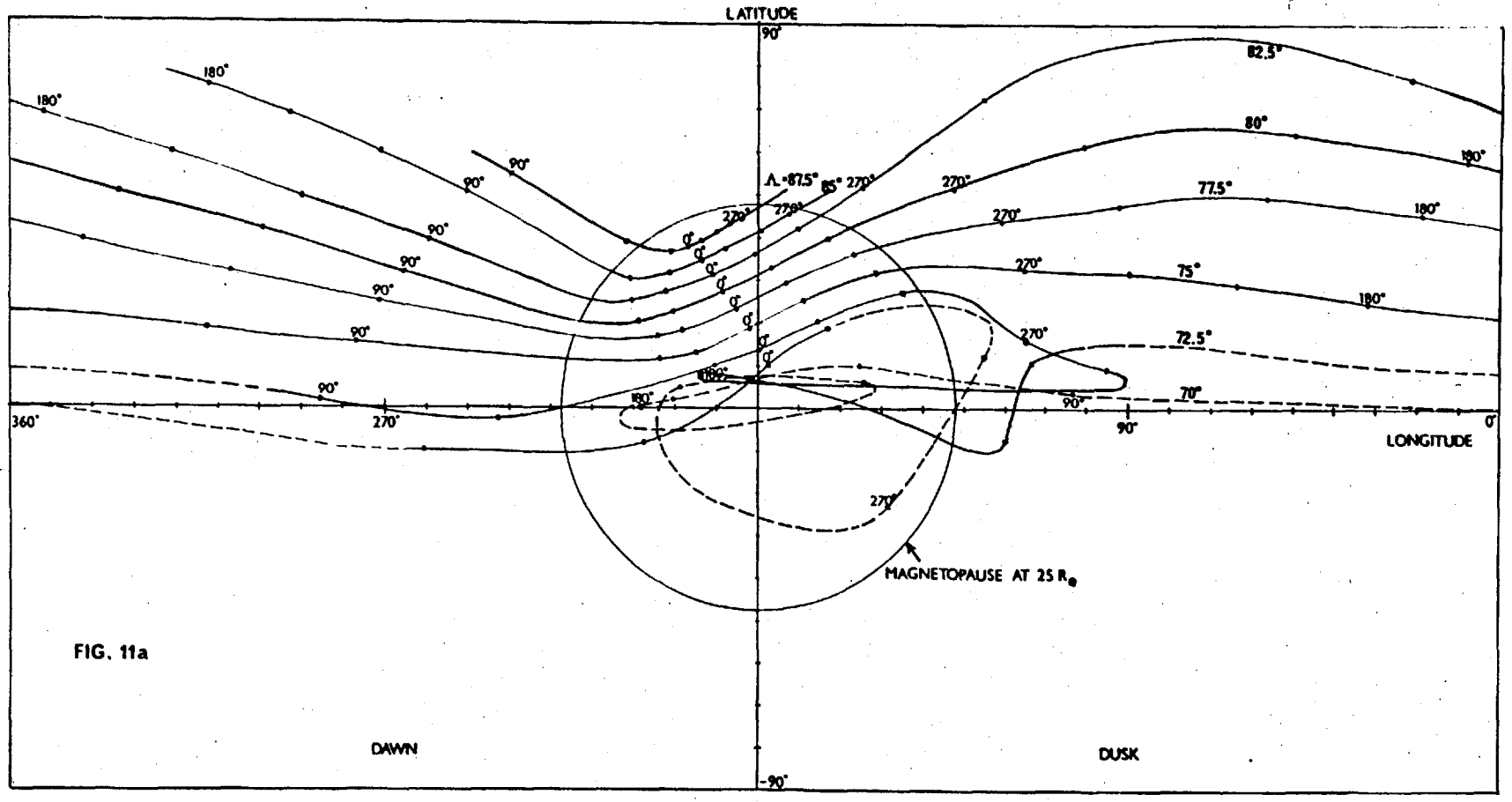

44 MEV PROTON TRAJECTORIES AT 25 $R_\oplus$

40 GAMMA TAIL FIELD

Fig. 36a

Magnetopause entry diagram for the northern polar cap for 44 MeV protons derived from trajectory calculations.

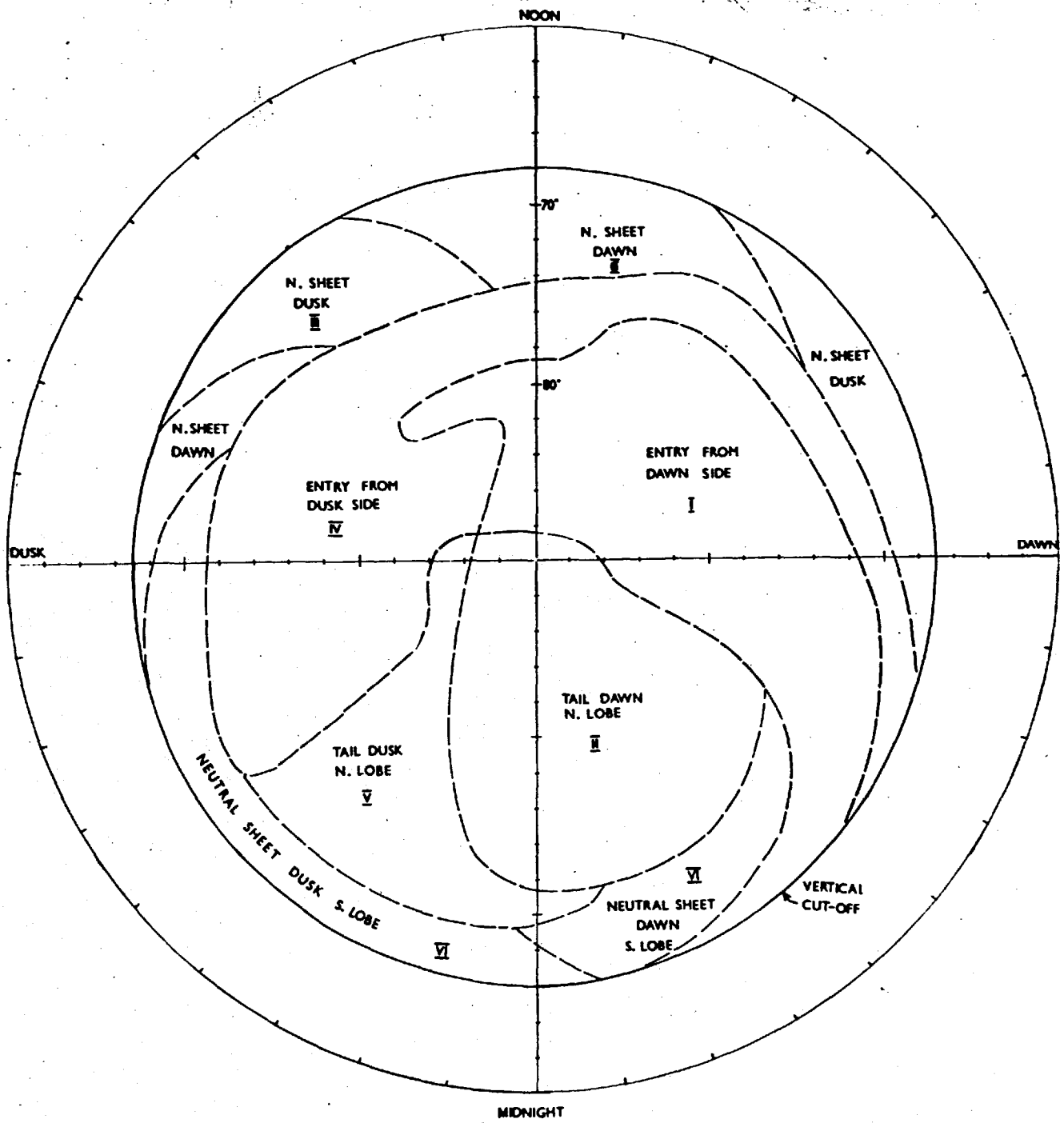

Fig. 36b

Polar cap intensity structure expected for an interplanetary anisotropy directed along the Parker spiral direction for 44 MeV protons.

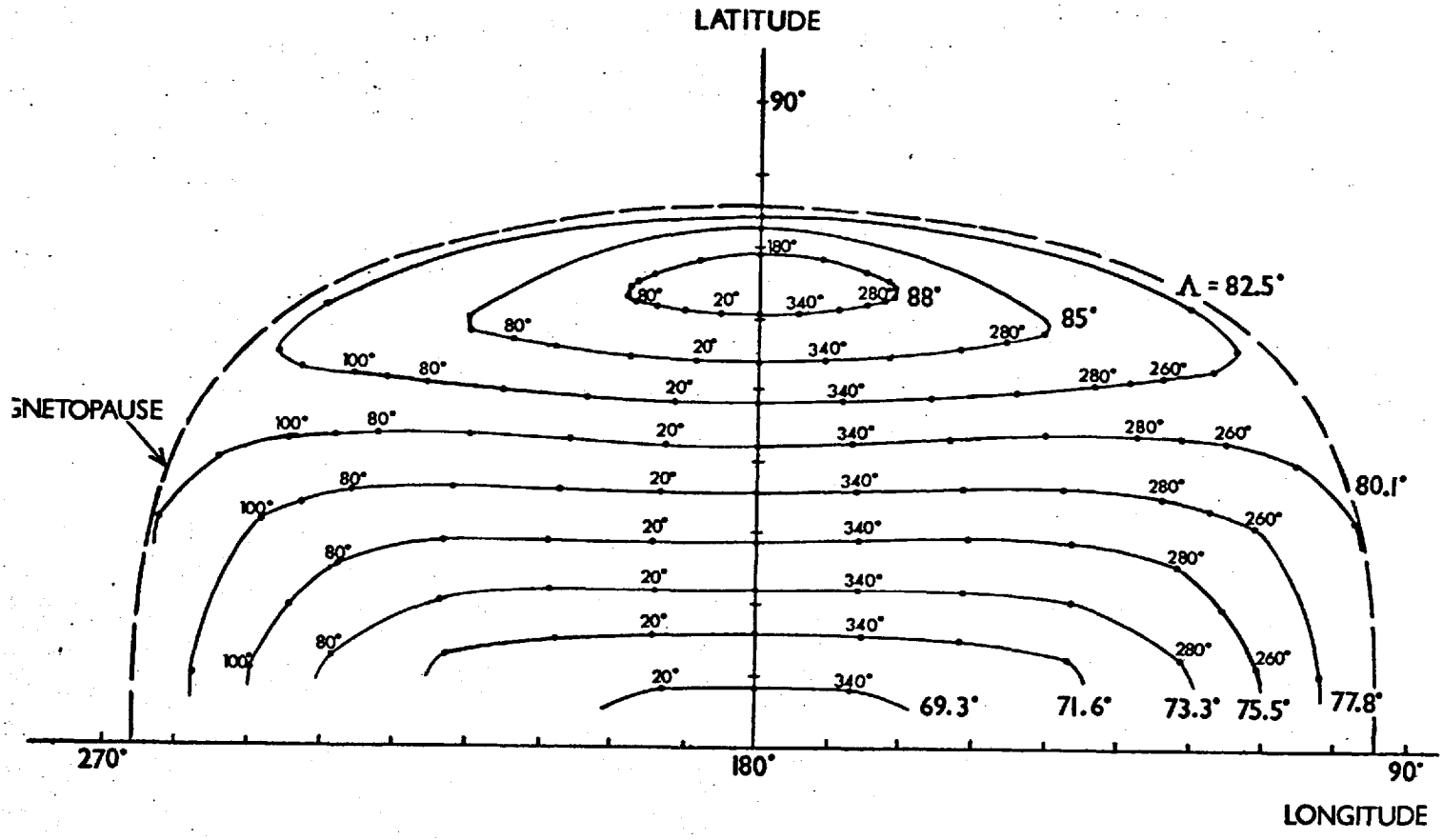

FIELD LINES MAPPED IN THE TAIL AT 15 R_e

40 GAMMA TAIL FIELD

Fig. 37a

Result of field line integration out to 15 R_E in the magnetotail. Positions of field lines at 15 R_E are given (latitude, longitude in solar magnetospheric co-ordinates) for various invariant latitudes and magnetic local time longitudes. Very low energy particles follow field lines closely, so that this diagram can be used to calculate intensity distributions in the geomagnetic tail, or to map equal flux contours (from the magnetopause or neutral sheet) back over the polar cap. Since the centre of the tail lobe corresponds to an invariant latitude of $\sim 78.5^{\circ}$ at local midnight, better ordering of data is expected if a new co-ordinate system, based on equal flux from the magnetopause and neutral sheet, is used. This can be done for different tail field strengths so that the co-ordinates are useful at all times.

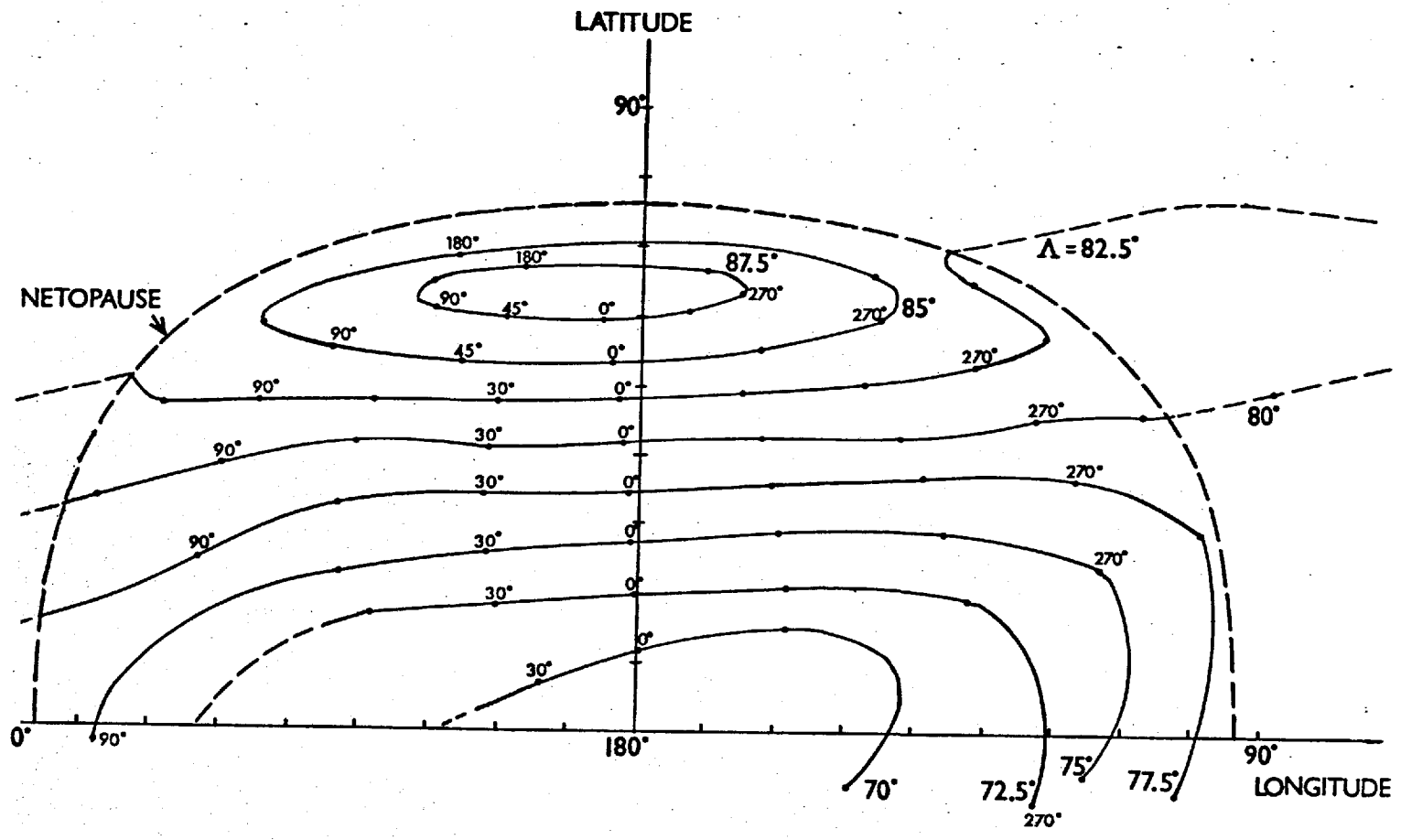

3.4 MEV PROTON TRAJECTORIES AT 15 R_e

40 GAMMA TAIL FIELD

Fig. 37b

Magnetopause entry diagram for the northern polar cap for 3.4 MeV protons derived from trajectory calculations. Except for trajectories near the last closed field line, and the longitudinal drift at high invariant latitudes, this diagram is similar to Fig. 37a. The position of the magnetopause at 15 R_E was taken from Mead (1964).

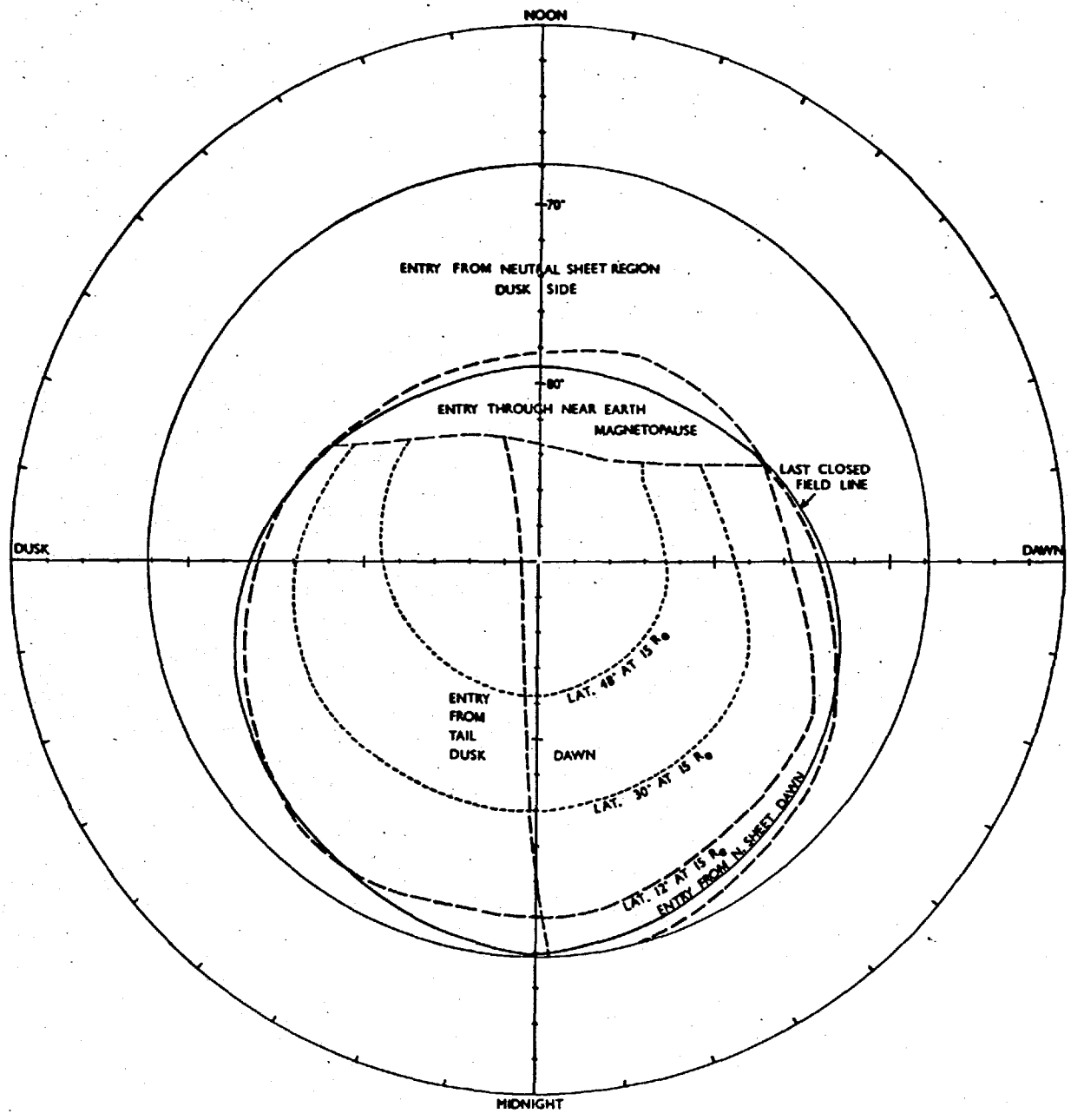

ACCESS REGIONS OVER THE N.-POLAR CAP FOR 3.4 MEV PROTONS
INV. LATITUDE V. MAG. LOC. TIME

Fig. 37c

Access regions over the northern polar cap for 3.4 MeV protons showing entry through magnetopause, from the tail and from the neutral sheet regions.

(see Fig. 23). For the November 18th and February 25th flares, the model was used in this way, and correlation of polar cap features with the interplanetary anisotropy was exceptionally clear. This is shown in sections 5.7 and 5.8.

5.4 STRUCTURE CAUSED BY GRADIENTS

Gradients exist in the solar proton interplanetary flux for two reasons. On an isotropic diffusion model, including energy loss, the number density is always greatest at the source and a negative gradient exists at all other places. Solar wind sweeping modifies this picture so that after about 4 days a positive gradient may exist. Secondly the local guiding by field lines, together with the occurrence of a filamentary field structure, can lead to an almost random distribution of local gradient directions, superimposed on a broad azimuthal gradient associated with the longitude of flare particle emission.

5.4.1 Overall Radial Gradient

No exact solution of the Fokker-Planck equation known to be valid at all energies and over a wide region of interplanetary space is available, mainly due to lack of knowledge of interplanetary scattering processes as a function of radial distance from the sun. Two crude extremes may be mentioned. If diffusion was very slight, the divergence of flux under conditions of almost free propagation immediately yields $U \propto {}^{1}/_{r^2}$.

$$\frac{1}{U}\frac{\partial U}{\partial r} = {}^{-2}/_{r} \qquad (5.4.1)$$

where U is the differential number density.

Alternatively, the approximation of Gleeson, Krimigis and Axford (1971) with a vanishing diffusion coefficient yields the extreme where solar wind convection dominates. The solution of the Fokker-Planck equation

$$\frac{1}{r^2}\frac{\partial}{\partial r}\left(r^2 VU - r^2 k \frac{\partial U}{\partial r}\right) - \frac{1}{3r^2}\frac{\partial}{\partial r}\left(r^2 V\right)\frac{\partial}{\partial \tau}\left(\propto \tau U\right) = 0$$

for spherical symmetry, diffusion coefficient k, is

$$\frac{1}{U}\frac{\partial U}{\partial r} = -\frac{2}{r} C(r, t) \qquad (5.4.2)$$

where $C(r,t) = \frac{4+2M}{3}$ is the low energy Compton-Getting factor for and integral intensity $J_0(\frac{\tau}{\tau_0})^{-M}$.

Thus until the final stages of the event, a gradient of $\frac{1}{r}$ is plausible, and for a tail length $\sim$ 0.1 A.U., an intensity differential of 20% $\rightarrow$ 40% is available if M $\sim$ 1, which is reasonable at 1 MeV.

A gradient between the auroral zone, where asymptotic directions generally go out close to the earth, and deep in the polar cap, where field lines may go right to the end of the tail, of 20% $\rightarrow$ 40% is possible due to this mechanism.

5.4.2 Local Interplanetary Particle Density Gradients

At certain times during a solar proton event, rapid fluctuations in the interplanetary flux are seen in a time scale short compared with the overall characteristics of the event.

A particular example is between 18.00 and 20.00 hrs. U.T. on February 25th, 1969 in the 1 - 13 MeV solar proton energy channel as observed by HEOS A-1 (Balogh and Hynds, 1969) where 100% intensity changes occurred within periods of 10 - 30 minutes. Since the 1 MeV protons took 37 hours to reach maximum intensity, these short term fluctuations can only be related to local filamentary structure, because all source variations of short time scale will have been obliterated by diffusion in a simple isotropic model. Quenby and Sear (1970) show that for typical tangentional discontinuities a distance of at least 1 A.U. must be traversed before the discontinuity can be crossed by 1 MeV solar protons (equivalent to $\sim \frac{1}{2}$ hour flight time for 1 MeV protons). Thus there is a possibility of maintaining low energy solar proton gradients in special cases for several hours. McCracken and Ness (1966) first put foward evidence suggesting that filaments can maintain detailed longitudinal structure out to 1 A.U.

If ∇N is the spatial gradient of number density N, and two points on the same polar cap (e.g. one at dawn, one at dusk) are accessible from different points on the magnetopause, separated by a distance R, then the intensities observed at these two points will differ by $R.\nabla N$.

The solar wind speed at 1 A.U. is of the order of 4 R_E/minute, and this is therefore the speed with which discontinuities are convected away from the sun. Hence a 100% intensity change observed over a period of 10 minutes by a satellite which is almost stationary is equivalent to a 100% intensity gradient over a distance of $\sim$ 40 R_E. This can lead to polar cap intensity variations of similar magnitude, whenever the trajectories from two points on the polar cap happen to lie either side of the discontinuity.

During the November 18th (1968) event at about 16.30 U.T. a similar rapid change in intensity occurred for interplanetary 1 MeV protons (Van Allen et.al., 1970) associated with a change in anisotropy direction. The magnetic field measured in interplanetary space at the same time also showed a sudden change in direction, supporting the filamentary structure explanation.

Incidentally, it may be remarked that such gradients in particle density can cause anisotropies in flux perpendicular to the field direction. The anisotropy due to a flux gradient has an amplitude in the peak intensity direction of

$$\xi = \frac{v\nabla \underline{N} \times \underline{B}}{\omega} \qquad (5.4.3)$$

for particle velocity v, Larmor angular frequency ω and field direction $\underline{B}$. Corresponding to a gradient of 100% change in 40 R_E, a 30% flow anisotropy is expected, sufficient to cause the noticable departures of the particle flow direction from the field direction apparently observed by Quenby et.al. (1969) during the February 25th event.

5.5 DELAYED ENTRY INTO TAIL

A number of authors have discussed the delay in observing a time variation deep in the polar cap or in the tail as compared to the occurrence of a definite interplanetary feature seen near the earth (Kane et.al., 1968; Lanzerotti et.al., 1970; Montgomery and Singer, 1969; Evans and Stone, 1969).

Our interpretation is that a sharp discontinuity in flux bounded by a tangentional discontinuity, is seen at 1 A.U. and is then convected at solar wind speed down the tail. Anderson (1969) has made a similar suggestion. The intensity seen over the polar cap is delayed, therefore, until the discontinuity passes the region of the tail from which the particle trajectory to the polar cap intersects the magnetopause. Figs. 37b and 37c can be used for evaluating this distance for a given tail field configuration. Results of these trajectory integrations suggest that for a rising interplanetary particle flux, intensity enhancements should be found near the last closed field line and in the pseudotrapping region. For a decreasing interplanetary flux, these enhancements should occur at invariant latitudes, corresponding to particle trajectories from deep in the tail. From the mechanism described, no velocity dependence of any magnitude should be seen, because it is the solar wind velocity which dominates the process. This is in agreement with observations made so far (Lanzerotti et.al., 1970; Montgomery and Singer, 1969). the 110 minute time delay of Kane et.al., (1968) requires, for example, a coherent tail length of about 400 R_E. Another example, during the February 25th 1969 event, can be seen by comparing Figs. 39 (section 5.7) showing the polar cap structure at 2 MeV and 38 showing the interplanetary time profile at 1 MeV. While the polar cap passes were rather featureless from 10.48 U.T. to at least 17.34 U.T., interplanetary changes roughly 100% in amplitude started at $\sim$ 16.30 U.T. Using observations such as these can place limits on the amount of tail divergence, field line diffusion and breaking off of tail field at given times.

The difference between the time structure of solar protons in interplanetary space and in the magnetotail observed by Lanzerotti et.al. during the September 18th 1967 flare (at ~ 14.30 U.T.), where the structure in the tail was found to be less sharp, is in accord with trajectory integrations. As mentioned, trajectories starting near the neutral sheet with large initial pitch angles leave the tail closer to the earth than those with small initial pitch angles. If the sudden change in interplanetary particle flux is bounded by tangentional discontinuity and convects down the tail at solar wind speed, it is expected that the change in particle flux observed in the tail should be smoothed due to the different trajectory lengths in the tail. This method of access would also predict a pitch angle distribution in the tail peaked initially perpendicularly to the field, and approaching isotropy when the interplanetary discontinuity has passed the point where the longest trajectory crosses the magnetopause.

Calculations starting from the position of the Vela satellite at the time of the observations (14.30 U.T.) agree both with the observed time delays of 25 minutes (corresponding to 100 R_E at solar wind speed) and the changed structure of the interplanetary impulse as observed in the tail (corresponding to a dispersion in trajectory length of ~ 40 R_E). This is shown in Fig. 33 (section 5.3.2).

It is concluded that diffusion in the tail for protons of energy ~1 MeV is not necessary to explain observed results.

This example illustrates that in order to estimate the length of a coherent tail by a particle delay method, one must select data corresponding to particle trajectories which can actually go far down the tail, since otherwise smaller delay times will be observed. The delays observed by Vela 4 A at nearly 18.00 U.T. during the same event is approximately 60 minutes. The spacecraft position is -30° solar magnetospheric latitude and 220° longitude, which corresponds to a distance of about 9 R_E from the solar magnetospheric x-y plane, and an injection distance of over 200 R_E down the tail.

The large delay observed by Evans and Stone (1969) for particle entry to high latitudes over the northern polar cap can perhaps be explained from the work done here by a persistent particle anisotropy arriving from the south in the meridian plane. The ratio of $\frac{\text{North cap max flux}}{\text{North cap min flux}}$ decreases gradually over a period of 20 hours similar to the typical behaviour of anisotropy ratios for protons in the same energy ranges. We would require the particle density at $\sim$ 10 MeV across the tail to increase from north to south and the auroral zones to connect via plasma sheet trajectories to the direction of interplanetary anisotropy. This explanation also agrees with their observation that the flux enhancement in the northern auroral zone extends to a higher latitude at the lowest energies observed. This is because the pseudo-trapping region extends up to the last closed field line at these lowest energies.

5.6 ELECTRONS

Some preliminary observations suggest that structure over the polar cap for solar electrons is less than for protons. We may note that for $\sim$ 40 keV electrons, being nearly relativistic particles, local gradient convection down the tail cannot be such an effective method for causing structure as it is for 1 MeV protons. Similarly, impact zone effects are also not possible due to the small gyroradii of these particles when crossing the magnetopause.

It has been observed (Lin and Anderson, 1967) that electron events do not show much filamentary structure. V. Allen (1969) shows that electron event time histories track extremely well, whether they are observed $\sim$ 100 R_E apart in interplanetary space, or whether they are observed $\sim$ 100 R_E apart in the tail and in interplanetary space. We suggest that the reason why polar cap structure, due to local intensity gradients, is less marked for 40 keV electrons than for 1 MeV protons is the difficulty of sustaining large local gradients in the flux. The diffusion coefficient, parallel to the magnetic field, is

$$D_{//} = \frac{\lambda v}{3} \qquad (5.6.1)$$

where v is the particle velocity.

If the mean free path, λ , is independent of rigidity in interplanetary space as is suggested by the similarity of the time behaviour of relativistic electrons and protons of ~ 1 GV (F. B. McDonald and T. L. Cline, 1968)

$$D_{//} \propto v$$

50 keV electrons would be expected to show as little local gradient structure as 130 MeV protons, i.e. much less structure than 1 MeV protons. This is because the velocity of diffusive flow is more than an order of magnitude greater along the field lines and local discontinuities maintaining the gradients are more easily short-circuited. The only structure effects expected are due to a dawn-dusk gradient in the short initial anisotropic stage of the electron event and to the overall radial gradient. Neither of these effects is likely to produce intensity changes greater than 50%.

5.7 FEBRUARY 25TH FLARE

Data obtained from two satellites was used. One was the ESRO II satellite, the other was the HEOS-A1 spacecraft, which was launched on 5th December, 1968 into a highly elliptical orbit, with perigee 1800 kms, apogee 222300 kms and inclination 44^{o}. At the time of the event, this spacecraft was well outside the magnetosphere, close to its apogee of 35 R_E at a solar ecliptic latitude 50^{o}N and longitude 56^{o}W.

The class 2B flare responsible for the proton increase occurred on February 25th at W36^{o} heliographic longitude. The optical flare began at 0900 U.T., neutron monitor increases were detected at 0915 U.T. and the first solar proton data available to us from the ESRO II satellite commenced at 1048 U.T. Magnetospheric conditions throughout this time were very quiet; the mean value of the Kp index during the first 12 hours was 2.

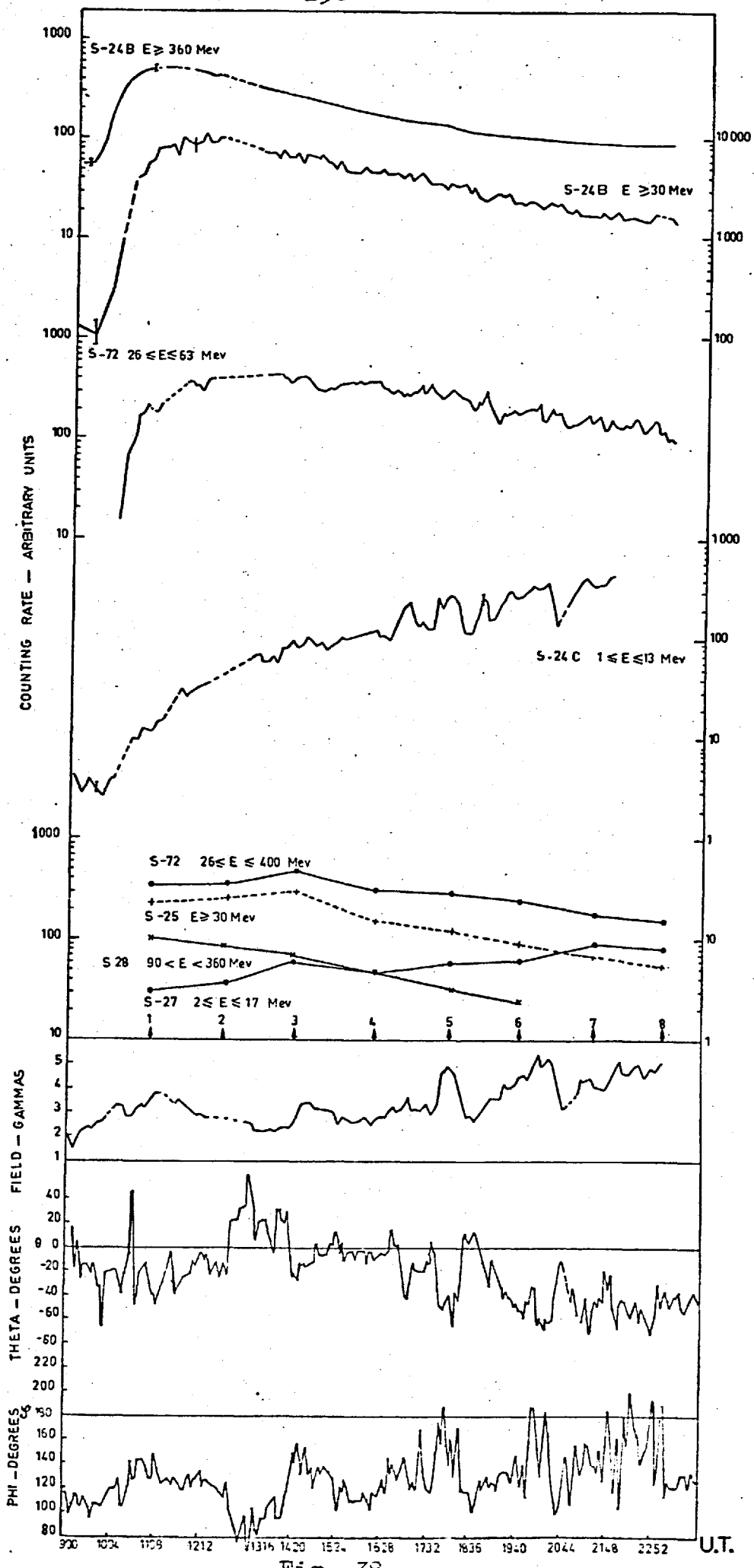

Fig. 38

Particle and magnetic field data during the early stages of the February 25th solar flare event.

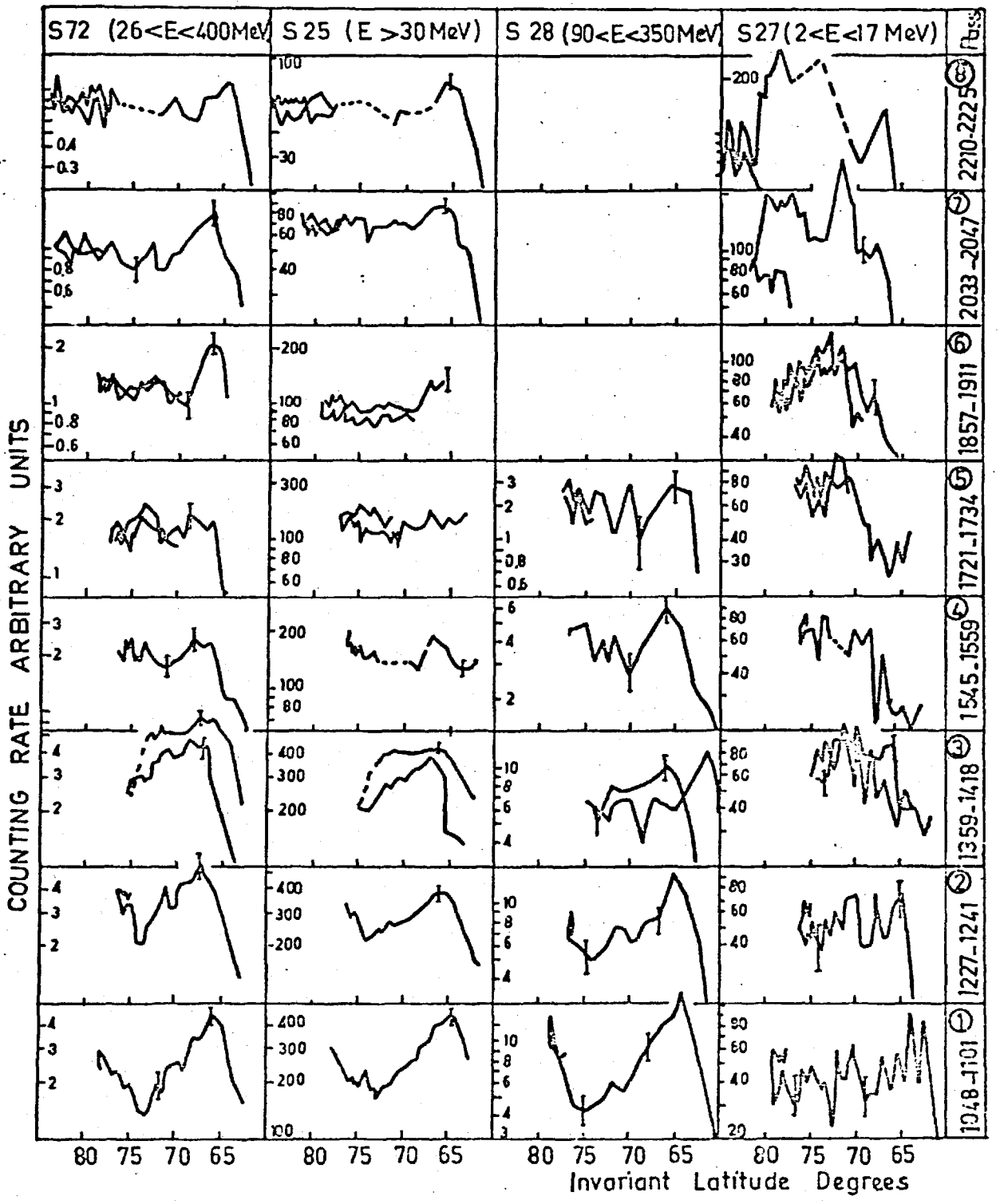

Fig. 39

Polar cap intensity structure at different energies for solar protons observed on the ESRO II satellite during the February 25th solar flare event.

Fig. 38 shows the time history of the available particle and magnetic field data during the early stages of this event. The important points to notice here are :

(a) Large rapid intensity changes in 1-13 MeV energy particle flux occur after 1700 U.T. in interplanetary space

(b) The interplanetary magnetic field is southerly directed except for some time at about 1300 U.T., and in general follows the Parker spiral direction, with the field vector pointing outwards from the sun.

(c) The time variation in intensity observed over the polar cap follows the corresponding variation at the same energy in interplanetary space fairly well.

Fig. 39 gives the time history of low altitude polar passes for four detectors. These detectors are :

S.25 is a shielded Geiger counter (Anton 302) which responds to protons of energy $\gtrsim$ 30 MeV. This detector is omnidirectional.

S.27 is a solid state detector pointing at right angles to the satellite spin axis. The satellite spin rate is faster than the experimental sampling time of 16 seconds, so that this instrument measures the average proton intensity in the plane perpendicular to this axis. The energy range observed by this detector is 2 to 17 MeV.

S.72 is another solid state detector, but pointing parallel to the satellite spin axis. The energy range covered by this instrument is 26 to 400 MeV. Pulse height analysis is performed in this energy range so that spectral data is available.

S.28 has already been described.

The figure shows that a great deal of structure was observed at energies greater than 26 MeV during the initial stages of

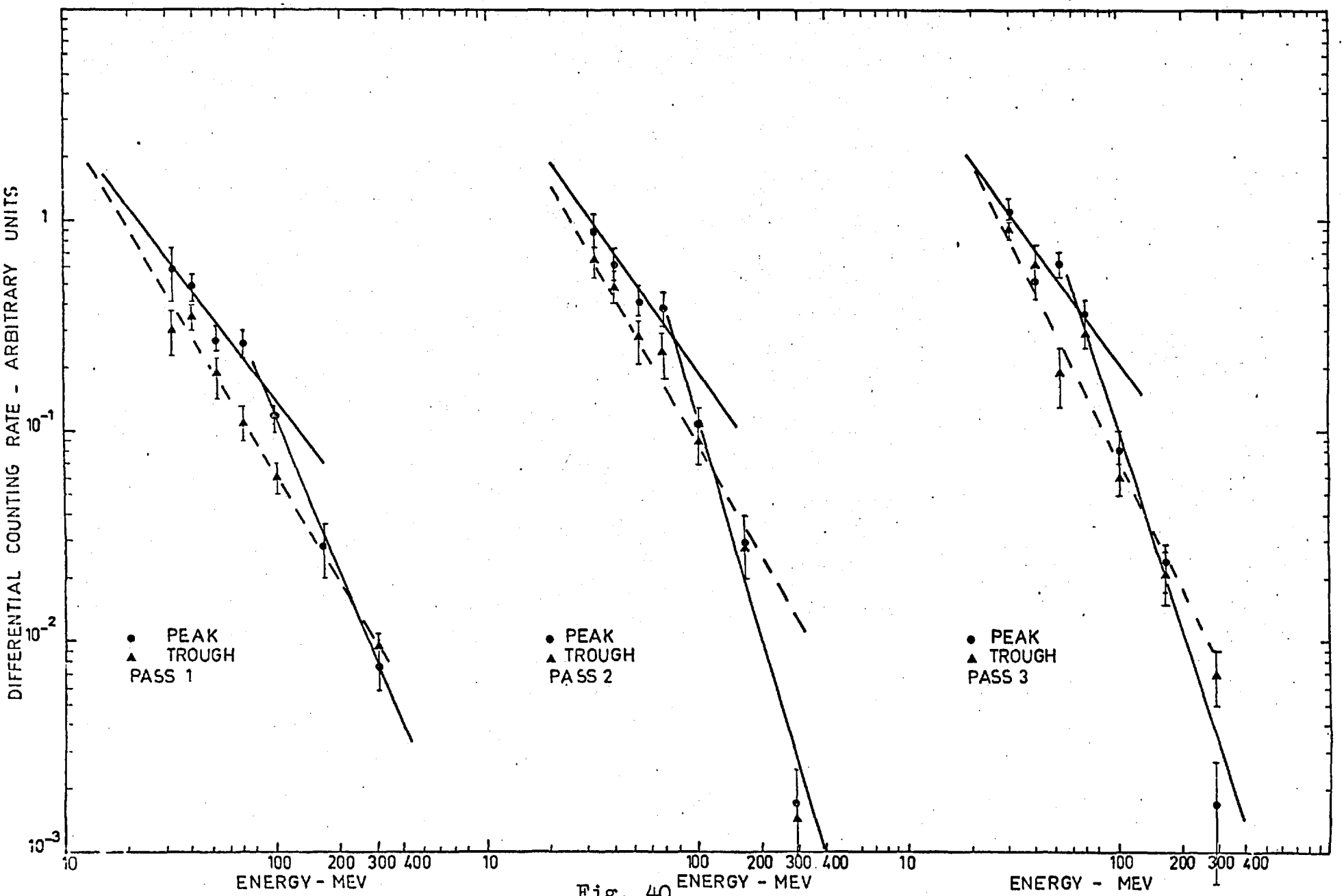

Fig. 40

Energy spectrum measured in the dusk peak and trough by S.72 during the first three passes (February 25th).

this event, whereas for low energies (~ 2 MeV) no significant structure was observed until the later stages of the event when there were also rapid interplanetary intensity changes. Unfortunately, the spacecraft tape recorder was not working during the February event so that only the dusk half of the polar passes are available as real time data.

Fig. 40 shows the energy spectrum in the auroral zone enhancement and in the trough (which is located at higher than auroral latitudes on the dusk side of the polar cap) during the first three passes after the onset of the flare. From the work done in the previous chapters this is interpreted as the observation at low altitudes over the polar cap of an interplanetary particle anisotropy. The straight lines drawn through the points are least squares fits. Use of two straight lines to fit the 'peak' particle intensity reduces the mean square deviation of the fit by a large amount in all three orbits. We interpret this as representing a true excess of particles with energies ~90 MeV. It is not expected that the peak/valley ratio should always be the same as the interplanetary anisotropy ratio I_{max}/I_{min}. As mentioned earlier, magnetopause effects, whether they are multiple crossings or isotropisation at energies of the order of 1 MeV, can reduce the observed polar cap ratio with respect to the interplanetary value, and at high energies, where generally much wider energy channels are used, there may be a great deal of dispersion in the trajectories of different energy protons arriving at the same invariant latitude. Fig. 41 is a plot derived from trajectory integrations for the first polar pass after the onset of the flare. It shows the angle between the particle velocity vector and the interplanetary anisotropy maximum direction observed by Engel (1970). Proton energies are indicated, and the pass is split up into 6 regions as follows: (negative particles going backwards are considered here)

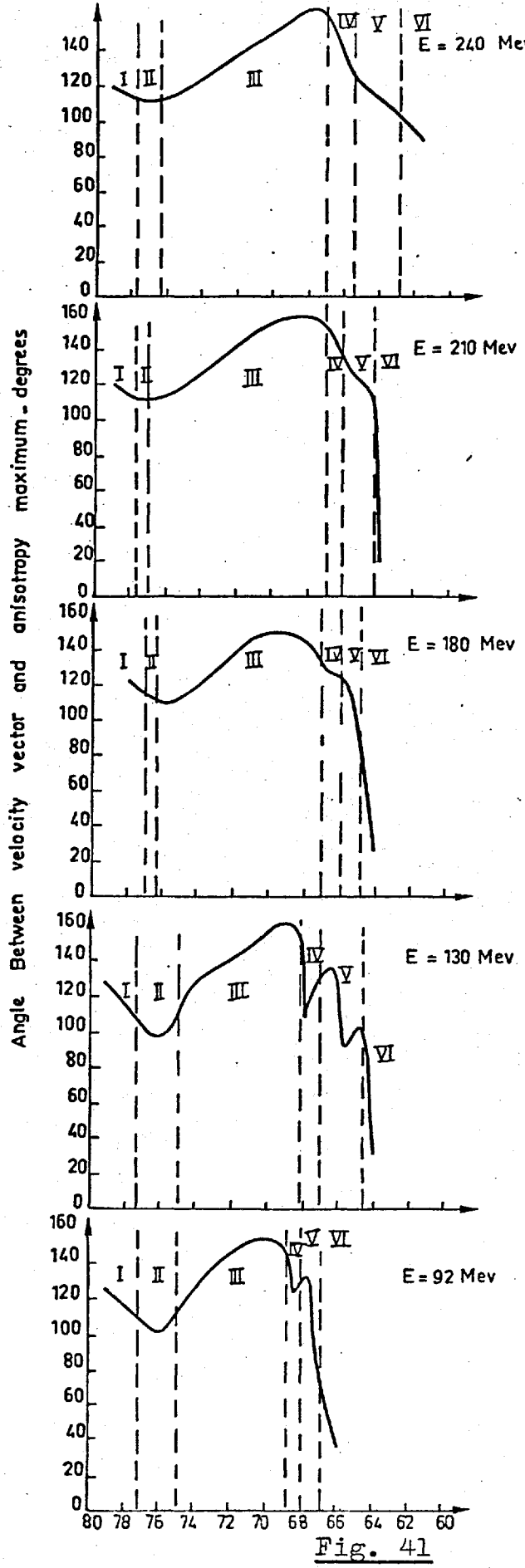

Fig. 41

Angles between the calculated asymptotic viewing directions of detectors on board the ESRO II satellite during the first polar pass of the February 25th flare (at different energies) and the measured interplanetary anisotropy maximum direction. The different regions shown here are explained in the text.

Region I :
Trajectories, when discontinued at 25 R_E from the earth, were contained wholly within the northern tail lobe, i.e. the guiding centres and radii of gyration of the trajectories were contained inside the tail lobe.

Region II :
Trajectories were still inside the tail boundary when the integration was stopped at 25 R_E from the earth, but some part of their radii of gyration was outside the tail lobe, so that the particles would escape further down the tail.

Region III :
Particles leave the tail on the dusk side of the magnetopause less than 25 R_E from the earth.

Region IV :
Similar to Region II, except the southern tail lobe is involved.

Region V :
Particle guiding centres are close to the neutral sheet, pitch angles are fairly large, and particles drift across to the dawn side of the magnetopause

Region VI :
Particles end up by crossing the magnetopause on the dawn side. The lower latitude boundary of region VI represents the nominal cosmic ray rigidity cut-off.

For energies between 20 MeV and 90 MeV, region VI and V cannot be clearly separated. This is because the longitudinal drift per bounce for these particles is much less than 90°at the latitudes considered. However, as shown in chapter 5.3.2, it would be difficult to observe the difference for the two cases, as they both correspond to near-maximum interplanetary fluxes. We thus expect the low energy peak at the dusk auroral zone to cover a larger range of invariant latitudes, than the high energy peak. This is in agreement with observations made sc far.

Finally, the decay of the > 360 MeV energy interplanetary proton anisotropy has been plotted and has been compared with the polar cap auroral zone peak and the trough intensity variations at > 90 MeV. This is shown in Fig. 42 and demonstrates the extremely good correlation.

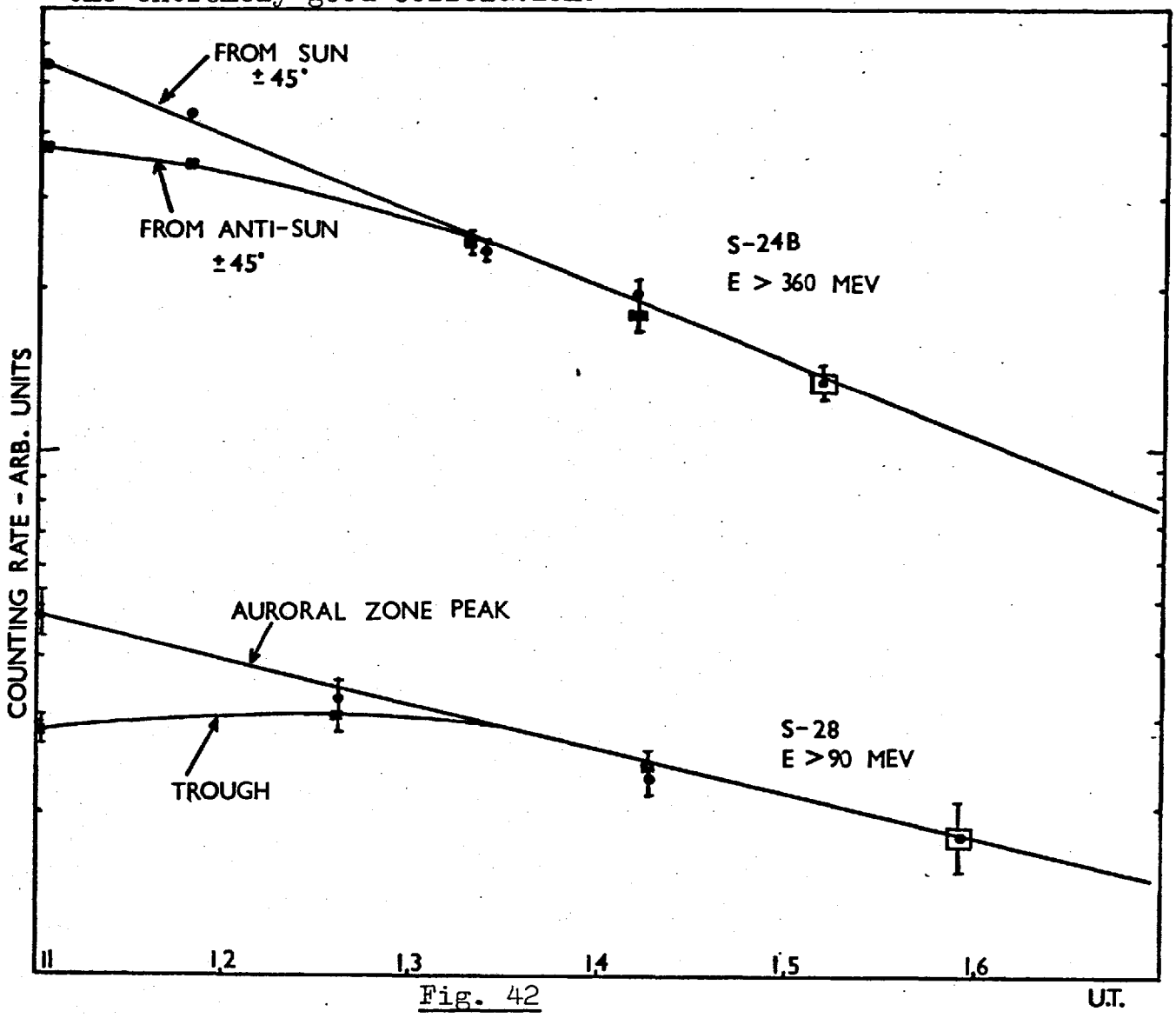

Fig. 42

The intensity enhancement at high latitudes is clearly marked for the first two passes at energies > 26 MeV although we cannot say from the data whether the enhancement is a peak or a plateau covering the whole of the dawn side of the polar cap. As shown in chapter 5.3.2, the polar cap structure actually seen depends very largely on the orbit of the spacecraft. In the case of the first two orbits here, it would be expected that the high latitude enhancement is a peak rather than the edge of a plateau.

5.8 NOVEMBER 18TH FLARE

5.8.1 ESRO II Satellite Observations

The flare which caused the proton increase occurred on November 18th at W.84° heliographic longitude. The flare began in H alpha light at 10.25 U.T. and was classified by most observers as having an importance of 1B. Auroral zone and equatorial H component magnetograms show the very quiet magnetic conditions that prevailed from about 11.15 U.T. till 16.30 U.T. when there was a large sudden increase associated with a sharp interplanetary field change which has been identified as being a filament probably bounded by tangentional discontinuities. The interplanetary magnetic field was southerly directed most of the time, and was exceptionally smooth, along the Parker spiral direction with the magnetic field vector pointing towards the sun.

Fig. 43 shows the general magnetic conditions during the first six polar passes after the onset of the flare.

The 90-360 MeV proton counting rate profiles for the first seven passes over the northern polar cap are shown in Fig. 44. The structure in the proton intensity persists for the first 5 passes, a period longer than 7 hours. The approach to isotropy is clearly shown as the amplitude of the polar cap structure slowly becomes less marked until the seventh pass show approximately constant intensity. Proton trajectories have been calculated for the first four orbits. The rigidity of 0.5 GV was selected, since it corresponds to the weighted mean of the energy channel used here.

For pass 1 a 40 γ tail field produces the best correlation, whereas for passes 2, 3 and 4, a 15 γ tail field fits the observations best. Clearly, one must look for physical evidence or tail field measurements to explain this fact. Such evidence is indeed available. It is well known that after a substorm the tail field decreases in strength (Behannon and Fairfield, 1970). Examination of the auroral zone magnetograms shows that there was a substorm just prior to the first polar

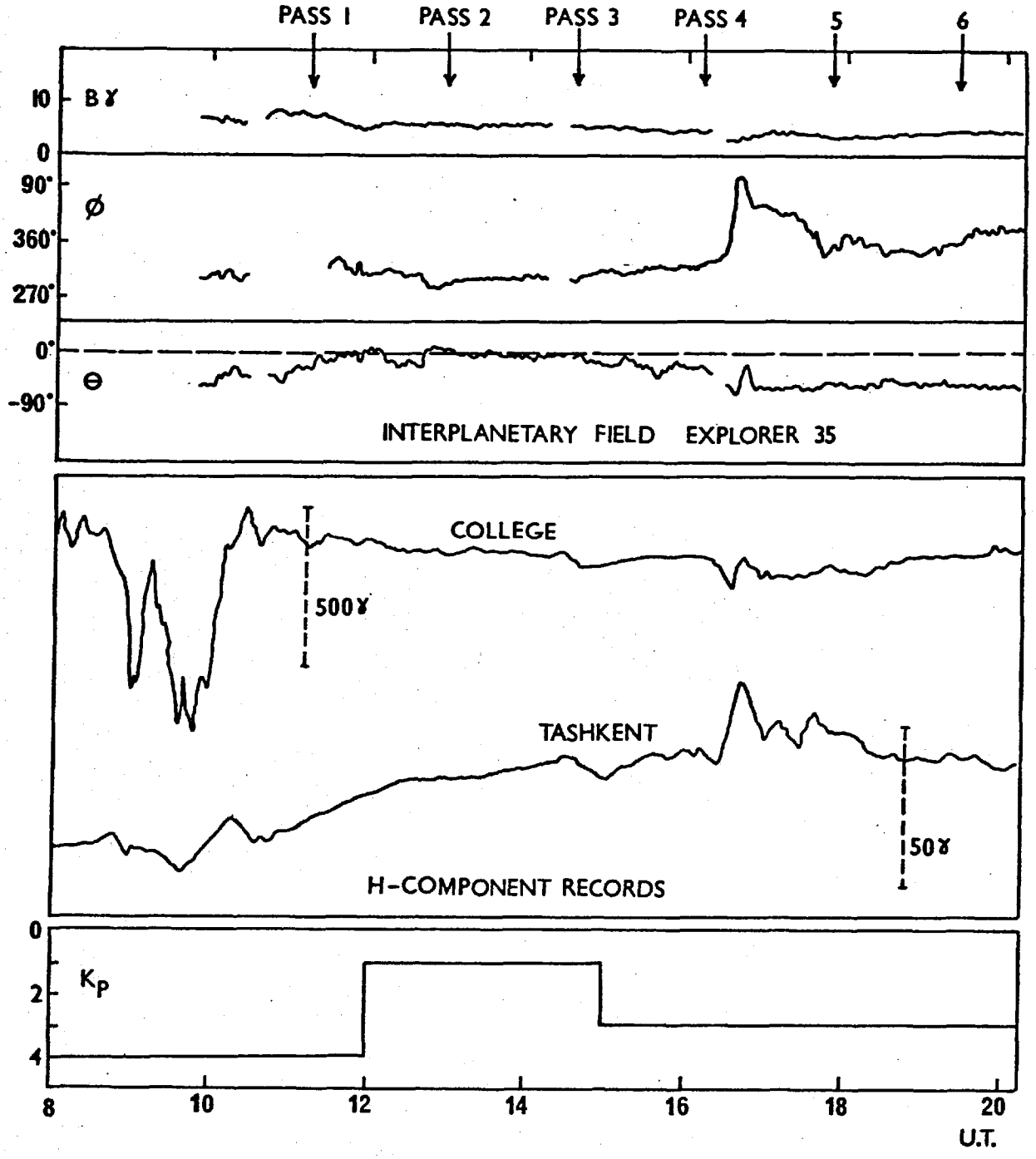

Fig. 43

Magnetic conditions during the first six polar passes of ESRO II after the onset of the November 18th solar flare event.

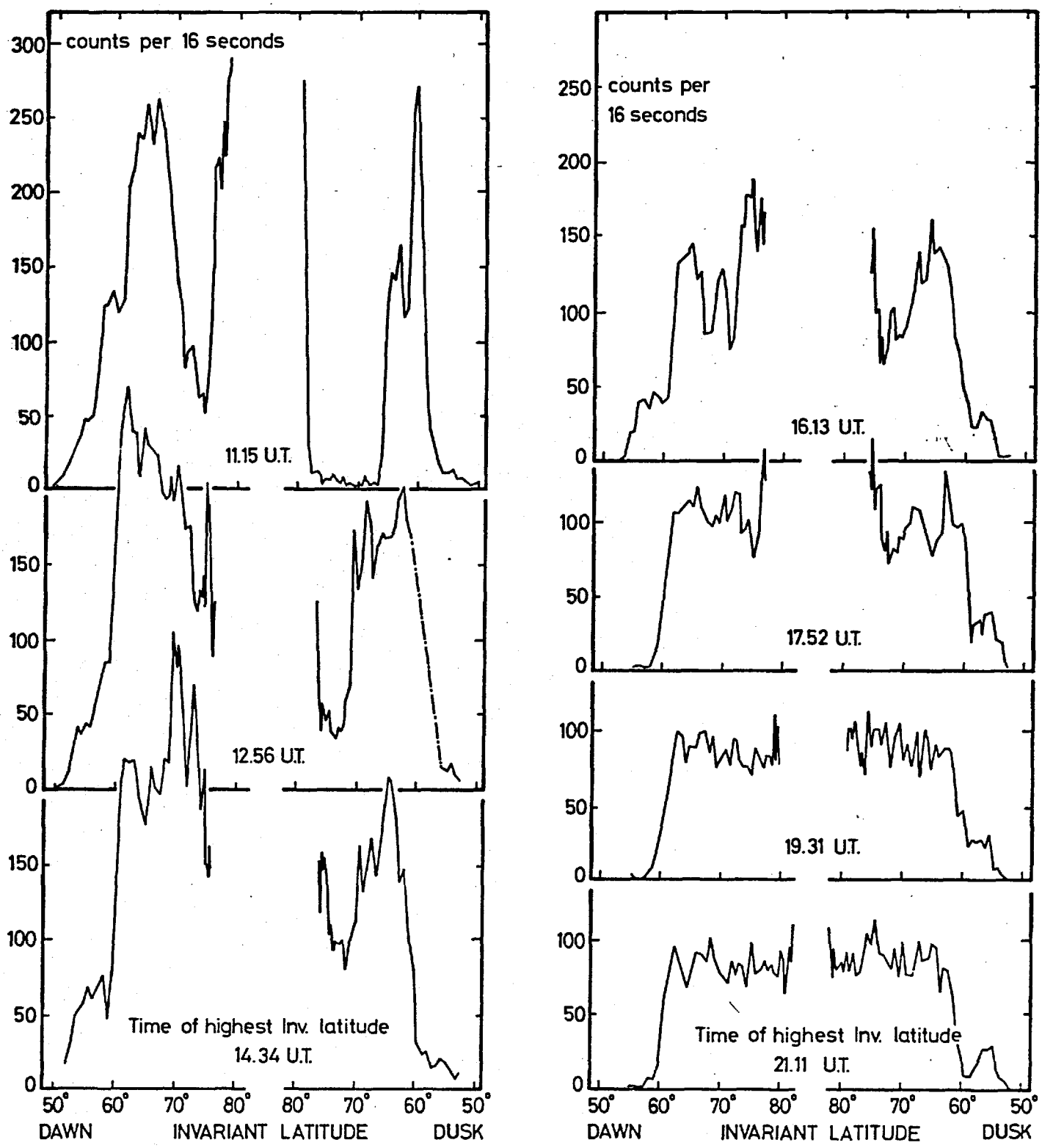

TIME VARIATION OF PROTON INTENSITY STRUCTURE OVER THE NORTHERN POLAR CAP.

Fig. 44

Polar cap intensity structure for $90 < E < 360$ MeV solar protons during the first seven orbits after the onset of the November 18th solar flare event.

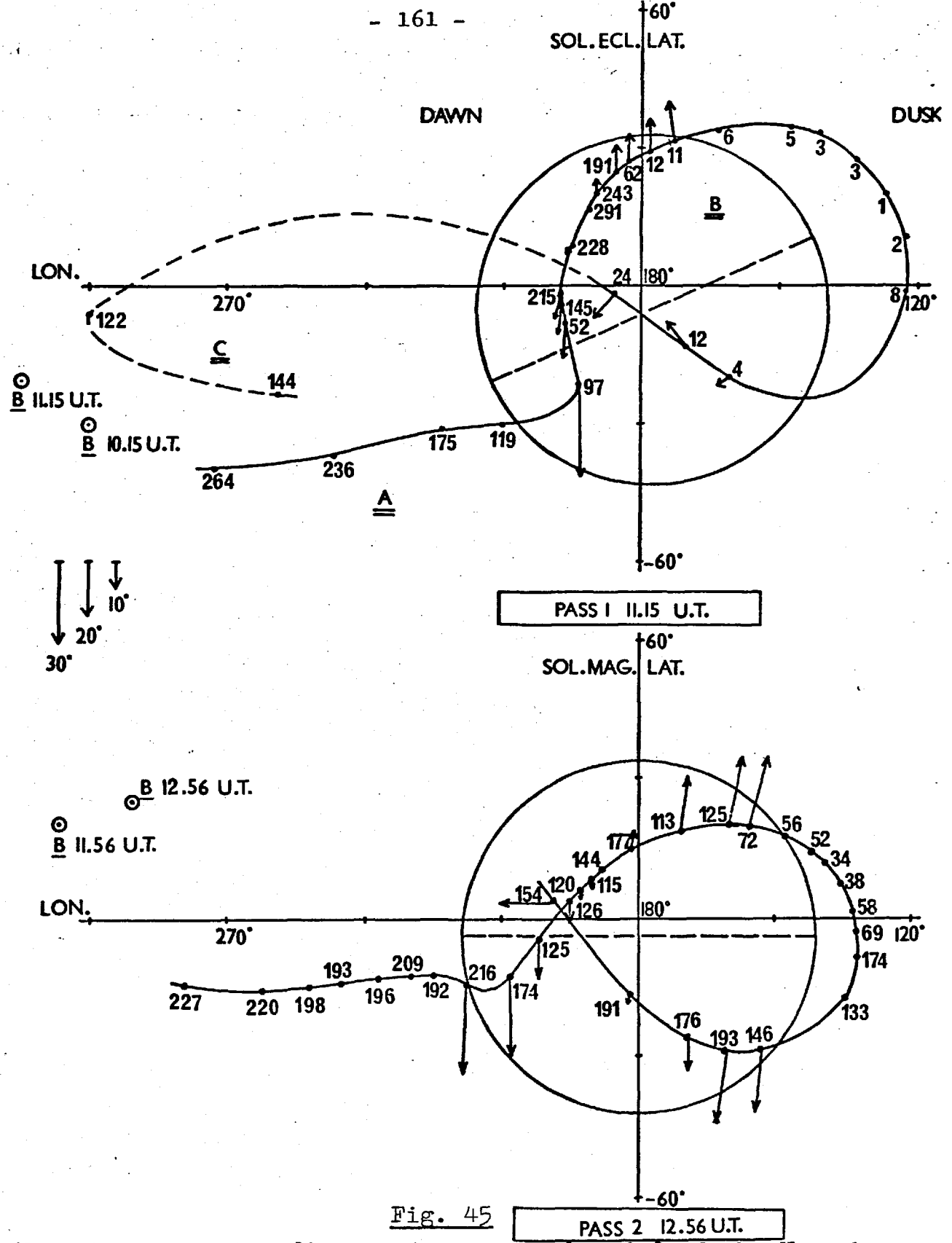

Fig. 45

Magnetopause entry diagram for passes 1 and 2 of the November 18th solar flare. Pass 1 has been shown earlier, but in addition, the asymptotic velocity vector of the 125 MeV particle in the tail only, is projected onto a plane perpendicular to the earth-sun line and represented here as an arrow, the length of which denotes the size of the particle pitch angle. Note that the velocity vector is for a negative particle going backward. The magnetic field direction in interplanetary space is also given.

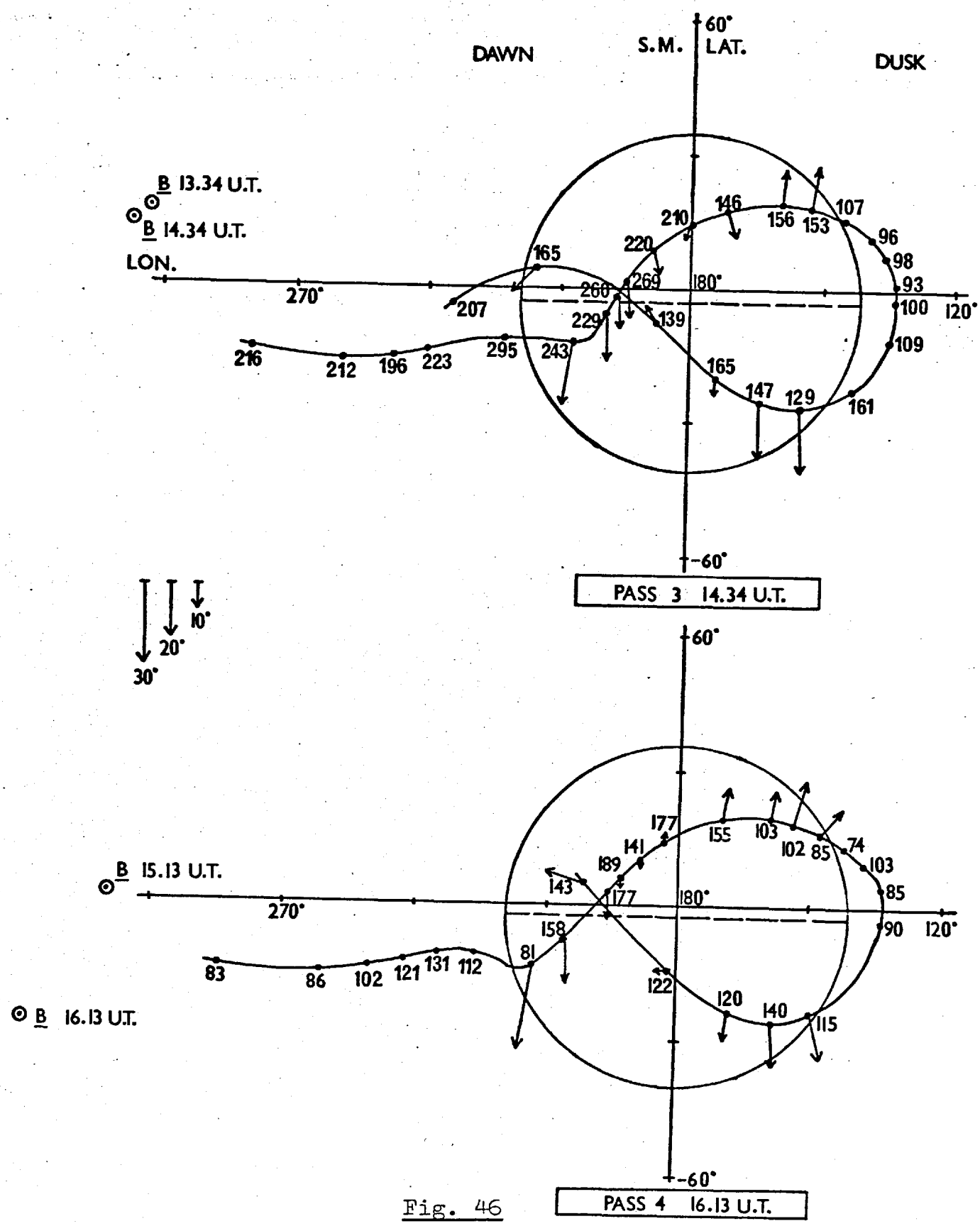

Fig. 46

Magnetopause entry diagram for passes 3 and 4 of the November 18th solar flare. For further explanation see Fig. 45.

pass considered, so that there is indeed evidence for weak tail fields, certainly for passes 2, 3 and 4. This evidence in turn proves the sensitivity of the trajectory calculations in the magnetic field model employed here.

Magnetopause entry diagrams for passes 1 to 4 are shown in Figs. 45 and 46. These trajectory derived curves give the particle position in terms of latitude and longitude when it enters the magnetopause or a plane situated 25 R_E down the tail. Pass 1 is in solar ecliptic and passes 2, 3 and 4 in solar magnetospheric co-ordinates. Also indicated on these diagrams is the particle asymptotic velocity vector, $\underline{V}_\perp$, projected onto the plane perpendicular to the earth-sun line. The size of the arrow, which denotes $\underline{V}_\perp$ gives the pitch angle of the particle in the tail. The velocity vector shown here is for a negative particle going backward, i.e. the equivalent incoming proton would have the arrow pointing in the opposite direction, and would move clockwise round the tail field lines in the northern lobe as seen from the sun. Pitch angle information is important when deciding for instance whether a particle trajectory is near the neutral sheet, or whether it is wholly embedded in the tail lobe. In the second case the particle may enter tail-like field at many hundreds of earth radii down the tail, and thus provide information on the distant tail, or alternatively on the strength of the scattering processes acting on the particles in the tail.

It is possible to calculate the pitch angle distribution expected in interplanetary space, if the polar cap structure is produced by simply observing an interplanetary anisotropy. The distribution is obtained by plotting polar cap counting rate I as a function of α , where α is obtained from

$$\cos\alpha = \underline{V}\cdot\underline{B} \;/\; |\underline{V}|\cdot|\underline{B}|$$

Here $\underline{V}$ is the asymptotic velocity of the 0.5 GV particle incident vertically at the satellite, and $\underline{B}$ is the interplanetary magnetic field vector. This has been done for passes 1, 2 and 3. No allowance was made for field line draping in the

magnetosheath, or the finite size of the asymptotic viewing cone. Multiple magnetopause crossings were also not considered, so that the distributions obtained are only approximate, with best results near 0^{o} and 180^{o}. As can be seen (Fig. 47) the pitch angle distributions obtained in this way are typical of those observed in interplanetary space, both in their shape and temporal characteristics - except for the intensity observed to be coming up the tail. Only those points were selected for these distributions where multiple magnetopause crossings were thought to be unlikely, or where the trajectories were wholly contained inside the northern tail lobe. The tail model which allows peak interplanetary fluxes to enter the distant magnetotail in such a way that the particle velocity vector nearly reverses its interplanetary direction, and which allows particles to remain inside the tail with small pitch angles, has been described earlier.

There may be occasions when the high latitude intensity is less than the auroral zone intensity, e.g. pass 2. This could be due to reduced field line reconnection across the magnetopause when the interplanetary magnetic field is northerly directed. Also, a high latitude intensity greater than the auroral zone counting rate is possible during the decaying phase of the flare since the high latitude trajectories enter the tail several 100 R_E downwind, and thus these regions observe an earlier part of the interplanetary particle distribution. This could account for the structure in passes 4 and 5, provided the particles enter tail-like field at about 500 R_E away from the earth.

There is further evidence that interplanetary anisotropies cause a large amount of the polar cap structure observed for protons of energy > 20 MeV. In section 5.3.5 the northern polar cap structure was predicted on the basis of trajectory integrations. Fig. 48 shows the prediction together with two orbits of the ESRO I satellite, and four orbits of the ESRO II satellite during the November flare. ESRO I is essentially a noon midnight orbiting satellite, and the data used here is for > 30 MeV proton channels on both spacecraft.

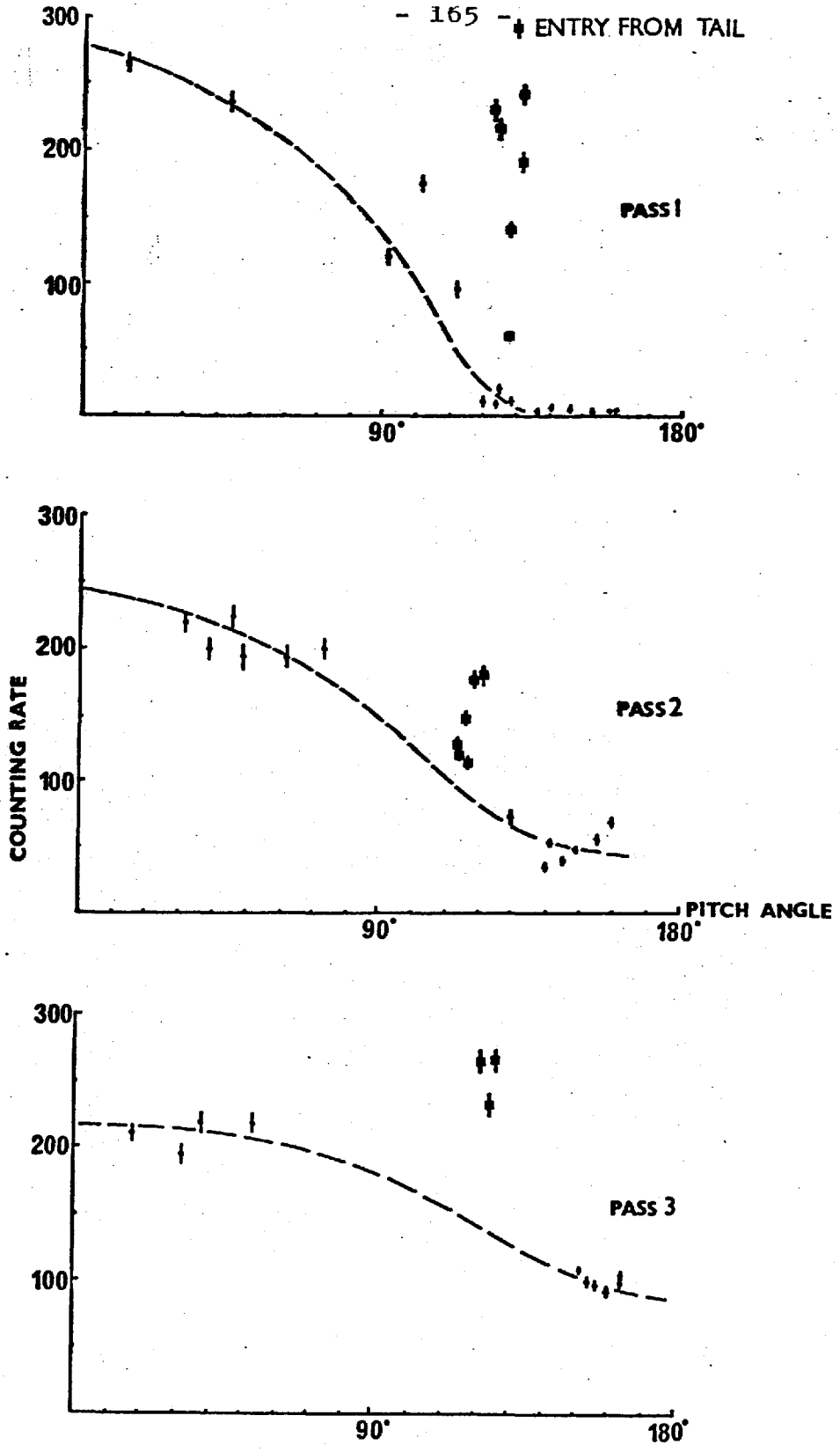

Fig. 47

Pitch angle distributions in interplanetary space calculated from the asymptotic velocity directions and the observed polar cap structure during the first three polar cap passes of the November 18th solar flare.

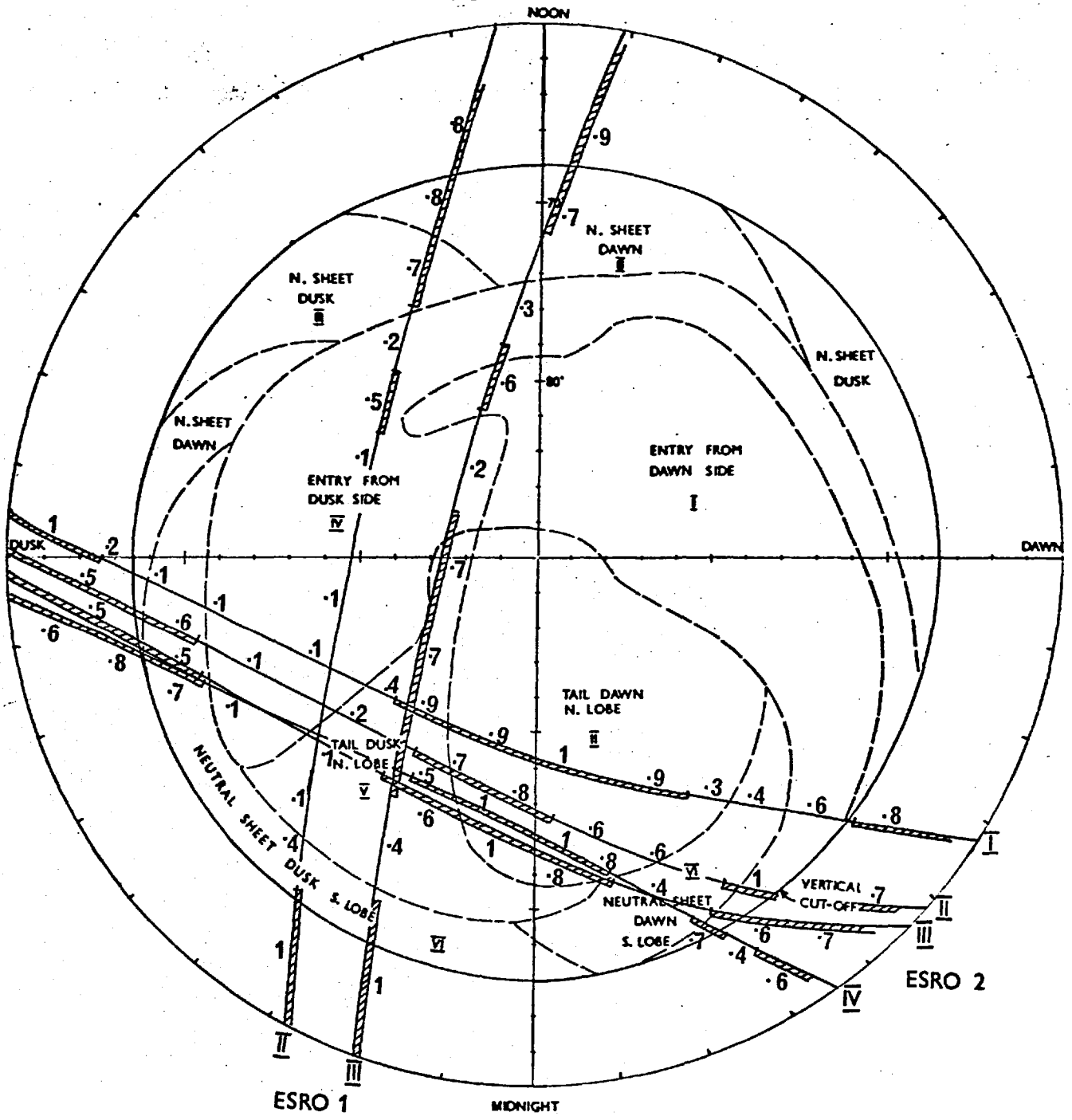

HATCHED SECTIONS OF THE ORBIT REPRESENT HIGH PARTICLE FLUXES. COUNTING RATES ARE EXPRESSED RELATIVE TO THE MAXIMUM OF EACH POLAR PASS CONCERNED.

Fig. 48

Observation of an interplanetary anisotropy over the northern polar cap. Detectors on board the two satellites (ESRO I, - noon-midnight orbits and ESRO II, dawn-dusk orbits) are for solar protons of energy > 30 MeV, superimposed on the 44 MeV polar cap plot of Fig. 36b.

Regions of peak and minimum counting rates are indicated and show very good agreement with the predicted high and low intensity regions calculated from trajectory integrations in section 5.3.5 for 44 MeV protons. These observations verify the predicted polar cap structure for nearly all local times and invariant latitudes. Inward diffusion and electric field drifts allow particle access to below the nominal cut-off.

5.8.2 Analysis of Neutron Monitor Data During the Initial Stages of the November 18th Flare

Another feature of the tail model, which was developed to account for the enhancements at high latitudes, is that it does not predict high latitude peaks for energies much above 300 MeV. Neutron monitor data has been analysed during the initial stages of the November flare, to see if this prediction holds.

In order to examine the various neutron monitor responses, allowance must be made for cut-off, spectral response and the incident proton spectrum.

After Quenby (1967), the neutron monitor counting rate increase is given by :

$$\Delta N_f = \int_{P_a}^{\infty} \mathcal{J}(P, A_m, t) \quad S(P).dP \qquad (5.8.1)$$

where :

A_m = mean asymptotic viewing direction weighted for the energy spectrum of the protons and the neutron monitor response,

P_a = atmospheric cut-off rigidity threshold

$S(P)$ = specific yield function given by

$$\mathcal{J}_o(P,t) \quad S(P) = \frac{dN}{dP}$$

Here $\mathcal{J}_o$ is the cosmic ray differential spectrum, and $\frac{dN}{dP}$ is the change in counting rate with vertical threshold rigidity for a counter.

The percentage increase is then:

$$P = 100\Delta N_f / Ng$$

where $Ng = \int_{P_a}^{\infty} \mathcal{J}_o(P,t)\ S(P)\ dP$

Hence : $$\frac{\Delta N_f}{Ng} = \int_{P_a}^{\infty} \mathcal{J}(P,\ A_m, t)\ \frac{1}{\mathcal{J}_o(P,t)}\ \frac{dN}{dP}\ dP \Big/ \int_{P_a}^{\infty} \frac{dN}{dP}\ dP \quad (5.8.2)$$

Using a flare differential spectrum of $\mathcal{J} \propto P^{-2.92}$ as deduced from ESRO II and Explorer 33 spectral information, the cosmic ray rigidity spectrum at near sunspot maximum from Webber (1957), and the $\frac{dN}{dP}$ values from Quenby (1957), the figures given in table 1 are computed.

In this case, all the percentages are normalised to the maximum Goose Bay neutron monitor increase and are expressed as a percentage of that value. The asymptotic viewing cones of all the stations, from which data was obtainable, were plotted in solar magnetospheric co-ordinates. These viewing cones are formed by the spread in the incident direction, at the magnetopause, of protons arriving at the position of the observatory at 20 km altitude with all allowed zenith angles. The rigidity interval used here was 2 GV to 5 GV. Folding the flare spectrum into the neutron monitor response curve shows that over 70% of the flare particles must have arrived through these viewing cones. The data used here was taken mainly from Shea and Smart (1969). Although the field model used by them is inaccurate at distances greater than 10 earth radii (see Appendix 1), the neutron monitor particles are energetic enough not to be influenced too much by this. The normalised increases in counting rates have been plotted on these asymptotic viewing cone diagrams for 5 minute averages. One such diagram is shown in Fig. 49.

TABLE 1

Station	Code	%age increase wrt. GOO at 10.55		
		10.45-10.50	10.50-10.55	10.55-11.00
Thule	THU	5	4.3	49
Alert	ALE	2.4	3.1	11
Resolute	RES	0	0	43
Dumont d'Urville	DUM	0	26	68
McMurdo	MCM	22	70	66
South Pole	SOU	84	165	150
Inuvik	INU	7.9	0	28
Churchill	CHU	11	72	78
Goose Bay	GOO	30	100	78
Tiksi Bay	TIK	2	3	5.5
Oulu	OUL	7.2	12	0
Sanae	SAN	7	13	35
Deep River	DEE	32	80	67
Calgary	CAL	28	82	69
Sulphur Mountain	SMT	25	90	82
Port aux Francais	POR	7.2	13	11
Mount Washington	MTW	22	85	69
Durham	DUR	25	34	11
Victoria	VIC	46	81	41
Swarthmore	SWA	23	33	20
Leeds	LEE	7	21	7
Kiel	KIE	0	5	12
Dallas	DAL	20	19	8

Station	Code	11.00-11.05	11.05-11.10	11.10-11.15
Thule	THU	48	52	41
Alert	ALE	37	53	20
Resolute	RES	21	6.5	0
Dumont d'Urville	DUM	52	35	17
McMurdo	MCM	54	46	33
South Pole	SOU	117	96	85
Inuvik	INU	51	46	40
Churchill	CHU	47	37	27
Goose Bay	GOO	53	48	31
Tiksi Bay	TIK	6.5	7	8
Oulu	OUL	0	0	12
Sanae	SAN	28	25	21
Deep River	DEE	46	35	28
Calgary	CAL	52	41	29
Sulphur Mountain	SMT	64	49	47
Port aux Francais	POR	15	21	8.7
Mount Washington	MTW	60	50	36
Durham	DUR	37	20	27
Victoria	VIC	30	23	24
Swarthmore	SWA	10	12	18
Leeds	LEE	15	7	4
Kiel	KIE	5	0	4
Dallas	DAL	8	0	0

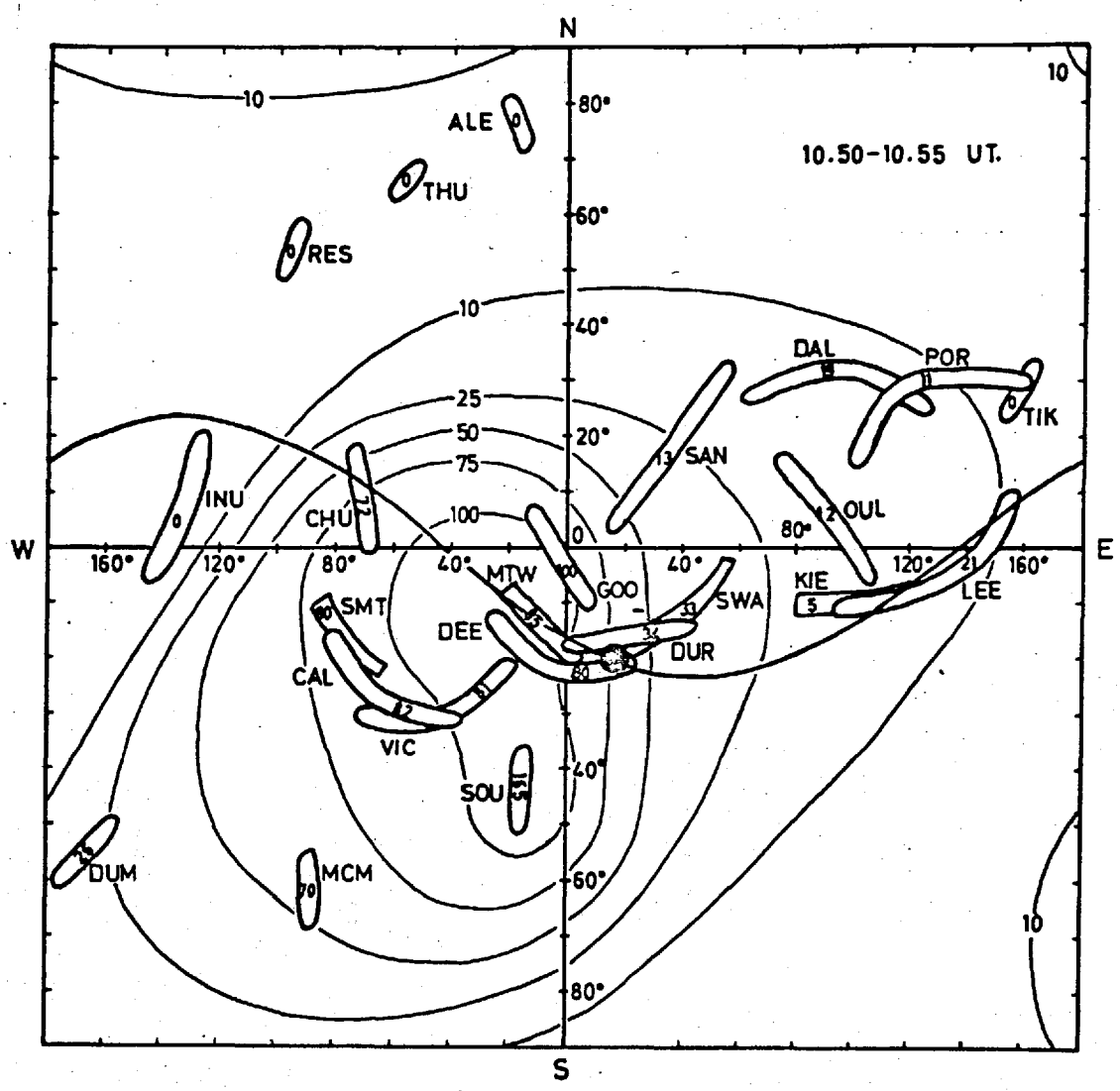

Fig. 49

Contour lines are drawn and allow us to calculate the pitch angle distribution in the ecliptic plane. This is shown in Fig. 50 for each 5 minute average. As can be seen, during the early stages the anisotropy is 100% with no return flux towards the sun, and the maximum particle intensity direction is aligned very closely with the interplanetary magnetic field ($\theta = -20^{\circ}$, $\phi = -45^{\circ}$). The intensity distribution is seen to approach isotropy asymmetrically about the field direction. In Fig. 51 the longitudes of the half maximum flux values are plotted as a function of time to illustrate the spread of the pitch angle distributions in the ecliptic plane. Also shown is the intensity time profile for the peak and minimum directional flux, showing the decrease in the anisotropy of these high energy solar protons.

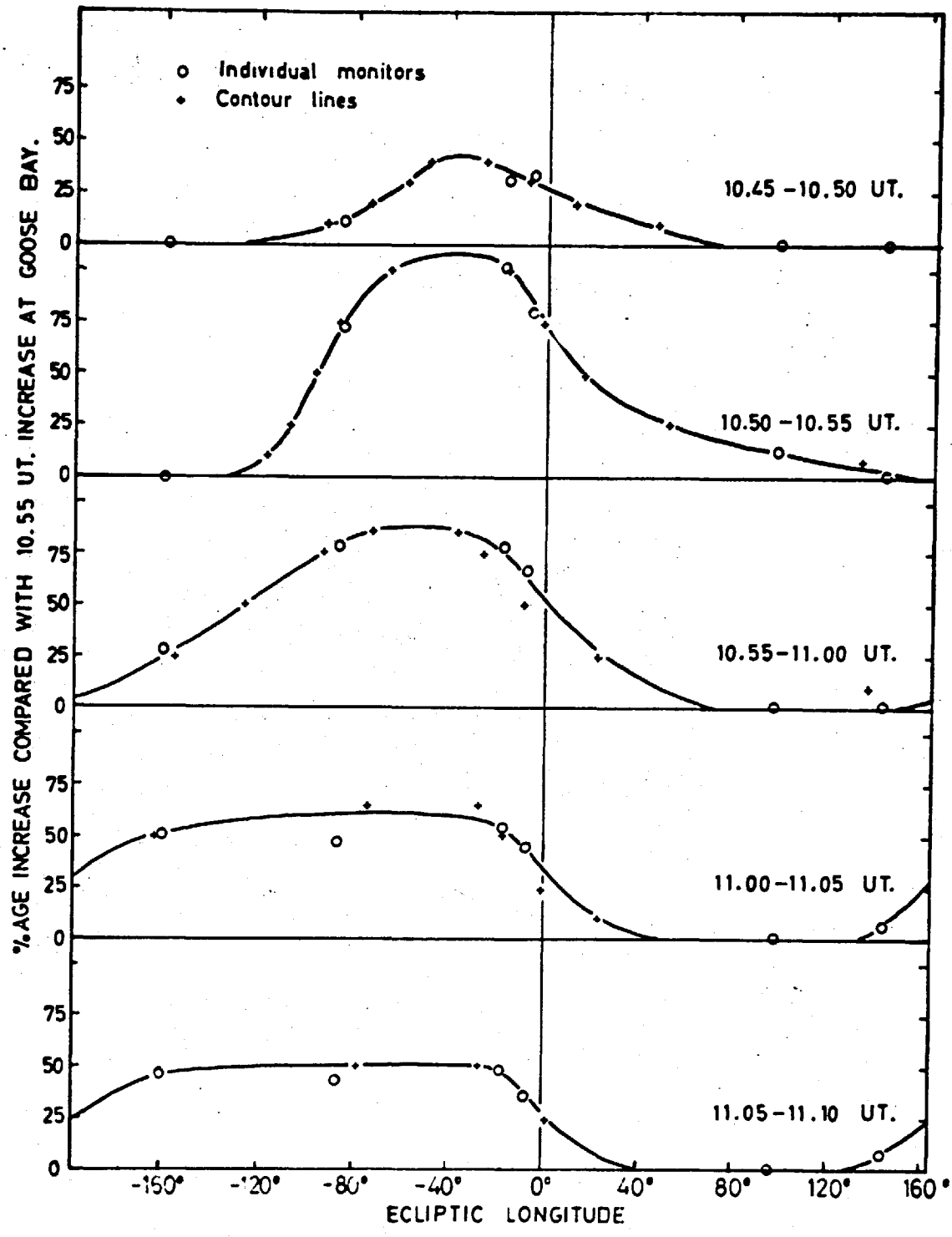

Fig. 50

Intensity variation of protons with rigidity > 1.5 GV in the ecliptic plane, as established from neutron monitor increases. Distributions are given for 5 minute averages during the first half hour of the November 18th 1968 solar flare.

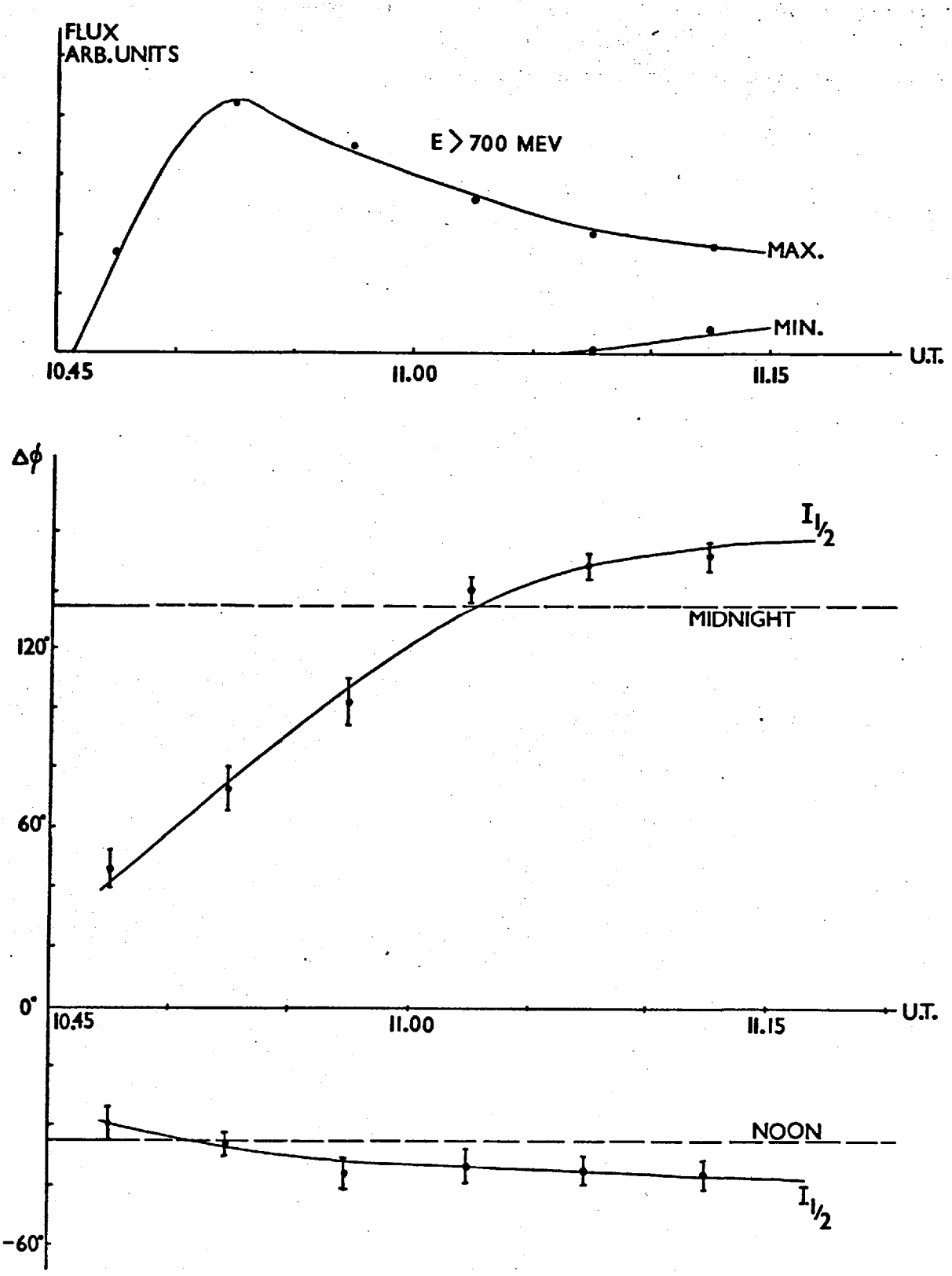

Fig. 51

Analysis of the interplanetary magnetic field provides an explanation for these observations. The asymmetric approach to isotropy means that near 90° pitch angles, which would arrive at the earth from ~ 50° ecliptic longitude, are not allowed whereas those which arrive at the earth from ~ -130° ecliptic

longitude are allowed. At about 16.30 U.T. a sudden change in the interplanetary magnetic field convects past the earth. This is interpreted here as being the boundary (possibly a tangentional discontinuity) of a new field regime, not connected to the injection region near the sun. The normal of the boundary between the two field regimes is calculated from

$$\underline{n} = \frac{\underline{B}_1 \times \underline{B}_2}{|\underline{B}_1 \times \underline{B}_2|} \qquad (5.8.3)$$

and has the components

$$\underline{n} = \underline{i} \times 0.622 + \underline{j} \times 0.359 + \underline{k} \times 0.694$$

where $\underline{i}$, $\underline{j}$ and $\underline{k}$ are the unit vectors in the solar ecliptic cartesian co-ordinate system. The colatitude of $\underline{n}$ is approximately 46°, and the solar ecliptic longitude is $\sim 30^\circ$. From the time it takes at solar wind speed (on average 4 R_E per minute) to convect this discontinuity towards the earth, and the calculated normal to this boundary, it is estimated that at the onset of the flare, this boundary was between 400 and 600 R_E away from the earth in the solar ecliptic y-z plane. The estimated position at $\sim$ 10.45 U.T. is shown in Fig. 52 where the boundary, magnetic fields etc. have all been projected into the solar ecliptic y-z and x-y planes respectively. Also indicated are the directions of arrival of high energy protons with large pitch angles. A proton of rigidity 3.5 GV has a gyroradius

$$\rho = P/_{300\ B}$$

where $\rho \simeq 300\ R_E$ in a 5 γ field.

Hence particles which arrive with large pitch angles at the earth from regions at $\sim 50^\circ$ to 120° ecliptic longitude must have crossed the discontinuity prior to being observed at the earth.

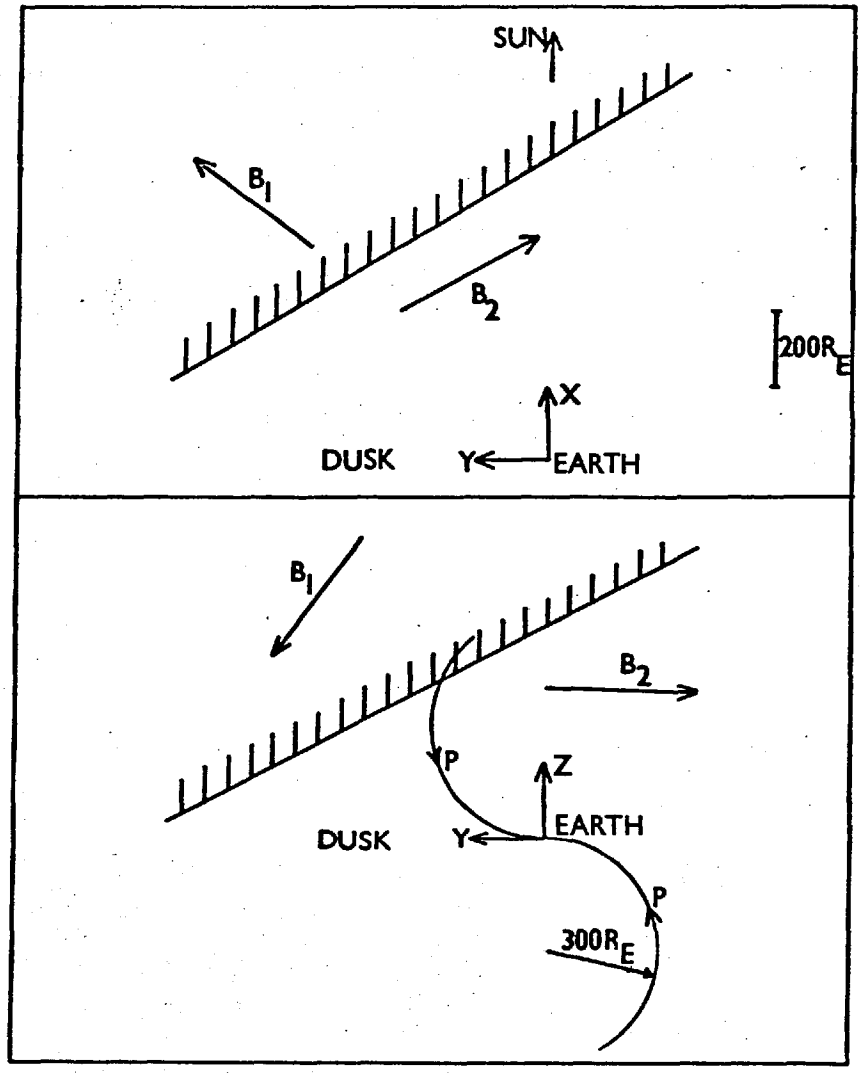

Fig. 52

The magnetic field in region I is nearly antiparallel to the field in region II, and with such a field configuration, large pitch angle particles are prevented from arriving on the dusk side of the earth.

The effect of the magnetotail on high energy (> 2 GV) particles can be investigated.

The magnetopause occurs at $\pm$ 140° longitude in Fig. 50. The pitch angle distributions show no evidence whatsoever of particles being turned round in a similar way as the 90 MeV particles observed by the ESRO II satellite detector S.28.

From the known flare spectrum and the neutron monitor response curves, we find that 14% of the increase is due to particles with rigidity less than 2.5 GV, and 45% due to particles with rigidity less than 4 GV. If we assume that the multiple magnetopause crossings, which explain the particle intensity arriving from the tail at a rigidity of about 0.5 GV, become

ineffective when Larmor radius $\gtrsim$ tail diameter, as seems likely from scattering theory, then the observations made with the neutron monitors give an upper limit of about 80 R_E to the tail diameter at large distances away from the earth (several 100 R_E). A larger diameter would produce a measurable return flux of particles. These results support theoretical calculations, and the few measurements available, that the tail does not flare out significantly.

5.9 CONCLUSIONS

Study of the entry of solar protons to the polar cap over a wide range of energies can yield several important pieces of information on the magnetotail.

Detailed studies of the effects of anisotropies in the interplanetary flux have shown that apart from a direct impact zone at auroral latitudes, transfer from interplanetary to tail field lines takes place under conditions approaching a discontinuity model for the tail magnetopause. Field departures from this discontinuity model of the interface must be small compared to the gyroradius of $>$ 26 MeV particles, so that coherent refraction of a proton beam is possible. Connection of tail field lines across the magnetopause to the interplanetary lines is required on the adopted model (Fig. 53). Surface waves, due perhaps to the Kelvin Helmholtz instability, have amplitudes comparable with the Larmor radius of a 1 MeV proton, and therefore structure can become smoothed out near the magnetopause at these energies. However, a density gradient across the tail still results. Low energy proton structure over the polar cap can also be a result of interplanetary intensity gradients. Local interplanetary intensity gradients produced by interplanetary magnetic filamentary structure, and convected at solar wind speed down the tail, can lead to large polar cap features, and can be used to estimate the length of a coherent magnetotail using the time delay between the intensity changes outside and inside the magnetosphere. Results so far indicate a coherent tail at least 500 R_E long.

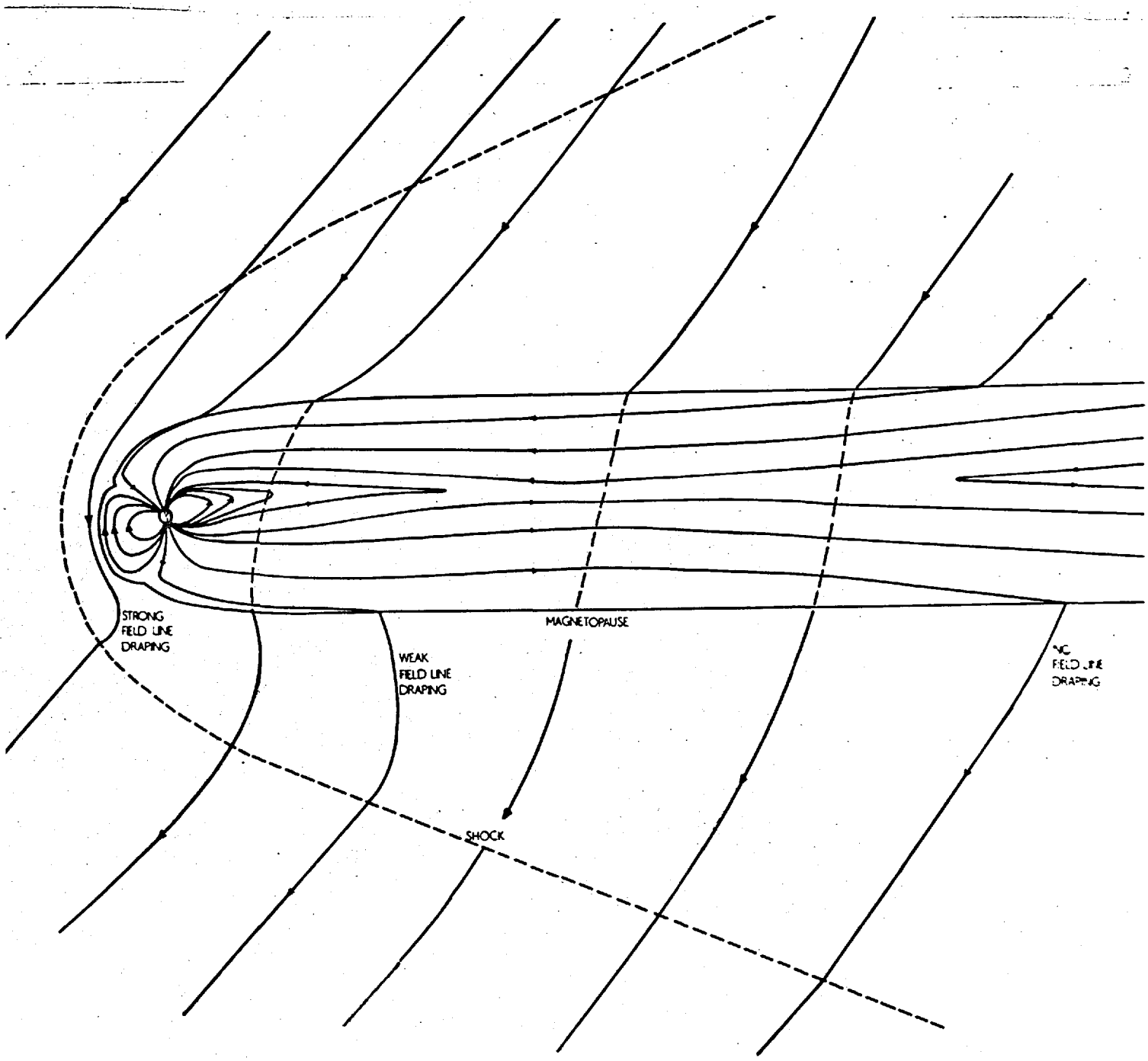

Fig. 53

Model of the geomagnetic field and tail field which agrees with the observations made and reviewed in this work.

Using the trajectory derived curves of Figs. 35a, 36a and 37b, it is possible to project a low altitude satellite orbit into the 'asymptotic' co-ordinate system produced, and to investigate fully any intensity structure in the tail.

Results from power spectral analysis, and the small amount of smoothing of interplanetary intensity time changes, when observed inside the tail, suggest that scattering is relatively unimportant in the tail. Mean free paths for 1 MeV protons are calculated to be approximately 200 R_E, and for 100 MeV protons, 700 R_E.

Simultaneous observation of particle intensity at different magnetic local times at the same drift shell in the pseudo-trapping region, should provide an estimate for the mean free path on the day side of the magnetosphere. This may be smaller than the tail mean free path because of the proximity of the shock.

A result of trajectory calculations is presented in Fig. 34, which shows that particle motion is nonadiabatic in the pseudotrapping region, especially at high latitudes where the ratio $\frac{\text{Larmor radius}}{\text{field curvature}}$ is greatest.

APPENDIX 1

The field produced by currents flowing in the magnetopause has been described by Mead (1964), who solved the 3 dimensional Chapman-Ferraro problem. Usually the field is calculated from a spherical harmonic expansion. Presently available trajectory programs (e.g. Gall et.al, 1968; Shea and Smart, 1968) use only the first two terms of this field description.

In this appendix we investigate the deficiencies of the Williams and Mead field model, when the current systems are described by an insufficient expansion.

Integration of solar proton trajectories in a high degree simulation of the geomagnetic field is necessary for the study of impact zones connected with the entry of solar protons to the polar caps. An accurate field representation out to about 20 earth radii (within the magnetosphere) is required in this work, since it is only at this distance that the tail field is sufficiently uniform to allow adiabatic extrapolations of further particle motion. Various experimental results have shown the Williams and Mead model (Mead, 1964; Williams and Mead, 1965) to provide an adequate representation of the field. These include comparisons of (i) the field model with equatorial measured constant B curves (J. G. Roederer, 1969), (ii) the calculated positions of the last closed field lines with 40 keV electron boundary and (iii) the last closed drift shell with the outer belt electron boundary.

The field model, which incorporates a dipole perpendicular to the solar wind, has been used extensively in the past (Gall et.al., 1968, 1969; M. Shea and D. Smart, 1968), but these authors only use the two-term expansion for the magnetopause current field. Mead (1964) states that this approximation was fitted to points out to 7 earth radii and results in an unrealistic representation at distances greater than 10 earth radii. Gall et.al. (1968) integrated particle trajectories for a magnetic field model, using the two-term expansion. Two of these trajectories are shown in Fig. 54 together with the tail field, calculated here, resulting from

this expansion. Although in Figs. 2 and 6 of the Gall et.al. paper, the trajectories did not follow field lines, use of the appropriate reference field in fact shows the almost adiabatic nature of the motion.

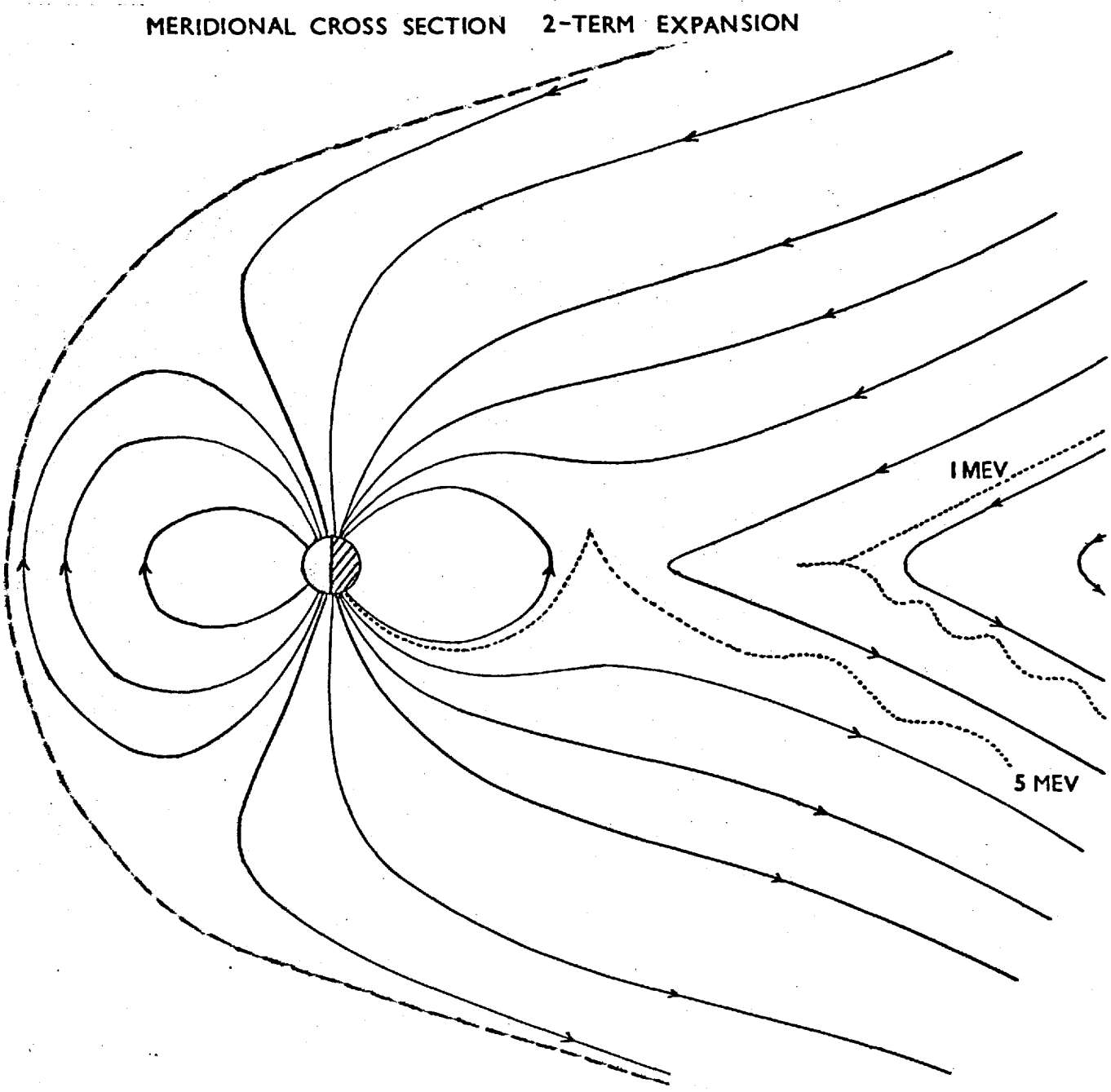

1MeV and 5MeV trajectories taken from Gall et.al. (JGR. 73, March 1968) Figs. 6 and 2 with reference field calculated here.

Fig. 54

Integrations of particle trajectories have been performed using a modified McCracken (1962) program. The geomagnetic field is described by a 6-term expansion (Finch and Leaton) of the internal field, and the Williams and Mead external field due to currents in the magnetopause (6-term expansion) and tail (plane current sheet). The model magnetopause is a surface of revolution as used by Gall et.al. Computations were performed on a CDC 6600 computer. Fig. 55 shows the difference in asymptotic approach direction when the full 6-term surface current field expansion is used and when the 2-term approximation is used. Trajectories are terminated at the magnetopause or at 25 earth radii along the tail in both cases, and the adjustable Williams and Mead parameters are the same (stand-off distance 10 R_E, R_1 = 10 R_E, R_2 = 40 R_E and tail field 40 γ). Crosses represent directions calculated using the 6-term expansion.

As can be seen, there is good agreement when the particle crosses the magnetopause on the day side, where the two-term expansion still holds, but for trajectories which go down the tail, results may be 50° longitude different, much greater than the spread due to the phase angle of the initial velocity vector direction. This is due entirely to the fact that the 2-term expansion was used in the tail where it no longer holds. In the tail region, where the trajectory is arbitrarily terminated at some distance, certain important conclusions can be reached, if the particle pitch angle is calculated, e.g. whether the particle will cross the current sheet and thus drift rapidly across the tail, whether the magnetopause is reached during the next cycle, resulting in a near-earth magnetopause crossing, or whether the particle is wholly contained in one or other of the tail lobes. In this case the information which can be obtained about the geomagnetic tail at long distances from the earth by observing solar protons in a high inclination satellite close to the earth depends only on the diffusion and scattering which the particle encounters on its way to low altitudes over the polar caps.

For the calculation of cut-off rigidities, or iso-rigidity contours, the two term expansion for the magnetopause current field might be sufficiently accurate, but the full expansion should probably be used in this case also, to avoid anomalous results at high latitudes.

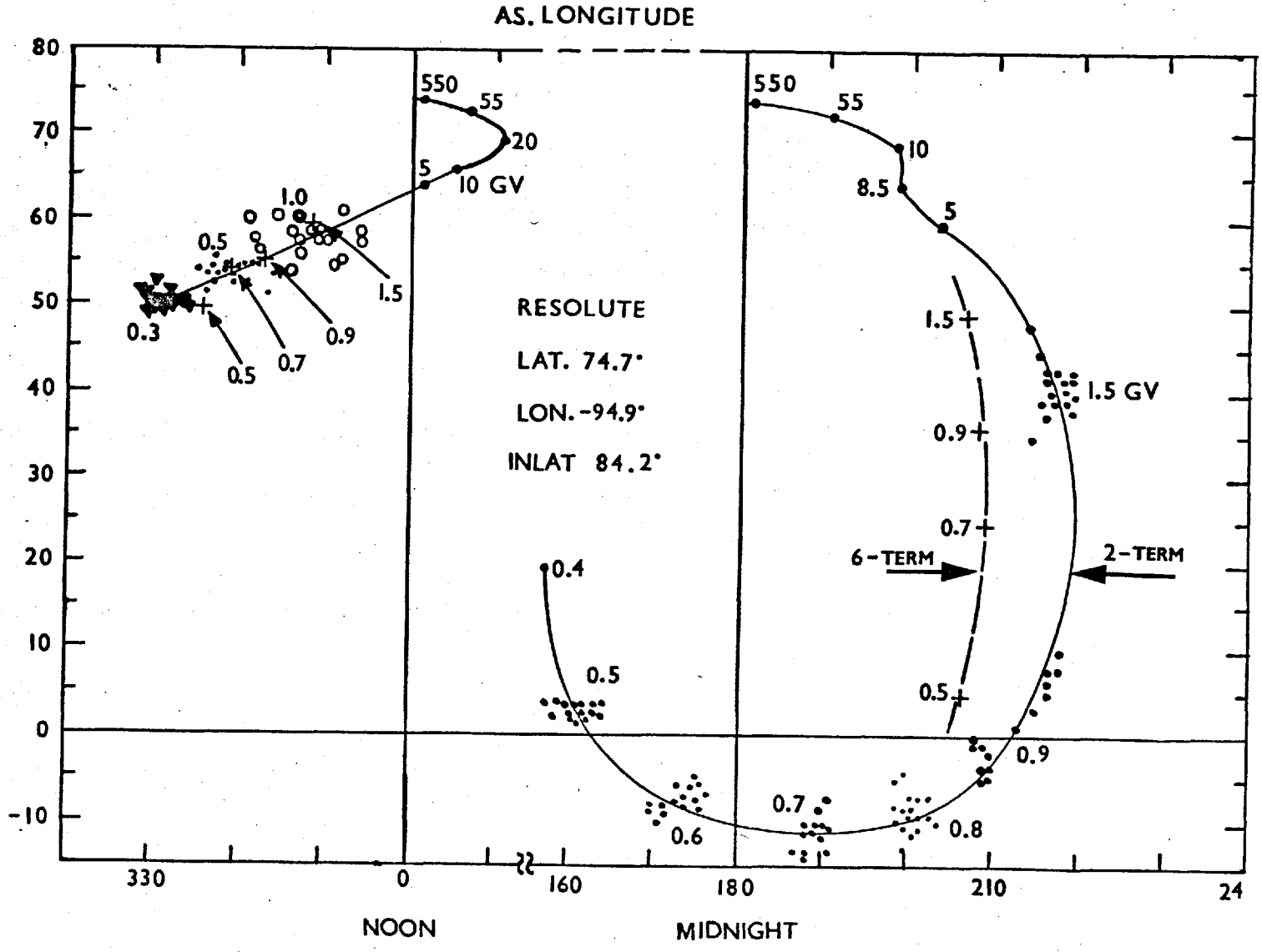

Fig. 55

APPENDIX 2

This appendix describes the different co-ordinate systems used, solar ecliptic, solar magnetospheric and geographic, and the co-ordinate transformations required to assemble the field model.

Due to the particular symmetries involved, the external sources are most easily expressed in solar magnetospheric co-ordinates, while the internal field expansion, which is fitted to experimental observations, is usually given in geographic co-ordinates. For a given time of the year, the coefficients of the transformation matrices are calculated, and then used in the magnetic field assembly program. This minimises the number of additional steps in the computations.

Definition of Co-ordinate Systems Used:

In the ecliptic frame :

x-axis parallel earth-sun line, + ve noon
z-axis perpendicular to ecliptic plane, +ve north
y-axis +ve east (orthogonal w.r.t. x and z)

In the geographic frame :

x-axis in equatorial plane, +ve passing through 0° longitude

z-axis is rotation axis of earth, +ve north
y-axis +ve east (in equatorial plane, passing through 90° longitude)

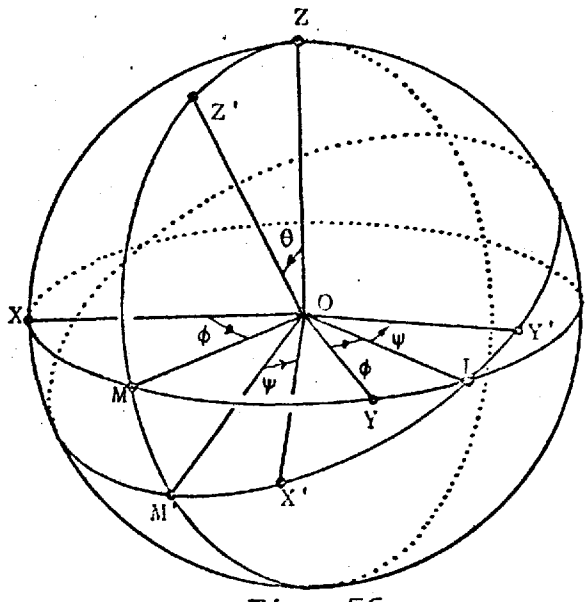

Fig. 56

θ, ϕ and ψ are the Euler angles used in transformations.

θ = angle between geographic and ecliptic z-axes = 23.5°.

θ' = geographic colatitude of position vector

ϕ' = geographic longitude of position vector

ϕ = geographic longitude passing through ecliptic z-axis

$$= \pi - \frac{U.T.}{12}\pi + (DREF - DAY)\, 2\pi/365$$

where

U.T. = universal time in decimal hours

$DREF = \frac{27}{36} \times 365 \pm 80$ (i.e. DREF - DAY $\equiv 270^{\circ}$ at spring equinox)

The solar magnetospheric co-ordinate system, rotated through an angle $-\Omega$ about its x-axis, coincides with the solar ecliptic system. Ω is the angle between the ecliptic z-axis and the projection of the dipole axis of the internal earth field in the ecliptic y-z plane.

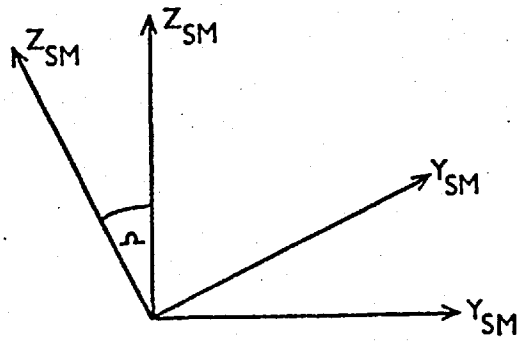

Fig. 57

Co-ordinate Transformations

Transformations of position and field vectors are necessary from geographic, solar ecliptic and solar magnetospheric co-ordinates.

Transformation from solar ecliptic to solar magnetospheric polar co-ordinates used, is :

$$r_{sM} = r_{sE}$$

$$\theta_{sM} = \cos^{-1} (\cos\theta_{sE}\cos\Omega - \sin\theta_{sE}\sin\phi_{sE}\sin\Omega)$$

$$\phi_{sM} = \tan^{-1} (\tan\phi_{sE}\cos\Omega + \cot\theta_{sE}\sec\phi_{sE}\sin\Omega)$$

where r, θ and ϕ refer to radius, colatitude and longitude in the respective system.

Transformation of a vector $\underline{B}$ from solar magnetospheric to solar ecliptic co-ordinates used, is :

$$B_x(sE) = B_x(sM)$$

$$B_y(sE) = B_y(sM)\cos\Omega - B_z(sM)\sin\Omega$$

$$B_z(sE) = B_z(sM)\cos\Omega + B_y(sM)\sin\Omega$$

Calculation of Solar Ecliptic Co-ordinates

θ_{sE}, the solar ecliptic colatitude of the position vector, is obtained from

$$\cos\theta_{sE} = \cos\theta\cos\theta' + \sin\theta\sin\theta'\cos(\phi-\phi')$$

in terms of known quantities

ϕ_{sE}, the solar ecliptic longitude of the position vector, is derived from

$$\phi_{sE} = \phi'_{sE} + N$$

Here ϕ'_{sE} = solar ecliptic longitude passing through the geographic z-axis

= (DREF - DAY) $2\pi/365$

in terms of known quantities.

N is calculated from

$$\cos N = (\cos\theta' - \cos\theta_{sE} \cos\theta) \;/\; \sin\theta' \sin\theta$$

N is negative if $0 < \phi' - \phi < \pi$ and $\phi < \pi$

or $0 > \phi - \phi' > \pi$ and $\phi > \pi$

The only shortcoming of this transformation is the fact that a centre dipole is used rather than an eccentric dipole. However, the errors introduced are smaller than the inherent errors in the field model and can be safely ignored.

To change the vector $\underline{B}$ from the ecliptic frame to the geographic frame, we must find the three Euler angles, and then use the transformation matrix. This gives :

$$\begin{aligned} B_x(G) &= B_x(sE) \,.\, (\cos\psi\cos\theta\cos\phi - \sin\psi\sin\phi) \\ &+ B_y(sE) \,.\, (-\sin\psi\cos\theta\cos\phi - \cos\psi\sin\phi) \\ &+ B_z(sE) \,.\, (\sin\theta\cos\phi) \end{aligned}$$

$$\begin{aligned} B_y(G) &= B_x(sE) \,.\, (\cos\psi\cos\theta\sin\phi + \sin\psi\cos\phi) \\ &+ B_y(sE) \,.\, (-\sin\psi\cos\theta\sin\phi + \cos\psi\cos\phi) \\ &+ B_z(sE) \,.\, (\sin\theta \sin\phi) \end{aligned}$$

$$\begin{aligned} B_z(G) &= B_x(sE) \,.\, (-\cos\psi\sin\theta) \\ &+ B_y(sE) \,.\, (\sin\psi\sin\theta) \\ &+ B_z(sE) \,.\, (\cos\theta) \end{aligned}$$

θ and ϕ are known, and the third euler angle,

$$\psi = \pi - \phi'_{sE}$$

where ϕ'_{sE} has been derived earlier.

Transformation to geographic polar co-ordinates is necessary before the external field can be added to the internal field, i.e. :

$$B_r(G) = B_z(G) \cos\theta' + B_x(G) \cos\phi' \sin\theta' + B_y(G) \sin\phi' \sin\theta'$$

$$B_{\theta'}(G) = -B_z(G) \sin\theta' + B_x(G) \cos\phi' \cos\theta' + B_y(G) \sin\phi' \cos\theta'$$

$$B_{\phi'}(G) = -B_x(G) \sin\phi' + B_y(G) \cos\phi'$$

Calculation of λ and Ω , the angles used for the tail field

θ_M = colatitude of magnetic N-pole in the geographic co-ordinate system

$= 11.8^\circ$

ϕ_M = longitude of magnetic N-pole in the geographic co-ordinate system

$= -69^\circ$

The solar ecliptic colatitude, α , is then obtained from

$$\cos\alpha = \cos\theta_M \cos\theta + \sin\theta_M \sin\theta \cos(\phi - \phi_M)$$

The solar ecliptic longitude of the magnetic N-pole, ϕ_{MSE}, is given by :

$$\phi_{MSE} = \phi'_{SE} + M$$

where M is calculated from

$$\cos M = (\cos\theta_M - \cos\alpha \cos\theta) / \sin\theta_M \sin\theta$$

M is negative, if $0 < \phi_M - \phi < \pi$ and $\phi < \pi$

or $0 > \phi - \phi_M > \pi$ and $\phi > \pi$

The angles Ω and λ are then calculated

$$\tan\Omega = -\tan\alpha\sin\phi_{MSE}$$

$$\tan\lambda = -\tan\alpha\cos\phi_{MSE}$$

The convention is, therefore,

Ω is negative, if $\phi_{MSE} < \pi$

λ is positive, if $\frac{\pi}{2} < \phi_{MSE} < \frac{3\pi}{2}$

A computer program has been developed which needs for the input variables :

1) geographic latitude of satellite (degrees)

2) geographic longitude of satellite (degrees)

3) rigidity of particle (GV)

4) azimuth and zenith angles of initial velocity vector (degrees)

5) altitude (km)

6) universal time in hours, minutes, seconds

7) day number

plus associated parameters such as step length and maximum number of steps.

Pitch angles are calculated from $\cos\beta = \underline{v}.\underline{B}$,

$$\cos\beta = v_r B_r + v_\theta B_\theta + v_\phi B_\phi$$

The magnetopause model used is the same as that used by Gall et.al. (1968).

REFERENCES

Anand et.al., Proc. Indian Academy Science, 67A, (1968), 267

Anand et. al., Phys. Rev. Letters, 20, (1968), 764

Anderson, K.A. and Lin, R.P., J.G.R., 74, (1969), 3953

Anderson, K.A., Proceedings of Santa Barbara Conference, August, 1969, B.M. McCormack

Balogh, A., A.C. Durney, H. Elliot, A.R. Engel, G. Morfill and J.J. Quenby, XI International Conference on Cosmic Rays, Budapest 1969 (to be published 1970)

Balogh, A. and R.J.Hynds, Paper presented at the third ESLAB/ESRIN symposium at Noordwijk, Holland, 1969

Bame, S.J., J.R. Ashbridge, H.E. Felthauser, E.W. Hones and I.B. Strong, J.G.R., 72, (1967), 113

Bartley et.al., J.G.R., 71, (1966), 3298

Behannon, K.W. and D.H. Fairfield, Planetary Space Science, 17, (1969), 1803

Behannon, K.W., J.G.R., 75, (1970), 743

Clark, G.W., G.P. Garmire, W.L. Kraushaar, Astrophys,J., 153, (1968), 6203

Clayton, Craddock, Astrophys, J., 142, (1965), 189

Coleman, P.J., Jr., Polar ionosphere and magnetosphere meeting Royal Society, December 1970

Cooke, B.A., R.E. Griffiths, K.A. Pounds, Nature, March 1970

Cowsik R., Yash Pal, 1969, XI Conf. on Cosmic Rays, Budapest

Davisson, C.M., R.D. Evans, Rev. Mod. Phys., 24, (1952), 79

Dessler, A.J., J.G.R., 69, (1964), 3913

Dessler, A.J., Proc. of S.Barbara Conference, 1969

Dolan, J.F., Astrophys. J., 75, (1970) 223

Dungey, J.W., Phys. Rev. Letters, 6, (1961), 47

Dungey, J.W., J.G.R., 70 (1965), 1753

Durney, A.C., and G. Morfill, to be published in 1971

Durney, A.C., G. Morfill and J.J. Quenby, to be published in 1971, in J.G.R.

Dyer, C.S., G. Morfill to be published in 1971

Elliot, H., Proceedings of the Bergen Advanced Study Institute, August 1965

Engel, A., Balogh, A., H. Elliot, P.C. Hedgecock, R.J. Hynds, J.F. Sear and J.J. Quenby, XI Int. Conf. on Cosmic Rays, Budapest, 1969

Engel, A.R., XI Intern. Conf. on Cosmic Rays, Budapest 1969 (to be published 1970)

Engelmann, J., R.J. Hynds, G. Morfill, F. Axisa, A. Bewick, A.C. Durney and L. Koch, to be published, 1971 in J.G.R.

Evans, L.C. and E.C. Stone, J.G.R., 74, (1969), 5127

Fairfield, D.H., G.S.F.C. preprint X-612-68-124, April 1968

Fairfield, D.H., G.S.F.C. preprint X-692-70-163 (1970)

Felten, J.E., P. Morrison, Phys. Rev. Letters, 10, (1963), 453

Felten, J.E., R.J. Gould, Phys. Rev. Letters, 17, (1966), 401

Felten, J.E., P. Morrison, Astrophys. J., 146, (1966), 686

Firor, J., J. Phys. Rev., 94, (1954), 1017

Fisk, L.A. and W.I. Axford, Univ. of Calif., San Diego preprint IPAPS 68/69-268, November 1968

Frank, L.A. and H.D. Owens, Univ. of Iowa preprint 69-32, 1969

Gall, R., J. Jimenez and A. Orozco, J.G.R., 74, (1969), 3529

Gall, R., J. Jimenez and L. Comacho, J.G.R., 73, (1968), 1593

Garmire, G., J.G.R., 68, (1963)

Ginzburg, V.L., S.I. Syrovatsky, Ann. Rev. Astron. Astrophysics 3, (1965), 297

Gleeson, L.J., S.M. Krimigis and W.I. Axford, to be published in J.G.R., (1971)

Gold, T., XI International Cosmic Ray Symposium, Budapest, 1969

Gould, R.J., G.R. Burbidge, Astrophys. J., 138, (1963), 969

Gould, R.J., Phys. Rev. Letters, 15, (1965), 511

Gould, R.J., Amer. J. of Physics, 35, (1967), 376

Gursky, H., ESRO Scientific note 77, 1967

Haymes, R.C., Rice University Preprint, OSO1 data

Hudson, P.D., and H.R. Anderson, J.G.R., 74, (1969), 2881

Hudson,P.D., Pl. Space Science, 18, (1970), 1611

Jokipii, J.R., Astrophys. J., 146, (1966), 480

Kane, S.R., J.R. Winckler and D.J. Hoffman, Pl. Space Science, 16, (1968), 1381

Kniffen, D.A., C.E. Fichtel, Astrophys. J., 161, (1970), L157

Lanzerotti, L.J., M.D. Montgomery and S.Singer, J.G.R., 75, (1970), 3729

Lanzerotti, L.J., Phys. Rev. Letters, 21, (1968), 929

Lin, R.P. and K.A. Anderson, Solar Physics, 1, (1967), 446

Mariani, F., B. Bavassano and N.F. Ness, G.S.F.C. preprint X-616-69-541, December 1969

Mariani, F. and N.F. Ness, J.G.R., 74, (1969), 5633

McCracken, K.G., U.R. Rao and M.A. Shea, Technical Report 77, Massachusetts Institute of Technology, 1962

McCracken, K.G. and N.F. Ness, J.G.R., 71, (1966), 3315

McCracken, K.G., U.R. Rao, R.P. Bukata and E.P. Keath, Submitted to Solar Physics (1971)

McDonald, F.B., and T.L. Cline, Solar Physics 5, (1968), 507

McKenzie, J.F., and K.O. Westphal, Phys. Fluids, 11, (1968), 2350

Mead, G.D., J.G.R., 69, (1964), 1181

Michel, F.C., Planetary and Space Science 13, (1965), 753

Michel, F.C. and A.J. Dessler, (1970), Preprint

Mihalov, J.D., D.S. Colburn and C.P. Sonett, Pl. Sp. Science, 18, (1970), 239

Montgomery, M.D. and S. Singer, J.G.R., 74, (1969), 2869

Morfill, G., to be published in Pl. Sp. Science, 1971

Morrison, P., Ann. Rev. Astron. and Astrophysics 5, (1967), 325

Nagel, H.H., Zeit. für Physik, 186, (1965), 319

Ness, N.F., J.G.R., 10, (1965), 2989

Olson, W.P., J.G.R., 74, (1969), 5642

Olson, W.P., McDonnell Douglas preprint MDAC paper WD 1332 (1970)

Peterson, L.E., H.E.A.O. proposal for U.C.S.D.

Pieper, G.F., A.J. Zmuda, C.O. Bostrom and B.J. O'Brien, J.G.R., 67, (1962), 4959

Quenby, J.J., and W.R. Webber, Cosmic rays and the earth's magnetic field p. 78 of 'Time Variations of Low Rigidity Cosmic Rays during the Recent Sunspot Cycle' by W.R. Webber. Vol. 6, 'Progress in Elementary Particle and Cosmic Ray Physics', North Holland (1962)

Quenby, J.J. and W.R. Webber, Phil. Mag. 4, (1959), 90

Quenby, J.J., A. Balogh, A. Engel, H. Elliot, P.C. Hedgecock, R.J. Hynds and J.F. Sear, XI Int. Conf. on Cosmic Rays, Budapest, 1969

Quenby, J.J., XI Int. Cosmic Ray Conf., Budapest, 1969

Quenby, J.J., and J.F. Sear, to be published in Pl. Space Science, 1971

Ray, E.C., J.G.R., 65, (1960), 1125

Rossi, B., M.I.T. Report, 1967

Sandage, A.R., Astrophys. J., 141, (1965), 1560

Sanderson, T.R., Thesis (Imp. Coll) (1970)

Schwartz, D.A., Thesis (VCSD) (1969)

Shivanandan et.al., Phys. Rev. Letters, 21, (1968), 1460

Shivanandan et.al., Astrophys. J., 157, (1969)

Seward, F.D., L.R.L. Report UCID - 15622

Smart, D.F., M.A. Shea and R. Gall, J.G.R., 74, (1969), 4731

Sood, R.K., Thesis (Imp. Coll) 1970

Southwood, J.D., Plan. Space Science, 16, (1968), 587

Speiser, T.W. and N.E. Ness, J.G.R., 72, (1967), 131

Spreiter, J.R., A.Y. Alksne and B. Abraham-Shrauner, Pl. Sp. Science, 14, (1966a), 1207

Spreiter, J.R., A.L. Summers and A.Y. Alksne, Pl. Sp. Science, 14, (1966b), 223

Spreiter, J.R., A.Y. Alksne and A.L. Summers, Physics of the Magnetosphere, Proceedings of Conf. at Boston College, 1967, p.301

Stein, J.A., W. Lewin, M.I.T. preprint 2098-243, 1966

Trombka, J.I., GSFC preprint T015215 (1970)

Van Allen, J.A., Energetic Particle phenomena in the earth's magnetospheric tail, Proc. of S. Barbara Conf., 1969

Van Allen, J.A., On the electric field in the earth's distant magnetotail, J.G.R., 75, (1970), 29

Venkatarangan, P., D. Venkatesan and J.A. van Allen, Solar flare increases in cosmic ray intensity on November 18, 1968, February 25, 1969 and March 30, 1969, University of Iowa preprint 69-47 (1969)

Vette, J.I., J.G.R., 67, (1962), No. 5

Vette, J.I., NASA SP - 3024 report (1966)

Williams, D.J. and G.D. Mead, Nightside magnetospheric configuration as obtained from trapped electrons at 1100 km., J.G.R., 70, (1965), 3017,

Williams, D.J. and C.O. Bostrom, Proton entry into the magnetosphere on May 26, 1967, J.G.R., 74, (1969), 3019